

HYDRODEOXYGENATION OF FURFURAL TO 2-METHYLFURAN USING  
MOLYBDENUM CARBIDES-BASED CATALYSTS

Letícia Forrer Sosa

Tese de Doutorado apresentada ao Programa de Pós-graduação em Engenharia Química, COPPE, da Universidade Federal do Rio de Janeiro, como parte dos requisitos necessários à obtenção do título de Doutor em Engenharia Química como parte do acordo de cotutela de doutorado entre a Universidade Federal do Rio de Janeiro e a Centrale Lille.

Orientadores: Fábio Souza Toniolo

Fábio Bellot Noronha

Sébastien Paul

Rio de Janeiro

Março de 2023

HYDRODEOXYGENATION OF FURFURAL TO 2-METHYLFURAN USING  
MOLYBDENUM CARBIDES-BASED CATALYSTS

Letícia Forrer Sosa

TESE SUBMETIDA AO CORPO DOCENTE DO INSTITUTO ALBERTO LUIZ  
COIMBRA DE PÓS-GRADUAÇÃO E PESQUISA DE ENGENHARIA DA  
UNIVERSIDADE FEDERAL DO RIO DE JANEIRO COMO PARTE DOS  
REQUISITOS NECESSÁRIOS PARA A OBTENÇÃO DO GRAU DE DOUTOR EM  
CIÊNCIAS EM ENGENHARIA QUÍMICA.

Orientadores: Fábio Souza Toniolo

Fábio Bellot Noronha

Sébastien Paul

Aprovada por: Prof. Fábio Souza Toniolo

Prof. Fábio Bellot Noronha

Prof. Sébastien Paul

Prof<sup>a</sup>. Karine Vigier de Oliveira

Prof. Marco André Fraga

Prof<sup>a</sup>. Cristiane Assumpção Henriques

Prof. Johannes Hendrik Bitter

RIO DE JANEIRO, RJ - BRASIL

MARÇO DE 2023

Sosa, Leticia Forrer

Hydrodeoxygenation of furfural to 2-methylfuran using molybdenum carbides-based catalysts / Leticia Forrer Sosa. – Rio de Janeiro: UFRJ/COPPE, 2023.

XXIX, 279 p.: il.; 29,7 cm.

Orientadores: Fábio Souza Toniolo

Fábio Bellot Noronha

Sébastien Paul

Tese (doutorado) – UFRJ/ COPPE/ Engenharia Química, 2023.

Referências Bibliográficas: p. 5-6, 63-75, 91-92, 146-150, 200-208, 252-255, 279.

1. Hidrodesoxigenação. 2. Furfural. 3. Carbetos de molibdênio. I. Toniolo, Fábio Souza *et al.*. II. Universidade Federal do Rio de Janeiro, COPPE, Programa de Engenharia Química. III. Título.

## ACKNOWLEDGMENTS

First, I would like to thank my parents Vânia and Luiz Antônio, my sister Mariana and my aunt Lorena who always encouraged my studies and supported me throughout this trajectory. Without them, nothing of this would be possible. Thanks for being always by my side.

I would like to dedicate my thesis to my friend and eternal mentor Victor Luis dos Santos Teixeira da Silva, who inspired and encouraged me during my academic and professional development. His commitment, competence, and integrity will always be an example to me.

I would like to express my gratitude to my advisors Fábio Souza Toniolo, Sébastien Paul, and Fábio Bellot Noronha for their support and guidance during the Ph.D.

I would like to thank all my colleagues and the technical staff at UCCS in France, especially Svetlana Heyte, Joelle Thuriot, and Johann Jezequel for their assistance during my laboratory activities in Lille. I also thank the Chemical Engineering Program of COPPE and my colleagues in NUCAT, especially Dora and Macarrão for all their help and patience, and for promptly making it possible to perform any experiment in the laboratory.

A special thanks to the friends I made along the way, Raphaela Azevedo, Deizi Peron, Elise Albuquerque, Leandro Souza, Mateus Paiva, Débora Dionízio, Priscilla Magalhães, Marcelo Avelar, Jonathan Bassut, Camila Ferraz and the international friends.

Finally, I thank CAPES and the CAPES-COFECUB program for the financial support to me and my program, without which this work could not have been accomplished.



Resumo da Tese apresentada à COPPE/UFRJ como parte dos requisitos necessários para a obtenção do grau de Doutor em Ciências (D.Sc.)

## HIDRODESOXIGENAÇÃO DO FURFURAL A 2-METILFURANO EMPREGANDO CATALISADORES À BASE DE CARBETOS DE MOLIBÊNIO

Letícia Forrer Sosa

Março/2023

Orientadores: Fábio Souza Toniolo

Fábio Bellot Noronha

Sébastien Paul

Programa: Engenharia Química

Carbetos de molibdênio com teor de 20% em massa de fase ativa foram sintetizados, caracterizados e avaliados na reação de hidrodesoxigenação do furfural a 2-metilfurano. Os catalisadores foram sintetizados por carburação dos precursores preparados por impregnação ao ponto úmido seguida de calcinação. Nesta tese, vários fatores com relação à natureza dos carbetos foram avaliados: (i) efeito das fases cristalográficas ( $\alpha$ -MoC e  $\beta$ -Mo<sub>2</sub>C); (ii) efeito da adição de promotores de Ni e Cu; (iii) efeito da passivação e reativação; (iv) efeito do suporte (SiO<sub>2</sub>, TiO<sub>2</sub>, ZrO<sub>2</sub>, ZSM-5). Os catalisadores foram caracterizados por ICP-OES, análise elementar, fisissorção de N<sub>2</sub>, DRX, TPC, TPD-NH<sub>3</sub>, XAS e espectroscopia Raman. Os testes catalíticos foram realizados em reatores batelada a 30 bar de H<sub>2</sub> e 200 °C em 2-butanol e ciclopentil metil éter. Os resultados mostram que a fase  $\beta$ -Mo<sub>2</sub>C é mais ativa que a fase  $\alpha$ -MoC, mas que a mesma distribuição de produtos é observada em iso-conversão. A adição de Ni e Cu teve um efeito positivo e negativo, respectivamente, na atividade do carbetos. Diferentes graus de oxidação ocorreram durante a passivação dos carbetos, o que foi relacionado à dispersão dos mesmos e a reativação não os regenerou completamente. Os diferentes suportes afetaram principalmente a primeira etapa de reação, assim como o estado final dos carbetos de Mo.

Abstract of Thesis presented to COPPE/UFRJ as partial fulfillment of the requirements for the degree of Doctor of Science (D.Sc.)

HYDRODEOXYGENATION OF FURFURAL TO 2-METHYLFURAN USING  
MOLYBDENUM CARBIDES-BASED CATALYST

Letícia Forrer Sosa

March/2023

Advisors: Fábio Souza Toniolo

Fábio Bellot Noronha

Sébastien Paul

Department: Chemical Engineering

Molybdenum carbides containing 20 wt.% of active phase were synthesized, characterized, and evaluated for the hydrodeoxygenation reaction of furfural to 2-methylfuran. The catalysts were synthesized by carburization of the precursors prepared by incipient wetness impregnation followed by calcination. In this thesis, several factors concerning the nature of carbides were evaluated: (i) the effect of crystallographic phases ( $\alpha$ -MoC and  $\beta$ -Mo<sub>2</sub>C); (ii) the effect of the addition of Ni and Cu promoters; (iii) the effect of passivation and reactivation; (iv) effect of support (SiO<sub>2</sub>, TiO<sub>2</sub>, ZrO<sub>2</sub>, ZSM-5). The catalysts were characterized by ICP-OES, elemental analysis, N<sub>2</sub> physisorption, XRD, TPC, TPD-NH<sub>3</sub>, XAS, and Raman spectroscopy. Catalytic tests were carried out in batch reactors at 30 bar of H<sub>2</sub> and 200 °C in 2-butanol and cyclopentyl methyl ether. The results show that the  $\beta$ -Mo<sub>2</sub>C phase is more active than the  $\alpha$ -MoC phase, but the same distribution of products is observed in iso-conversion. The addition of Ni and Cu had a positive and negative effect, respectively, on the carbide activity. Different degrees of oxidation occurred during the passivation of carbides, which was related to their dispersion and reactivation did not regenerate them. The different supports mainly affected the first step of the reaction, as well as the final state of the Mo carbides.

Résumé de la thèse présentée à la COPPE/UFRJ en tant qu'accomplissement partiel des exigences pour l'obtention du diplôme de Docteur en Sciences (D.Sc.)

HYDRODESOUXYGENATION DU FURFURAL EN 2-METHYLFURANE A L'AIDE  
D'UN CATALYSEUR A BASE DE CARBURE DE MOLYBDENE

Letícia Forrer Sosa

Mars/2023

Directeurs : Fábio Souza Toniolo

Fábio Bellot Noronha

Sébastien Paul

Département : Génie Chimique

Des carbures de molybdène contenant 20% en masse de phase active ont été synthétisés, caractérisés et évalués pour la réaction d'hydrodésoxygénation du furfural en 2-méthylfurane. Les catalyseurs ont été synthétisés par carburation des précurseurs préparés par imprégnation par voie humide suivie d'une calcination. Dans cette thèse, plusieurs facteurs concernant la nature des carbures ont été évalués : (i) l'effet des phases cristallographiques ( $\alpha$ -MoC et  $\beta$ -Mo<sub>2</sub>C) ; (ii) l'effet de l'addition des promoteurs Ni et Cu ; (iii) l'effet de la passivation et de la réactivation ; (iv) l'effet du support (SiO<sub>2</sub>, TiO<sub>2</sub>, ZrO<sub>2</sub>, ZSM-5). Les catalyseurs ont été caractérisés par ICP-OES, analyse élémentaire, physisorption de N<sub>2</sub>, XRD, TPC, TPD-NH<sub>3</sub>, XAS, et spectroscopie Raman. Les tests catalytiques ont été réalisés dans des réacteurs batch à 30 bar de H<sub>2</sub>, 200 °C dans le 2-butanol et le cyclopentyl méthyl éther. Les résultats montrent que la phase  $\beta$ -Mo<sub>2</sub>C est plus active que la phase  $\alpha$ -MoC, mais la même distribution des produits est observée en iso-conversion. L'ajout de Ni et de Cu a eu un effet positif et négatif, respectivement, sur l'activité du carbure. Différents degrés d'oxydation ont eu lieu pendant la passivation des carbures, ce qui était lié à leur dispersion et la réactivation ne les a pas régénérés. Les différents supports ont principalement affecté la première étape de la réaction ainsi que l'état final des carbures de Mo.

# CONTENT

CHAPTER 1 - Introduction.....	1
1. Introduction .....	2
1.1 References .....	5
CHAPTER 2 - Bibliographic review.....	7
2. Bibliographic review .....	8
2.1 Biomass as an alternative to fossil fuels.....	8
2.1.1 Lignocellulosic biomass .....	9
2.1.2 Biorefinery: Biomass valorization.....	10
2.2 Furfural: a sustainable platform molecule.....	13
2.2.1 Reductive conversion of furfural.....	18
2.3 2-Methylfuran.....	20
2.3.1 Hydrodeoxygenation of furfural to 2-methylfuran.....	22
2.3.1.1 Effect of the reaction conditions.....	37
2.3.1.1.1 Temperature, pressure, and reaction time.....	37
2.3.1.1.2 Effect of substrate concentration and catalyst amount.....	39
2.3.1.1.3 Solvent effect.....	41
2.3.1.2 Catalyst for furfural hydrodeoxygenation .....	43
2.3.1.2.1 Support effect .....	43
2.3.1.2.2 Nature of the metal phase .....	46
2.4 Transition metal carbides.....	55
2.4.1 Definition and properties .....	56
2.4.2 Synthesis of carbides .....	56

2.4.3 The use of carbides in hydrodeoxygenation reactions .....	61
2.5 Conclusions .....	61
2.6 References .....	63
CHAPTER 3. Methodology .....	76
3. Methodology.....	77
3.1 Preparation of the catalysts.....	77
3.1.1 Treatment of the supports.....	77
3.1.2 Preparation of the precursors.....	77
3.1.3 Synthesis of molybdenum carbides.....	78
3.1.4 Passivation.....	79
3.2 Characterization.....	79
3.2.1 Chemical analyses .....	79
3.2.1.1 Inductively Coupled Plasma Optical Emission Spectroscopy (ICP-OES)	
.....	79
3.2.1.2 Elemental analysis (EA).....	80
3.2.2 Textural and morphological properties .....	80
3.2.2.1 N <sub>2</sub> physisorption .....	80
3.2.2.2 X-Ray diffraction (XRD) .....	80
3.2.2.3 Temperature-programmed carburization (TPC).....	81
3.2.2.4 Temperature-programmed desorption of NH <sub>3</sub> (TPD-NH <sub>3</sub> ).....	82
3.2.3 Spectroscopic techniques.....	82
3.2.3.1 X-Ray absorption spectroscopy (XAS).....	82
3.3 Catalytic performance evaluation.....	85
3.3.1 Materials.....	85
3.3.2 Experimental set-up.....	85

3.3.2.1 Screening Pressure Reactor (SPR) .....	85
3.3.2.2 Parr reactor .....	86
3.3.2.3 Description of catalysts activation in H <sub>2</sub> .....	87
3.3.2.4 Description of the experimental catalytic tests.....	88
3.3.3 Analytical methods .....	89
3.4 References .....	91
CHAPTER 4. Characterization of unsupported and SiO <sub>2</sub> -supported Mo <sub>2</sub> C and metal-promoted Mo carbides by <i>in situ</i> X-ray absorption spectroscopy, temperature-programmed carburization, and x-ray diffraction.....	93
4. Introduction .....	94
4.1 Results and discussions .....	95
4.1.1 Characterization.....	95
4.2 Conclusion.....	144
4.3 References .....	146
CHAPTER 5. Hydrodeoxygenation of furfural over unsupported and SiO <sub>2</sub> -supported Mo <sub>2</sub> C and metal-promoted Mo carbides. Tuning the selectivity between 2-methylfuran and C <sub>10</sub> furoins diesel precursors.....	151
5. Introduction .....	152
5.1 Results and discussions .....	154
5.1.1 Characterization.....	154
5.1.2 Catalytic results .....	189
5.1.3 Conclusions .....	198
5.2 References .....	200
CHAPTER 6. Hydrodeoxygenation of furfural to 2-methylfuran using supported Mo carbides. Study of the support effect. ....	209
6. Introduction .....	210

6.1 Results and discussions .....	211
6.1.1 Characterization.....	211
6.1.2 Catalytic results .....	243
6.2 Conclusions .....	250
6.3 References .....	252
7. Conclusions and suggestions.....	256
ANNEX A - Typical chromatograms and mass spectra.....	260
A.1. References.....	279

## LIST OF FIGURES

Figure 1.1. World primary energy consumption by fuel. ....	2
Figure 2.1. Lignocellulosic biomass main components. ....	9
Figure 2.2. Main technologies for the conversion of lignocellulosic biomass. ....	11
Figure 2.3. Main products derived from furfural. ....	16
Figure 2.4. Reductive conversion of furfural to value-added chemicals. ....	18
Figure 2.5. The structural formula of 2-methylfuran. ....	20
Figure 2.6. Production of an alkane mixture suitable to be mixed with commercial diesel fuel from 2MF alkylation/hydroxyalkylation followed by hydrodeoxygenation reaction. ....	22
Figure 2.7. Possible CTH reaction pathways: direct/indirect hydrogen transfer mechanisms. ....	24
Figure 2.8. Solvent effects on product yields of FF hydrogenation on $\alpha$ -MoC catalysts. ....	42
Figure 2.9. Possible reaction pathway for the hydrogenolysis of FF over Cu/AC catalyst. ....	47
Figure 2.10. Reaction pathways in the HDO of furfural to 2MF. ....	52
Figure 2.11. Reaction mechanism of FA hydrogenolysis to 2MF via (i) direct hydrogenolysis and (ii) hydrogenolysis via furan ring activation. ....	52
Figure 2.12. CTH of furfural by alcohol on $\alpha$ -MoC surfaces. ....	54
Figure 2.13. H <sub>2</sub> O and CO formation profiles during carburation of MoO <sub>3</sub> in an atmosphere of (a) 20% (v/v) CH <sub>4</sub> /H <sub>2</sub> and (b) H <sub>2</sub> . ....	58
Figure 2.14. Diffractograms obtained during the TPC of molybdic acid in 10% (v/v) CH <sub>4</sub> /H <sub>2</sub> atmosphere. ....	60
Figure 2.15. Routes for Mo carbide formation from MoO <sub>3</sub> by TPC. ....	60



Figure 3.1. Screening Pressure Reactor (SPR).....	86
Figure 3.2. Parr reactor.....	87
Figure 4.1. XANES spectra recorded at the Mo K-edge for the calcined precursors. Comparison with reference MoO <sub>3</sub> .....	97
Figure 4.2. EXAFS signals recorded at the Mo K-edge for the calcined precursors. Comparison with reference MoO <sub>3</sub> .....	98
Figure 4.3. Fourier transforms of the EXAFS signals recorded at the Mo K-edge for the calcined precursors ( $k = 3.5 - 15 \text{ \AA}^{-1}$ ). Comparison with reference MoO <sub>3</sub> .....	99
Figure 4.4. Raman spectra for the calcined precursors of Cu-Mo <sub>x</sub> C <sub>y</sub> /SiO <sub>2</sub> , Ni-Mo <sub>x</sub> C <sub>y</sub> /SiO <sub>2</sub> , and Mo <sub>2</sub> C/SiO <sub>2</sub> (recorded at room temperature).....	100
Figure 4.5. Diffractograms of the calcined precursors of unsupported and SiO <sub>2</sub> -supported Mo carbides. ....	101
Figure 4.6. XANES spectra recorded at the Mo K-edge for the carburized catalysts (spectra recorded at room temperature). Comparison with reference $\beta$ -Mo <sub>2</sub> C. ....	102
Figure 4.7. EXAFS signals recorded at the Mo K-edge for the carburized catalysts (spectra recorded at room temperature). Comparison with reference $\beta$ -Mo <sub>2</sub> C. ....	103
Figure 4.8. Fourier transforms of the EXAFS signals recorded at the Mo K-edge for the carburized catalysts (spectra recorded at room temperature, $k = 3.5 - 15 \text{ \AA}^{-1}$ ). Comparison with reference $\beta$ -Mo <sub>2</sub> C.....	104
Figure 4.9. XAS data at the Mo K-edge after carburization of a) $\beta$ -Mo <sub>2</sub> C after reactivation in H <sub>2</sub> at 400 °C, and b) Mo <sub>2</sub> C/SiO <sub>2</sub> (spectra recorded at room temperature). Fit of the first and second shells of neighbors: Fourier transform (left) and EXAFS oscillations (right). $k = 3.5 - 15 \text{ \AA}^{-1}$ .....	106
Figure 4.10. XAS data at the Mo K-edge after carburization of a) Ni-Mo <sub>x</sub> C <sub>y</sub> /SiO <sub>2</sub> and b) Cu-Mo <sub>x</sub> C <sub>y</sub> /SiO <sub>2</sub> (spectra recorded at room temperature). Fit of the first and second shells of neighbors: Fourier transform (left) and EXAFS oscillations (right). $k = 3.5 - 15 \text{ \AA}^{-1}$ .....	107

Figure 4.11. Evolution of the XAS spectra of Mo <sub>2</sub> C/SiO <sub>2</sub> at the Mo K-edge upon carburization (from room temperature, dark blue, to 650 °C, red). For the sake of clarity, every 8 <sup>th</sup> spectrum is shown only. ....	109
Figure 4.12. Evolution of the XAS spectra of Ni-Mo <sub>x</sub> C <sub>y</sub> /SiO <sub>2</sub> at the Mo K-edge upon carburization (from room temperature, dark blue, to 650 °C, red). For the sake of clarity, every 2 <sup>nd</sup> spectrum is shown only. ....	109
Figure 4.13. Evolution of the XAS spectra of Cu-Mo <sub>x</sub> C <sub>y</sub> /SiO <sub>2</sub> at the Mo K-edge upon carburization (from room temperature, dark blue, to 650 °C, red). For the sake of clarity, every 2 <sup>nd</sup> spectrum is shown only. ....	110
Figure 4.14. MCR-ALS analysis at the Mo-K edge of the carburization ramp: characteristics of the first spectral components. a) XANES spectra, b) EXAFS oscillations. ....	111
Figure 4.15. MCR-ALS analysis at the Mo-K edge of the carburization ramp: characteristics of the second components. a) XANES spectra and b) derivatives, c) EXAFS oscillations, d) Fourier transforms ( $k = 3.5 - 15 \text{ \AA}^{-1}$ ). Comparison with references MoO <sub>3</sub> and MoO <sub>2</sub> . ....	113
Figure 4.16. MCR-ALS analysis at the Mo-K edge of the carburization ramp: characteristics of the third components. a) XANES spectra and b) derivatives, c) EXAFS oscillations, d) Fourier transforms ( $k = 3.5 - 15 \text{ \AA}^{-1}$ ). Comparison with references MoO <sub>2</sub> and Mo foil. ....	115
Figure 4.17. MCR-ALS analysis at the Mo K-edge of the carburization of Cu-Mo <sub>x</sub> C <sub>y</sub> /SiO <sub>2</sub> . Fit of the first and second shells of neighbors for the second spectral component (a) compared with reference monoclinic MoO <sub>2</sub> (b): Fourier transform ( $k = 3.5 - 15 \text{ \AA}^{-1}$ , left) and EXAFS oscillations (right). See Table 4.2. ....	117
Figure 4.18. MCR-ALS analysis at the Mo K-edge of the carburization of Cu-Mo <sub>x</sub> C <sub>y</sub> /SiO <sub>2</sub> . Fit of the first and second shells of neighbors for the second spectral component (a) compared with reference monoclinic MoO <sub>2</sub> (b): Fourier transform ( $k = 3.5 - 15 \text{ \AA}^{-1}$ , left) and EXAFS oscillations (right). See Table 4.2. ....	118

Figure 4.19. MCR-ALS analysis at the Mo-K edge of the carburization ramp: characteristics of the fourth components. a) XANES spectra, b) EXAFS oscillations. Dotted lines: EXAFS oscillations of the carburized catalysts recorded at room temperature.....	120
Figure 4.20. Evolution of the XAS spectra of Ni-Mo <sub>x</sub> C <sub>y</sub> /SiO <sub>2</sub> at the Ni K-edge upon carburization (from room temperature, dark blue, to 650 °C, red).....	121
Figure 4.21. XAS data at the Ni K-edge of the Ni-Mo <sub>x</sub> C <sub>y</sub> /SiO <sub>2</sub> calcined precursor. a) XANES spectrum and b) EXAFS oscillations, comparison with reference NiO. Fit of the first and second shells of neighbors: c) Fourier transform and d) EXAFS oscillations, k = 3 - 13 Å <sup>-1</sup> . .....	122
Figure 4.22. XAS data at the Ni K-edge of the Ni-Mo <sub>x</sub> C <sub>y</sub> /SiO <sub>2</sub> catalyst, recorded during carburization, at 400 °C. a) XANES spectrum and b) EXAFS oscillations, comparison with reference Ni foil. c) Comparison of the Fourier transforms, k = 3 - 13 Å <sup>-1</sup> . .....	124
Figure 4.23. XAS data at the Ni K-edge of the Ni-Mo <sub>x</sub> C <sub>y</sub> /SiO <sub>2</sub> catalyst after carburization. a) XANES spectrum and b) EXAFS oscillations, comparison with reference NiO. Spectra recorded at room temperature. ....	125
Figure 4.24. XAS data a) of Ni-Mo <sub>x</sub> C <sub>y</sub> /SiO <sub>2</sub> at the Ni K-edge and b) of Cu-Mo <sub>x</sub> C <sub>y</sub> /SiO <sub>2</sub> at the Cu K-edge, after carburization (spectra recorded at room temperature). Fit of the first shell of neighbors: Fourier transform (left) and EXAFS oscillations (right), k = 3 - 13 Å <sup>-1</sup> at the Ni K-edge, k = 3.5 - 14 Å <sup>-1</sup> at the Cu K-edge.....	126
Figure 4.25. MCR-ALS analysis at the Ni-K edge of the carburization of Ni-Mo <sub>x</sub> C <sub>y</sub> /SiO <sub>2</sub> : comparison of the first component with the calcined precursor. a) XANES spectrum, b) EXAFS oscillations, c) Fourier transform, k = 3 - 13 Å <sup>-1</sup> . .....	127
Figure 4.26. MCR-ALS analysis at the Ni-K edge of the carburization of Ni-Mo <sub>x</sub> C <sub>y</sub> /SiO <sub>2</sub> : comparison of the second component with the spectrum recorded at 400 °C during carburization. a) XANES spectrum, b) EXAFS oscillations, c) Fourier transform, k = 3 - 13 Å <sup>-1</sup> . .....	128
Figure 4.27. MCR-ALS analysis at the Ni-K edge of the carburization of Ni-Mo <sub>x</sub> C <sub>y</sub> /SiO <sub>2</sub> : comparison of the third component with the spectrum recorded after	

carburization at room temperature. a) XANES spectrum, b) EXAFS oscillations, c) Fourier transform, $k = 3 - 13 \text{ \AA}^{-1}$ .....	129
Figure 4.28. Evolution of the XAS spectra of Cu-Mo <sub>x</sub> C <sub>y</sub> /SiO <sub>2</sub> at the Cu K-edge upon carburization (from room temperature, dark blue, to 650 °C, red).....	130
Figure 4.29. XAS data at the Cu K-edge of the Cu-Mo <sub>x</sub> C <sub>y</sub> /SiO <sub>2</sub> calcined precursor. a) XANES spectrum and b) EXAFS oscillations, comparison with reference CuO. Fit of the first shell of neighbors: c) Fourier transform and d) EXAFS oscillations, $k = 3.5 - 14 \text{ \AA}^{-1}$ .....	131
Figure 4.30. XAS data at the Cu K-edge of the Cu-Mo <sub>x</sub> C <sub>y</sub> /SiO <sub>2</sub> catalyst, recorded during carburization, at 200 °C: a) XANES spectrum and b) EXAFS oscillations; and at 240 °C: c) XANES spectrum and d) EXAFS oscillations. Comparison with references Cu foil and Cu <sub>2</sub> O.....	133
Figure 4.31. Comparison of the Fourier transforms at the Cu-K edge of catalyst Cu-Mo <sub>x</sub> C <sub>y</sub> /SiO <sub>2</sub> at two stages of carburization (200 and 240 °C), and reference metallic Cu foil and Cu <sub>2</sub> O (FT shifted along the vertical axis). $k = 3.5 - 14 \text{ \AA}^{-1}$ .....	134
Figure 4.32. XAS data at the Cu K-edge of the Cu-Mo <sub>x</sub> C <sub>y</sub> /SiO <sub>2</sub> catalyst after carburization (spectrum recorded at room temperature). a) XANES spectrum and b) EXAFS oscillations, comparison with reference Cu foil. ....	135
Figure 4.33. MCR-ALS analysis at the Cu-K edge of the carburization of Cu-Mo <sub>x</sub> C <sub>y</sub> /SiO <sub>2</sub> : comparison of the first component with the calcined precursor. a) XANES spectrum, b) EXAFS oscillations, c) Fourier transform, $k = 3.5 - 14 \text{ \AA}^{-1}$ .....	136
Figure 4.34. MCR-ALS analysis at the Cu-K edge of the carburization of Cu-Mo <sub>x</sub> C <sub>y</sub> /SiO <sub>2</sub> : comparison of the second component with references Cu foil and Cu <sub>2</sub> O. a) XANES spectrum, b) EXAFS oscillations, c) Fourier transform, $k = 3.5 - 14 \text{ \AA}^{-1}$ ....	137
Figure 4.35. MCR-ALS analysis at the Cu-K edge of the carburization of Cu-Mo <sub>x</sub> C <sub>y</sub> /SiO <sub>2</sub> : comparison of the third component with reference Cu foil. a) XANES spectrum, b) EXAFS oscillations, c) Fourier transform, $k = 3.5 - 14 \text{ \AA}^{-1}$ .....	138

Figure 4.36. MCR-ALS analysis at the Cu-K edge of the carburization of Cu-Mo <sub>x</sub> C <sub>y</sub> /SiO <sub>2</sub> : comparison of the fourth component with reference Cu foil. a) XANES spectrum, b) EXAFS oscillations, c) Fourier transform, $k = 3.5 - 14 \text{ \AA}^{-1}$ . .....	139
Figure 4.37. Water and CO formation profiles during temperature-programmed carburization of the calcined precursors of Cu-Mo <sub>x</sub> C <sub>y</sub> /SiO <sub>2</sub> , Ni-Mo <sub>x</sub> C <sub>y</sub> /SiO <sub>2</sub> , Mo <sub>2</sub> C/SiO <sub>2</sub> , and Mo <sub>2</sub> C.....	140
Figure 4.38. Concentrations profiles of Mo, Ni, and Cu species during TPC of the calcined precursors of a) Mo <sub>2</sub> C/SiO <sub>2</sub> , b) Ni-Mo <sub>x</sub> C <sub>y</sub> /SiO <sub>2</sub> , and c) Cu-Mo <sub>x</sub> C <sub>y</sub> /SiO <sub>2</sub> from MCR-ALS analysis of the Mo, Ni, and Cu K-edge data. ....	142
Figure 5.1. N <sub>2</sub> adsorption-desorption isotherms of SiO <sub>2</sub> and passivated catalysts.....	155
Figure 5.2. Diffractograms of SiO <sub>2</sub> and passivated Mo carbides. $\blacklozenge$ $\beta$ -Mo <sub>2</sub> C, $\bullet$ $\alpha$ -MoC, $\circ$ SiO <sub>2</sub> .....	157
Figure 5.3. XANES spectra recorded at the Mo K-edge for the passivated catalysts (spectra recorded at room temperature). Comparison with references MoO <sub>3</sub> and metallic Mo (dotted lines). ....	159
Figure 5.4. EXAFS signals recorded at the Mo K-edge for the passivated catalysts (spectra recorded at room temperature). Comparison with reference MoO <sub>3</sub> . ....	160
Figure 5.5. Fourier transforms of the EXAFS signals recorded at the Mo K-edge for the passivated catalysts ( $k = 3.5 - 15 \text{ \AA}^{-1}$ , spectra recorded at room temperature). Comparison with reference MoO <sub>3</sub> .....	161
Figure 5.6. Analysis of the data recorded at the Mo K-edge for the passivated catalysts (spectra recorded at room temperature), using linear combinations of MCR-ALS components (see Table 5.2). XANES spectrum (left) and EXAFS oscillations (right), a) $\beta$ -Mo <sub>2</sub> C and b) $\beta$ -Mo <sub>2</sub> C/SiO <sub>2</sub> .....	164
Figure 5.7. Analysis of the data recorded at the Mo K-edge for the passivated catalysts (spectra recorded at room temperature), using linear combinations of MCR-ALS components (see Table 5.2). XANES spectrum (left) and EXAFS oscillations (right), a) Ni-Mo <sub>x</sub> C <sub>y</sub> /SiO <sub>2</sub> and b) Cu-Mo <sub>x</sub> C <sub>y</sub> /SiO <sub>2</sub> . ....	165

Figure 5.8. XANES spectra recorded at the Mo K-edge for the reactivated catalysts (spectra recorded at room temperature). Comparison with references MoO <sub>3</sub> and metallic Mo (dotted lines). .....	166
Figure 5.9. EXAFS signals recorded at the Mo K-edge for the passivated catalysts after reactivation (spectra recorded at room temperature). Comparison with reference β-Mo <sub>2</sub> C.....	167
Figure 5.10. Fourier transforms of the EXAFS signals recorded at the Mo K-edge for the passivated catalysts after reactivation (k = 3.5 - 15 Å <sup>-1</sup> , spectra recorded at room temperature). Comparison with reference β-Mo <sub>2</sub> C. ....	168
Figure 5.11. XAS data at the Mo K-edge of the passivated catalysts after reactivation (spectrum recorded at room temperature). Fit of the first and second shells of neighbors: Fourier transform (k = 3.5 - 15 Å <sup>-1</sup> , left) and EXAFS oscillations (right), a) β-Mo <sub>2</sub> C and b) β-Mo <sub>2</sub> C /SiO <sub>2</sub> . ....	169
Figure 5.12. XAS data at the Mo K-edge of the passivated catalysts after reactivation (spectrum recorded at room temperature). Fit of the first and second shells of neighbors: Fourier transform (left) and EXAFS oscillations (right), a) Ni-Mo <sub>x</sub> C <sub>y</sub> /SiO <sub>2</sub> and b) Cu-Mo <sub>x</sub> C <sub>y</sub> /SiO <sub>2</sub> .....	170
Figure 5.13. Analysis of the data recorded at the Mo K-edge for the passivated catalysts after reactivation (spectra recorded at room temperature), using linear combinations of MCR-ALS components (see Table 5.2). XANES spectrum (left) and EXAFS oscillations (right), a) Ni-Mo <sub>x</sub> C <sub>y</sub> /SiO <sub>2</sub> and b) Cu-Mo <sub>x</sub> C <sub>y</sub> /SiO <sub>2</sub> . ....	172
Figure 5.14. XAS data at the Cu K-edge of the Cu-Mo <sub>x</sub> C <sub>y</sub> /SiO <sub>2</sub> catalyst after passivation. a) XANES spectrum and b) EXAFS oscillations, comparison with references CuO and Cu <sub>2</sub> O. Fit of the first shell of neighbors: c) Fourier transform and d) EXAFS oscillations. k = 3.5 - 14 Å <sup>-1</sup> .....	173
Figure 5.15. XAS data at the Cu K-edge of the passivated Cu-Mo <sub>x</sub> C <sub>y</sub> /SiO <sub>2</sub> catalyst after reactivation (spectrum recorded at room temperature). a) XANES spectrum and b) EXAFS oscillations, comparison with reference Cu foil. Fit of the first shell of neighbors: c) Fourier transform and d) EXAFS oscillations. k = 3.5 - 14 Å <sup>-1</sup> . ....	175

Figure 5.16. XAS data at the Ni K-edge of the Ni-Mo <sub>x</sub> C <sub>y</sub> /SiO <sub>2</sub> catalyst after passivation. a) XANES spectrum and b) EXAFS oscillations, comparison with reference NiO. Fit of the first and second shells of neighbors: c) Fourier transform and d) EXAFS oscillations. $k = 3 - 13 \text{ \AA}^{-1}$ . .....	177
Figure 5.17. XAS data at the Ni K-edge of the passivated Ni-Mo <sub>x</sub> C <sub>y</sub> /SiO <sub>2</sub> catalyst after reactivation (spectrum recorded at room temperature). a) XANES spectrum and b) EXAFS oscillations, comparison with reference Ni foil. Fit of the first shell of neighbors: c) Fourier transform and d) EXAFS oscillations. $k = 3 - 13 \text{ \AA}^{-1}$ . .....	179
Figure 5.18. Evolution of the XAS spectra of passivated $\beta$ -Mo <sub>2</sub> C at the Mo K-edge upon reactivation (from room temperature, dark blue, to 400 °C, red). Every 8 <sup>th</sup> spectrum is shown only. ....	180
Figure 5.19. Evolution of the XAS spectra of passivated $\beta$ -Mo <sub>2</sub> C/SiO <sub>2</sub> at the Mo K-edge upon reactivation (from room temperature, dark blue, to 400 °C, red). For the sake of clarity, every 8 <sup>th</sup> spectrum is shown only. ....	181
Figure 5.20. Evolution of the XAS spectra of passivated Ni-Mo <sub>x</sub> C <sub>y</sub> /SiO <sub>2</sub> at the Mo K-edge upon reactivation (from room temperature, dark blue, to 400 °C, red). ....	182
Figure 5.21. Evolution of the XAS spectra of passivated Ni-Mo <sub>x</sub> C <sub>y</sub> /SiO <sub>2</sub> at the Ni K-edge upon reactivation (from room temperature, dark blue, to 400 °C, red). ....	183
Figure 5.22. MCR-ALS analysis of the reduction of passivated Ni-Mo <sub>x</sub> C <sub>y</sub> /SiO <sub>2</sub> : comparison of the first component with NiO. a) XANES spectrum, b) EXAFS oscillations, c) Fourier transform. $k = 3 - 13 \text{ \AA}^{-1}$ . ....	184
Figure 5.23. MCR-ALS analysis of the reduction of passivated Ni-Mo <sub>x</sub> C <sub>y</sub> /SiO <sub>2</sub> : comparison of the second component with the spectrum recorded after reactivation at room temperature. a) XANES spectrum, b) EXAFS oscillations, c) Fourier transform. $k = 3 - 13 \text{ \AA}^{-1}$ . ....	185
Figure 5.24. Evolution of the XAS spectra of passivated Cu-Mo <sub>x</sub> C <sub>y</sub> /SiO <sub>2</sub> at the Mo K-edge upon reactivation (from room temperature, dark blue, to 400 °C, red). ....	186
Figure 5.25. Evolution of the XAS spectra of passivated Cu-Mo <sub>x</sub> C <sub>y</sub> /SiO <sub>2</sub> at the Cu K-edge upon reactivation (from room temperature, dark blue, to 400 °C, red). ....	187

Figure 5.26. Concentrations profiles of Mo, Ni, and Cu species during reactivation in H <sub>2</sub> of the passivated a) $\beta$ -Mo <sub>2</sub> C, b) $\beta$ -Mo <sub>2</sub> C/SiO <sub>2</sub> , c) Ni-Mo <sub>x</sub> C <sub>y</sub> /SiO <sub>2</sub> , and d) Cu-Mo <sub>x</sub> C <sub>y</sub> /SiO <sub>2</sub> catalysts from MCR-ALS analysis of the Mo, Ni, and Cu K-edge data..	188
Figure 5.27. Product yields versus FF conversion for Ni-Mo <sub>x</sub> C <sub>y</sub> /SiO <sub>2</sub> , $\beta$ -Mo <sub>2</sub> C/SiO <sub>2</sub> , and $\alpha$ -MoC/SiO <sub>2</sub> catalysts .....	198
Figure 6.1. N <sub>2</sub> adsorption-desorption isotherms of the passivated Mo carbides and respective supports. ....	212
Figure 6.2. Diffractograms of the different supports for the Mo carbides. ....	214
Figure 6.3. Diffractograms of the calcined precursors of Mo carbides supported on different materials. $\diamond$ MoO <sub>3</sub> , $\blacktriangleright$ ZSM-5, $\blacktriangle$ m-ZrO <sub>2</sub> , $\clubsuit$ a-TiO <sub>2</sub> , $\triangle$ r-TiO <sub>2</sub> .....	215
Figure 6.4. Water and CO formation profiles during TPC of the calcined precursors of Mo <sub>2</sub> C/SiO <sub>2</sub> , Mo <sub>2</sub> C/TiO <sub>2</sub> , Mo <sub>2</sub> C/ZrO <sub>2</sub> , and Mo <sub>2</sub> C/ZSM-5.....	216
Figure 6.5. XANES spectra recorded at the Mo K-edge for the calcined precursors of Mo <sub>2</sub> C/SiO <sub>2</sub> and Mo <sub>2</sub> C/TiO <sub>2</sub> . Comparison with reference MoO <sub>3</sub> . ....	218
Figure 6.6. EXAFS signals recorded at the Mo K-edge for the calcined precursors of Mo <sub>2</sub> C/SiO <sub>2</sub> and Mo <sub>2</sub> C/TiO <sub>2</sub> . Comparison with reference MoO <sub>3</sub> . ....	219
Figure 6.7. Fourier transforms of the EXAFS signals recorded at the Mo K-edge for the calcined precursors of Mo <sub>2</sub> C/SiO <sub>2</sub> and Mo <sub>2</sub> C/TiO <sub>2</sub> ( $k = 3.5 - 15 \text{ \AA}^{-1}$ ). Comparison with reference MoO <sub>3</sub> .....	220
Figure 6.8. Raman spectra of the calcined precursors of Mo <sub>2</sub> /SiO <sub>2</sub> and Mo <sub>2</sub> C/TiO <sub>2</sub> (recorded at room temperature). ....	221
Figure 6.9. XANES spectra recorded at the Mo K-edge for carburized Mo <sub>2</sub> C/SiO <sub>2</sub> and Mo <sub>2</sub> C/TiO <sub>2</sub> (spectra recorded at room temperature). Comparison with reference $\beta$ -Mo <sub>2</sub> C.....	222
Figure 6.10. EXAFS signals recorded at the Mo K-edge for carburized Mo <sub>2</sub> C/SiO <sub>2</sub> and Mo <sub>2</sub> C/TiO <sub>2</sub> (spectra recorded at room temperature). Comparison with reference $\beta$ -Mo <sub>2</sub> C.....	223



Figure 6.11. Fourier transforms of the EXAFS signals recorded at the Mo K-edge for carburized Mo <sub>2</sub> C/SiO <sub>2</sub> and Mo <sub>2</sub> C/TiO <sub>2</sub> (spectra recorded at room temperature, $k = 3.5 - 15 \text{ \AA}^{-1}$ ). Comparison with reference $\beta$ -Mo <sub>2</sub> C. ....	224
Figure 6.12. XAS data at the Mo K-edge of a) $\beta$ -Mo <sub>2</sub> C (reactivated in H <sub>2</sub> at 400 °C) and after carburization of b) Mo <sub>2</sub> C/SiO <sub>2</sub> and c) Mo <sub>2</sub> C/TiO <sub>2</sub> (spectra recorded at room temperature). Fit of the first and second shells of neighbors: Fourier transform (left) and EXAFS oscillations (right). $k = 3.5 - 15 \text{ \AA}^{-1}$ . ....	225
Figure 6.13. XANES spectra recorded at the Mo K-edge for passivated $\beta$ -Mo <sub>2</sub> C, Mo <sub>2</sub> C/SiO <sub>2</sub> , Mo <sub>2</sub> C/TiO <sub>2</sub> and Mo <sub>2</sub> C/ZSM-5 (spectra recorded at room temperature). Comparison with references MoO <sub>3</sub> and metallic Mo (dotted lines). ....	227
Figure 6.14. EXAFS signals recorded at the Mo K-edge for passivated $\beta$ -Mo <sub>2</sub> C, Mo <sub>2</sub> C/SiO <sub>2</sub> , Mo <sub>2</sub> C/TiO <sub>2</sub> and Mo <sub>2</sub> C/ZSM-5 (spectra recorded at room temperature). Comparison with reference MoO <sub>3</sub> . ....	228
Figure 6.15. Fourier transforms of the EXAFS signals recorded at the Mo K-edge for passivated $\beta$ -Mo <sub>2</sub> C, Mo <sub>2</sub> C/SiO <sub>2</sub> , Mo <sub>2</sub> C/TiO <sub>2</sub> and Mo <sub>2</sub> C/ZSM-5 (spectra recorded at room temperature). Comparison with reference MoO <sub>3</sub> . $k = 3.5 - 15 \text{ \AA}^{-1}$ . ....	229
Figure 6.16. Analysis of the data recorded at the Mo K-edge for the passivated catalysts (spectra recorded at room temperature), using linear combinations of MCR-ALS components (see Table 6.3). XANES spectrum (left) and EXAFS oscillations (right), a) $\beta$ -Mo <sub>2</sub> C and b) Mo <sub>2</sub> C/SiO <sub>2</sub> . ....	231
Figure 6.17. Analysis of the data recorded at the Mo K-edge for the passivated catalysts (spectra recorded at room temperature), using linear combinations of MCR-ALS components (see Table 6.3). XANES spectrum (left) and EXAFS oscillations (right), a) Mo <sub>2</sub> C/TiO <sub>2</sub> and b) Mo <sub>2</sub> C/ZSM-5. ....	232
Figure 6.18. Diffractograms of supports and passivated Mo carbides supported on different materials. $\blacklozenge$ $\beta$ -Mo <sub>2</sub> C, $\blacktriangledown$ ZSM-5, $\blacktriangle$ m-ZrO <sub>2</sub> , $\clubsuit$ a-TiO <sub>2</sub> , $\triangle$ r-TiO <sub>2</sub> , $\circ$ SiO <sub>2</sub> ...	234
Figure 6.19. XANES spectra recorded at the Mo K-edge for reactivated $\beta$ -Mo <sub>2</sub> C, Mo <sub>2</sub> C/SiO <sub>2</sub> , Mo <sub>2</sub> C/TiO <sub>2</sub> and Mo <sub>2</sub> C/ZSM-5 (spectra recorded at room temperature). Comparison with references MoO <sub>3</sub> and metallic Mo (dotted lines). ....	235

Figure 6.20. EXAFS signals recorded at the Mo K-edge for reactivated $\beta$ -Mo <sub>2</sub> C, Mo <sub>2</sub> C/SiO <sub>2</sub> , Mo <sub>2</sub> C/TiO <sub>2</sub> and Mo <sub>2</sub> C/ZSM-5 (spectra recorded at room temperature).	236
Figure 6.21. Fourier transforms of the EXAFS signals recorded at the Mo K-edge for reactivated $\beta$ -Mo <sub>2</sub> C, Mo <sub>2</sub> C/SiO <sub>2</sub> , Mo <sub>2</sub> C/TiO <sub>2</sub> and Mo <sub>2</sub> C/ZSM-5 (spectra recorded at room temperature). $k = 3.5 - 15 \text{ \AA}^{-1}$	237
Figure 6.22. XAS data at the Mo K-edge of the catalysts after reactivation (spectrum recorded at room temperature). Fit of the first and second shells of neighbors: Fourier transform ( $k = 3.5 - 15 \text{ \AA}^{-1}$ , left) and EXAFS oscillations (right), a) $\beta$ -Mo <sub>2</sub> C and b) Mo <sub>2</sub> C/SiO <sub>2</sub> .	239
Figure 6.23. XAS data at the Mo K-edge of the catalysts after reactivation (spectrum recorded at room temperature). Fit of the first and second shells of neighbors: Fourier transform ( $k = 3.5 - 15 \text{ \AA}^{-1}$ , left) and EXAFS oscillations (right), a) Mo <sub>2</sub> C/TiO <sub>2</sub> and b) Mo <sub>2</sub> C/ZSM-5.	240
Figure 6.24. NH <sub>3</sub> desorption profiles of supports and reactivated Mo carbides.	242
Figure 6.25. Product yields versus FF conversion for Mo <sub>2</sub> C/SiO <sub>2</sub> and Mo <sub>2</sub> C/TiO <sub>2</sub> catalysts	250
Figure A.1. Typical chromatograms of the a) reaction products for the HDO of furfural using Mo carbides-based catalysts and b) reaction mixture (0.25 or 0.5 M of FF in 2BuOH).	260
Figure A.2. Mass spectrum of 2-butene (2BTE).	261
Figure A.3. Mass spectrum of 2-methylfuran (2MF).	261
Figure A.4. Mass spectrum of 2-butanone (2BTNE).	262
Figure A.5. Mass spectrum of 2-(sec-butoxymethyl)furan (SBMF).	262
Figure A.6. Mass spectrum of furfural (FF).	263
Figure A.7. Mass spectrum of 2-(dibutoxymethyl)furan (FDA).	263
Figure A.8. Mass spectrum of furfuryl alcohol (FA).	264
Figure A.9. Mass spectrum of 2-(furan-2-methyl)-5-methylfuran (FMMF).	264

Figure A.10. Mass spectrum of 2,2-(1,2-ethenediyl)bis-furan (EBF).....	265
Figure A.11. Calibration curve for furfural (FF) in 2-butanol.....	266
Figure A.12. Calibration curve for furfuryl alcohol (FA) in 2-butanol.....	266
Figure A.13. Calibration curve for 2-methylfuran (2MF) in 2-butanol.....	267
Figure A.14. Calibration curve for alcohol tetrahydrofuran (THFA) in 2-butanol.....	267
Figure A.15. Calibration curve for 2-methyltetrahydrofuran (2MTHF) in 2-butanol...	268
Figure A.16. Calibration curve for tetrahydrofuran (THF) in 2-butanol.....	268
Figure A.17. Calibration curve for furan (F) in 2-butanol.....	269
Figure A.18. Calibration curve for cyclopentane (CPA) in 2-butanol.....	269
Figure A.19. Calibration curve for cyclopentene (CPE) in 2-butanol.....	270
Figure A.20. Calibration curve for cyclopentanone (CPO) in 2-butanol.....	270
Figure A.21. Calibration curve for cyclopentanol (CPOH) in 2-butanol.....	271
Figure A.22. Calibration curve for 1,4-pentanediol (1,4PDO) in 2-butanol.....	271
Figure A.23. Calibration curve for 1,5-pentanediol (1,5PDO) in 2-butanol.....	272
Figure A.24. Calibration curve for levulinic acid (LA) in 2-butanol.....	272
Figure A.25. Calibration curve for $\gamma$ -valerolactone (GVL) in 2-butanol.....	273
Figure A.26. Calibration curve for 2-butanone (2BTNE) in 2-butanol.....	273

## LIST OF TABLES

Table 2.1. Main physical properties of furfural.....	13
Table 2.2. Physicochemical properties of 2MF compared to gasoline, bioethanol, biodiesel, and diesel.....	21
Table 2.3. Furfural hydrodeoxygenation to 2-methylfuran.....	26
Table 2.4. Furfural hydrodeoxygenation to 2-methylfuran.....	27
Table 2.5. Furfural hydrodeoxygenation to 2-methylfuran.....	28
Table 2.6. Furfural hydrodeoxygenation to 2-methylfuran.....	29
Table 2.7. Furfural hydrodeoxygenation to 2-methylfuran.....	30
Table 2.8. Furfural hydrodeoxygenation to 2-methylfuran.....	31
Table 2.9. Furfural hydrodeoxygenation to 2-methylfuran.....	32
Table 2.10. Furfural hydrodeoxygenation to 2-methylfuran.....	33
Table 2.11. Furfural hydrodeoxygenation to 2-methylfuran.....	34
Table 2.12. Furfural hydrodeoxygenation to 2-methylfuran.....	35
Table 2.13. Furfural hydrodeoxygenation to 2-methylfuran.....	36
Table 3.1. GC analytical methods parameters.....	89
Table 4.1. Fitted parameters at the Mo K-edge ( $E_0 = 20013$ eV, $S02 = 0.98$ ) determined from the EXAFS analysis of spectra recorded at room temperature on carburized catalysts. $k = 3.5 - 15 \text{ \AA}^{-1}$ . Fit of the first peaks from the Fourier transform between 1 and 3 $\text{\AA}$ . .....	108
Table 4.2. Fitted parameters at the Mo K-edge ( $E_0 = 20013$ eV, $S02 = 0.98$ ) determined from the EXAFS analysis of the second and third components extracted by MCR-ALS procedure during the carburization of $\text{Cu-Mo}_x\text{C}_y/\text{SiO}_2$ . $k = 3.5 - 14 \text{ \AA}^{-1}$ . .....	119
Table 4.3. Fitted parameters at the Ni K-edge ( $E_0 = 8339 \pm 2$ eV, $S02 = 0.80$ ) or at the Cu K-edge ( $E_0 = 8987 \pm 4$ eV, $S02 = 0.91$ ) determined from the EXAFS analysis of	

spectra recorded at room temperature. $k = 3 - 13 \text{ \AA}^{-1}$ at the Ni K-edge, $k = 3.5 - 14 \text{ \AA}^{-1}$ at the Cu K-edge. Fit of the first peak(s) from the Fourier transform between 1 and 3 $\text{\AA}$ . .....	123
Table 5.1. Chemical composition and textural properties of $\text{SiO}_2$ and passivated catalysts, and crystallite diameter ( $D_c$ ) of Mo carbide phase calculated from XRD. ...	155
Table 5.2. Composition of the passivated and reactivated catalysts evaluated from the linear combination of standard spectra and MCR-ALS analysis ( <i>italics</i> ) at the Mo K-edge.....	163
Table 5.3. Fitted parameters at the Mo K-edge ( $E_0 = 20013 \text{ eV}$ , $S_{02} = 0.98$ ) determined from the EXAFS analysis of spectra recorded at room temperature on catalysts after passivation and reactivation in $\text{H}_2$ . $k = 3.5 - 15.5 \text{ \AA}^{-1}$ . Fit of the first peak(s) from the Fourier transform between 1 and 3 $\text{\AA}$ . ....	171
Table 5.4. Fitted parameters at the Cu K-edge ( $E_0 = 8987 \pm 4 \text{ eV}$ , $S_{02} = 0.91$ ) determined from the EXAFS analysis of spectra recorded at room temperature. $k = 3.5 - 14 \text{ \AA}^{-1}$ . Fit of the first peak from the Fourier transform between 1 and 3 $\text{\AA}$ . ....	174
Table 5.5. Fitted parameters at the Ni K-edge ( $E_0 = 8339 \pm 2 \text{ eV}$ , $S_{02} = 0.80$ ) determined from the EXAFS analysis of spectra recorded at room temperature. $k = 3 - 13 \text{ \AA}^{-1}$ . Fit of the first peak(s) from the Fourier transform between 1 and 3 $\text{\AA}$ . ....	178
Table 5.6. FF conversion and product yields for the HDO of FF over Mo carbide-based catalysts .....	190
Table 5.7. FF conversion and product yields for the HDO of FF over unsupported and $\text{SiO}_2$ -supported Mo carbides catalysts .....	193
Table 6.1. Chemical composition and textural properties of the supports and Mo carbides catalysts. ....	213
Table 6.2. Fitted parameters at the Mo K-edge ( $E_0 = 20013 \text{ eV}$ , $S_{02} = 0.98$ ) determined from the EXAFS analysis of spectra recorded at room temperature on carburized catalysts. $k = 3.5 - 15 \text{ \AA}^{-1}$ . Fit of the first peak(s) from the Fourier transform between 1 and 3 $\text{\AA}$ . ....	226

Table 6.3. Fitted parameters at the Mo K-edge ( $E_0 = 20013$ eV, $S02 = 0.98$ ) determined from the EXAFS analysis of spectra recorded at room temperature on catalysts after passivation. $k = 3.5 - 15 \text{ \AA}^{-1}$ . Fit of the first peak(s) from the Fourier transform between 1 and 3 $\text{\AA}$ . .....	233
Table 6.4. Fitted parameters at the Mo K-edge ( $E_0 = 20013$ eV, $S02 = 0.98$ ) determined from the EXAFS analysis of spectra recorded at room temperature on catalysts after passivation and reactivation in $H_2$ . $k = 3.5 - 15 \text{ \AA}^{-1}$ . Fit of the first peak(s) from the Fourier transform between 1 and 3 $\text{\AA}$ . .....	241
Table 6.5. Acidic properties of supports and supported Mo carbides. ....	243
Table 6.6. FF conversion and product yields for the HDO of FF over supported Mo carbides catalysts .....	244
Table 6.7. FF conversion and product yields for the HDO of FF over supported Mo carbides catalysts .....	245
Table 6.8. FF conversion and product yields for the HDO of FF over supported Mo carbides catalysts .....	247
Table A.1. Comparison of the experimental and theoretical response factors of the commercially available compounds determined by calibration and ECN calculation, respectively.....	275
Table A.2. Comparison of the experimental and theoretical response factors of the commercially available compounds determined by calibration and ECN calculation, respectively.....	276
Table A.3. Determination of the theoretical response factors of the non-commercially available compounds determined by ECN calculation considering FF as reference.....	277
Table A.4. Determination of the theoretical response factors of the non-commercially available compounds determined by ECN calculation considering FF as reference.....	278

## ABBREVIATIONS AND ACRONYMS

- AC - Activated carbon
- ASAP - Accelerated Surface Area and Porosity
- A.U. - Arbitrary Unit
- BET - Brunauer-Emmett-Teller
- BFMF - 2,5-bis(furan-2-methyl)furan
- BJH - Barrett-Joyner-Halenda
- CCD - charge-coupled device
- CPA - Cyclopentane
- CPE - Cyclopentene
- CPME - Cyclopentyl methyl ether
- CPO - Cyclopentanone
- CPOH - Cyclopentanol
- CTH - Catalytic transfer hydrogenation
- DFE - 1,2-di-2-furyl-1,2-ethanediol
- DMSO - dimethyl sulfoxide
- EA - Elemental analysis
- EBF - 2,2-(1,2-ethenediyl)bis-furan
- ECN - Effective Carbon Number
- EXAFS - Extended X-ray absorption fine structure
- FA - Furfuryl alcohol
- FDA - 2-(dibutoxymethyl)furan
- FF - Furfural

FID - Flame-ionization detector

FMMF - 2-(furan-2-methyl)-5-methylfuran

FTIR of Py - Fourier-Transform Infrared Spectroscopy of Pyridine

GVL -  $\gamma$ -valerolactone

HDN - Hydrodenitrogenation

HDO - Hydrodeoxygenation

HDS - Hydrodesulfurization

HPTE - 5-hydroxy-2-pentanone (HPTE)

ICP - OES - inductively coupled plasma-optic emission spectroscopy

IMP - Impregnation method

JCPDF - ICDD - Joint Committee on Powder Diffraction Standards - International Center for Diffraction Data

LA - Levulinic acid

MCR-ALS - Multivariate Curve Resolution with Alternating Least Squares

MPV - Meerwein-Ponndorf-Verley

MS - mass spectrometer

PDF - Powder Diffraction File

RON - Research octane number

SBMF - 2-(sec-butoxymethyl)furan (SBMF)

SBOP - sec-butyl 4-oxopentanoate

STP - Standard Temperature and Pressure

SPR - Screening Pressure Reactor

TCD - thermal conductivity detector

THF - Tetrahydrofuran



THFA - Tetrahydrofurfuryl alcohol

TPC -Temperature-programmed carburization

TPD-NH<sub>3</sub> - Temperature-programmed desorption of NH<sub>3</sub>

XANES - X-ray absorption near edge structure

XAS - X-Ray absorption spectroscopy

XRD - X-ray Diffraction

1,4PDO - 1,4-Pentanediol

1,5PDO - 1,5-Pentanediol

2BTNE - 2-Butanone

2BuOH - 2-Butanol

2MF - 2-Methylfuran

2MTHF - 2-Methyltetrahydrofuran

hcp - hexagonal close-package

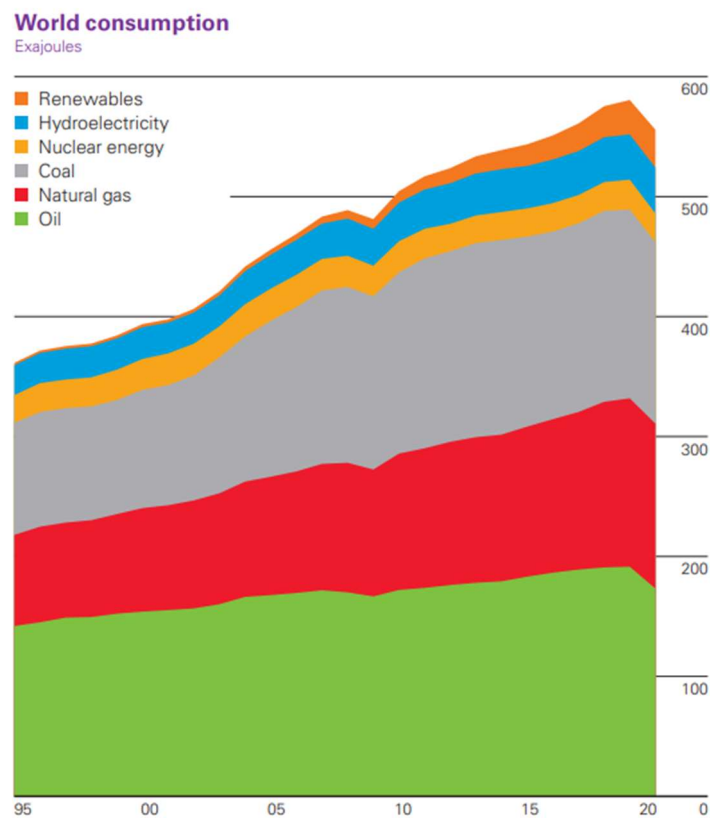
fcc - face-centered cubic

# **CHAPTER 1 - INTRODUCTION**

# 1. INTRODUCTION

The increase in world population and global economic development causes a continuous growth in energy demand. The energy consumption is projected to increase by 1.1% per annum, reaching  $7.4 \times 10^{20}$  J in 2030 (Nanda *et al.*, 2015). Nowadays, a large portion of the energy consumed worldwide comes from fossil fuels such as oil, coal, and natural gas (Figure 1.1), which is associated with massive emissions of greenhouse gases such as CO<sub>2</sub>. For this reason, the use of these non-renewable energy sources in the future is not recommended.

Figure 1.1. World primary energy consumption by fuel.



Reference: BP Statistical Review of World Energy (2021)

In this sense, considering the growing environmental concern and the need for energy supply, the search for alternative sources of energy to replace fossil fuels, minimizing environmental impacts, becomes indispensable.

An important fraction of the world's energy consumption, more particularly for electricity or heat production, could be provided by sources such as wind, solar, geothermal, and nuclear energy. However, in terms of producing liquid fuels for the transport sector and raw materials for the entire chemical industry, other resources should be explored (Nanda *et al.*, 2015). In this context, waste plant biomasses emerge as a potential resource to be used, because it is a renewable, low-cost, and abundant raw material worldwide (Bhatia *et al.*, 2020).

Biomass valorization can be accomplished by employing thermal, chemical, biochemical, and electrochemical processes. Among these, catalytic and biochemical routes for biomass-derived sugars are gaining prominence, as they enable the production of chemicals and liquid fuels (Liu *et al.*, 2019).

Furfural (FF) can be produced from hemicellulose fraction of lignocellulosic biomass. Furfural is a platform molecule, already produced industrially for one century, which presents in its structures multi functionalities that make it very reactive and able to be transformed into a wide range of compounds. The reduction of FF, for example, allows the generation of high-value-added compounds such as furfuryl alcohol (FA), 2-methylfuran (2MF), 2-methyltetrahydrofuran (2MTHF), and tetrahydrofurfuryl alcohol (THFA). Among them, 2MF stands out for its applications as a solvent, fuel additive, and biofuel (Mariscal *et al.*, 2016; Tarazanov *et al.*, 2020; Tuan Hoang and Viet Pham, 2021).

In general, the most used heterogeneous catalysts for furfural conversion are based on Cu-Cr or noble metals catalysts such as Pd and Pt. However, Cu-Cr catalysts suffer from deactivation by coke deposition, and Cr is toxic and harmful to the environment, which makes its use inadvisable. Meanwhile, noble metals are rare, scarce, and expensive materials, which makes their use on an industrial scale not always economically viable (Shilov *et al.*, 2018).

Alternative materials such as transitional metal carbides, on the other hand, exhibit properties and catalytic activity that resemble those of noble metals in hydrogenation, hydrogenolysis, hydrotreatment, and isomerization reactions (Alexander and Hargreaves, 2010; Leclercq *et al.*, 1979; Ramanathan and Oyama, 1995). Recently, they have been pointed out as being selective in hydrodeoxygenation (HDO) reactions of biomass-derived molecules (Pang *et al.*, 2019; Smith, 2020; Zhou *et al.*, 2021).

Taking this into account and adding the fact that the selective conversion of FF to 2MF with high selectivity under mild reaction conditions would be of high interest to the chemical industry, molybdenum carbides were selected as catalysts to be investigated in the HDO of furfural in liquid phase.

Therefore, the main goal of this work is to study the performance of unsupported and supported Mo carbides-based catalysts for the HDO of FF to 2MF, correlating their physicochemical properties, determined by characterizations techniques, with their catalytic results.

The specific goals of this work were divided as detailed hereafter (i) to investigate the effect of the crystalline phases of molybdenum carbide ( $\beta$ -Mo<sub>2</sub>C/SiO<sub>2</sub> and  $\alpha$ -MoC/SiO<sub>2</sub>), (ii) the effect of metal dispersion by comparing an unsupported  $\beta$ -Mo<sub>2</sub>C with a SiO<sub>2</sub>-supported  $\beta$ -Mo<sub>2</sub>C (iii) the effect of addition of Ni/Cu as promoters to  $\beta$ -Mo<sub>2</sub>C/SiO<sub>2</sub> catalyst; (iv) to investigate the effect of the support (SiO<sub>2</sub>, TiO<sub>2</sub>, ZrO<sub>2</sub>, and ZSM-5) for Mo<sub>2</sub>C catalysts; (v) to study the chemical transformations during the carburization, passivation, and reactivation of the Mo carbides by X-ray absorption spectroscopy.

## 1.1 References

- Alexander, A.-M., Hargreaves, J.S.J., 2010. Alternative catalytic materials: carbides, nitrides, phosphides and amorphous boron alloys. *Chem. Soc. Rev.* 39, 4388. <https://doi.org/10.1039/b916787k>
- Bhatia, S.K., Jagtap, S.S., Bedekar, A.A., Bhatia, R.K., Patel, A.K., Pant, D., Rajesh Banu, J., Rao, C.V., Kim, Y.-G., Yang, Y.-H., 2020. Recent developments in pretreatment technologies on lignocellulosic biomass: Effect of key parameters, technological improvements, and challenges. *Bioresource Technology* 300, 122724. <https://doi.org/10.1016/j.biortech.2019.122724>
- Dale, S. 2021. BP statistical review of world energy, BP Plc, London, United Kingdom, pp. 14-16, 2021.
- Leclercq, L., Imura, K., Yoshida, S., Barbee, T., Boudart, M., 1979. Synthesis of New Catalytic Materials: Metal Carbides of the Group VI B Elements, in: *Studies in Surface Science and Catalysis*. Elsevier, pp. 627–639. [https://doi.org/10.1016/S0167-2991\(09\)60240-8](https://doi.org/10.1016/S0167-2991(09)60240-8)
- Liu, Y., Nie, Y., Lu, X., Zhang, X., He, H., Pan, F., Zhou, L., Liu, X., Ji, X., Zhang, S., 2019. Cascade utilization of lignocellulosic biomass to high-value products. *Green Chem.* 21, 3499–3535. <https://doi.org/10.1039/C9GC00473D>
- Mariscal, R., Maireles-Torres, P., Ojeda, M., Sádaba, I., López Granados, M., 2016. Furfural: a renewable and versatile platform molecule for the synthesis of chemicals and fuels. *Energy Environ. Sci.* 9, 1144–1189. <https://doi.org/10.1039/C5EE02666K>
- Nanda, S., Azargohar, R., Dalai, A.K., Kozinski, J.A., 2015. An assessment on the sustainability of lignocellulosic biomass for biorefining. *Renewable and Sustainable Energy Reviews* 50, 925–941. <https://doi.org/10.1016/j.rser.2015.05.058>
- Pang, J., Sun, J., Zheng, M., Li, H., Wang, Y., Zhang, T., 2019. Transition metal carbide catalysts for biomass conversion: A review. *Applied Catalysis B: Environmental* 254, 510–522. <https://doi.org/10.1016/j.apcatb.2019.05.034>

- Ramanathan, S., Oyama, S.T., 1995. New Catalysts for Hydroprocessing: Transition Metal Carbides and Nitrides. *J. Phys. Chem.* 99, 16365–16372. <https://doi.org/10.1021/j100044a025>
- Shilov, I., Smirnov, A., Bulavchenko, O., Yakovlev, V., 2018. Effect of Ni–Mo Carbide Catalyst Formation on Furfural Hydrogenation. *Catalysts* 8, 560. <https://doi.org/10.3390/catal8110560>
- Smith, K.J., 2020. Metal carbides, phosphides, and nitrides for biomass conversion. *Current Opinion in Green and Sustainable Chemistry* 22, 47–53. <https://doi.org/10.1016/j.cogsc.2019.11.008>
- Tarazanov, S., Grigoreva, K., Shipitcyna, A., Repina, O., Ershov, M., Kuznetsova, S., Nikulshin, P., 2020. Assessment of the chemical stability of furfural derivatives and the mixtures as fuel components. *Fuel* 271, 117594. <https://doi.org/10.1016/j.fuel.2020.117594>
- Tuan Hoang, A., Viet Pham, V., 2021. 2-Methylfuran (MF) as a potential biofuel: A thorough review on the production pathway from biomass, combustion progress, and application in engines. *Renewable and Sustainable Energy Reviews* 148, 111265. <https://doi.org/10.1016/j.rser.2021.111265>
- Zhou, M., Doan, H.A., Curtiss, L.A., Assary, R.S., 2021. Identification of Active Metal Carbide and Nitride Catalytic Facets for Hydrodeoxygenation Reactions. *J. Phys. Chem. C* 125, 8630–8637. <https://doi.org/10.1021/acs.jpcc.1c02387>

## **CHAPTER 2 - BIBLIOGRAPHIC REVIEW**



## 2. BIBLIOGRAPHIC REVIEW

### 2.1 Biomass as an alternative to fossil fuels

The development of new technologies and the search for alternative resources for the sustainable production of chemicals and fuels have been motivated by growing environmental concerns, rising fuel prices, domestic energy security, and dependence on non-renewable energy sources (Nanda *et al.*, 2015).

The world energy matrix is constantly changing and in recent decades it has been observed an increasing contribution of alternative sources such as solar, wind, hydroelectric, and biomass in energy production. Among these sources, however, only biomass is capable of generating high-value-added compounds, since this raw material is considered the only sustainable source of organic compounds with potential equivalent to oil (Climent *et al.*, 2014; Okolie *et al.*, 2021).

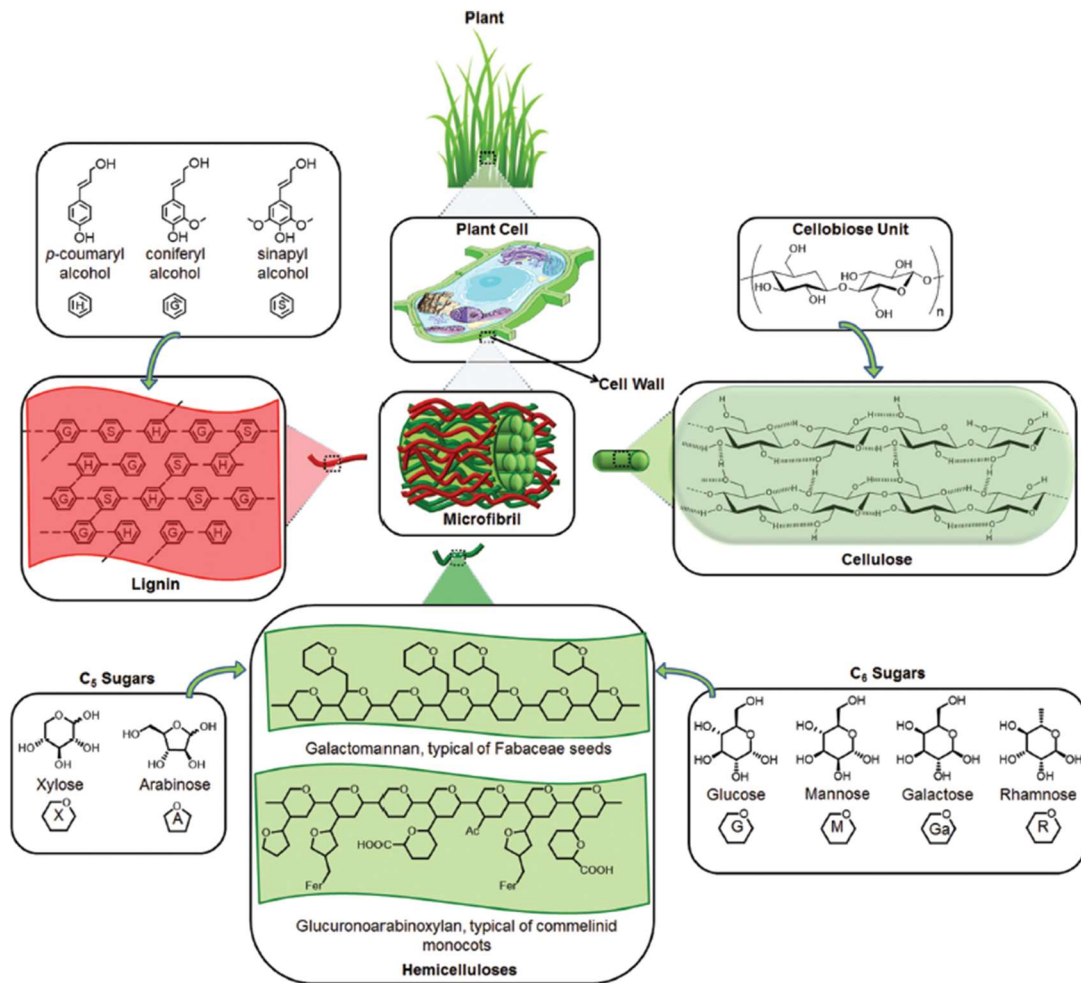
Biomass is generated from atmospheric CO<sub>2</sub> (released by natural or anthropogenic sources), sunlight, and water through biological photosynthesis, which makes it a neutral source of organic carbon capable of contributing, thus, to the maintaining or even decreasing of CO<sub>2</sub> emission levels and the reduction of air pollution (Isikgor and Becer, 2015). Biomass includes everything from plants, crops, bushes, and trees ranging from agricultural wastes, and forestry residues to municipal solid waste (Jaswal *et al.*, 2022; Yong *et al.*, 2022).

Among the different types of biomasses, lignocellulosic biomass has been identified as ideal for the synthesis of biochemicals and biofuels for several reasons. Lignocellulosic biomass grows much faster and can be obtained at lower costs compared to agriculturally valuable food crop feedstock. It is the most abundant among the biomass feedstocks and corresponds to the non-edible part of plants and, for this reason, does not compete with food production (Climent *et al.*, 2014; Jaswal *et al.*, 2022; Nanda *et al.*, 2015; Yong *et al.*, 2022).

## 2.1.1 Lignocellulosic biomass

The composition of lignocellulosic biomass depends on the plant species and the growth conditions, but in general, this raw material exhibits three main components: cellulose, hemicellulose, and lignin (Yong *et al.*, 2022), presented in Figure 2.1.

Figure 2.1. Lignocellulosic biomass main components.



Reference: Isikgor and Becer (2015)

The major component of lignocellulosic biomass is cellulose (40 - 50 wt.%), a water-insoluble linear polymer of high molecular weight composed of D-glucose monomers joined by β-1,4-glycosidic bonds that form rigid crystalline structures due to

Van der Waals forces and intra/intermolecular hydrogen bonds, which is also responsible for its high chemical stability (Kobayashi *et al.*, 2012; Okolie *et al.*, 2021; Wettstein *et al.*, 2012).

On the other hand, hemicellulose is a complex branched polysaccharide that presents a random and amorphous structure formed by pentoses (xylose, arabinose) and hexoses (galactose, glucose, and mannose), being xylose the most abundant sugar in its composition (Climent *et al.*, 2014). Hemicellulose corresponds to 25 - 35 wt.% of lignocellulosic biomass and provides structural resistance to plant cell walls (Alonso *et al.*, 2010; Isikgor and Becer, 2015; Okolie *et al.*, 2021).

Finally, lignin is a three-dimensional aromatic macromolecule with a structure composed of *p*-coumaryl, coniferyl, and sinapyl alcohols, responsible for providing cell wall rigidity and resistance to insects and pathogens. This fraction is equivalent to 15 - 20 wt.% of the lignocellulosic material (Alonso *et al.*, 2010; Bhatia *et al.*, 2020; Isikgor and Becer, 2015).

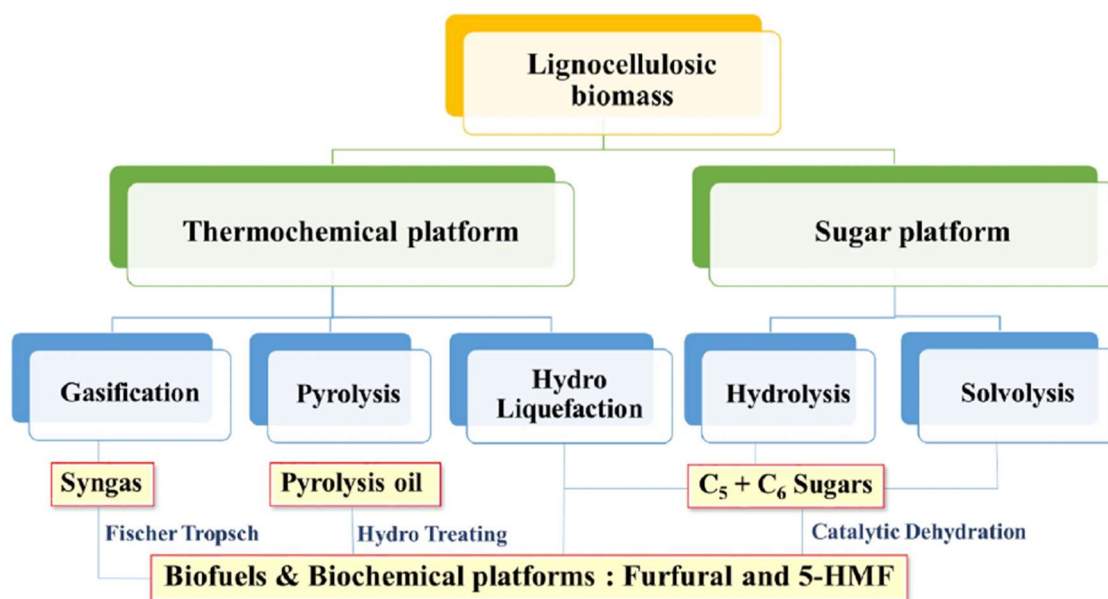
### **2.1.2 Biorefinery: Biomass valorization**

The use of lignocellulosic biomass is directly associated with the concept of biorefinery. A biorefinery is analogous to an oil refinery, since it integrates processes for the conversion of raw material into products of great commercial interest, maximizing the use of all components from this raw material, the by-products, and waste streams with reduced operating costs and energy efficiency (Werpy and Petersen, 2004).

The conversion of lignocellulosic biomass into high-value-added compounds can be carried out using various technologies. The most common technologies involve thermochemical and sugar conversions (Khemthong *et al.*, 2021). In the former, all biomass fractions are processed simultaneously at high pressures and/or temperatures to obtain products such as syngas (a mixture of carbon monoxide and hydrogen) by gasification or bio-oils by fast pyrolysis and/or liquefaction. Meanwhile, in sugar conversions, lignocellulosic biomass is first fractionated into its main constituents

(cellulose, hemicellulose, and lignin) by advanced hydrothermal process and then hydrolyzed into sugars (C<sub>5</sub>) and hexoses (C<sub>6</sub>) (Alonso *et al.*, 2010; Climent *et al.*, 2014; Khemthong *et al.*, 2021). The main technologies for lignocellulosic biomass conversion can be seen in Figure 2.2.

Figure 2.2. Main technologies for the conversion of lignocellulosic biomass.



Reference: Khemthong *et al.*, (2021)

The thermal routes offer greater simplicity of operation but produce fuels of poor quality and energy content due to their highly acidic nature and the presence of a large number of oxygenated compounds and water, which means that further processes such as Fisher-Tropsch synthesis, hydrodeoxygenation must be performed to adjust the properties of these fuels before they can be used commercially (Jaswal *et al.*, 2022).

On the other hand, the hydrolysis of the biomass fractions is more complex and presents a higher cost, but offers more selective processing options and greater operational flexibility when compared to thermochemical conversions (Alonso *et al.*, 2010; Wettstein *et al.*, 2012). In this methodology, cellulose and hemicellulose fractions are transformed into platform molecules, which are multifunctional molecules capable of originating a series of high value-added compounds via catalytic routes due to the

presence of versatile functional groups in their structures, which can be subjected to a wide variety of reactions.

Solvolysis is another interesting route that uses organic solvents, ionic liquids, or aqueous solvents to convert biomass. This approach presents many advantages because (i) it reduces the concentration of the compounds, which decreases the possibility of cross-linking among the molecules; (ii) lower reaction temperatures are used reducing the operation costs and; (iii) the solvents can significantly change the conversion rates of biomass and the selectivities of the target product. All these aspects make solvolysis ideal to convert biomass into platform chemicals, in particular furfural, since hemicellulose can be dissolved and transformed while cellulose and lignin remain unaltered, which results in higher FF yields and low by-products formation (Jaswal *et al.*, 2022).

In 2004, 12 molecules out of 300 were selected by the Department of Energy of the United States Government as potential chemical platforms to be used in biorefineries (Werpy and Petersen, 2004). Several indicators were considered for this selection, such as the availability of technologies for their production, their potential to be transformed into chemicals and fuels, and the applicability of the products obtained from these compounds. This list was later revised by Bozell and Petersen (2010). It included sugars (glucose, xylose), acids (succinic, levulinic, lactic), furans (furfural, 5-hydroxymethylfurfural), and polyols (sorbitol, xylitol, and glycerol).

Recently, furfural has been highlighted as one of the most promising platform molecules obtained from lignocellulosic biomass and many works have focused on the process of obtaining furfural and its subsequent conversion into biochemicals and biofuels (Chen *et al.*, 2018; Gupta *et al.*, 2018; Jaswal *et al.*, 2022; Khemthong *et al.*, 2021; Y. Luo *et al.*, 2019; Rachamontree *et al.*, 2020; Shen *et al.*, 2020; Wang *et al.*, 2019; Yong *et al.*, 2022).

## 2.2 Furfural: a sustainable platform molecule

Furfural ( $C_5H_4O_2$ ), alternatively referred to as 2-furaldehyde, is a colorless, viscous compound that has a pleasant almond-like odor and changes color when exposed to atmospheric air, turning dark (Rachamontree *et al.*, 2020; Yong *et al.*, 2022). The main physical properties of FF can be seen in Table 2.1.

Table 2.1. Main physical properties of furfural.

Parameter	Value
Molecular weight ( $g\ mol^{-1}$ )	96.08
Boiling point ( $^{\circ}C$ ) <sup>a</sup>	161.7
Freezing point ( $^{\circ}C$ )	- 36.5
Density at 25 $^{\circ}C$ ( $g\ cm^{-3}$ )	1.16
Refractive index at 25 $^{\circ}C$	1.5235
Critical pressure $P_c$ (MPa)	5.502
Critical temperature $T_c$ ( $^{\circ}C$ )	397
Solubility in water at 25 $^{\circ}C$ (wt.%)	8.3
Dielectric constant at 20 $^{\circ}C$	41.9
Heat of vaporization ( $kJ\ mol^{-1}$ )	42.8
Viscosity at 25 $^{\circ}C$ (mPa s)	1.49
Heat of combustion at 25 $^{\circ}C$ ( $kJ\ mol^{-1}$ )	234.4
Enthalpy of formation ( $kJ\ mol^{-1}$ )	- 151
Surface tension at 29.9 $^{\circ}C$ ( $mN\ m^{-1}$ )	40.7
Explosion limits in the air (% vol.)	2.1 - 19.3
Flashpoint ( $^{\circ}C$ ), tag closed cup	61.7
Autoignition temperature ( $^{\circ}C$ )	315

<sup>a</sup> Under atmospheric pressure

Reference: Yan *et al.*, (2014)

Furfural exhibits two very interesting functional groups in its structure: an aldehyde and an aromatic furan ring, which makes it a highly reactive molecule that can be transformed into a wide variety of high-value-added compounds (Yong *et al.*, 2022). The aldehyde function, for example, can undergo reduction, decarbonylation, amination, oxidation, condensation, acylation, and Grignard reactions. The aromatic furan ring, on

the other hand, can be transformed via hydrogenation, oxidation, halogenation, hydrogenolysis, and nitration reactions (Li *et al.*, 2016; Mariscal *et al.*, 2016; Yan *et al.*, 2014). As can be seen, a wide range of products can be obtained from FF depending on the reaction or combinations of reactions used.

Furfural is produced exclusively from pentoses derived from lignocellulosic biomass and can be obtained in one or two-step processes. In the first case, the pentoses are hydrolyzed to xylose in an acid medium, which is promptly dehydrated to furfural. In the two-step process, xylose hydrolysis occurs under milder conditions, followed by dehydration. The two-step process presents an advantage in the higher production of FF (Eseyin and Steele, 2015; Machado *et al.*, 2016).

As mentioned earlier, another technique to produce furfural is the solvent-thermal conversion, wherein H<sub>2</sub>O,  $\gamma$ -valerolactone (GVL), 2-methyltetrahydrofuran (2MTHF), and dimethyl sulfoxide (DMSO) can be used as solvents. To increase the FF yield, homogenous (mainly H<sub>2</sub>SO<sub>4</sub> and HCl) and heterogeneous catalysts, such as solid acids like SBA-15 materials and modified zeolites, are employed within the solvents. The use of homogenous catalysts, however, is associated with serious environmental pollution, because of the release of toxic chemicals in nature, while heterogeneous catalysts are more easily separated from the reaction medium (Tuan Hoang and Viet Pham, 2021).

The first-time furfural was produced on a commercial scale was in 1921 in the United States by the Quaker Oats company. The production of furfural can occur in either batch or continuous mode in temperatures ranging from 153 to 240 °C and pressures from 6 to 30 atm using mineral acids such as sulfuric acid (H<sub>2</sub>SO<sub>4</sub>) and phosphoric acid (H<sub>3</sub>PO<sub>4</sub>). In general, the commercial furfural yields remain around 50%, which is not ideal. This poor yield is attributed to undesired side reactions of condensation and polymerization (Jaswal *et al.*, 2022; Yong *et al.*, 2022).

A global furfural production of 360 kt was reported in 2016, with China accounting for 80% of this production with an annual volume of 300 kt. This nation uses mainly corn cobs as feedstock, which are generated at 3.8 million tons scale every year. The other important producers are the Dominican Republic and South Africa (Yong *et al.*, 2022).

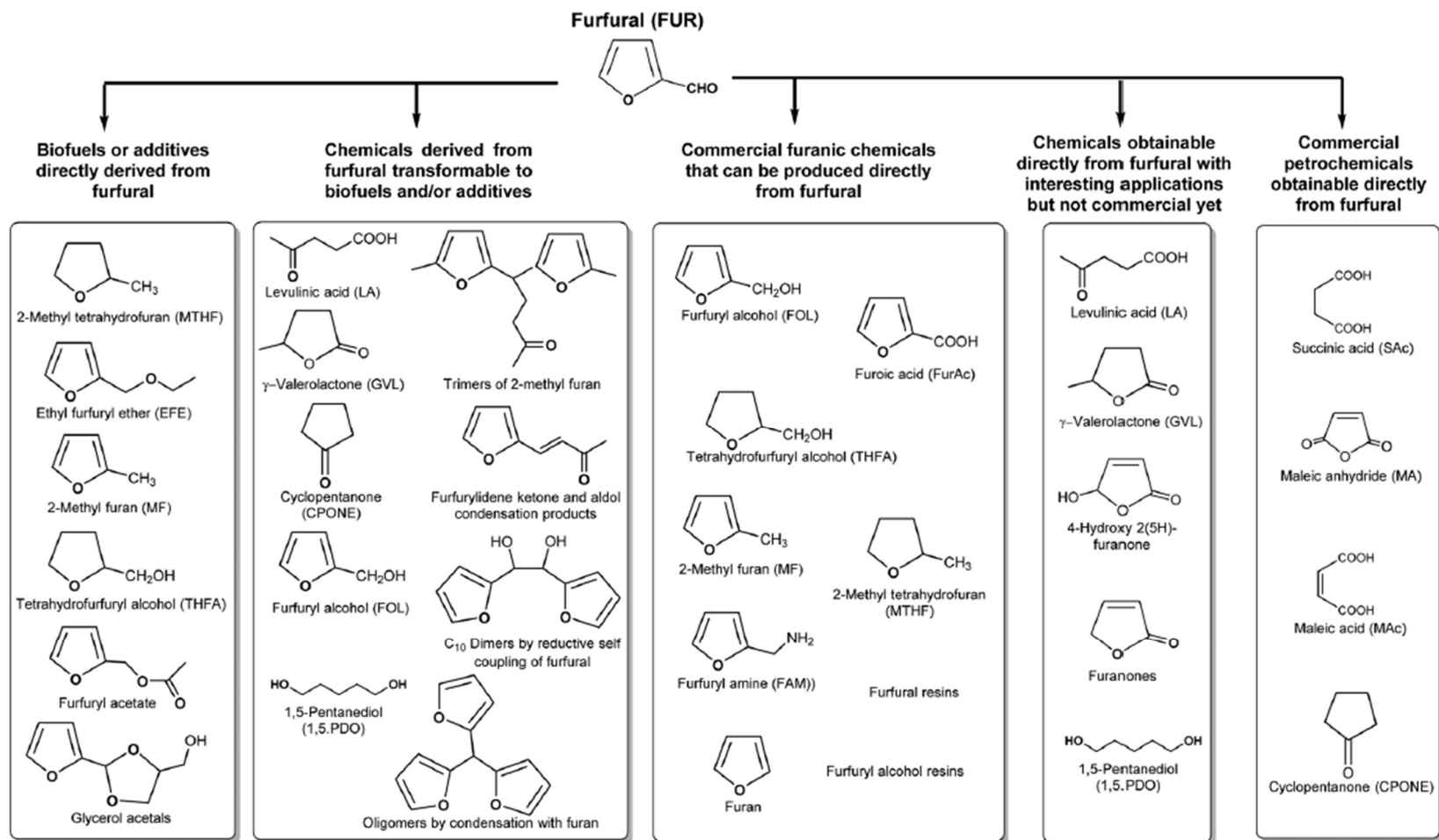
Furfural is described as a great versatility compound that exhibits multiple direct and indirect applications. The main use of this molecule is as a solvent due to its intermediate polarity (Mariscal *et al.*, 2016), which allows its use as a selective extractant in (i) removal of aromatics from lubricating oils improving the temperature/viscosity ratio, (ii) removal of aromatics from diesel to improve ignition properties and (iii) formation of cross-linked polymers (Yan *et al.*, 2014).

Furfural finds additional applications in agriculture/horticulture as an herbicide or as an active compound of nematicides, and in the composition of foods and beverages as a flavor concentrator (Eseyin and Steele, 2015).

Indirectly, furfural can be used as an intermediate in the synthesis of drugs, chemicals, and biopolymers. The main products derived from FF are presented in Figure 2.3.



Figure 2.3. Main products derived from furfural.



Reference: Mariscal *et al.*, (2016)

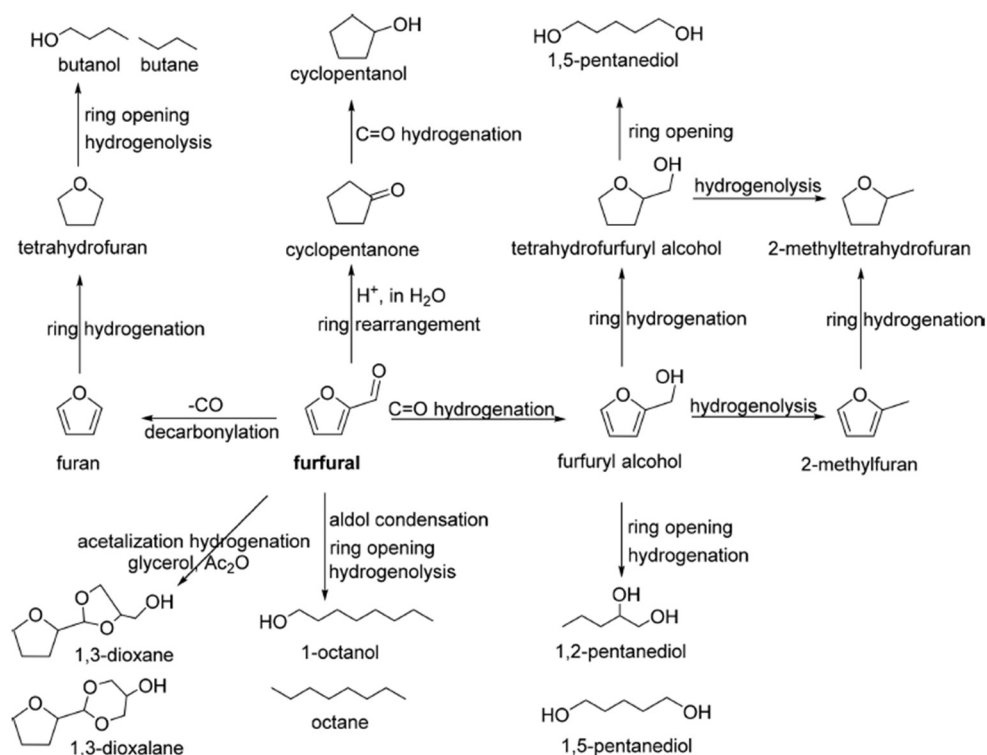
As mentioned earlier, furfural can be subjected to a wide variety of reactions. The oxidation of this molecule generates compounds such as maleic acid and furanic acid, which are used as raw materials in organic synthesis and as intermediates in the manufacture of perfumes and drugs (Choi *et al.*, 2015).

Furfuralamine is another interesting compound produced from FF. The conversion of the carbonyl group of furfural to an amine is possible in the presence of a reducing agent, usually NH<sub>3</sub>, by employing Co- and/or Ni-based catalysts. The furfuralamine formed has applications in the manufacture of pharmaceuticals, pesticides, and fibers (Corma *et al.*, 2007).

The catalytic decarboxylation of furfural at high temperatures generates furan together with a carbon monoxide molecule. Usually, this reaction occurs in parallel with the hydrogenation or hydrogenolysis of FF (Yan *et al.*, 2014). The produced furan can be used to increase the octane index of gasoline-containing blends and, its subsequent hydrogenation forms tetrahydrofuran (THF), an important industrial solvent (Corma *et al.*, 2007).

Despite all possible products derived from furfural, the focus of this work is on the production of 2-methylfuran, a compound obtained from furfural-reducing routes (Figure 2.4).

Figure 2.4. Reductive conversion of furfural to value-added chemicals.



Reference: Chen *et al.*, (2018)

## 2.2.1 Reductive conversion of furfural

Furfuryl alcohol (FA) is the main chemical derived from furfural, accounting for nearly 65% of the FF produced (Li *et al.*, 2016). The largest FA application occurs in the manufacture of casting resins, which are often made from cross-linked polymers of furfuryl alcohol or by mixing it with other compounds such as furfural, formaldehyde, phenolic compounds, and urea. The resins obtained are characterized by excellent chemical, mechanical and thermal properties, as well as high corrosion resistance (Jaswal *et al.*, 2022; Yan *et al.*, 2014).

FA is also used in the manufacture of polyurethane and polyester foams and as an intermediate in the synthesis of pharmaceuticals and fragrances (Machado *et al.*, 2016). In addition, along with 2-methylfuran, FA can be employed in the synthesis of antimicrobial agents. This compound is also the main ingredient of wood modification

processes making it suitable to be used in flooring and coatings (Eseyin and Steele, 2015).

The production of FA is based on the selective hydrogenation of the C=O group of furfural, which is reported to occur either in the liquid or gas phase using Cu-Cr-based catalysts. Industrially, the gas phase is preferred for furfuryl alcohol production, however, in this system, large amounts of hydrogen are required. In addition, the use of this copper chromite catalyst is strongly associated with environmental problems due to the high toxicity of Cr (Jaswal *et al.*, 2022).

Tetrahydrofurfuryl alcohol (THFA) is the product resulting from the full hydrogenation of furfural (Chen *et al.*, 2018). This compound has applications as a green solvent for the pharmaceutical industry (Zhang *et al.*, 2021) and is considered a biofuel and fuel additive because of the similarities of its physical and chemical properties with kerosene (Mariscal *et al.*, 2016).

THFA formation involves the C=C bond hydrogenation of the aromatic furan ring of FA (Chen *et al.*, 2018). For this reaction, it is preferable to use metals with high affinity for the C=C bond and, for this reason, Pd, Ni, and Ru-based catalysts are the most widely employed (Li *et al.*, 2016). Industrially, THFA is produced by the hydrogenation of furfuryl alcohol using Ni catalysts at moderate temperatures (50 - 100 °C) in liquid and gas phases (Mariscal *et al.*, 2016).

2-Methyltetrahydrofuran (2MTHF) is another compound obtained by FF reduction. It has applications as a solvent, biofuel, and gasoline blend additive. 2MTHF also found applications in organometallic chemistry and the transformations of bio-sourced molecules as an alternative to tetrahydrofuran (Chen *et al.*, 2018; Yan *et al.*, 2014).

2MTHF can be produced from both tetrahydrofurfuryl alcohol hydrogenolysis and 2-methylfuran hydrogenation or levulinic acid hydrogenation via  $\gamma$ -valerolactone formation as an intermediate (Chen *et al.*, 2018).

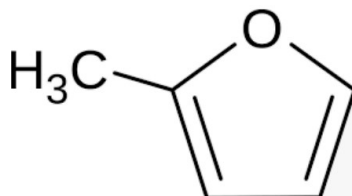
Finally, 2-methylfuran (2MF) is the most important biofuel derived from furfural. This compound is the product of interest in this work and, therefore, its production and application will be treated in more detail in the next section.

## 2.3 2-Methylfuran

2-Methylfuran (Figure 2.5), also known as sylvan, is a flammable and water-insoluble liquid that can be used as a solvent and as an intermediate for the production of antimalarial drugs, pesticides, 2-methyltetrahydrofuran, perfumes, and heterocyclic sulfur and nitrogen compounds, as well as substituted aliphatic compounds (Mariscal *et al.*, 2016).

It is one of the representative molecules of second-generation fuels that can be used in existing internal combustion engines. Because of its suitable physicochemical properties (Table 2.2), 2MF can be easily mixed with gasoline. Some of these properties include a lower fuel consumption compared to ethanol, a high research octane number (RON) that improves anti-detonating ability, a better combustion performance than ethanol, a low boiling point that facilitates the cold starting at low temperatures, and lower water solubility, which reduces the risk of atmospheric water contamination in the fuel mixture (Chen *et al.*, 2018; Tuan Hoang and Viet Pham, 2021).

Figure 2.5. The structural formula of 2-methylfuran.



Reference: own author (2023)

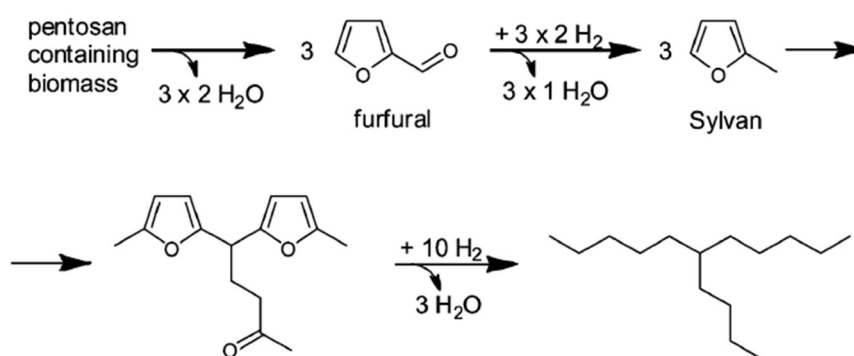
Table 2.2. Physicochemical properties of 2MF compared to gasoline, bioethanol, biodiesel, and diesel.

<b>Parameters</b>	<b>Gasoline</b>	<b>Bioethanol</b>	<b>2MF</b>	<b>Biodiesel</b>	<b>Diesel</b>
Chemical formula	C <sub>4</sub> - C <sub>12</sub>	C <sub>2</sub> H <sub>6</sub> O	C <sub>5</sub> H <sub>6</sub> O	C <sub>15</sub> - C <sub>17</sub> COOCH <sub>3</sub>	C <sub>12</sub> - C <sub>25</sub>
RON	96.8	109	103	-	20 - 30
Cetane number	10 - 15	8	9	46-60	52.1
Oxygen content (%)	0	34.78	19.51	10-12	0
Stoichiometric air/fuel ratio	14.7	8.95	10.05	14	14.3
Density at 20 °C (kg cm <sup>-3</sup> )	745	791	913	880	826
Latent heating at 25 °C (kJ kg <sup>-1</sup> )	373	919.6	358	252 - 258	270 - 301
Lower heating value (MJ kg <sup>-1</sup> )	42.9	26.9	31.2	41	42.5
Initial boiling point (°C)	32.8	78.4	64.7	340 - 375	180 - 370
Auto-ignition temperature (°C)	420	434	450	374 - 449	180 - 220

Reference: adapted from Tuan Hoang and Viet Pham, (2021)

In addition, 2-methylfuran is the key intermediate to produce renewable diesel. The alkylation/hydroxyalkylation reaction of 2MF yields a hydrophobic precursor with an adequate number of carbon atoms, in which subsequent complete hydrodeoxygenation results in an alkane mixture with excellent properties as diesel fuels. A scheme of this reaction is shown in Figure 2.6 (Corma *et al.*, 2012).

Figure 2.6. Production of an alkane mixture suitable to be mixed with commercial diesel fuel from 2MF alkylation/hydroxyalkylation followed by hydrodeoxygenation reaction.



Reference: Corma *et al.*, (2012)

The advantage of using 2MF for this reaction relies on the fast and selective alkylation/hydroxyalkylation only in the 2-position, which avoids undesired polymerization reactions. This step can be performed using 2MF with various molecules consisting mainly of aldehydes and ketones. In general, both homogeneous and heterogeneous catalysts containing acidic properties such as H<sub>2</sub>SO<sub>4</sub> and Nafion-212 are used (Corma *et al.*, 2012, 2011b, 2011a; G. Li *et al.*, 2014; Li *et al.*, 2013b, 2013a; S. Li *et al.*, 2014). Recently, Lewis acid sites found in Zr/SBA-15 catalysts were also reported to catalyze 2MF alkylation (Y.-J. Luo *et al.*, 2019).

For the hydrodeoxygenation step, catalysts based on noble metals such as Pt and Pd and carbides of Mo and W promoted with Ni are used. The conditions for this reaction are more severe in comparison with alkylation/hydroxyalkylation reactions. In the former case, temperatures above 350 °C and high pressures of 50 bar are necessary, while in the latter, temperatures below 70 °C are used (Corma *et al.*, 2012, 2011b, 2011a; G. Li *et al.*, 2014; Li *et al.*, 2013b, 2013a; S. Li *et al.*, 2014).

### 2.3.1 Hydrodeoxygenation of furfural to 2-methylfuran

The synthesis of 2-methylfuran can be performed by the selective hydrodeoxygenation of furfural (Tuan Hoang and Viet Pham, 2021) or by the C-O bond

hydrogenolysis of furfuryl alcohol in both gas or liquid phase. The major difficulty in commercially implementing the production of 2MF directly from furfural is related to its selectivity since many undesirable parallel reactions can occur such as furfural decarbonylation to furan or severe hydrogenation that transforms 2MF into 2MTHF, 2-pentanone, and 2-pentanol (Mariscal *et al.*, 2016).

In the gas phase, 2MF is produced using copper chromite catalysts supported on various materials. The gas-phase reaction processing, however, is associated with thermal polymerization and deactivation by coke deposition on the catalyst (Lange *et al.*, 2012). The aqueous phase reaction is employed as an alternative to circumvent these deactivation problems.

The mechanism for the 2MF synthesis is mainly influenced by the synergy between metal and acid sites in bifunctional catalysts, which can be achieved by metal-support interactions (Tuan Hoang and Viet Pham, 2021). It is reported that the support surface properties play an important role, favoring side reactions and reducing the catalyst's lifetime. The most common supports used for the HDO of furfural are SiO<sub>2</sub>, TiO<sub>2</sub>, Al<sub>2</sub>O<sub>3</sub>, and carbon (Khemthong *et al.*, 2021).

The production of 2MF furfural can be carried out using three different hydrogen sources: (i) molecular hydrogen, which comprises most of the papers published in the literature, (ii) formic acid or (iii) alcohols by catalytic transfer hydrogenation (CTH) reaction.

Recently, many types of research focused on FF conversion by CTH reactions. The use of this process presents advantages: (i) the lower cost associated with the purchase, transport, and handling of explosive H<sub>2</sub>, (ii) safety in operation, and (iii) the use of milder reaction conditions (Khemthong *et al.*, 2021; Xu *et al.*, 2020; Zhang *et al.*, 2021).

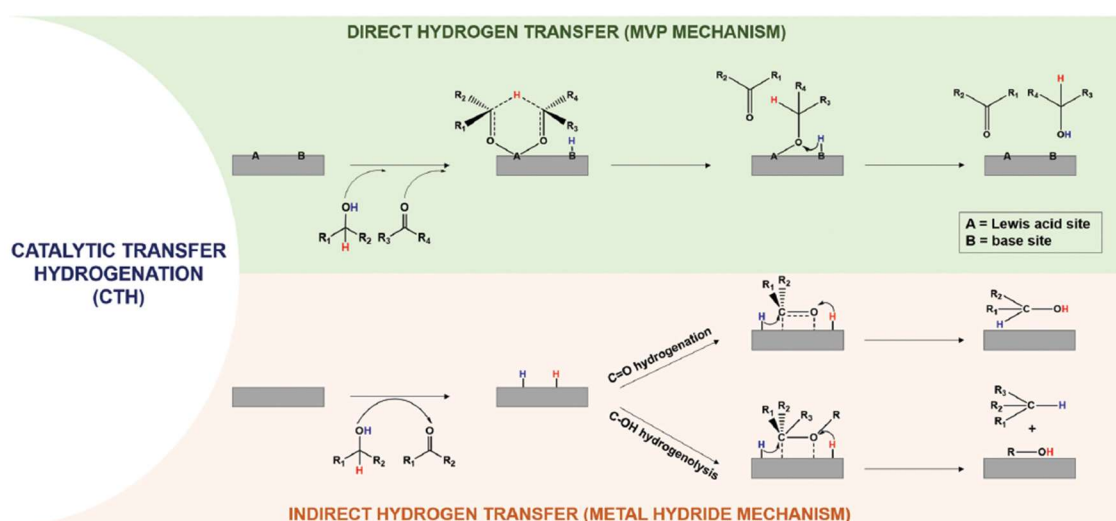
Two mechanisms can occur in the absence of added hydrogen. The first one is the Meerwein-Ponndorf-Verley (MPV) reduction, in which occurs the direct hydrogen transfer of the donor molecule to the acceptor. In this case, acid-base pair sites are necessary to mediate the CTH reaction, where the Lewis acid sites will be involved in the coordination of the hydroxyl (donor) and carbonyl (acceptor) groups, while the basic



sites take the hydrogen of the alcoholic group.

The other possibility is the formation of metal hybrid species (mono or dihydride) by the hydrogen transfer of the H-donor molecule to the catalyst surface. In the first route, monohydride, only the  $\alpha$ -hydrogen atom from the H-donor molecules is transferred, while in the case of dihydride, there is also the transfer of hydrogen from the hydroxyl group (Xu *et al.*, 2020). Both mechanisms are demonstrated in Figure 2.7.

Figure 2.7. Possible CTH reaction pathways: direct/indirect hydrogen transfer mechanisms.



Reference: Xu *et al.*, (2020)

Both formic acid and protic solvents such as alcohols can be used as hydrogen donors in the CTH reactions (Zhang *et al.*, 2021).

The use of lower alcohols is associated with low costs, convenient transportation and storage, easy preparation, and high availability. However, the reforming of methanol to  $H_2$ , for example, requires a higher temperature to perform the transfer hydrogenation to aldehydes. Meanwhile, the reaction conditions using ethanol, 2-propanol, 1-butanol, and 2-butanol are milder than those using methanol, which reduces side reactions and increases product selectivity (Zhang *et al.*, 2021). In general, secondary alcohols are more efficient in donating hydrogen than primary alcohols, since

they possess a higher reduction ability and a better stabilization of the secondary carbocation produced during the hydride transfer (Xu *et al.*, 2020).

The main disadvantage of using aliphatic solvents in FF conversion reactions is the formation of etherification by-products, especially in the presence of a catalyst containing acid properties (Xu *et al.*, 2020).

Formic acid is another compound that has the potential to be used as a hydrogen source in hydrogenation reactions. It is widely available and presents convenient transportation and safety. It can be produced from biomass oxidation or acid hydrolysis and under certain conditions can be decomposed in CO<sub>2</sub> and H<sub>2</sub>. The disadvantage of using formic acid compared to alcohols is the need to use corrosion-resistant equipment and the possibility of environmental contamination (Zhang *et al.*, 2021). The main studies involving the conversion of FF to 2MF using all types of hydrogen sources can be found in Table 2.3 - 2.13. The metal content of the catalysts is in wt.%.

Table 2.3. Furfural hydrodeoxygenation to 2-methylfuran.

Catalyst(s)	Reaction conditions				Best result	Reference
	T (°C)	P (bar)	t (h)	Solvent(s)		
x% Cu <sub>1</sub> Re <sub>0.14</sub> /γ-Al <sub>2</sub> O <sub>3</sub> (x = 10, 20) Cu <sub>y</sub> Re <sub>z</sub> /γ-Al <sub>2</sub> O <sub>3</sub> (y = 0, 1; z = 0, 0.04, 0.14, 0.34)	140 - 220	20 H <sub>2</sub>	0 - 6	2-propanol	20% Cu <sub>1</sub> Re <sub>0.14</sub> /γ-Al <sub>2</sub> O <sub>3</sub> 200 °C, 20 bar H <sub>2</sub> , 6 h, 2-propanol conv. = 100%, yield = 86% CB > 99%	Chuseang <i>et al.</i> , 2021
MAI/γ-Al <sub>2</sub> O <sub>3</sub> (M = Cu, Ni, Co) MCuAl/γ-Al <sub>2</sub> O <sub>3</sub> (M = Ni, Co)	180 - 220	5 N <sub>2</sub>	0.5 - 6	2-propanol	NiCuAl/γ-Al <sub>2</sub> O <sub>3</sub> 200 °C, 5 bar N <sub>2</sub> , 6 h, 2-propanol conv. = 100%, yield = 50% CB > 97%	Kalong <i>et al.</i> , 2021
10% Ni/SiO <sub>2</sub> 10% Ni <sub>17</sub> W <sub>13</sub> /SiO <sub>2</sub> x% Ni/W <sub>x</sub> C/SiO <sub>2</sub> (x = 0, 0.5, 1, 2.5, 4, 9)	200	65 H <sub>2</sub>	0 - 26	THF, 2-propanol	W <sub>x</sub> C/SiO <sub>2</sub> 200 °C, 65 bar H <sub>2</sub> , 24 h, 2-propanol conv. = 100%, yield = 45%	Bretzler <i>et al.</i> , 2020
x% Cu-Cu <sub>2</sub> O/ N-RGO (x = 5, 10, 15, 20) N-RGO = N-doped Reduced Graphene Oxide	180 - 240	10 - 30 H <sub>2</sub>	1 - 5	1,4-dioxane	15% Cu-Cu <sub>2</sub> O/N-RGO 240 °C, 15 bar H <sub>2</sub> , 3 h, 1,4-dioxane conv. = 100%, yield = 96% CB > 99%	Geng <i>et al.</i> , 2020

Reference: own author (2023)

Table 2.4. Furfural hydrodeoxygenation to 2-methylfuran.

Catalyst(s)	Reaction conditions				Best result	Reference
	T (°C)	P (bar)	t (h)	Solvent(s)		
NiP-P (P = H <sub>3</sub> PO <sub>4</sub> , TOP = trioctylphosphine)	250 - 350	50 H <sub>2</sub>	0.5 - 6	toluene, ethanol	NiP-TOP 350 °C, 50 bar H <sub>2</sub> , 3 h, toluene conv. = 100%, sel. = 77%	Golubeva and Maximov, 2020
Co/S (S = Al <sub>2</sub> O <sub>3</sub> , SiO <sub>2</sub> , TiO <sub>2</sub> , CeO <sub>2</sub> , MgO, ZrO <sub>2</sub> ) Ni/S (S = Al <sub>2</sub> O <sub>3</sub> , SiO <sub>2</sub> , CeO <sub>2</sub> )	150 - 230	1 - 10 H <sub>2</sub>	0.99 h <sup>-1</sup> (WHSV)	-	Co/Al <sub>2</sub> O <sub>3</sub> 180 °C, 10 bar H <sub>2</sub> conv. = 100%, sel. = 93% CB = 83%	Liu <i>et al.</i> , 2020
Ni <sub>2</sub> P-t-T (t = time = 0.5 - 2 h and T = temperature of synthesis = 280 - 340 °C)	120 - 280	5 - 20 H <sub>2</sub>	2 - 6	2-propanol	Ni <sub>2</sub> P-1-300 260 °C, 15 bar H <sub>2</sub> , 3 h, 2-propanol conv. = 100%, sel. = 91% CB > 95%	Wang <i>et al.</i> , 2020
5% Re/Al <sub>2</sub> O <sub>3</sub> 5% Cu - 3% M/Al <sub>2</sub> O <sub>3</sub> (M = Mn, Co, Re) 5% Cu - x% Re/Al <sub>2</sub> O <sub>3</sub> (x = 1, 3, 5) 5% Cu/Al <sub>2</sub> O <sub>3</sub> + 3% Re/Al <sub>2</sub> O <sub>3</sub>	160 - 240	-	1 - 10	2-propanol	5% Cu - 3% Re/Al <sub>2</sub> O <sub>3</sub> 220 °C, 4 h, 2-propanol conv. = 100%, yield = 94%	Zhou <i>et al.</i> , 2020

Reference: own author (2023)

Table 2.5. Furfural hydrodeoxygenation to 2-methylfuran.

Catalyst(s)	Reaction conditions				Best result	Reference
	T (°C)	P (bar)	t (h)	Solvent(s)		
Cu <sub>x</sub> Zn-Al-T (x = Cu/Zn = 0.5 - 4, calcination T = 400 - 800 °C)	160 - 200	1, 20, 40 N <sub>2</sub>	0.25 - 5	ethanol, butanol, 1-propanol, tert- butanol, 2-propanol	Cu <sub>2.5</sub> Zn-Al-600 180 °C, 1 bar N <sub>2</sub> , 4 h, 2-propanol conv. = 99%, yield = 72%	Niu <i>et al.</i> , 2019
Ni-Mo <sub>2</sub> C/SiO <sub>2</sub> (Ni/Mo = 0.1)	160, 200, 260	50 H <sub>2</sub>	2 - 6	-	Ni-Mo <sub>2</sub> C/SiO <sub>2</sub> 200 °C, 50 bar H <sub>2</sub> , 3 h conv. = 100%, yield = 75%	Smirnov <i>et al.</i> , 2019
ReO <sub>x</sub> (y)/SiO <sub>2</sub> (y = 0.5, 0.8, 1.1, 1.8) ReO <sub>x</sub> (1.4)/S (S = SiO <sub>2</sub> , Al <sub>2</sub> O <sub>3</sub> , SiO <sub>2</sub> -Al <sub>2</sub> O <sub>3</sub> )	150 - 250	30 - 50 H <sub>2</sub>	4	dodecane	ReO <sub>x</sub> (1.4)/SiO <sub>2</sub> 250 °C, 40 bar H <sub>2</sub> , 4 h, dodecane conv. = 95%, yield = 55% CB = 90%	Toledo <i>et al.</i> , 2019
x% PdNiTUD(y) (x = 1, 5, 7; y = Si/Ni = 10, 20, 50)	140, 170	formic acid	0 - 24	ethanol, 1-butanol	7% PdNiTUD(20) 170 °C, formic acid, 24 h, 1-butanol conv. = 98%, yield = 83%	Antunes <i>et al.</i> , 2018

Reference: own author (2023)

Table 2.6. Furfural hydrodeoxygenation to 2-methylfuran.

Catalyst(s)	Reaction conditions				Best result	Reference
	T (°C)	P (bar)	t (h)	Solvent(s)		
10% M/C (M = Pt, Co, Ni, Fe) 10% Ni - 10% Fe/C PtCo <sub>3</sub> NC (nanocrystals)	180	33 H <sub>2</sub>	-	1-propanol	10% Ni - 10% Fe/C 180 °C, 33 bar H <sub>2</sub> , space-time of 4 g min mL <sup>-1</sup> , 1-propanol conv. = 100%, yield = 88% CB > 90%	C. Wang <i>et al.</i> , 2018
4% Ir/S (S = Al <sub>2</sub> O <sub>3</sub> , C, ZrO <sub>2</sub> , MMT-K10 = montmorillonite) x% Ir/C (x = 1 - 6)	140 - 240	7 - 52 H <sub>2</sub>	1 - 5	2-propanol	5% Ir/C 220 °C, 7 bar H <sub>2</sub> , 5 h, 2-propanol conv. = 99%, sel. = 95%	Date <i>et al.</i> , 2018
α-MoC β-Mo <sub>2</sub> C γ-Mo <sub>2</sub> N MoO <sub>2</sub> MoO <sub>3</sub> Ni/SiO <sub>2</sub>	150	10 - 30 H <sub>2</sub>	6	cyclohexane, methanol, ethanol, 1-propanol, 2-propanol, 1-butanol, 2-butanol, tert-butanol	α-MoC 150 °C, 20 bar H <sub>2</sub> , 6 h, 2-butanol conv. = 100%, sel. = 90% CB > 95%	Deng <i>et al.</i> , 2018

Reference: own author (2023)

Table 2.7. Furfural hydrodeoxygenation to 2-methylfuran.

Catalyst(s)	Reaction conditions				Best result	Reference
	T (°C)	P (bar)	t (h)	Solvent(s)		
x% Pt - 3% Co/C (x = 0, 0.5, 1, 2, 3) 3% Pt - y% Co/C (y = 0, 1, 2)	160 - 200	0, 1, 5, 10 H <sub>2</sub> 10, 20 N <sub>2</sub>	2 - 10	toluene, tetrahydrofuran, methanol, ethanol, 2-propanol	3% Pt - 3% Co/C 180 °C, 5 bar H <sub>2</sub> , 8 h, 2-propanol conv. = 100%, yield = 59% CB = 100%	Dohade and Dhepe, 2018
23% Cu - 12% M/ γ-Al <sub>2</sub> O <sub>3</sub> (M = Co, Fe, Sn) 35% Cu/γ-Al <sub>2</sub> O <sub>3</sub>	177 - 227	10 - 50 H <sub>2</sub>	4	2MTHF	23% Cu - 12% Co/γ-Al <sub>2</sub> O <sub>3</sub> 220 °C, 30 bar H <sub>2</sub> , 4 h, 2-methyltetrahydrofuran conv. = 100%, yield = 80% CB = 83%	Gandarias <i>et al.</i> , 2018
x% Cu/AC (x = 10, 17, 23)	150 - 200	20 N <sub>2</sub>	1 - 8	methanol, ethanol, 2-propanol, 1-butanol, 2-butanol, 1-pentanol, 2-pentanol	17.1% Cu/AC 200 °C, 20 bar N <sub>2</sub> , 5 h, 2-propanol conv. = 100%, sel. = 92% CB > 94%	Gong <i>et al.</i> , 2018a
Cu/S (S = C, SiO <sub>2</sub> , ZrO <sub>2</sub> , Al <sub>2</sub> O <sub>3</sub> , CeO <sub>2</sub> ) Cu/SiO <sub>2</sub> -P (P = IM - impregnation, HT - hydrothermal)	220	-	2	cyclohexanol, dodecane, methanol, ethanol, 2-propanol	Cu/SiO <sub>2</sub> -HT 220 °C, 2 h, 2-propanol conv. = 100%, sel. = 90%	Li <i>et al.</i> , 2018

Reference: own author (2023)

Table 2.8. Furfural hydrodeoxygenation to 2-methylfuran.

Catalyst(s)	Reaction conditions				Best result	Reference
	T (°C)	P (bar)	t (h)	Solvent(s)		
x% M/S (x = 1.5, 3, 10; M = Pt, Ru, Ni; S = AC-S, AC-B; S = spruce, B = birch)	210 - 240	40 H <sub>2</sub>	0 - 5	2-propanol	3% Pt/AC-S 240 °C, 40 bar H <sub>2</sub> , 2 h, 2-propanol conv. = 100%, yield = 50%	Mäkelä <i>et al.</i> , 2018
5% Cu - x% Ni/Al <sub>2</sub> O <sub>3</sub> (x = 0, 0.5, 1.5, 3, 5) 5% Cu - x% Ni/TiO <sub>2</sub> (x = 0, 0.5, 1.5, 3, 5, 10)	200	35 H <sub>2</sub>	0.5 - 8	1,4-dioxane	5% Cu/Al <sub>2</sub> O <sub>3</sub> 200 °C, 35 bar H <sub>2</sub> , 8 h, 1,4-dioxane conv. = 100%, yield = 95% CB > 95%	Seemala <i>et al.</i> , 2018
NiMoC-SiO <sub>2</sub> (Ni/Mo = 0, 0.5, 1, 2, 4, 6; calcination at 400, 600, 700 °C; reduction at 600 °C)	150	60 H <sub>2</sub>	2 - 210 min	2-propanol	NiMoC-SiO <sub>2</sub> (calc. = 400 °C, red. = 600 °C) 150 °C, 60 bar H <sub>2</sub> , 210 min, 2-propanol conv. = 91%, yield = 29%	Shilov <i>et al.</i> , 2018
Cu - Co/Al <sub>2</sub> O <sub>3</sub>	170 - 230	20 - 50 H <sub>2</sub>	3 - 6	2-propanol	Cu - Co/Al <sub>2</sub> O <sub>3</sub> 220 °C, 40 bar H <sub>2</sub> , 5 h, 2-propanol conv. = 100%, yield = 87%	Srivastava <i>et al.</i> , 2018

Reference: own author (2023)



Table 2.9. Furfural hydrodeoxygenation to 2-methylfuran.

Catalyst(s)	Reaction conditions				Best result	Reference
	T (°C)	P (bar)	t (h)	Solvent(s)		
Ni <sub>2</sub> P (Ni:P = 0.5, 0.75, 1) MoP	210 - 250	10 - 30 H <sub>2</sub>	1 - 5	2-propanol	Ni <sub>2</sub> P (Ni:P = 0.5) 240 °C, 20 bar H <sub>2</sub> , 4 h, 2-propanol conv. = 100%, sel. = 83%	Wang <i>et al.</i> , 2018
10% Cu/AC 5% Ni/AC 3% M/AC (M = Pt, Pd)	130 - 150, 200	0 - 50 H <sub>2</sub>	5	methanol, ethanol, 2-propanol, cyclopentyl methyl ether (CPME)	5% Ni/AC 200 °C, 30 bar H <sub>2</sub> , 5 h, 2-propanol (batch) conv. = 85%, sel. = 78% CB = 93% 3% Pt/AC 150 °C, 50 bar H <sub>2</sub> , WHSV = 27 h <sup>-1</sup> , CPME (continuous) conv. = 100%, sel. = 82% CB = 100%	Yantao Wang <i>et al.</i> , 2018
60% M/Al <sub>2</sub> O <sub>3</sub> (M = Cu, Ni) x% Cu - y% Ni/Al <sub>2</sub> O <sub>3</sub> (x, y = 20, 30, 40)	190, 210, 230, 250	-	4	methanol, 2-propanol	20% Cu - 40% Ni/Al <sub>2</sub> O <sub>3</sub> 230 °C, 4 h, 2-propanol conv. = 100%, yield = 65%	Zhang <i>et al.</i> , 2018

Reference: own author (2023)

Table 2.10. Furfural hydrodeoxygenation to 2-methylfuran.

Catalyst(s)	Reaction conditions				Best result	Reference
	T (°C)	P (bar)	t (h)	Solvent(s)		
10% M/Al <sub>2</sub> O <sub>3</sub> (M = Ni, Cu) x% Ni - 10% Cu/ Al <sub>2</sub> O <sub>3</sub> (x = 2, 5, 8, 10)	170 - 250	10 N <sub>2</sub> + formic acid	1 - 7	toluene, dimethyl sulfoxide, tetrahydrofuran, water, 2-propanol	10% Ni - 10% Cu/ Al <sub>2</sub> O <sub>3</sub> 210 °C, formic acid, 7 h, 2-propanol conv. = 100%, sel. = 92% CB > 90%	Fu <i>et al.</i> , 2017
17% Cu/AC-T/t (temperature = T = 300 - 500 °C and time = t = 1 - 4 h of calcination)	80 - 170	1 - 40 H <sub>2</sub>	1 - 10	toluene, methanol, ethanol, 2-propanol	17% Cu/AC-400/2 170 °C, 30 bar H <sub>2</sub> , 4 h, 2-propanol conv. = 100%, yield = 100%	Gong <i>et al.</i> , 2017
x% Ni/C (x = 2, 5, 10) x% Cu/C (x = 1, 2, 5) y% CuNi/C (y = 2/2, 5/2, 2/5) y% CuFe/C (y = 2/2, 5/2) y% NiFe/C (y = 2/2, 5/2, 5/5)	200, 230	40 H <sub>2</sub>	0 - 5	2-propanol	10% Ni/C 230 °C, 40 bar H <sub>2</sub> , 2 h, 2-propanol conv. = 100%, sel. = 49%	Jaatinen <i>et al.</i> , 2017

Reference: own author (2023)

Table 2.11. Furfural hydrodeoxygenation to 2-methylfuran.

Catalyst(s)	Reaction conditions				Best result	Reference
	T (°C)	P (bar)	t (h)	Solvent(s)		
1% Pd/SiO <sub>2</sub> 1% Pd - 0.5% Fe/S (S = SiO <sub>2</sub> , Al <sub>2</sub> O <sub>3</sub> )	250	40 H <sub>2</sub>	1	decalin	1% Pd - 0.5% Fe/SiO <sub>2</sub> 250 °C, 40 bar H <sub>2</sub> , 1 h, decalin conv. = 84%, yield = 36% CB = 82%	Pino <i>et al.</i> , 2017
10% M/Al <sub>2</sub> O <sub>3</sub> (M = Ni, Cu) 10% Cu - x% Ni/Al <sub>2</sub> O <sub>3</sub> (x = 2.5, 5, 10)	130 - 230	40 H <sub>2</sub>	4	2-propanol	10% Cu - 10% Ni/Al <sub>2</sub> O <sub>3</sub> 210 °C, 40 bar H <sub>2</sub> , 4 h, 2-propanol conv. = 100%, yield = 84%	Srivastava <i>et al.</i> , 2017
x% Ru/NiFe <sub>2</sub> O <sub>4</sub> -T (x = 0, 2, 4, 6, 8, calcination T = 300, 400, 500 °C)	160 - 200	21 N <sub>2</sub>	2 - 10	2-propanol	8% Ru/NiFe <sub>2</sub> O <sub>4</sub> -400 180 °C, 21 bar N <sub>2</sub> , 6 h, 2-propanol conv. = 98%, yield = 83%	Wang <i>et al.</i> , 2017
Cu <sub>x</sub> Al-HTLc (x = Cu/Al = 1:1, 2:1, 3:1) HTLc = hydrotalcite	190 - 245	10 N <sub>2</sub>	0 - 5	methanol	Cu <sub>3</sub> Al-HTLc 240 °C, 10 bar N <sub>2</sub> , 1.5 h, methanol conv. = 98%, yield = 94%	Zhang and Chen, 2017
x% Pd/TiO <sub>2</sub> (x = 1, 2.5, 5) x% Ru - y% Pd/TiO <sub>2</sub> (x = 0.5 - 5; y = 0 - 4.5)	25	3 H <sub>2</sub>	30 - 180 min	1,2-dichloroethane, toluene, methanol, octane	1% Ru - 4% Pd/TiO <sub>2</sub> 25 °C, 3 bar H <sub>2</sub> , 2 h, octane conv. = 39%, sel. = 51%	Aldosari <i>et al.</i> , 2016

Reference: own author (2023)

Table 2.12. Furfural hydrodeoxygenation to 2-methylfuran.

Catalyst(s)	Reaction conditions				Best result	Reference
	T (°C)	P (bar)	t (h)	Solvent(s)		
10% Cu - 3% M/ZrO <sub>2</sub> (M = Ni, Ru, Pd) 10% Cu - x% Pd/ZrO <sub>2</sub> (x = 1, 5) 10% Cu - 3% Pd/S (S = Al <sub>2</sub> O <sub>3</sub> , SiO <sub>2</sub> , TiO <sub>2</sub> ) 10% Cu/ZrO <sub>2</sub> 3% Pd/ZrO <sub>2</sub> 10% Cu/ZrO <sub>2</sub> + 3% Pd/ZrO <sub>2</sub>	160 - 240	-	4	2-propanol	10% Cu - 1% Pd/ZrO <sub>2</sub> 220 °C, 4 h, 2-propanol conv. = 99%, yield = 64% CB > 84%	Chang <i>et al.</i> , 2016
x% Ni/C (x = 2, 5, 10)	180, 200, 230	20 - 40 H <sub>2</sub>	0 - 400 min	2-propanol	10% Ni/C 230 °C, 40 bar H <sub>2</sub> , 1 h, 2-propanol conv. = 100%, yield = 49%	Jaatinen <i>et al.</i> , 2016
Cu-Co/S (Cu/Co = 1, 2, 4; S = SiO <sub>2</sub> , Al <sub>2</sub> O <sub>3</sub> , ZSM-5)	140 - 200	40 H <sub>2</sub>	4	2-propanol	10% Cu - 10% Co/Al <sub>2</sub> O <sub>3</sub> 200 °C, 40 bar H <sub>2</sub> , 4 h, 2-propanol conv. = 100%, sel. = 78%	Srivastava <i>et al.</i> , 2016

Reference: own author (2023)

Table 2.13. Furfural hydrodeoxygenation to 2-methylfuran.

Catalyst(s)	Reaction conditions				Best result	Reference
	T (°C)	P (bar)	t (h)	Solvent(s)		
5% Ru-RuO <sub>2</sub> /C	110 - 200	20 N <sub>2</sub>	5, 10	ethanol, 1-propanol, 2-propanol, 1-butanol, 2-butanol, 2-methyl-2-butanol, tert-butanol, 2-pentanol	5% Ru-RuO <sub>2</sub> /C 180 °C, 20 bar N <sub>2</sub> , 10 h, 2-butanol conv. = 100%, yield = 76%	Panagiotopoulou <i>et al.</i> , 2014
5% Ru/C	120 - 200	20 N <sub>2</sub> 10 H <sub>2</sub> + 10 N <sub>2</sub>	0 - 16	2-propanol	5% Ru/C 180 °C, 20 bar N <sub>2</sub> , 10 h, 2-propanol conv. = 95%, yield = 61%	Panagiotopoulou and Vlachos, 2014
10% M/Fe <sub>2</sub> O <sub>3</sub> (M = Cu, Ni, Pd) x% Pd/Fe <sub>2</sub> O <sub>3</sub> (x = 2, 5, 10) 10% Pd/S (S = C, Al <sub>2</sub> O <sub>3</sub> , MgO)	150, 165, 180	15, 25 N <sub>2</sub>	0 - 7.5	ethanol, 1-propanol, 2-propanol, 2-butanol	2% Pd/Fe <sub>2</sub> O <sub>3</sub> 180 °C, 25 bar N <sub>2</sub> , 2-propanol conv. = 100%, yield = 26%	Scholz <i>et al.</i> , 2014

Reference: own author (2023)

### 2.3.1.1 Effect of the reaction conditions

#### 2.3.1.1.1 Temperature, pressure, and reaction time

The effect of temperature, pressure, and reaction time was widely investigated in the literature to produce 2MF from furfural in the liquid phase using various catalysts as can be seen in Table 2.3 - 2.13.

Recently, the effect of temperature (140 - 220 °C) in the hydrodeoxygenation of furfural in 2-propanol was studied at 20 bar of H<sub>2</sub> and 4 hours of reaction by Chuseang *et al.*, (2021) using Cu and Cu<sub>1</sub>Re<sub>0.14</sub> catalysts. Furfuryl alcohol and 2-methylfuran were the main products observed below 200 °C, while 2MTHF only appeared above this temperature. The increase in the temperature from 200 to 220 °C promoted the 2MF yield from 50 to 73% using Cu/ $\gamma$ -Al<sub>2</sub>O<sub>3</sub> as a catalyst. In any case, a higher 2MF yield was observed for the Cu<sub>1</sub>Re<sub>0.14</sub> catalyst throughout the temperature range investigated.

The authors also evaluated the reaction time (0 - 6 hours) at 200 °C. The 2MF yield increased sharply between 0.5 - 2 hours and then remained constant at 47% up to 6 hours over the Cu catalyst, but the use of higher reaction times led to the formation of by-products such as 1-pentanol, 1,2-pentanediol, and 1,4-pentanediol.

The effect of temperature (177 - 227 °C) and pressure (10 - 50 bar of H<sub>2</sub>) to produce 2MF from FF was also evaluated using 2MTHF as a solvent and 35% Cu/ $\gamma$ -Al<sub>2</sub>O<sub>3</sub> and 23% Cu - 12% Co/ $\gamma$ -Al<sub>2</sub>O<sub>3</sub> catalysts. Gandarias *et al.*, (2018) observed that the temperature has a much greater effect compared to pressure for this reaction. The increase in the temperature favored the conversion of FA to 2MF but also reduced the carbon balance due to the higher formation of condensation products. The authors suggest that the temperature should not exceed 220 °C to avoid side reactions. A complete conversion of FF and a selectivity of 80% to 2MF was achieved at 220 °C and 30 bar of H<sub>2</sub>.

Srivastava *et al.*, (2018) investigated the influence of temperature (170 - 230 °C), pressure (10 - 50 bar of H<sub>2</sub>), and reaction time (3 - 6 hours) for the HDO

of FF to 2MF in 2-propanol using Cu-Co/Al<sub>2</sub>O<sub>3</sub> as a catalyst. The temperature effect was evaluated in the mentioned range because furfuryl alcohol is the main product formed below 170 °C. They observed that high temperatures promote the formation of 2MF by C-O hydrogenolysis of FA since more energy is necessary to activate this bond. This same effect was observed when using longer reaction times, which had a positive effect on the 2MF yield since it is the subsequent product from FA intermediate. Finally, an ideal pressure is also needed for this reaction since at too high pressures the formation of ring hydrogenation products is favored. The highest selectivity to 2MF (87%) was obtained in full FF conversion at 220 °C, 40 bar of H<sub>2</sub>, and 5 hours.

Date *et al.*, (2018) studied the effect of temperature (140 - 240 °C), pressure (7 - 52 bar of H<sub>2</sub>), and reaction time (1 - 5 hours) for the HDO of furfural in 2-propanol using Ir/C catalyst. They observed that the 2MF selectivity was favored up to 220 °C because, above that, other hydrogenation by-products started to be produced. The increase in pressure up to 34 bar of H<sub>2</sub> did not affect the formation of 2MF, which remains constant, but above this value ring hydrogenation products such as 2MTHF and THFA was formed. Finally, a positive effect on the 2MF selectivity was found by increasing reaction time. The highest selectivity to 2MF (95%) was obtained in an FF conversion of 99% at 220 °C, 7 bar of H<sub>2</sub> for 5 hours.

The effect of pressure (10 - 30 bar of H<sub>2</sub>) was investigated by Deng *et al.*, (2018) using  $\alpha$ -MoC as a catalyst for the HDO of FF at 150 °C for 6 hours with 2-propanol. The authors observed a positive effect on the FF conversion and 2MF selectivity by increasing the pressure, which was accompanied by the reduction in the selectivity of by-products such as C<sub>10</sub> species formed from FF dimerization. The ideal pressure was chosen as 20 bar because the further increase to 30 bar does not significantly increase the selectivity to 2MF.

Smirnov *et al.*, (2019) used a Ni-Mo<sub>2</sub>C catalyst supported on  $\gamma$ -Al<sub>2</sub>O<sub>3</sub> to study the effect of different temperatures (160, 200, and 260 °C) and reaction times (2 - 6 hours) in the production of 2MF. Full FF conversions were obtained over all temperatures. At 160 °C, only low amounts of 2MF were observed, FA being the main product. The 2MF yield reached 75 and 85% at 220 and 260 °C, respectively, however,

the highest temperature led to the fast deactivation of the catalyst. The reaction times that most favored the 2MF yield were between 3 and 4 hours.

As could be seen, several works reported that 2MF formation is favored at temperatures between 180 and 220 °C. Below these temperatures, mainly furfuryl alcohol is observed, and above these temperatures, FF and FA may undergo condensation reactions or 2MF can be hydrogenated. Meanwhile, pressures up to 30 bar of H<sub>2</sub> are preferable to avoid ring hydrogenation (Gandarias *et al.*, 2018; Srivastava *et al.*, 2016) and longer reaction times have a positive effect on 2MF formation, however, prolonged times are not interesting for industrial applications.

#### **2.3.1.1.2 Effect of substrate concentration and catalyst amount**

In addition to temperature, pressure, and reaction time, other parameters such as substrate concentration and catalyst amount can also influence the FF conversion and product distribution.

The concentration of furfural in 2-propanol was investigated by Srivastava *et al.*, (2018) in the range of 1.75 - 3.25 M using Cu-Co/Al<sub>2</sub>O<sub>3</sub> as a catalyst at 220 °C, 40 bar H<sub>2</sub>, and 5 hours. The 2MF yield increased from 1.75 to 2.75 M but decreased with increasing FF concentration. A higher 2MF yield could be obtained using a lower FF amount (1.75 M). The substantial decrease in 2MF yield was ascribed to the lower availability of active sites to convert the intermediate FA to 2MF via hydrogenolysis. In addition, the use of high FF concentration was detrimental to the stability of the catalyst active sites due to FA polymerization.

The authors also evaluated the amount of catalyst used (0.5 - 1.25 g). They observed an increase in the activity by increasing the catalyst loading, which was ascribed to the availability of a greater number of active sites. However, a decrease in 2MF yield was observed for a catalyst amount higher than 0.75 g, which led to the further transformation of 2MF to MTHF and/or other over-hydrogenolysis products.

Scholz *et al.*, (2014) observed that using 2 wt.% Pd/Fe<sub>2</sub>O<sub>3</sub> under continuous flow conditions and 0.4 M of FF led to the formation of ring-hydrogenated products of



FA and 2MF, which were only detected in trace amounts in batch experiments at 180 °C, 25 bar of N<sub>2</sub> in 2-propanol. They found that the 2MF formation is inhibited as long as furfural is present in the system because there is competitive adsorption between the species. When FF is finally converted to FA, the hydrogenolysis reaction is accelerated forming other products besides 2MF. The use of a lower FF concentration (0.12 M), however, slightly promoted 2MF yield.

Different amounts of Ru/NiFe<sub>2</sub>O<sub>4</sub> (0.025, 0.05, 0.1, 0.13, 0.15 g) used as catalysts were investigated by Wang *et al.*, (2017) for the CTH reaction of FF to produce 2MF at 180 °C, 21 bar of N<sub>2</sub> for 4 hours. During the whole range, an increase in the FF conversion and 2MF yield was observed by increasing the amount of catalyst, but this was accompanied by the occurrence of side reactions. For this reason, according to the authors, the amount of catalyst should not exceed 0.15 g.

Yazhou Wang *et al.*, (2018) studied the Ni<sub>2</sub>P catalyst amount (0.04 - 0.16 g) to produce 2MF from FF at 240 °C, 20 bar of H<sub>2</sub>, and 4 hours. The conversion of FF was maximum regardless of the catalyst mass used. The highest 2MF selectivity (83%) was obtained using 0.1 g of catalyst. A further increase in the catalyst loading decreases the selectivity to 2MF and increased to 2MTHF and 2-pentanone. The results also show that the selectivity to difurfuryl ether, produced by FA dimerization, decreases with the enhancing amount of catalyst.

In summary, to produce 2MF with high selectivity several parameters related to the reaction conditions must be controlled. As could be seen, lower FF amounts in the reaction mixture favor the 2MF formation. In the presence of high concentrations, the active sites cannot fully convert the intermediate FA to 2MF and, for this reason, the surplus FA ends up being polymerized forming undesirable products or even poisoning the catalysts used. Finally, the use of too much catalyst ends up converting the 2MF into over-hydrogenated products.

### 2.3.1.1.3 Solvent effect

The effect of the solvent is, in some cases, related to the product distribution of a reaction, especially if it is carried out in the absence of H<sub>2</sub> as occurs for catalytic transfer hydrogenation reactions.

A pioneering work regarding the solvent effect in the CTH of furfural was carried out by Panagiotopoulou *et al.*, (2014) using 5 wt.% Ru-RuO<sub>2</sub>/C as a catalyst. The authors tested the hydrogen-donating ability of several alcohols (ethanol, 1-propanol, 2-propanol, 1-butanol, 2-butanol, 2-methyl-2-butanol, tert-butanol, and 2-pentanol) at 180 °C and 20 bar of N<sub>2</sub>. They observed that the use of smaller chain alcohols favors the etherification reaction of FF with the solvent, which competes with the hydrogenolysis reaction of FA to 2MF. However, at higher temperatures and longer reaction times, the ether formation tends to be reversed due to limitations in the reaction equilibrium.

Another interesting finding of this work is that hydrogenolysis is favored by the increased dehydrogenation capacity of the alcohol, while 2MF yield decreases with increasing solvent polarity, possibly due to the higher FF-alcohol interaction that slows the adsorption of this substrate onto the catalyst. Among the solvents, secondary alcohols showed higher hydrogen donating capacity, which was associated with either higher reduction potential to the respective ketones or the lower inductive electron release effect of one alkyl group compared to two alkyl groups.

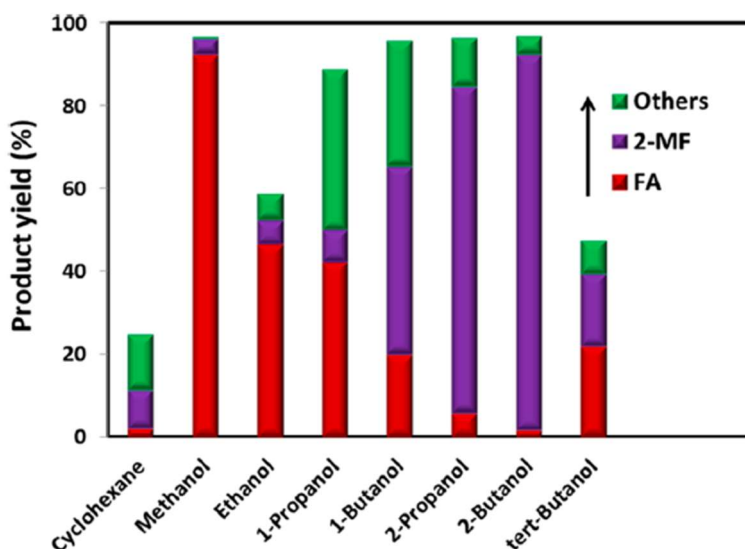
Different protic solvents (ethanol, 1-propanol, 2-propanol, 1-butanol, and 2-butanol) were evaluated by Niu *et al.*, (2019) for the production of 2MF from CTH of furfural using CuZnAl catalysts. It was observed that within the class of primary alcohols, molecules with smaller chains are preferable in obtaining 2MF, however, a better catalytic performance was observed in the presence of secondary alcohols. The highest 2MF yield (72%) was obtained over Cu<sub>2.5</sub>Zn-Al-600 catalyst at 180 °C, 1 bar of N<sub>2</sub> using 2-propanol as solvent.

Li *et al.*, (2018) investigated protic (methanol, ethanol, and 2-propanol) and aprotic (cyclohexanol and dodecane) solvents in the CTH reaction of FF at 220 °C using

Cu/SiO<sub>2</sub> as a catalyst. The use of methanol led to the highest formation of 2MF because it produced the highest amount of molecular hydrogen *in situ* in the presence of the catalyst.

The effect of nonpolar cyclohexane and polar C<sub>1</sub>-C<sub>4</sub> alcohols (methanol, ethanol, 1-propanol, 2-propanol, 1-butanol, 2-butanol, and tert-butanol) was studied by Deng *et al.*, (2018) using  $\alpha$ -MoC as a catalyst for the HDO of FF at 150 °C, 20 bar of H<sub>2</sub> for 6 hours. Firstly, the solvents with lack hydrogen donating ability (cyclohexane and tert-butanol) were compared. The yield of FF hydrogenation products (FA and 2MF) was higher in the tert-butanol, probably because of the polar nature of the furfural reactants. The 2MF yield in polar alcohols increased as follows: tertiary < primary < secondary alcohols, which agrees with their ability to donate hydrogen in CTH reactions. The higher 2MF yields were obtained over 2-propanol and 2-butanol. This study clearly showed the relationship between solvent and product distribution, since the formation of a certain compound is related to the type of solvent used as shown in Figure 2.8.

Figure 2.8. Solvent effects on product yields of FF hydrogenation on  $\alpha$ -MoC catalysts.



Reference: Deng *et al.*, (2018)

Alternatively, Fu *et al.*, (2017) tested formic acid together with 2-propanol as a hydrogen source in the FF hydrogenation to 2MF at 210 °C for 4 hours using Ni, Cu, and Ni-Cu catalysts supported on Al<sub>2</sub>O<sub>3</sub>. The monometallic catalysts were poorly selective to the desired product (< 40%). In contrast, the bimetallic catalysts favored 2MF selectivity, which was higher (76%) for catalysts with higher nickel contents (10% Ni - 10% Cu). The authors also evaluated the hydrogenation capacity of formic acid by performing tests in the presence or absence of this compound. Using only 2-propanol, a FA yield of 96% was achieved, while the addition of formic acid produced up to 79% yield of 2MF.

As can be seen from the works mentioned above, the effect of the solvent on the CTH reaction of FF not only depends on the hydrogen-donating capacity of the alcohol but also on the ability of the catalyst to dehydrogenate this alcohol.

Aprotic solvents such as 1,4-dioxane (Geng *et al.*, 2020; Seemala *et al.*, 2018), toluene (Golubeva and Maximov, 2020), 2MTHF (Gandarias *et al.*, 2018), octane (Aldosari *et al.*, 2016), dodecane (Toledo *et al.*, 2019) and decalin (Pino *et al.*, 2017) have also been evaluated to produce 2MF from furfural, but in general, the most used solvents are the protic ones, especially 2-propanol.

### **2.3.1.2 Catalyst for furfural hydrodeoxygenation**

#### **2.3.1.2.1 Support effect**

It is known that the physicochemical properties of a material used as support for catalysts can play an important role in both substrate conversion and product distribution depending on the reaction. The electronic effect of the supports can modify, for example, the metals or active phases disposition/dispersion and the adsorption/desorption of the reactants and products, and the catalytic properties of the active phase (Seemala *et al.*, 2018; Toledo *et al.*, 2019). In addition, the acidic properties can influence the type of products formed.

Recently, Liu *et al.*, (2020) tested Co-based catalysts supported on different materials (SiO<sub>2</sub>, TiO<sub>2</sub>, Al<sub>2</sub>O<sub>3</sub>, CeO<sub>2</sub>) for the HDO of FF at 180 °C and 10 bar of H<sub>2</sub>. The selectivity obtained was associated with the different amounts of Lewis acid sites present on the supports since the catalysts showed similar metallic dispersions. These highly electrophilic sites strongly interacted with the oxygen of the formyl group of FF facilitating the cleavage of the C-O bond from the substrate. Adjacent metal sites were also required to provide hydrogen atoms to the carbonyl bond. In this sense, an efficient 2MF production was provided using a bifunctional catalyst presenting both metallic and Lewis acidic sites. The Co/Al<sub>2</sub>O<sub>3</sub> catalyst showed the best catalytic performance exhibiting full conversion of furfural and 2MF selectivity of 93%.

In opposition to this, the acidic nature of the support did not influence the selectivity to 2MF when using ReO<sub>x</sub> catalysts supported on bare SiO<sub>2</sub> and Al<sub>2</sub>O<sub>3</sub> and SiO<sub>2</sub>-Al<sub>2</sub>O<sub>3</sub> at 250 °C, 40 bar of H<sub>2</sub> during 4 hours as observed by Toledo *et al.*, (2019).

Srivastava *et al.*, (2016) evaluated the influence of the type of support (SiO<sub>2</sub>,  $\gamma$ -Al<sub>2</sub>O<sub>3</sub>, and ZSM-5) on the performance of Cu-Co catalysts in the FF hydrodeoxygenation reaction at 220 °C, 40 bar of H<sub>2</sub> for 4 hours. Uniform distributions and similar active phase dispersions were observed on SiO<sub>2</sub> and Al<sub>2</sub>O<sub>3</sub>, but large metal crystallite sizes were formed over the Cu-Co/SiO<sub>2</sub> catalyst. In contrast, using ZSM-5 as support led to a non-uniform distribution of the Cu-Co nanoparticles. The catalytic results revealed that large Cu particles on Cu-Co/SiO<sub>2</sub> catalyst produced mainly FA, while the highest selectivity to 2MF (78%) was observed over the catalyst supported on  $\gamma$ -Al<sub>2</sub>O<sub>3</sub>. This was associated with the additional number of ordered Cu-CoO<sub>x</sub> species with uniform porosity and support, in which aluminum would seize electrons from the metal copper increasing its oxophilic nature and contributing to the C-O bond hydrogenolysis in FA.

Bimetallic Cu-Ni catalysts supported on Al<sub>2</sub>O<sub>3</sub> and TiO<sub>2</sub> were studied by Seemala *et al.*, (2018) in the hydrodeoxygenation of FF at 200 °C, 35 bar of H<sub>2</sub> using 1,4-dioxane as solvent. For the catalysts supported on Al<sub>2</sub>O<sub>3</sub>, the authors observed that the addition of Ni (0.5 - 3%) to Cu (5%) did not favor the selectivity to 2MF, while when these metals were supported on TiO<sub>2</sub>, a higher 2MF selectivity was obtained. The TiO<sub>2</sub>-supported catalyst containing 5% Cu and 1.5% Ni was the one that most favored

the production of 2MF since higher Ni contents (3, 5, and 10%) led to the formation of 2MTHF.

The addition of Ni to Cu catalysts and the metal arrangement on the different supports modifies the FF adsorption configuration on the surface of the catalyst and, for this reason, distinct hydrogenation products were observed. The characterizations and catalytic evaluation suggest that on Al<sub>2</sub>O<sub>3</sub>, Ni has minimal interaction with Cu, while on TiO<sub>2</sub> these metals would be found as alloys. These configurations cause the dispersed Ni on Cu-Ni/TiO<sub>2</sub> catalyst to be unable to adsorb the furan ring of the reactants preferentially producing 2MF, while the opposite occurs over the Cu-Ni/Al<sub>2</sub>O<sub>3</sub> catalyst, which produces THFA. Finally, the difference in the activities of the monometallic Cu catalysts was attributed to the greater dispersion of this metal in alumina compared to titania, while the acidity of the supports did not seem to influence the reactivity of the catalyst.

Different commercially available supports (SiO<sub>2</sub>, TiO<sub>2</sub>, ZrO<sub>2</sub>, and Al<sub>2</sub>O<sub>3</sub>) were tested at 220 °C and 4 hours by Chang *et al.*, (2016) in the CTH of furfural in 2-propanol using Cu-Pd catalysts. A full FF conversion was achieved over all catalysts, however, higher 2MF yields (around 61%) were obtained for the catalysts supported on TiO<sub>2</sub> and ZrO<sub>2</sub>. In fact, in this work, the authors desired the formation of both 2MF and 2MTHF. The use of ZrO<sub>2</sub> as support also promoted the 2MTHF formation without compromising the 2MF yield. This was associated with the acid-base sites of this support, which assist the adsorption of alcohols and the dissociation of hydrogen from them in CTH reactions. These properties of ZrO<sub>2</sub>, however, did not promote the 2MF yield in comparison to TiO<sub>2</sub>.

In the work of Mäkelä *et al.*, (2018), the use of activated carbon (AC) produced by lignocellulosic biomass residue from both Finnish birch (B) and spruce (S) did not influence the 2MF yield (around 50%) obtained at 240 °C and 40 bar of H<sub>2</sub>, which was mainly associated to the metal dispersion and particle size of Pt/AC-S and Ru/AC-B in comparison to Ni/AC-S catalyst. However, this effect was not related to the metal load.

Finally, Date *et al.*, (2018) performed a screening of Ir catalysts supported on different materials (C, ZrO<sub>2</sub>, Al<sub>2</sub>O<sub>3</sub>, and MMT - montmorillonite) to produce 2MF from FF at 220 °C, 7 bar of H<sub>2</sub>, and 5 hours. All catalysts showed similar activities, but 2MF

yield varied as a function of support in the following order  $C > \text{ZrO}_2 > \text{Al}_2\text{O}_3 = \text{MMT}$ . Similar selectivities of 2MF and THFA were found over  $\text{ZrO}_2$ , while a mix of products (FA, 2MF, THFA, 1,2-pentanediol) were formed over  $\text{Al}_2\text{O}_3$  and MMT supports. The highest selectivity to 2MF (80%) was observed using C, but unfortunately, the different product distributions were not explained and correlated with the support properties in the paper.

These works demonstrate that it is difficult to draw any conclusions about the support effect since in some cases the production of 2MF is not influenced by the support (Chang *et al.*, 2016; Mäkelä *et al.*, 2018; Toledo *et al.*, 2019) and in others is related to the arrangement and dispersion of the metals caused by the supports (Seemala *et al.*, 2018; Srivastava *et al.*, 2016) or directly connected to its acidic properties (Liu *et al.*, 2020).

For these reasons,  $\text{SiO}_2$ ,  $\text{TiO}_2$ ,  $\text{ZrO}_2$ , and ZSM-5 were selected in this work as supports for Mo-based catalysts to be studied in the HDO of furfural. The idea is to investigate the influence of the total amount and the nature of acid sites in these materials. Silica has scarcely acidic properties, while  $\text{TiO}_2$  and  $\text{ZrO}_2$  exhibit Lewis acidic sites and ZSM-5 possesses both Lewis and Bronsted acid sites.

### **2.3.1.2.2 Nature of the metal phase**

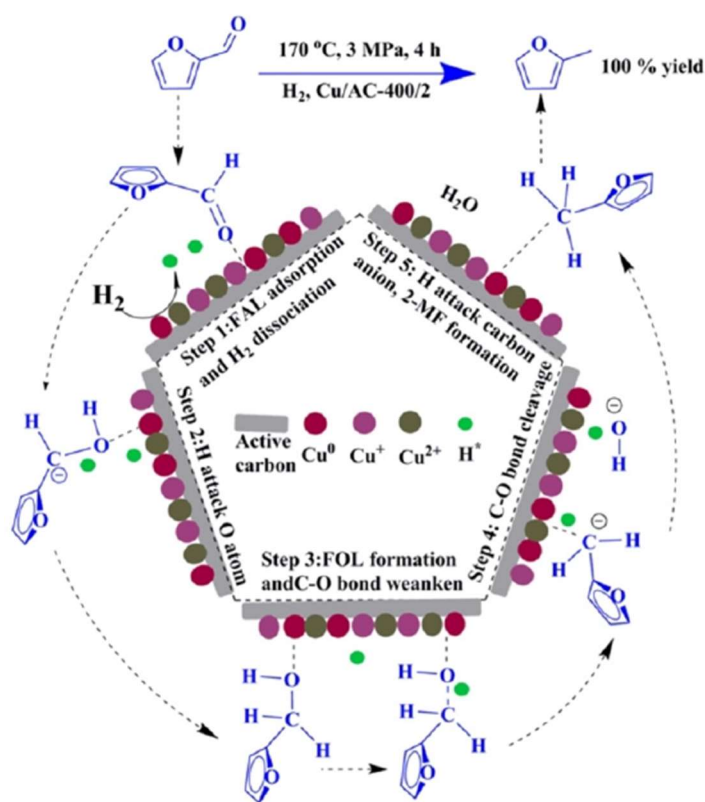
The works summarized in Table 2.3 - 2.13 show that 2MF production from hydrodeoxygenation of furfural in the liquid phase can be carried out using monometallic and bimetallic catalysts based on both noble and non-noble metals.

Cu-based catalysts are the most used for HDO of FF to produce 2MF since Cu is an affordable and available metal that shows the ability in performing the hydrogenation of carbonyl groups (Gupta *et al.*, 2018; Khemthong *et al.*, 2021). Furfural is adsorbed on Cu in the  $\eta^1\text{-}(\text{O})$  configuration via aldehyde function because there is a strong repulsion force between Cu (111) and the furan ring due to the incomplete overlaying of the 3 d band of Cu atoms and the antibonding orbital in the furan ring, which prevents its hydrogenation (Chen *et al.*, 2018).

An excellent catalytic performance was achieved by a monometallic Cu catalyst supported on activated carbon (AC) in the HDO of FF using 2-propanol at 170 °C, 30 bar of H<sub>2</sub>, and 4 hours. According to Gong *et al.*, (2017), a full FF conversion and selectivity to 2MF were obtained due to the presence of different Cu species in the Cu/AC catalyst calcined at 400 °C for 2 hours. Electron-deficient copper oxide species (Cu<sup>+</sup> and Cu<sup>2+</sup>) acted as Lewis acidic sites attracting and weakening the C=O bond in FF, which was hydrogenated by activated hydrogen species formed on Cu<sup>0</sup> centers. Finally, the C-O bond in furfuryl alcohol was dissociated on Cu<sup>+</sup> sites forming 2MF. The reaction mechanism proposed by the authors can be seen in Figure 2.9.

Notwithstanding, the recyclability tests of this catalyst showed a reduction in the catalyst performance after six cycles, which was attributed to the reduction of CuO<sub>x</sub> to the metallic state Cu<sup>0</sup>, and a slight reduction in the 2MF selectivity was observed from the third cycle.

Figure 2.9. Possible reaction pathway for the hydrogenolysis of FF over Cu/AC catalyst.



Reference: Gong *et al.*, (2017)



The same group studied the effect of Cu loadings (10, 17, and 23 wt.%) for Cu/AC catalysts in the CTH reaction of FF to produce 2MF in 2-propanol at 170 °C, 20 bar of N<sub>2</sub> for 5 hours. They observed that increasing the Cu loading from 10 to 17 wt.% led to a higher FF conversion and 2MF selectivity, but a slight decrease was observed after a further increase to 23 wt.% of Cu (Gong *et al.*, 2018a). This effect, however, is not clearly explained in the paper, since all catalysts exhibited similar physicochemical properties.

Along with Cu, Ni catalysts are also employed in the production of 2MF. In general, Ni has a greater ability to dissociate H<sub>2</sub> than Cu (Pozzo and Alfè, 2009), but it tends to adsorb furfural in the  $\eta^2$ -(C,O)-aldehyde adsorption mode (Chen *et al.*, 2018), which also favors the formation of by-products from the ring hydrogenation of furfural or other intermediates, since in this case there is an interaction of both carbonyl group and the furan ring of FF onto the metal surface.

This effect was observed by Jaatinen *et al.*, (2017) at 230 °C and 40 bar of H<sub>2</sub> when using Ni/AC as catalysts for the HDO of furfural to 2MF. The formation of THFA and 2MTHF increased as a function of the metal loading (2 - 10 wt.%), which shows that Ni tends to hydrogenate C=C bonds. In that same study, the addition of copper to Ni did not influence the furfural consumption rate in comparison with monometallic Ni/AC catalyst but increased the 2MF yield and decelerated the formation of side products.

For these reasons, some researchers focused on studying bimetallic catalysts to combine the properties of the metals and achieve better catalytic performances. It is well known that the addition of a second metal tunes the geometry and electron density of the catalyst's active sites enhancing the catalytic activity and stability (Gupta *et al.*, 2018).

Srivastava *et al.*, (2017) studied Ni/Cu monometallic and Ni-Cu bimetallic catalysts with different contents (Cu/Ni = 1, 2, 4, Cu = 10 wt.%) supported on Al<sub>2</sub>O<sub>3</sub> in the HDO of FF to 2MF. The authors observed a low 2MF selectivity over the monometallic catalysts that preferentially formed FA. Knowing the low capacity of copper to dissociate H<sub>2</sub>, the researchers promoted this catalyst with Ni to obtain a

spillover effect, in which the most active metal (Ni) would be responsible for dissociating H<sub>2</sub> that would be passed to Cu sites where FF hydrogenation takes place.

It was also observed that the presence of Ni increased Cu dispersion, which they reported to be an important factor in C-O bond hydrogenolysis. Finally, increasing Ni content in the Ni-Cu/Al<sub>2</sub>O<sub>3</sub> catalyst caused an increase in the selectivity to 2MF, which was associated with a greater number of weak acid sites responsible for promoting C-O bond hydrogenolysis due to the oxophilic nature of these sites. The best result (2MF selectivity of 84%) was observed for the 10 wt.% Ni - 10 wt.% Cu/Al<sub>2</sub>O<sub>3</sub> catalyst after 2 hours at 210 °C and 40 bar of H<sub>2</sub>.

In comparison with Cu and Ni metals, Scholz *et al.*, (2014) tested Pd supported on Fe<sub>2</sub>O<sub>3</sub> for the CTH reaction of furfural to 2MF at 180 °C, 1 bar of N<sub>2</sub> for 7.5 hours. The catalytic results showed that FA is the main product formed over the first two metals, while the Pd catalyst displayed activity for the furan ring hydrogenation enabling THF, THFA, and 2MTHF. This occurred because furan derivatives may coordinate through the  $\pi$ -system of the ring by an adsorption  $\eta^2$ -(C,O)-aldehyde configuration. Finally, this  $\eta^2$ -aldehyde could be transformed into a more stable  $\eta^1$ -(C)-acyl species, which are intermediates in the decarbonylation, yielding furan. This effect was confirmed by increasing the Pd loading from 2 to 10 wt.%, which resulted in the decrease of the selectivity towards 2MF, while the furan selectivity increased.

These same adsorptions configurations are commonly observed for other noble metals such as Pt and Ir (Chen *et al.*, 2018). Ir catalysts with different metal contents (1 - 6 wt.%) were evaluated by Date *et al.*, (2018) to produce 2MF from FF at 220 °C, 7 bar of H<sub>2</sub>, and 5 hours. The authors observed that increasing Ir content up to 5 wt.% favored the formation of the desired product, in which Ir<sup>0</sup> species were responsible for the initial hydrogenation of furfural to FA and IrO<sub>2</sub> to the ultimate formation of 2MF. The use of 6 wt.% of metal, however, led to the formation of ring hydrogenation products.

Re-based catalysts, on the other hand, were found to be more selective to 2MF compared to Pd and Ir noble metals. The nature of Re oxide species was insensitive to metal loading to produce 2MF from HDO of furfural at 200 °C and 40 bar of H<sub>2</sub> for

4 hours. The active sites in the catalysts according to Toledo *et al.*, (2019) are oxophilic partially reduced  $\text{ReO}_x$  species, which contain oxygen vacancies that have a strong affinity for  $\eta^2\text{-(C,O)}$  surface species and breaking of C-O bonds. A linear increase in activity was observed loading up to 1.4 of Re atoms per  $\text{nm}^2$  in  $\text{ReO}_x/\text{SiO}_2$  catalysts, which was associated with a higher amount of active vacancy sites. A subsequent increase in Re surface concentration, however, reduced these vacancies by metal agglomeration

The tendency of Ru to perform preferentially HDO reactions was found when the increase in the loading of this metal (2 - 8 wt.%) supported on  $\text{NiFe}_2\text{O}_4$  showed a positive effect in the 2MF formation while keeping the yields of ring hydrogenation and decarbonylation products such as THFA and furan below 3%. This was correlated by Wang *et al.*, (2017) to the influence of the calcination temperature on  $\text{Ru}/\text{NiFe}_2\text{O}_4$  catalysts.

The researchers observed that different calcination temperatures did not influence the conversion of FF at 180 °C, 21 bar of  $\text{N}_2$  for 4 hours, but only the product distribution. At low calcination temperatures (300 °C), FA selectivity was higher, because  $\text{RuO}_x$  species on the catalyst surface were easily reduced to  $\text{Ru}^0$ , causing a decrease in the ability of the catalyst to perform hydrogenolysis. The best 2MF selectivity (75%) was achieved at an FF conversion of 98% over the catalyst calcined at 400 °C since an increase in the calcination temperature to 500 °C reduced the selectivity to 2MF (69%) due to the reduction in the specific area and formation of larger Ru particles.

As seen, besides the intrinsic nature of the metals, the conditions of preparation and synthesis of the catalysts can affect their final physicochemical properties and modify the performance of the materials.

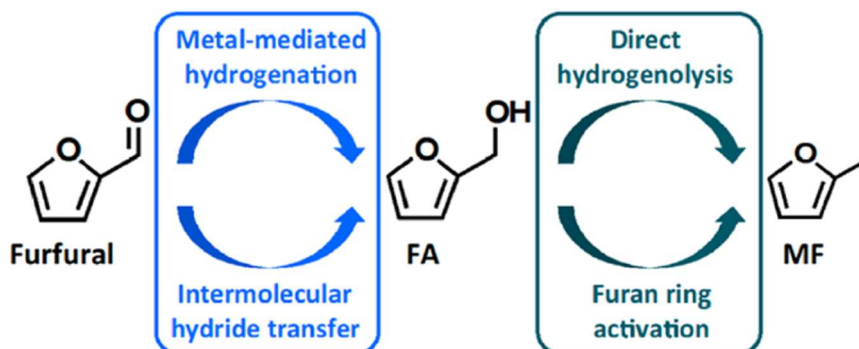
Niu *et al.*, (2019) found a strong influence in 2MF formation with high yields when studying the effect of different Cu/Zn molar ratios (0.5 - 4) and calcination temperatures (400 - 800 °C) on  $\text{CuZnAl}$  catalysts for the CTH of furfural. Lower calcination temperatures such as 400 and 500 °C produced amorphous phases or only  $\text{CuO}$ , respectively, while higher temperatures ( $> 600$  °C) generated a mixture of  $\text{CuO}$  and  $\text{CuAl}_2\text{O}_4$  phases. The use of very high temperatures (700 or 800 °C) hindered the

reduction of the catalysts. In addition, high Cu/Zn contents caused aggregation of Cu species ( $\text{Cu}^0$  and  $\text{CuAl}_2\text{O}_4$ ) responsible for breaking the furfuryl alcohol C-O bond. The highest 2MF yield (72%) was observed over  $\text{Cu}_{2.5}\text{Zn-Al-600}$  catalyst at 180 °C, 1 bar of  $\text{N}_2$  using 2-propanol as solvent.

By studying the CTH reaction of FF at 220 °C, Li *et al.*, (2018) observed that changing the preparation method of Cu catalysts supported on  $\text{SiO}_2$  profoundly modified the selectivity to 2MF. For the catalyst prepared by the impregnation method (IMP), 2MF selectivity was very low (2%), while for the one synthesized by the hydrothermal method (HT) a full FF conversion and a 2MF selectivity of 90% were achieved. This effect was associated by the authors with the formation of different phases in the catalysts, since when Cu was impregnated only  $\text{CuO}$  and  $\text{Cu}^0$  phases were observed after calcination and reduction, respectively, while by the other method  $\text{CuO}$  and  $\text{Cu}_2\text{O.SiO}_2$  phases were obtained. For the researchers, the active phases in the HT-catalyst were the surface species  $\text{Cu@Cu}_2\text{O.SiO}_2$  at the interface with the  $\text{CuSiO}_3@\text{SiO}_2$  main layer.

Most of these works demonstrate the relevance of using bifunctional catalysts containing both metallic and Lewis acidic sites to obtain 2MF. A mechanism study using a slightly oxidized  $\text{Ru/RuO}_x/\text{C}$  catalyst was proposed by Gilkey *et al.*, (2015). This study described the possible paths to obtain 2MF through furfural (Figure 2.10). In the first step, the hydrogenation of FF can proceed via metal mediation, in which the atomic hydrogen adsorbed on metal sites is added to the C and O in the carbonyl group or via Lewis acidic-mediated intermolecular hydride transfer of the  $\beta$ -H in the alcohol to the carbonyl group following the MPV mechanism as occurs in the presence of protic solvents.

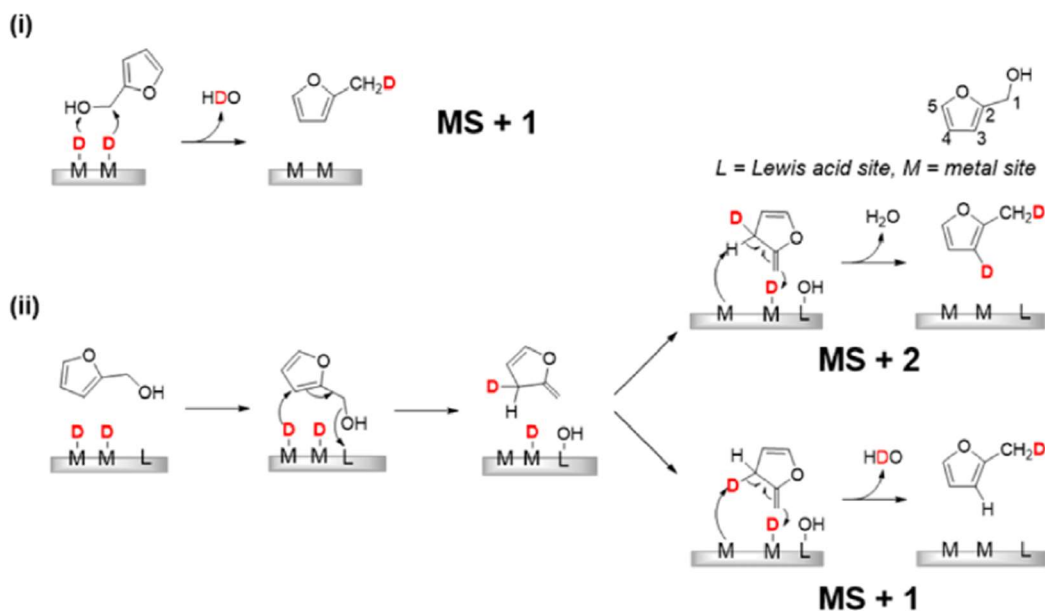
Figure 2.10. Reaction pathways in the HDO of furfural to 2MF.



Reference: Gilkey *et al.*, (2015)

Meanwhile, the hydrogenolysis of the C-OH bond in FA to 2MF can proceed via direct route by adding atomic hydrogen adsorbed metal sites or via activation of the furan ring, in which H is added to the ring to break the ring aromaticity and facilitate OH removal on Lewis acidic sites as presented in Figure 2.11.

Figure 2.11. Reaction mechanism of FA hydrogenolysis to 2MF via (i) direct hydrogenolysis and (ii) hydrogenolysis via furan ring activation.



Reference: Gilkey *et al.*, (2015)

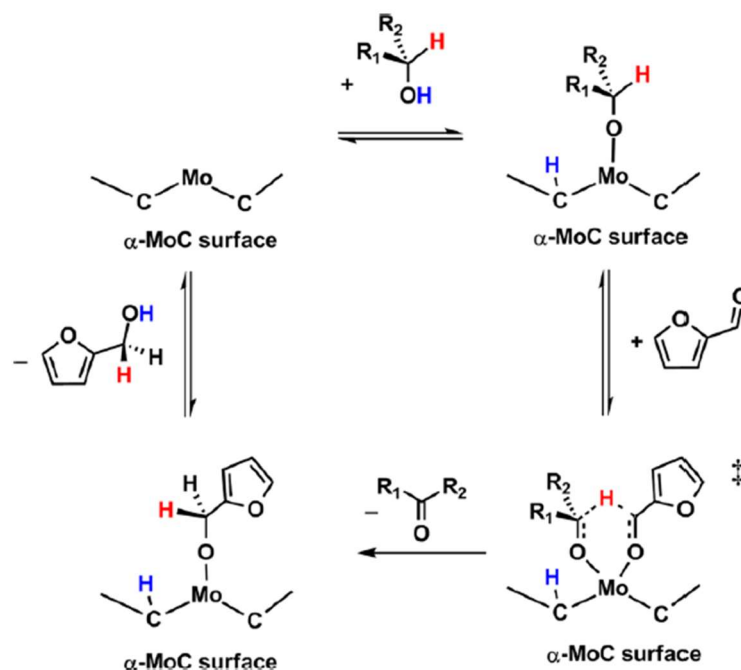
The Lewis acid sites are coordinatively unsaturated cations found in metals that are not fully reduced or in acidic oxides used as supports. Species that are not fully reduced can be obtained by controlling synthesis parameters such as preparation method, calcination temperature, and reduction conditions. However, the nature of these species can change during the reaction by their total reduction, which causes them to lose their function. For this reason, supporting metals on Lewis acidic supports could be a strategy to achieve both functionalities.

To avoid the use of scarcely and expensive noble metals in the hydrodeoxygenation of furfural in the liquid phase, some researchers also tested alternative materials such as carbides, nitrides, and phosphides to produce 2MF.

Deng *et al.*, (2018) compared unsupported Mo carbides ( $\alpha$ -MoC,  $\beta$ -Mo<sub>2</sub>C) and nitride ( $\gamma$ -Mo<sub>2</sub>N) for the HDO of FF at 150 °C, 20 bar H<sub>2</sub> for 6 hours using 2-propanol. Among the evaluated materials, a higher activity (96%) and selectivity to 2MF (82%) were observed using  $\alpha$ -MoC as a catalyst (FF conversion of 67% for  $\beta$ -Mo<sub>2</sub>C and 21% for  $\gamma$ -Mo<sub>2</sub>N), which was attributed to the higher oxophilicity of the  $\alpha$ -phase. In addition, comparing the different crystalline phases of Mo carbide in 2-butanol showed that the solvent was more strongly bound to the  $\beta$ -Mo<sub>2</sub>C phase than to  $\alpha$ -MoC, which made the surface of the former less accessible to furfural, resulting in a lower hydrogenation rate. In any case, no C=C bond hydrogenation products such as THFA and 2MTHF were identified in the system indicating that Mo catalysts are selective for C=O bond hydrogenation.

In this study, it was also reported that Mo Lewis acid sites found on  $\alpha$ -MoC surfaces mediated the CTH reaction of furfural by MPV mechanism, in which the  $\beta$ -H atom of alcohol is transferred to the carbonyl C atom of FF via a concerted six-membered ring transition state as shown in Figure 2.12.

Figure 2.12. CTH of furfural by alcohol on  $\alpha$ -MoC surfaces.



Reference: Deng *et al.*, (2018)

Shilov *et al.*, (2018) studied the use of molybdenum carbides with  $SiO_2$  promoted with Ni containing different Ni/Mo ratios (0, 0.5, 1, 2, 4, and 6) in the hydrodeoxygenation of FF at 150 °C, 60 bar of  $H_2$  in the presence of 2-propanol. The researchers observed that increasing the Ni content in the catalysts promoted catalytic activity and generated materials with distinct crystalline phases, which caused the distribution of the reaction products to change. The presence of Ni in the catalysts prevented the formation of coke since this metal hydrogenates the C deposited on the surface forming gaseous products. On the other hand, its existence in large quantities led to the formation of Ni-Mo metal alloys reducing the content of the carbide phases, which ended up generating hydrogenation by-products such as THFA and 2MTHF. The highest selectivity of the desired product was obtained over the catalyst containing the lowest Ni content ( $Ni_{0.5}MoC-SiO_2$ ).

Unsupported phosphides were evaluated for the production of 2MF by Yazhou Wang *et al.*, (2018), who compared MoP and  $Ni_2P$  catalysts with various Ni/P ratios (0.5, 0.75, 1) in the conversion of FF at 240 °C and 20 bar of  $H_2$  in 2-propanol. The

researchers achieved a full conversion over all catalysts after 4 hours of reaction, but significant differences in the product selectivities depending on the catalyst. While Ni phosphide (Ni/P ratio = 0.5) showed the highest selectivity to 2MF (83%), the MoP catalyst led to a lower selectivity for this product (60%). The best performance of Ni<sub>2</sub>P was attributed to the synergistic effect between the Ni<sup>δ+</sup> and P-OH species in this catalyst, while the lower 2MF yield for MoP was associated with its greater tendency to form by-products such as difurfuryl ether, obtained by condensation reactions on acid sites. Nevertheless, a reduction in 2MF selectivity was seen after the fifth reuse due to the phase change of Ni<sub>2</sub>P to Ni<sub>12</sub>P<sub>5</sub>.

These studies show that this class of materials is very active and selective in producing 2MF. Their ability to perform C=O/C-OH/C-O-C bond cleavage in hydrodeoxygenation reactions has already been pointed out before (Akhmetzyanova *et al.*, 2019; Smith, 2020; Sullivan *et al.*, 2016; Zhou *et al.*, 2021). Nevertheless, most works use unsupported carbides, nitrides, and phosphides or have never evaluated the use of different supports for these materials in the HDO of furfural in the liquid phase.

## 2.4 Transition metal carbides

In the last decades, many researchers have focused on the use of carbides as alternative materials to noble metals in reactions of industrial interest. The excellent performance of precious metals (Ru, Pt, Pd, Ir, and Rh) relies on their moderate interaction with the substrates and reaction products, which can be explained by the Sabatier principle that states that the interaction should not be so weak that there is no contact between the catalyst and the substrate, but not so strong as to poison the catalyst (Leclercq *et al.*, 1979).

Normally, transition metals of groups 4, 5, and 6 exhibit a strong interaction with the reactants due to their electron deficiency in the d orbital. The presence of heteroatoms such as C in the metal network, however, moderates the reactivity of these metals, since it does not allow their complete exposure causing these materials to



behave similarly to noble metals. For this reason, carbides are potentially catalytic materials to be used.

### **2.4.1 Definition and properties**

Carbides are materials with unique chemical and physical properties that can be produced by the incorporation of heteroatoms such as carbon into the interstices of transition metals (Oyama, 1992). These materials are very attractive since they have physical properties similar to those of ceramics and electronic and magnetic behavior similar to that of metals. In addition, they exhibit high melting points, high values for hardness, tensile strength, corrosion resistance, excellent electronic properties, thermal stability, and good catalytic properties when compared to the oxides that originate them (Oyama, 1992; Rasaki *et al.*, 2018).

As mentioned before, the presence of heteroatoms in the lattice of transition metals makes carbides have catalytic activity similar to that of noble metals. This occurs because the insertion of C lengthens the metal-metal bond distance changing the d-band electron density of metals at the Fermi level (Choi *et al.*, 2000; Oyama, 1992), which becomes similar to that found in precious metals.

### **2.4.2 Synthesis of carbides**

Transition metal carbides can be prepared by solid-solid phase reactions or solid-gas phase reactions when the carbon source is in the solid phase or the gas phase, respectively. Initially, the carbides catalysts were synthesized by powder metallurgy method in which the metal oxide precursor is carburized in the presence of a solid carbon at high temperatures (1800 K). Later, the carbothermal method was developed. In this methodology, a solid carbon reacts with vaporized metal oxides at temperatures higher than 1000 K (Pang *et al.*, 2019).

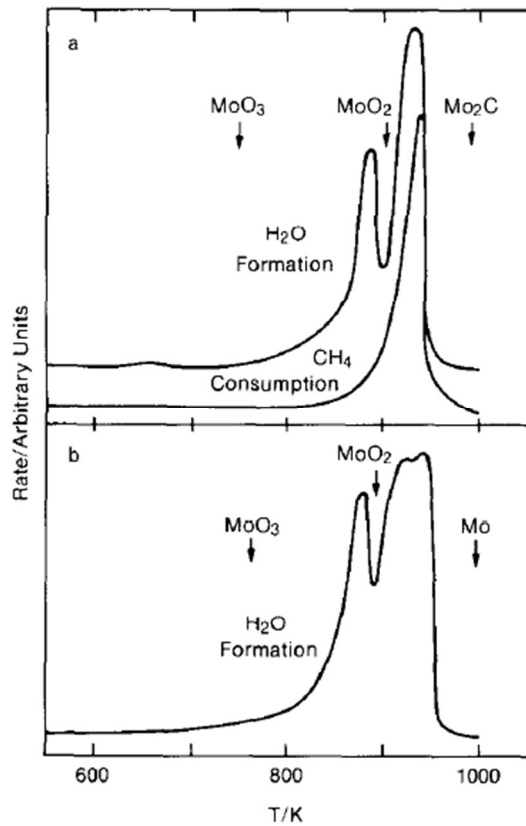
The use of these techniques leads to the formation of low-area materials, which are not very interesting for catalysis. These low areas are usually related to the rapid transformations of the solid intermediates, such as the formation of the metal phase, which then undergoes the incorporation of heteroatoms, along with slow reduction kinetics that result in extensive grain growth (Roy *et al.*, 2015).

The temperature-programmed reaction (TPR) technique, however, enables the direct transformation of the precursor oxide into a carbide/nitride by suppressing the formation of the metallic state, which has a greater tendency to sinter (Oyama, 1992).

Temperature-programmed carburization (TPC) is the most widely used technique in catalysis to prepare transition metal carbides. In this methodology, a metal oxide is heated at a specific rate in a carburizing atmosphere of CO or a hydrocarbon (CH<sub>4</sub>, C<sub>2</sub>H<sub>6</sub>, C<sub>3</sub>H<sub>8</sub>, C<sub>4</sub>H<sub>10</sub>) used as a carbon source, co-fed or not with hydrogen (Pang *et al.*, 2019). This procedure was originally proposed by (Volpe and Boudart, 1985), who obtained molybdenum and tungsten carbides from their respective oxides (MoO<sub>3</sub> and WO<sub>3</sub>) via the formation of nitrides as intermediates.

Years later, the direct synthesis of Mo carbides with a high specific area was presented by Lee (1987). In this study, molybdenum oxide MoO<sub>3</sub> was heated at a controlled heating ramp under 20% (v/v) of methane in hydrogen. The water formation and methane consumption profiles were accompanied by chromatography (Figure 2.13). The reduction of MoO<sub>3</sub> was followed under pure hydrogen at the same carburization conditions to compare the water formation profiles during both processes. This way, the authors showed that carburization occurs in two steps, in which the first peak of water formation was related to the reduction of MoO<sub>3</sub> to MoO<sub>2</sub> and the second one to the simultaneous reduction and carburization of MoO<sub>2</sub> to  $\beta$ -Mo<sub>2</sub>C. All crystalline phases formed were confirmed by X-ray diffraction.

Figure 2.13. H<sub>2</sub>O and CO formation profiles during carburization of MoO<sub>3</sub> in an atmosphere of (a) 20% (v/v) CH<sub>4</sub>/H<sub>2</sub> and (b) H<sub>2</sub>.



Reference: Lee (1987)

The same group continued to investigate the influence of synthesis parameters on the final properties of the carbides. As mentioned before, starting with MoO<sub>3</sub> under an atmosphere of CH<sub>4</sub>/H<sub>2</sub> produces the thermodynamically stable hexagonal close-package (hcp)  $\beta$ -Mo<sub>2</sub>C. In contrast, by doping the oxide precursor with 0.25 wt.% Pt led to the formation of the metastable face-centered cubic (fcc)  $\alpha$ -MoC (Lee, 1988). These are the most common phases of molybdenum carbides obtained by TPC (Lee, 1988; Volpe and Boudart, 1985; Xu *et al.*, 2014). The formation of the  $\alpha$ -MoC phase was also reported to occur by first reacting the metal oxide with ammonia before being exposed to the carburizing mixture (Lee, 1988).

The effect of metal (Pt, Pd, Ni, Co, Cu) loading on the synthesis of Mo carbides from MoO<sub>3</sub> using a mixture of CH<sub>4</sub>/H<sub>2</sub> was studied by (Jung *et al.*, 2004a). The authors observed that the addition of a metal lowered the first stage of reduction

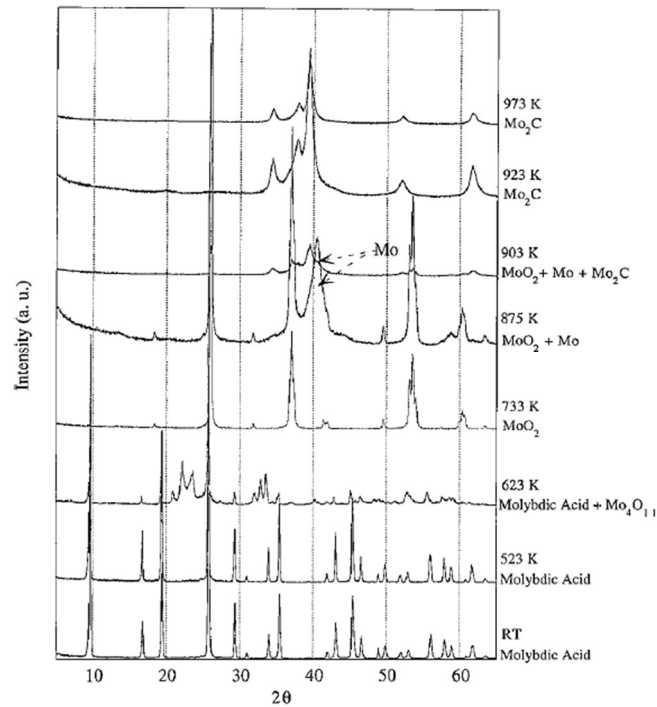
( $\text{MoO}_3 \rightarrow \text{MoO}_2$  or an oxycarbide) by 100 - 250 °C for all materials, while a reduction in the temperature of 50 °C occurred in the final transformation ( $\text{MoO}_2$  or an oxycarbide  $\rightarrow$  Mo carbide) for the catalysts containing Cu, Ni, Pd, and Pt. These lower reduction temperatures were promoted by the ability of metals to activate hydrogen. This effect was most pronounced for Ni, Pd, and Pt metals, which produced the  $\alpha$ -MoC by topotactic solid transformations, in which the crystalline structure is conserved. While the  $\beta$ -Mo<sub>2</sub>C phase was formed when Cu and Co metals were used.

Finally, in the presence of long-chain hydrocarbons or higher concentrations of hydrocarbon in the reagent mixture, the formation of fcc  $\alpha$ -MoC can also occur (Mo *et al.*, 2016a). Lower carburization temperatures are observed when long-chain hydrocarbons are employed (Claridge *et al.*, 2000; Xiao *et al.*, 2001) since they are more easily decomposed generating carbon and hydrogen. Although low synthesis temperatures generate high-area materials, the excess carbon generated can be deposited on the catalyst surface, which can end up poisoning it.

As noted, the properties of the resulting carbides are greatly dependent on the synthesis conditions, which include the nature of the reacting gases, the heating rates, the space velocity of the gases, the final synthesis temperature as well as the time the samples are exposed to this temperature (Li *et al.*, 1998).

Starting from molybdic acid, other intermediates besides  $\text{MoO}_2$  were observed during the synthesis of Mo carbide as shown in Figure 2.14. In this case,  $\text{Mo}_2\text{C}$  is formed at a temperature higher than 650 °C (Choi *et al.*, 2000).

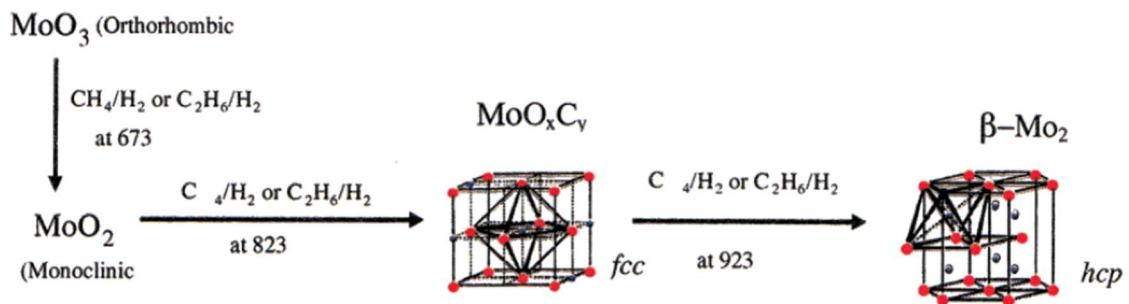
Figure 2.14. Diffractograms obtained during the TPC of molybdic acid in 10% (v/v) CH<sub>4</sub>/H<sub>2</sub> atmosphere.



Reference: Choi *et al.*, (2000)

The effect of the heating rate was studied by Hanif *et al.*, (2002) who observed that a decrease in the heating rate from 10 to 2 °C min<sup>-1</sup> causes a reduction in the initial carburation temperature from 600 to 380 °C. Using thermogravimetric analysis, the authors proposed that the synthesis of carbide from MoO<sub>3</sub> in an atmosphere of both CH<sub>4</sub>/H<sub>2</sub> and C<sub>2</sub>H<sub>6</sub>/H<sub>2</sub> occurred via the formation of an oxycarbide (MoO<sub>x</sub>C<sub>y</sub>) as shown in Figure 2.15.

Figure 2.15. Routes for Mo carbide formation from MoO<sub>3</sub> by TPC.



Reference: Hanif *et al.*, (2002)

### 2.4.3 The use of carbides in hydrodeoxygenation reactions

The hydrodeoxygenation reaction is a very important technology to be employed in biomass-derived compounds. As it is known, the products derived from biomass, unlike those derived from petroleum, present a large amount of oxygenates and, for this reason, must undergo deoxygenation reactions to remove oxygen as water by adding hydrogen. This procedure allows the adjustment of their properties so that these compounds can be later commercialized (Robinson *et al.*, 2016).

The hydrotreating ability of carbides has already been demonstrated in hydrodesulfurization (HDS) and hydrodenitrogenation (HDN) reactions (Dolce *et al.*, 1997; X. Li *et al.*, 2018; Oyama, 2003; Oyama *et al.*, 2009; Ramanathan and Oyama, 1995). Recently, carbides have been pointed out as potential materials to be used in HDO reactions since they are selective in the C=O/C-OH/C-O-C bond cleavage rather than C=C scission (Zhou *et al.*, 2021). In addition, the platinum-like properties of carbides have already been demonstrated by Levy and Boudart, (1973). A similar furfural activity was observed for Fe/Pt and Fe/Mo<sub>2</sub>C catalysts in the HDO of furfural, for example, demonstrating that Mo<sub>2</sub>C has the potential to replace noble metals (Wan *et al.*, 2018).

In general, the ability of carbides in performing deoxygenation reactions relies on the presence of both metallic and acid sites (Robinson *et al.*, 2016). The introduction of oxygen by passivation procedure reduces the metallic character of carbides while increasing the acid character of the catalysts yielding oxycarbides (Smith, 2020).

## 2.5 Conclusions

The literature review showed that high yields of 2-methylfuran from furfural are obtained in the presence of bifunctional catalysts containing metal and acid sites, especially Lewis acidic sites. In this sense, in this work, we chose to use Mo carbide catalysts, which are reported to present catalytic performance similar to that of noble

metal-based catalysts, supported on SiO<sub>2</sub>, TiO<sub>2</sub>, ZrO<sub>2</sub>, and ZSM-5. These materials used as supports have no (SiO<sub>2</sub>) or different acidic properties (TiO<sub>2</sub>, ZrO<sub>2</sub>, and, ZSM-5) that will allow to investigate of the effect of the total amount of acid sites as well as the nature of the acid sites and therefore they were selected to be tested for the HDO of furfural.

In parallel, aiming for a higher yield to 2MF, the temperature, and pressure selected to perform the catalytic tests were 200 °C and 30 bar H<sub>2</sub> based on the temperature and pressure ranges most used in the literature. Meanwhile, 2-butanol was chosen to be used as a solvent because it led to an even higher selectivity to 2MF in the presence of Mo carbides (Deng *et al.*, 2018), instead of 2-propanol, the solvent most often used for this reaction. In addition, cyclopentyl methyl ether, an aprotic green solvent was also tested and compared to the protic 2-butanol to verify the effect of *in situ* hydrogen donation and the influence of the catalytic hydrogen reaction.

## 2.6 References

- Akhmetzyanova, U., Tišler, Z., Sharkov, N., Skuhrovcová, L., Pelíšková, L., Kikhtyanin, O., Mäki-Arvela, P., Opanasenko, M., Peurla, M., Murzin, D.Yu., 2019. Molybdenum Nitrides, Carbides and Phosphides as Highly Efficient Catalysts for the (hydro)Deoxygenation Reaction. *ChemistrySelect* 4, 8453–8459. <https://doi.org/10.1002/slct.201901634>
- Aldosari, O.F., Iqbal, S., Miedziak, P.J., Brett, G.L., Jones, D.R., Liu, X., Edwards, J.K., Morgan, D.J., Knight, D.K., Hutchings, G.J., 2016. Pd–Ru/TiO<sub>2</sub> catalyst – an active and selective catalyst for furfural hydrogenation. *Catal. Sci. Technol.* 6, 234–242. <https://doi.org/10.1039/C5CY01650A>
- Alexander, A.-M., Hargreaves, J.S.J., 2010. Alternative catalytic materials: carbides, nitrides, phosphides and amorphous boron alloys. *Chem. Soc. Rev.* 39, 4388. <https://doi.org/10.1039/b916787k>
- Alonso, D.M., Bond, J.Q., Dumesic, J.A., 2010. Catalytic conversion of biomass to biofuels. *Green Chem.* 12, 1493. <https://doi.org/10.1039/c004654j>
- Antunes, M.M., Lima, S., Fernandes, A., Ribeiro, M.F., Chadwick, D., Hellgardt, K., Pillinger, M., Valente, A.A., 2018. One-pot hydrogen production and cascade reaction of furfural to bioproducts over bimetallic Pd-Ni TUD-1 type mesoporous catalysts. *Applied Catalysis B: Environmental* 237, 521–537. <https://doi.org/10.1016/j.apcatb.2018.06.004>
- Bhatia, S.K., Jagtap, S.S., Bedekar, A.A., Bhatia, R.K., Patel, A.K., Pant, D., Rajesh Banu, J., Rao, C.V., Kim, Y.-G., Yang, Y.-H., 2020. Recent developments in pretreatment technologies on lignocellulosic biomass: Effect of key parameters, technological improvements, and challenges. *Bioresource Technology* 300, 122724. <https://doi.org/10.1016/j.biortech.2019.122724>
- Bozell, J.J., Petersen, G.R., 2010. Technology development for the production of biobased products from biorefinery carbohydrates—the US Department of Energy’s “Top 10” revisited. *Green Chem.* 12, 539. <https://doi.org/10.1039/b922014c>



- Bretzler, P., Huber, M., Nickl, S., Köhler, K., 2020. Hydrogenation of furfural by noble metal-free nickel modified tungsten carbide catalysts. *RSC Adv.* 10, 27323–27330. <https://doi.org/10.1039/D0RA02003F>
- Chang, X., Liu, A.-F., Cai, B., Luo, J.-Y., Pan, H., Huang, Y.-B., 2016. Catalytic Transfer Hydrogenation of Furfural to 2-Methylfuran and 2-Methyltetrahydrofuran over Bimetallic Copper-Palladium Catalysts. *ChemSusChem* 9, 3330–3337. <https://doi.org/10.1002/cssc.201601122>
- Chen, S., Wojcieszak, R., Dumeignil, F., Marceau, E., Royer, S., 2018. How Catalysts and Experimental Conditions Determine the Selective Hydroconversion of Furfural and 5-Hydroxymethylfurfural. *Chem. Rev.* 118, 11023–11117. <https://doi.org/10.1021/acs.chemrev.8b00134>
- Choi, J.-S., Bugli, G., Djéga-Mariadassou, G., 2000. Influence of the Degree of Carburization on the Density of Sites and Hydrogenating Activity of Molybdenum Carbides. *Journal of Catalysis* 193, 238–247. <https://doi.org/10.1006/jcat.2000.2894>
- Choi, S., Song, C.W., Shin, J.H., Lee, S.Y., 2015. Biorefineries for the production of top building block chemicals and their derivatives. *Metabolic Engineering* 28, 223–239. <https://doi.org/10.1016/j.ymben.2014.12.007>
- Chuseang, J., Nakwachara, R., Kalong, M., Ratchahat, S., Koo-amornpattana, W., Klysubun, W., Khemthong, P., Faungnawakij, K., Assabumrungrat, S., Itthibenchapong, V., Srifa, A., 2021. Selective hydrogenolysis of furfural into fuel-additive 2-methylfuran over a rhenium-promoted copper catalyst. *Sustainable Energy Fuels* 5, 1379–1393. <https://doi.org/10.1039/D1SE00036E>
- Claridge, J.B., York, A.P.E., Brungs, A.J., Green, M.L.H., 2000. Study of the Temperature-Programmed Reaction Synthesis of Early Transition Metal Carbide and Nitride Catalyst Materials from Oxide Precursors. *Chem. Mater.* 12, 132–142. <https://doi.org/10.1021/cm9911060>
- Climent, M.J., Corma, A., Iborra, S., 2014. Conversion of biomass platform molecules into fuel additives and liquid hydrocarbon fuels. *Green Chem.* 16, 516. <https://doi.org/10.1039/c3gc41492b>

Corma, A., de la Torre, O., Renz, M., 2012. Production of high-quality diesel from cellulose and hemicellulose by the Sylvan process: catalysts and process variables. *Energy Environ. Sci.* 5, 6328. <https://doi.org/10.1039/c2ee02778j>

Corma, A., de la Torre, O., Renz, M., 2011a. High-Quality Diesel from Hexose- and Pentose-Derived Biomass Platform Molecules. *ChemSusChem* 4, 1574–1577. <https://doi.org/10.1002/cssc.201100296>

Corma, A., de la Torre, O., Renz, M., Villandier, N., 2011b. Production of High-Quality Diesel from Biomass Waste Products. *Angew. Chem. Int. Ed.* 50, 2375–2378. <https://doi.org/10.1002/anie.201007508>

Corma, A., Iborra, S., Velty, A., 2007. Chemical Routes for the Transformation of Biomass into Chemicals. *Chem. Rev.* 107, 2411–2502. <https://doi.org/10.1021/cr050989d>

Date, N.S., Hengne, A.M., Huang, K.-W., Chikate, R.C., Rode, C.V., 2018. Single pot selective hydrogenation of furfural to 2-methylfuran over carbon-supported iridium catalysts. *Green Chem.* 20, 2027–2037. <https://doi.org/10.1039/C8GC00284C>

Deng, Y., Gao, R., Lin, L., Liu, T., Wen, X.-D., Wang, S., Ma, D., 2018. Solvent Tunes the Selectivity of Hydrogenation Reaction over  $\alpha$ -MoC Catalyst. *J. Am. Chem. Soc.* 140, 14481–14489. <https://doi.org/10.1021/jacs.8b09310>

Dohade, M.G., Dhepe, P.L., 2018. One pot conversion of furfural to 2-methylfuran in the presence of PtCo bimetallic catalyst. *Clean Techn Environ Policy* 20, 703–713. <https://doi.org/10.1007/s10098-017-1408-z>

Dolce, G.M., Savage, P.E., Thompson, L.T., 1997. Hydrotreatment Activities of Supported Molybdenum Nitrides and Carbides. *Energy Fuels* 11, 668–675. <https://doi.org/10.1021/ef960083y>

Eseyin, A., E., Steele, P., H., 2015. An overview of the applications of furfural and its derivatives. *IJAC* 3, 42. <https://doi.org/10.14419/ijac.v3i2.5048>

Fu, Z., Wang, Z., Lin, W., Song, W., Li, S., 2017. High efficient conversion of furfural to 2-methylfuran over Ni-Cu/Al<sub>2</sub>O<sub>3</sub> catalyst with formic acid as a hydrogen donor. *Applied Catalysis A: General* 547, 248–255. <https://doi.org/10.1016/j.apcata.2017.09.011>

- Gandarias, I., García-Fernández, S., Obregón, I., Agirrezabal-Telleria, I., Arias, P.L., 2018. Production of 2-methylfuran from biomass through an integrated biorefinery approach. *Fuel Processing Technology* 178, 336–343. <https://doi.org/10.1016/j.fuproc.2018.05.037>
- Geng, W., Li, W., Liu, Lin, Liu, J., Liu, Liying, Kong, X., 2020. Facile assembly of Cu-Cu<sub>2</sub>O/N-reduced graphene oxide nanocomposites for efficient synthesis of 2-methylfuran. *Fuel* 259, 116267. <https://doi.org/10.1016/j.fuel.2019.116267>
- Gilkey, M.J., Panagiotopoulou, P., Mironenko, A.V., Jenness, G.R., Vlachos, D.G., Xu, B., 2015. Mechanistic Insights into Metal Lewis Acid-Mediated Catalytic Transfer Hydrogenation of Furfural to 2-Methylfuran. *ACS Catal.* 5, 3988–3994. <https://doi.org/10.1021/acscatal.5b00586>
- Golubeva, M.A., Maximov, A.L., 2020. Hydroprocessing of furfural over in situ generated nickel phosphide-based catalysts in different solvents. *Applied Catalysis A: General* 608, 117890. <https://doi.org/10.1016/j.apcata.2020.117890>
- Gong, W., Chen, C., Fan, R., Zhang, H., Wang, G., Zhao, H., 2018. Transfer-hydrogenation of furfural and levulinic acid over supported copper catalyst. *Fuel* 231, 165–171. <https://doi.org/10.1016/j.fuel.2018.05.075>
- Gong, W., Chen, C., Zhang, H., Wang, G., Zhao, H., 2017. Efficient Synthesis of 2-Methylfuran from Bio-Derived Furfural over Supported Copper Catalyst: The Synergistic Effect of CuO<sub>x</sub> and Cu. *ChemistrySelect* 2, 9984–9991. <https://doi.org/10.1002/slct.201702206>
- Gupta, K., Rai, R.K., Singh, S.K., 2018. Metal Catalysts for the Efficient Transformation of Biomass-derived HMF and Furfural to Value Added Chemicals. *ChemCatChem* 10, 2326–2349. <https://doi.org/10.1002/cctc.201701754>
- Hanif, A., Xiao, T., York, A.P.E., Sloan, J., Green, M.L.H., 2002. Study on the Structure and Formation Mechanism of Molybdenum Carbides. *Chem. Mater.* 14, 1009–1015. <https://doi.org/10.1021/cm011096e>
- Isikgor, F.H., Becer, C.R., 2015. Lignocellulosic biomass: a sustainable platform for the production of bio-based chemicals and polymers. *Polym. Chem.* 6, 4497–4559. <https://doi.org/10.1039/C5PY00263J>

- Jaatinen, S.K., Karinen, R.S., Lehtonen, J.S., 2017. Liquid Phase Furfural Hydrotreatment to 2-Methylfuran with Carbon Supported Copper, Nickel, and Iron Catalysts. *ChemistrySelect* 2, 51–60. <https://doi.org/10.1002/slct.201601947>
- Jaatinen, S.K., Karinen, R.S., Lehtonen, J.S., 2016. Liquid Phase Furfural Hydrotreatment to 2-Methylfuran on Carbon Supported Nickel Catalyst - Effect of Process Conditions. *ChemistrySelect* 1, 5363–5373. <https://doi.org/10.1002/slct.201601333>
- Jaswal, A., Singh, P.P., Mondal, T., 2022. Furfural – a versatile, biomass-derived platform chemical for the production of renewable chemicals. *Green Chem.* 24, 510–551. <https://doi.org/10.1039/D1GC03278J>
- Jung, K.T., Kim, W.B., Rhee, C.H., Lee, J.S., 2004. Effects of Transition Metal Addition on the Solid-State Transformation of Molybdenum Trioxide to Molybdenum Carbides. *Chem. Mater.* 16, 307–314. <https://doi.org/10.1021/cm030395w>
- Kalong, M., Hongmanorom, P., Ratchahat, S., Koo-amornpattana, W., Faungnawakij, K., Assabumrungrat, S., Srifa, A., Kawi, S., 2021. Hydrogen-free hydrogenation of furfural to furfuryl alcohol and 2-methylfuran over Ni and Co-promoted Cu/ $\gamma$ -Al<sub>2</sub>O<sub>3</sub> catalysts. *Fuel Processing Technology* 214, 106721. <https://doi.org/10.1016/j.fuproc.2020.106721>
- Khemthong, P., Yimsukanan, C., Narkkun, T., Srifa, A., Witoon, T., Pongchaiphol, S., Kiatphuengporn, S., Faungnawakij, K., 2021. Advances in catalytic production of value-added biochemicals and biofuels via furfural platform derived lignocellulosic biomass. *Biomass and Bioenergy* 148, 106033. <https://doi.org/10.1016/j.biombioe.2021.106033>
- Kobayashi, H., Ohta, H., Fukuoka, A., 2012. Conversion of lignocellulose into renewable chemicals by heterogeneous catalysis. *Catal. Sci. Technol.* 2, 869. <https://doi.org/10.1039/c2cy00500j>
- Lange, J.-P., van der Heide, E., van Buijtenen, J., Price, R., 2012. Furfural-A Promising Platform for Lignocellulosic Biofuels. *ChemSusChem* 5, 150–166. <https://doi.org/10.1002/cssc.201100648>

- Leclercq, L., Imura, K., Yoshida, S., Barbee, T., Boudart, M., 1979. Synthesis of New Catalytic Materials: Metal Carbides of the Group VI B Elements, in: *Studies in Surface Science and Catalysis*. Elsevier, pp. 627–639. [https://doi.org/10.1016/S0167-2991\(09\)60240-8](https://doi.org/10.1016/S0167-2991(09)60240-8)
- Lee, J., 1988. Molybdenum carbide catalysts II. Topotactic synthesis of unsupported powders. *Journal of Catalysis* 112, 44–53. [https://doi.org/10.1016/0021-9517\(88\)90119-4](https://doi.org/10.1016/0021-9517(88)90119-4)
- Lee, J., 1987. Molybdenum carbide catalysts I. Synthesis of unsupported powders. *Journal of Catalysis* 106, 125–133. [https://doi.org/10.1016/0021-9517\(87\)90218-1](https://doi.org/10.1016/0021-9517(87)90218-1)
- Levy, R.B., Boudart, M., 1973. Platinum-Like Behavior of Tungsten Carbide in Surface Catalysis. *Science* 181, 547–549. <https://doi.org/10.1126/science.181.4099.547>
- Li, B., Li, L., Sun, H., Zhao, C., 2018. Selective Deoxygenation of Aqueous Furfural to 2-Methylfuran over  $\text{Cu}^0/\text{Cu}_2\text{O}\cdot\text{SiO}_2$  Sites via a Copper Phyllosilicate Precursor without Extraneous Gas. *ACS Sustainable Chem. Eng.* 6, 12096–12103. <https://doi.org/10.1021/acssuschemeng.8b02425>
- Li, G., Li, N., Li, S., Wang, A., Cong, Y., Wang, X., Zhang, T., 2013a. Synthesis of renewable diesel with hydroxyacetone and 2-methyl-furan. *Chem. Commun.* 49, 5727. <https://doi.org/10.1039/c3cc42296h>
- Li, G., Li, N., Wang, Xinkui, Sheng, X., Li, S., Wang, A., Cong, Y., Wang, Xiaodong, Zhang, T., 2014. Synthesis of Diesel or Jet Fuel Range Cycloalkanes with 2-Methylfuran and Cyclopentanone from Lignocellulose. *Energy Fuels* 28, 5112–5118. <https://doi.org/10.1021/ef500676z>
- Li, G., Li, N., Yang, J., Wang, A., Wang, X., Cong, Y., Zhang, T., 2013b. Synthesis of renewable diesel with the 2-methylfuran, butanal, and acetone derived from lignocellulose. *Bioresource Technology* 134, 66–72. <https://doi.org/10.1016/j.biortech.2013.01.116>
- Li, S., Kim, W.B., Lee, J.S., 1998. Effect of the Reactive Gas on the Solid-State Transformation of Molybdenum Trioxide to Carbides and Nitrides. *Chem. Mater.* 10, 1853–1862. <https://doi.org/10.1021/cm9800229>

- Li, S., Li, N., Li, G., Wang, A., Cong, Y., Wang, X., Zhang, T., 2014. Synthesis of diesel range alkanes with 2-methylfuran and mesityl oxide from lignocellulose. *Catalysis Today* 234, 91–99. <https://doi.org/10.1016/j.cattod.2014.01.028>
- Li, X., Jia, P., Wang, T., 2016. Furfural: A Promising Platform Compound for Sustainable Production of C<sub>4</sub> and C<sub>5</sub> Chemicals. *ACS Catal.* 6, 7621–7640. <https://doi.org/10.1021/acscatal.6b01838>
- Li, X., Luo, X., Jin, Y., Li, J., Zhang, H., Zhang, A., Xie, J., 2018. Heterogeneous sulfur-free hydrodeoxygenation catalysts for selectively upgrading the renewable bio-oils to second-generation biofuels. *Renewable and Sustainable Energy Reviews* 82, 3762–3797. <https://doi.org/10.1016/j.rser.2017.10.091>
- Liu, P., Sun, L., Jia, X., Zhang, C., Zhang, W., Song, Y., Wang, H., Li, C., 2020. Efficient one-pot conversion of furfural into 2-methyltetrahydrofuran using non-precious metal catalysts. *Molecular Catalysis* 490, 110951. <https://doi.org/10.1016/j.mcat.2020.110951>
- Liu, Y., Nie, Y., Lu, X., Zhang, X., He, H., Pan, F., Zhou, L., Liu, X., Ji, X., Zhang, S., 2019. Cascade utilization of lignocellulosic biomass to high-value products. *Green Chem.* 21, 3499–3535. <https://doi.org/10.1039/C9GC00473D>
- Luo, Y., Li, Z., Li, X., Liu, X., Fan, J., Clark, J.H., Hu, C., 2019. The production of furfural directly from hemicellulose in lignocellulosic biomass: A review. *Catalysis Today* 319, 14–24. <https://doi.org/10.1016/j.cattod.2018.06.042>
- Luo, Y.-J., Zhou, Y.-H., Huang, Y.-B., 2019. A New Lewis Acidic Zr Catalyst for the Synthesis of Furanic Diesel Precursor from Biomass Derived Furfural and 2-Methylfuran. *Catal Lett* 149, 292–302. <https://doi.org/10.1007/s10562-018-2599-6>
- Machado, G., Leon, S., Santos, F., Lourega, R., Dullius, J., Mollmann, M.E., Eichler, P., 2016. Literature Review on Furfural Production from Lignocellulosic Biomass. *NR* 07, 115–129. <https://doi.org/10.4236/nr.2016.73012>
- Mäkelä, E., Lahti, R., Jaatinen, S., Romar, H., Hu, T., Puurunen, R.L., Lassi, U., Karinen, R., 2018. Study of Ni, Pt, and Ru Catalysts on Wood-based Activated Carbon Supports and their Activity in Furfural Conversion to 2-Methylfuran. *ChemCatChem* 10, 3269–3283. <https://doi.org/10.1002/cctc.201800263>

- Mariscal, R., Maireles-Torres, P., Ojeda, M., Sádaba, I., López Granados, M., 2016. Furfural: a renewable and versatile platform molecule for the synthesis of chemicals and fuels. *Energy Environ. Sci.* 9, 1144–1189. <https://doi.org/10.1039/C5EE02666K>
- Mo, T., Xu, J., Yang, Y., Li, Y., 2016. Effect of carburization protocols on molybdenum carbide synthesis and study on its performance in CO hydrogenation. *Catalysis Today* 261, 101–115. <https://doi.org/10.1016/j.cattod.2015.07.014>
- Nanda, S., Azargohar, R., Dalai, A.K., Kozinski, J.A., 2015. An assessment on the sustainability of lignocellulosic biomass for biorefining. *Renewable and Sustainable Energy Reviews* 50, 925–941. <https://doi.org/10.1016/j.rser.2015.05.058>
- Niu, H., Luo, J., Li, C., Wang, B., Liang, C., 2019. Transfer Hydrogenation of Biomass-Derived Furfural to 2-Methylfuran over CuZnAl Catalysts. *Ind. Eng. Chem. Res.* 58, 6298–6308. <https://doi.org/10.1021/acs.iecr.9b00408>
- Okolie, J.A., Nanda, S., Dalai, A.K., Kozinski, J.A., 2021. Chemistry and Specialty Industrial Applications of Lignocellulosic Biomass. *Waste Biomass Valor* 12, 2145–2169. <https://doi.org/10.1007/s12649-020-01123-0>
- Oyama, S.T., 2003. Novel catalysts for advanced hydroprocessing: transition metal phosphides. *Journal of Catalysis* 216, 343–352. [https://doi.org/10.1016/S0021-9517\(02\)00069-6](https://doi.org/10.1016/S0021-9517(02)00069-6)
- Oyama, S.T., 1992. Preparation and catalytic properties of transition metal carbides and nitrides. *Catalysis Today* 15, 179–200. [https://doi.org/10.1016/0920-5861\(92\)80175-M](https://doi.org/10.1016/0920-5861(92)80175-M)
- Oyama, S.T., Gott, T., Zhao, H., Lee, Y.-K., 2009. Transition metal phosphide hydroprocessing catalysts: A review. *Catalysis Today* 143, 94–107. <https://doi.org/10.1016/j.cattod.2008.09.019>
- Panagiotopoulou, P., Martin, N., Vlachos, D.G., 2014. Effect of hydrogen donor on liquid phase catalytic transfer hydrogenation of furfural over a Ru/RuO<sub>2</sub>/C catalyst. *Journal of Molecular Catalysis A: Chemical* 392, 223–228. <https://doi.org/10.1016/j.molcata.2014.05.016>
- Panagiotopoulou, P., Vlachos, D.G., 2014. Liquid phase catalytic transfer hydrogenation of furfural over a Ru/C catalyst. *Applied Catalysis A: General* 480, 17–24. <https://doi.org/10.1016/j.apcata.2014.04.018>

- Pang, J., Sun, J., Zheng, M., Li, H., Wang, Y., Zhang, T., 2019. Transition metal carbide catalysts for biomass conversion: A review. *Applied Catalysis B: Environmental* 254, 510–522. <https://doi.org/10.1016/j.apcatb.2019.05.034>
- Pino, N., Sitthisa, S., Tan, Q., Souza, T., López, D., Resasco, D.E., 2017. Structure, activity, and selectivity of bimetallic Pd-Fe/SiO<sub>2</sub> and Pd-Fe/ $\gamma$ -Al<sub>2</sub>O<sub>3</sub> catalysts for the conversion of furfural. *Journal of Catalysis* 350, 30–40. <https://doi.org/10.1016/j.jcat.2017.03.016>
- Pozzo, M., Alfè, D., 2009. Hydrogen dissociation and diffusion on transition metal (=Ti, Zr, V, Fe, Ru, Co, Rh, Ni, Pd, Cu, Ag)-doped Mg(0001) surfaces. *International Journal of Hydrogen Energy* 34, 1922–1930. <https://doi.org/10.1016/j.ijhydene.2008.11.109>
- Rachamontree, P., Douzou, T., Cheenkachorn, K., Sriariyanun, M., Rattanaporn, K., 2020. Furfural: A Sustainable Platform Chemical and Fuel. *j.asep* 13. <https://doi.org/10.14416/j.asep.2020.01.003>
- Ramanathan, S., Oyama, S.T., 1995. New Catalysts for Hydroprocessing: Transition Metal Carbides and Nitrides. *J. Phys. Chem.* 99, 16365–16372. <https://doi.org/10.1021/j100044a025>
- Rasaki, S.A., Zhang, B., Anbalgam, K., Thomas, T., Yang, M., 2018. Synthesis and application of nano-structured metal nitrides and carbides: A review. *Progress in Solid State Chemistry* 50, 1–15. <https://doi.org/10.1016/j.progsolidstchem.2018.05.001>
- Robinson, A.M., Hensley, J.E., Medlin, J.W., 2016. Bifunctional Catalysts for Upgrading of Biomass-Derived Oxygenates: A Review. *ACS Catal.* 6, 5026–5043. <https://doi.org/10.1021/acscatal.6b00923>
- Roy, A., Serov, A., Artyushkova, K., Brosha, E.L., Atanassov, P., Ward, T.L., 2015. Facile synthesis of high surface area molybdenum nitride and carbide. *Journal of Solid State Chemistry* 228, 232–238. <https://doi.org/10.1016/j.jssc.2015.05.007>
- Scholz, D., Aellig, C., Hermans, I., 2014. Catalytic Transfer Hydrogenation/Hydrogenolysis for Reductive Upgrading of Furfural and 5-(Hydroxymethyl)furfural. *ChemSusChem* 7, 268–275. <https://doi.org/10.1002/cssc.201300774>



- Seemala, B., Cai, C.M., Kumar, R., Wyman, C.E., Christopher, P., 2018. Effects of Cu–Ni Bimetallic Catalyst Composition and Support on Activity, Selectivity, and Stability for Furfural Conversion to 2-Methylfuran. *ACS Sustainable Chem. Eng.* 6, 2152–2161. <https://doi.org/10.1021/acssuschemeng.7b03572>
- Shen, G., Andrioletti, B., Queneau, Y., 2020. Furfural and 5-(hydroxymethyl)furfural: Two pivotal intermediates for bio-based chemistry. *Current Opinion in Green and Sustainable Chemistry* 26, 100384. <https://doi.org/10.1016/j.cogsc.2020.100384>
- Shilov, I., Smirnov, A., Bulavchenko, O., Yakovlev, V., 2018. Effect of Ni–Mo Carbide Catalyst Formation on Furfural Hydrogenation. *Catalysts* 8, 560. <https://doi.org/10.3390/catal8110560>
- Smith, K.J., 2020. Metal carbides, phosphides, and nitrides for biomass conversion. *Current Opinion in Green and Sustainable Chemistry* 22, 47–53. <https://doi.org/10.1016/j.cogsc.2019.11.008>
- Srivastava, S., Jadeja, G.C., Parikh, J., 2018. Copper-cobalt catalyzed liquid phase hydrogenation of furfural to 2-methylfuran: An optimization, kinetics and reaction mechanism study. *Chemical Engineering Research and Design* 132, 313–324. <https://doi.org/10.1016/j.cherd.2018.01.031>
- Srivastava, S., Jadeja, G.C., Parikh, J., 2017. Synergism studies on alumina-supported copper-nickel catalysts towards furfural and 5-hydroxymethylfurfural hydrogenation. *Journal of Molecular Catalysis A: Chemical* 426, 244–256. <https://doi.org/10.1016/j.molcata.2016.11.023>
- Srivastava, S., Jadeja, G.C., Parikh, J., 2016. A versatile bi-metallic copper–cobalt catalyst for liquid phase hydrogenation of furfural to 2-methylfuran. *RSC Adv.* 6, 1649–1658. <https://doi.org/10.1039/C5RA15048E>
- Sullivan, M.M., Chen, C.-J., Bhan, A., 2016. Catalytic deoxygenation on transition metal carbide catalysts. *Catal. Sci. Technol.* 6, 602–616. <https://doi.org/10.1039/C5CY01665G>
- Tarazanov, S., Grigoreva, K., Shipitcyna, A., Repina, O., Ershov, M., Kuznetsova, S., Nikulshin, P., 2020. Assessment of the chemical stability of furfural derivatives and the

mixtures as fuel components. *Fuel* 271, 117594.  
<https://doi.org/10.1016/j.fuel.2020.117594>

Toledo, F., Ghampson, I.T., Sepúlveda, C., García, R., Fierro, J.L.G., Videla, A., Serpell, R., Escalona, N., 2019. Effect of Re content and support in the liquid phase conversion of furfural to furfuryl alcohol and 2-methyl furan over ReOx catalysts. *Fuel* 242, 532–544. <https://doi.org/10.1016/j.fuel.2019.01.090>

Tuan Hoang, A., Viet Pham, V., 2021. 2-Methylfuran (MF) as a potential biofuel: A thorough review on the production pathway from biomass, combustion progress, and application in engines. *Renewable and Sustainable Energy Reviews* 148, 111265. <https://doi.org/10.1016/j.rser.2021.111265>

Volpe, L., Boudart', M., n.d. Compounds of Molybdenum and Tungsten with High Specific Surface Area 9.

Wan, W., Jiang, Z., Chen, J.G., 2018. A Comparative Study of Hydrodeoxygenation of Furfural Over Fe/Pt(111) and Fe/Mo<sub>2</sub>C Surfaces. *Top Catal* 61, 439–445. <https://doi.org/10.1007/s11244-018-0901-x>

Wang, B., Li, C., He, B., Qi, J., Liang, C., 2017. Highly stable and selective Ru/NiFe<sub>2</sub>O<sub>4</sub> catalysts for transfer hydrogenation of biomass-derived furfural to 2-methylfuran. *Journal of Energy Chemistry* 26, 799–807. <https://doi.org/10.1016/j.jechem.2017.04.008>

Wang, C., Luo, J., Liao, V., Lee, J.D., Onn, T.M., Murray, C.B., Gorte, R.J., 2018. A comparison of furfural hydrodeoxygenation over Pt-Co and Ni-Fe catalysts at high and low H<sub>2</sub> pressures. *Catalysis Today* 302, 73–79. <https://doi.org/10.1016/j.cattod.2017.06.042>

Wang, Y., Feng, X., Yang, S., Xiao, L., Wu, W., 2020. Influence of acidity on the catalytic performance of Ni<sub>2</sub>P in liquid-phase hydrodeoxygenation of furfural to 2-methylfuran. *J Nanopart Res* 22, 67. <https://doi.org/10.1007/s11051-020-04784-z>

Wang, Yazhou, Liu, F., Han, H., Xiao, L., Wu, W., 2018. Metal Phosphide: A Highly Efficient Catalyst for the Selective Hydrodeoxygenation of Furfural to 2-Methylfuran. *ChemistrySelect* 3, 7926–7933. <https://doi.org/10.1002/slct.201800929>

- Wang, Yantao, Prinsen, P., Triantafyllidis, K.S., Karakoulia, S.A., Trikalitis, P.N., Yezpez, A., Len, C., Luque, R., 2018. Comparative Study of Supported Monometallic Catalysts in the Liquid-Phase Hydrogenation of Furfural: Batch Versus Continuous Flow. *ACS Sustainable Chem. Eng.* 6, 9831–9844. <https://doi.org/10.1021/acssuschemeng.8b00984>
- Wang, Y., Zhao, D., Rodríguez-Padrón, D., Len, C., 2019. Recent Advances in Catalytic Hydrogenation of Furfural. *Catalysts* 9, 796. <https://doi.org/10.3390/catal9100796>
- Werpy, T., Petersen, G., 2004. Top Value Added Chemicals from Biomass: Volume I -- Results of Screening for Potential Candidates from Sugars and Synthesis Gas (No. DOE/GO-102004-1992, 15008859). <https://doi.org/10.2172/15008859>
- Wettstein, S.G., Alonso, D.M., Gürbüz, E.I., Dumesic, J.A., 2012. A roadmap for conversion of lignocellulosic biomass to chemicals and fuels. *Current Opinion in Chemical Engineering* 1, 218–224. <https://doi.org/10.1016/j.coche.2012.04.002>
- Xiao, T., York, A.P.E., Coleman, K.S., Claridge, J.B., Sloan, J., Charnock, J., Green, M.L.H., 2001. [No title found]. *J. Mater. Chem.* 11, 3094–3098. <https://doi.org/10.1039/b104011c>
- Xu, C., Paone, E., Rodríguez-Padrón, D., Luque, R., Mauriello, F., 2020. Recent catalytic routes for the preparation and the upgrading of biomass-derived furfural and 5-hydroxymethylfurfural. *Chem. Soc. Rev.* 49, 4273–4306. <https://doi.org/10.1039/D0CS00041H>
- Xu, W., Ramirez, P.J., Stacchiola, D., Rodriguez, J.A., 2014. Synthesis of  $\alpha$ -MoC<sub>1-x</sub> and  $\beta$ -MoC<sub>y</sub> Catalysts for CO<sub>2</sub> Hydrogenation by Thermal Carburization of Mo-oxide in Hydrocarbon and Hydrogen Mixtures. *Catal Lett* 144, 1418–1424. <https://doi.org/10.1007/s10562-014-1278-5>
- Yan, K., Wu, G., Lafleur, T., Jarvis, C., 2014. Production, properties, and catalytic hydrogenation of furfural to fuel additives and value-added chemicals. *Renewable and Sustainable Energy Reviews* 38, 663–676. <https://doi.org/10.1016/j.rser.2014.07.003>
- Yong, K.J., Wu, T.Y., Lee, C.B.T.L., Lee, Z.J., Liu, Q., Jahim, J.M., Zhou, Q., Zhang, L., 2022. Furfural production from biomass residues: Current technologies, challenges,

and future prospects. *Biomass and Bioenergy* 161, 106458. <https://doi.org/10.1016/j.biombioe.2022.106458>

Zhang, J., Chen, J., 2017. Selective Transfer Hydrogenation of Biomass-Based Furfural and 5-Hydroxymethylfurfural over Hydrotalcite-Derived Copper Catalysts Using Methanol as a Hydrogen Donor. *ACS Sustainable Chem. Eng.* 5, 5982–5993. <https://doi.org/10.1021/acssuschemeng.7b00778>

Zhang, J., Li, D., Yuan, H., Wang, S., Chen, Y., 2021. Advances on the catalytic hydrogenation of biomass-derived furfural and 5-hydroxymethylfurfural. *Journal of Fuel Chemistry and Technology* 49, 1752–1766. [https://doi.org/10.1016/S1872-5813\(21\)60135-4](https://doi.org/10.1016/S1872-5813(21)60135-4)

Zhang, Z., Pei, Z., Chen, H., Chen, K., Hou, Z., Lu, X., Ouyang, P., Fu, J., 2018. Catalytic in-Situ Hydrogenation of Furfural over Bimetallic Cu–Ni Alloy Catalysts in Isopropanol. *Ind. Eng. Chem. Res.* 57, 4225–4230. <https://doi.org/10.1021/acs.iecr.8b00366>

Zhou, K., Chen, J., Cheng, Y., Chen, Z., Kang, S., Cai, Z., Xu, Y., Wei, J., 2020. Enhanced Catalytic Transfer Hydrogenation of Biomass-Based Furfural into 2-Methylfuran over Multifunctional Cu–Re Bimetallic Catalysts. *ACS Sustainable Chem. Eng.* 8, 16624–16636. <https://doi.org/10.1021/acssuschemeng.0c06026>

Zhou, M., Doan, H.A., Curtiss, L.A., Assary, R.S., 2021. Identification of Active Metal Carbide and Nitride Catalytic Facets for Hydrodeoxygenation Reactions. *J. Phys. Chem. C* 125, 8630–8637. <https://doi.org/10.1021/acs.jpcc.1c02387>

## **CHAPTER 3. METHODOLOGY**

## **3. METHODOLOGY**

### **3.1 Preparation of the catalysts**

#### **3.1.1 Treatment of the supports**

Silica ( $\text{SiO}_2$ , Aerosil 200, Evonik Industries) was moistened with deionized water, dried at  $120\text{ }^\circ\text{C}$  for 3 hours, and then calcined at  $500\text{ }^\circ\text{C}$  ( $10\text{ }^\circ\text{C min}^{-1}$ ) for 6 hours under static air. This procedure was carried out to facilitate the handling of the material, which has a low density. Titania ( $\text{TiO}_2$ , Aeroxide P25, Degussa Brazil LTDA) and zirconia ( $\text{ZrO}_2$ , Saint-Gobain) were dried at  $110\text{ }^\circ\text{C}$  overnight under static air. Finally, the zeolite (ZSM-5, Fábrica Carioca de Catalisadores S.A.) was heated up to  $110\text{ }^\circ\text{C}$  ( $10\text{ }^\circ\text{C min}^{-1}$ ), remaining at this temperature for 30 minutes, and then calcined at  $500\text{ }^\circ\text{C}$  ( $10\text{ }^\circ\text{C min}^{-1}$ ) for another 3 hours under static air. This protocol was followed to remove  $\text{NH}_3$  from the material and achieve its protonic form.

#### **3.1.2 Preparation of the precursors**

Incipient wetness impregnation was used to prepare the supported monometallic and Ni or Cu-promoted molybdenum carbides containing a final loading of 20 wt.% of active phase (20 wt.% for the monometallic and 17 wt.% Mo and 3 wt.% Ni or Cu for the promoted materials).

To prepare the monometallic carbides, an adequate amount of ammonium heptamolybdate ( $(\text{NH}_4)_6\text{Mo}_7\text{O}_{24}\cdot 4\text{H}_2\text{O}$ , Sigma-Aldrich,  $0.173\text{ g mL}^{-1}$ ) was solubilized in distilled water and then the solution obtained was impregnated on the supports ( $\text{SiO}_2$ ,  $\text{TiO}_2$ ,  $\text{ZrO}_2$ , ZSM-5). During the impregnation, several dryings were performed at  $110\text{ }^\circ\text{C}$  for 1 hour until the solution was depleted. Final drying was performed at the same temperature overnight.

For the promoted carbides, adequate amounts of nickel nitrate ( $\text{Ni}(\text{NO}_3)_2 \cdot 6\text{H}_2\text{O}$ , Sigma-Aldrich,  $0.076 \text{ g mL}^{-1}$ ) or copper nitrate ( $\text{Cu}(\text{NO}_3)_2 \cdot \text{H}_2\text{O}$ , Sigma-Aldrich,  $0.045 \text{ g mL}^{-1}$ ) and ammonium heptamolybdate ( $(\text{NH}_4)_6\text{Mo}_7\text{O}_{24} \cdot 4\text{H}_2\text{O}$ , Sigma-Aldrich,  $0.16 \text{ g mL}^{-1}$ ) were solubilized individually in distilled water. Firstly, the solution containing Mo was impregnated onto the support (only  $\text{SiO}_2$ , in this case) and dried at  $110 \text{ }^\circ\text{C}$  for 1 hour until it was depleted. After that, the material was dried overnight at the same temperature and then the solution containing Ni or Cu was added using the same procedure.

For comparison,  $\text{Ni}/\text{SiO}_2$  and  $\text{Cu}/\text{SiO}_2$  containing 3 wt.% of Ni or Cu were prepared by incipient wetness impregnation of  $\text{SiO}_2$ . Nickel nitrate ( $\text{Ni}(\text{NO}_3)_2 \cdot 6\text{H}_2\text{O}$ , Sigma-Aldrich,  $0.117 \text{ g mL}^{-1}$ ) or copper nitrate ( $\text{Cu}(\text{NO}_3)_2 \cdot \text{H}_2\text{O}$ , Sigma-Aldrich,  $0.087 \text{ g mL}^{-1}$ ) were solubilized in distilled water and then each solution was impregnated individually on  $\text{SiO}_2$ . After impregnation, the materials were dried at  $110 \text{ }^\circ\text{C}$  overnight. Finally, all samples were calcined under static air at  $500 \text{ }^\circ\text{C}$  ( $5 \text{ }^\circ\text{C min}^{-1}$ ) for 3 hours to obtain the calcined precursors.

### 3.1.3 Synthesis of molybdenum carbides

To synthesize the unsupported  $\beta\text{-Mo}_2\text{C}$  and supported Mo carbides, 1 g of molybdenum trioxide ( $\text{MoO}_3$ , Sigma-Aldrich) or calcined precursors were carburized at  $650 \text{ }^\circ\text{C}$  ( $2.5 \text{ }^\circ\text{C min}^{-1}$ ) for 2 hours with a mixture containing 20% (v/v)  $\text{CH}_4/\text{H}_2$  ( $200 \text{ mL min}^{-1}$  STP) (Sousa *et al.*, 2012). The  $\alpha$ -phase of the carbide supported on  $\text{SiO}_2$  was obtained by first nitriding the calcined precursor with 20% (v/v)  $\text{N}_2/\text{H}_2$  ( $200 \text{ mL min}^{-1}$  STP) under a three-stage heating ramp:  $30 - 350 \text{ }^\circ\text{C}$  ( $10 \text{ }^\circ\text{C min}^{-1}$ ),  $350 - 500 \text{ }^\circ\text{C}$  ( $1 \text{ }^\circ\text{C min}^{-1}$ ),  $500 - 700 \text{ }^\circ\text{C}$  ( $2 \text{ }^\circ\text{C min}^{-1}$ ) and then left at  $700 \text{ }^\circ\text{C}$  for 2 hours (Chen *et al.*, 2017) and finally carburized at  $700 \text{ }^\circ\text{C}$  for 2 hours with 20% (v/v)  $\text{CH}_4/\text{H}_2$  ( $200 \text{ mL min}^{-1}$  STP). The carbides catalysts were designated as  $\beta\text{-Mo}_2\text{C}$ ,  $\beta\text{-Mo}_2\text{C}/\text{SiO}_2$  (or  $\text{Mo}_2\text{C}/\text{SiO}_2$ ),  $\alpha\text{-MoC}/\text{SiO}_2$ ,  $\text{Ni-Mo}_x\text{C}_y/\text{SiO}_2$ ,  $\text{Cu-Mo}_x\text{C}_y/\text{SiO}_2$ ,  $\text{Mo}_2\text{C}/\text{TiO}_2$ ,  $\text{Mo}_2\text{C}/\text{ZrO}_2$ ,  $\text{Mo}_2\text{C}/\text{ZSM-5}$ , and the reference catalysts as  $\text{Ni}/\text{SiO}_2$  and  $\text{Cu}/\text{SiO}_2$ .

### **3.1.4 Passivation**

Considering the pyrophoric nature of molybdenum carbides, it was necessary to perform a passivation step for storage and further handling of these materials to avoid their complete oxidation when exposed to air. This procedure consisted in passing a mixture containing 0.5% (v/v) O<sub>2</sub>/N<sub>2</sub> (30 mL min<sup>-1</sup> STP) through the Mo carbide for 14 hours at room temperature. Before the catalytic tests, the passivation layers will be removed as detailed in Topic 3.3.2.3.

## **3.2 Characterization**

### **3.2.1 Chemical analyses**

#### **3.2.1.1 Inductively Coupled Plasma Optical Emission Spectroscopy (ICP-OES)**

Mo, Ni, and Cu species in the catalysts were detected and quantified by inductively coupled plasma-optic emission spectroscopy (ICP-OES) using a 720-ES ICP-OES spectrometer (Agilent) with axial viewing and simultaneous charge-coupled device (CCD) detector. About 10 mg of the sample were dissolved in 250  $\mu$ L HF and 4 mL aqua regia and then the resulting solutions were heated at 110 °C for 2 hours in the autodigestor Vulcan 42 (Questron). Then, the samples were neutralized with 2 mL of a basic commercial solution of triethylenetetramine (UNSI). Finally, the samples were diluted up to 20 mL with ultrapure water before analysis.



### **3.2.1.2 Elemental analysis (EA)**

The carbon content in the catalysts was determined using a Thermo Scientific FlashSmart automated analyzer. For that, the samples were weighed in tin containers and introduced into the combustion reactor. The reactor was filled with copper oxide followed by wire-reduced nickel, maintained at 950 °C, and operated with dynamic flash combustion of the sample. Carbon was detected as CO<sub>2</sub>. The resulting gases were separated on a packed column heated at 65 °C in an oven and detected by a thermal conductivity detector (TCD). The analysis duration was 10 minutes.

## **3.2.2 Textural and morphological properties**

### **3.2.2.1 N<sub>2</sub> physisorption**

The textural properties of the supports and passivated catalysts were measured by nitrogen adsorption at -196 °C using a Micromeritics TriStar II Plus analyzer and a Micromeritics Accelerated Surface Area and Porosity (ASAP) depending on the porous type in the materials. Before the analysis, the samples were degassed under a vacuum at 75 °C for 1 hour and then at 300 °C for up to 24 hours. The specific surface areas were estimated using the Brunauer-Emmett-Teller (BET) method, while the mesopores and micropores volumes were determined by Barrett-Joyner-Halenda (BJH) and t-plot methods, respectively.

### **3.2.2.2 X-Ray diffraction (XRD)**

X-ray Diffraction (XRD) analysis was performed using a Bruker AXS D8 Advance diffractometer employing Cu K $\alpha$  radiation ( $\lambda = 0.1538$  nm). The diffractograms were obtained in a  $2\theta$  range between 5 - 80° at a scan rate of 0.02°/step

and a scan time of 1 s/step. The identification of the phases was carried out by comparison between the diffractograms obtained experimentally and the diffraction standards (PDF - Powder Diffraction File) available in the Joint Committee on Powder Diffraction Standards – International Center for Diffraction Data (JCPDF - ICDD). The average crystallite size ( $D_c$ ) of the Mo carbides was determined by the Scherrer equation (Equation 3.1) using the line corresponding to the (110) plane at  $2\theta = 61.5^\circ$  for  $\beta$ -Mo<sub>2</sub>C and (108) plane at  $2\theta = 61.9^\circ$  for  $\alpha$ -MoC. Characteristic lines at higher diffraction angles ( $2\theta = 61.5$  or  $61.9^\circ$ ) were used to avoid interference from the supports. To estimate  $D_c$  for the metal particles on the reference catalysts (Ni/SiO<sub>2</sub> and Cu/SiO<sub>2</sub>), the lines corresponding to the (111) plane at  $2\theta = 44.5^\circ$  for Ni<sup>0</sup> and  $2\theta = 43.3^\circ$  for Cu<sup>0</sup> were used.

$$D_c = \frac{K\lambda}{\beta \cos\theta} \quad \text{Equation 3.1}$$

where

$D_c$  is the average crystallite size (nm),

$\lambda$  is the wavelength of the X-ray radiation (for Cu K<sub>α</sub>, 0.1538 nm),

$K$  is Debye–Scherrer’s constant = 0.9 (spherical particles),

$\beta$  is the peak width at half-maximum intensity (FWHM) (radian),

$\theta$  is the angle of diffraction.

### 3.2.2.3 Temperature-programmed carburization (TPC)

Temperature-programmed carburization (TPC) was performed to follow the formation of the Mo carbides in a multipurpose unit coupled to a Pfeiffer Vacuum mass spectrometer (MS) model QME 200. Before the TPC analysis, the calcined precursors of the carbides (0.1 g) were treated under He (50 mL min<sup>-1</sup> STP) at 200 °C (10 °C min<sup>-1</sup>) for 1 hour to remove water and then cooled to 30 °C. Then, He was replaced by a

20% (v/v) CH<sub>4</sub>/H<sub>2</sub> mixture (100 mL min<sup>-1</sup> STP), and the temperature was increased up to 900 °C (2.5 °C min<sup>-1</sup>). The signals of H<sub>2</sub>O (m/z = 18), CH<sub>4</sub> (m/z = 15) and CO (m/z = 28) ions were continuously monitored on the mass spectrometer to follow the carburization.

### **3.2.2.4 Temperature-programmed desorption of NH<sub>3</sub> (TPD-NH<sub>3</sub>)**

The total acidity of the supports and catalysts was estimated by temperature-programmed desorption of NH<sub>3</sub>. Before the analysis, the supports (0.1 g) were treated at 200 °C (10 °C min<sup>-1</sup>) for 1 hour in He (50 mL min<sup>-1</sup>) to eliminate water. The passivated catalysts (0.1 g) were reduced at 450 °C (10 °C min<sup>-1</sup>) for 1 hour in H<sub>2</sub> (50 mL min<sup>-1</sup>) to eliminate the passivation layer. After heat treatment, all materials were cooled down to 100 °C in He (50 mL min<sup>-1</sup>) and purged for 15 minutes. The NH<sub>3</sub> adsorption was performed at 100 °C for 30 minutes using 10% (v/v) NH<sub>3</sub>/He (30 mL min<sup>-1</sup>) and then the surface of the material was purged with He (50 mL min<sup>-1</sup>) for 2 hours. The NH<sub>3</sub> desorption was performed by heating the samples in He (30 mL min<sup>-1</sup>) up to 500 °C (10 °C min<sup>-1</sup>) and kept at this temperature until the NH<sub>3</sub> signal returns to the baseline (around 2 hours). The experiments were conducted in the equipment AutoChem II from Micromeritics equipped with a thermal conductivity detector and a mass spectrometer, in which the signals of NH<sub>3</sub> (m/z = 17, 16, and 15) and H<sub>2</sub>O (m/z = 18, 17, and 16) ions were monitored.

## **3.2.3 Spectroscopic techniques**

### **3.2.3.1 X-Ray absorption spectroscopy (XAS)**

Characterization by X-Ray absorption spectroscopy (XAS) was carried out in the transmission mode at the ROCK Quick-EXAFS beamline at the French synchrotron radiation facility SOLEIL (Briois *et al.*, 2016). The beamline benefits from a 2.81 Tesla

Super-Bend source which delivers nearly  $10^{12}$  ph s<sup>-1</sup> between 8 to 20 keV. Spectra were acquired in *in situ* conditions, either at the Mo K-edge for monometallic systems, or alternatively at the Ni (8333 eV) / Cu (8979 eV) and Mo (20000 eV) K-edges for the bimetallic Ni-Mo and Cu-Mo systems, during carburization under 20% (v/v) CH<sub>4</sub>/H<sub>2</sub> and during reactivation in H<sub>2</sub> of passivated catalysts. The monochromator used is based on a Si (111) channel-cut installed on a tilt table allowed to oscillate around the Bragg angle characteristic of the element of interest, i.e., 13.4332° for Ni, 12.2886° for Cu and 5.6550° for Mo, with an amplitude of 2.0° for Ni and Cu and 0.5° for Mo. The Si (111) channel-cut oscillation frequency was set to 2 Hz and recorded two quick-EXAFS spectra were every 0.5 s. Every 10 acquired spectra were merged to improve the signal/noise ratio. Ionization chambers were filled with nitrogen for Ni and Cu K edge measurements and a mixture of 50:50 of nitrogen and argon for the Mo K edge measurements. The beam size at the sample position was ~ 500 μm (H) x 300 μm (V).

Experiments were performed using a dedicated gas-feeding set-up installed on the ROCK beamline (La Fontaine *et al.*, 2013). A quartz capillary (1.5 mm x 80 mm x 0.04 mm) was used as a sample holder. The powder catalyst bed (length ~ 8 - 9 mm) was maintained at the center of the capillary between two pieces of quartz wool and heated using a gas blower. The *in situ* temperature-programmed carburization of the calcined precursors of the Mo<sub>2</sub>C/SiO<sub>2</sub>, Ni-Mo<sub>x</sub>C<sub>y</sub>/SiO<sub>2</sub>, Cu-Mo<sub>x</sub>C<sub>y</sub>/SiO<sub>2</sub>, and Mo<sub>2</sub>C/TiO<sub>2</sub> catalysts were performed by heating the capillary from room temperature to 650 °C (2.5 °C min<sup>-1</sup>) under a 20% (v/v) CH<sub>4</sub>/H<sub>2</sub> flow (5 mL min<sup>-1</sup> STP). The reactivation was performed on catalysts that had been previously passivated (β-Mo<sub>2</sub>C, Mo<sub>2</sub>C/SiO<sub>2</sub>, Ni-Mo<sub>x</sub>C<sub>y</sub>/SiO<sub>2</sub>, Cu-Mo<sub>x</sub>C<sub>y</sub>/SiO<sub>2</sub>, Mo<sub>2</sub>C/TiO<sub>2</sub>, Mo<sub>2</sub>C/ZSM-5, Ni/SiO<sub>2</sub>, and Cu/SiO<sub>2</sub>). For this, the samples were heated up to 400 °C (5 °C min<sup>-1</sup>) under an H<sub>2</sub> flow (5 mL min<sup>-1</sup> STP). All experiments were kept isothermal until no changes were observed in the spectra. Spectra were then recorded back at room temperature.

Energy calibration concerning the reference metal foil (Mo, Ni, Cu) and a XAS data-normalization procedure were first carried out using the Python `normal_gui` graphical interface developed at SOLEIL for the fast handling of Quick-XAS data (Lesage *et al.*, 2019). The EXAFS signal extraction and Fourier transform of the EXAFS spectra was done using the Athena graphical interface software (Ravel and Newville, 2005). EXAFS fitting of coordination numbers N, Debye-Waller factors  $\sigma^2$

and interatomic distances  $R$  was simultaneously performed on  $k$ -,  $k^2$ - and  $k^3$ -weighted  $\chi(k)$  functions with the Artemis interface to IFEFFIT using least-squares refinements (Newville, 2001), fits were first performed on the metallic foil references for the determination of the  $S_0^2$  factor. Fourier-transformed EXAFS signals are presented as  $k^3\text{-}\chi(k)$  functions and Fourier transforms are shown without phase correction.

The proportions of different Mo, Ni, and Cu species during the different stages of carburization and reduction were determined by a chemometric procedure, the Multivariate Curve Resolution by Alternative-Least Squares (MCR-ALS) methodology, using the free MCR-ALS GUI 2.0 toolbox developed by the Tauler group on the Matlab platform (Jaumot *et al.*, 2015). XAS spectra are considered to be linear combinations of individual spectral components (matrix  $S$ ) weighted by their concentration that varies with temperature or time (matrix  $C$ ). The determination of matrices  $S$  and  $C$  takes place without initial hypotheses on the chemical nature of the different species appearing along the thermal treatment, by a least-square minimization of a residue matrix. The determination of the most likely number of spectral components takes place via a preliminary Principal Component Analysis by Singular-Value Decomposition (PCA-SVD). MCR-ALS spectral components (XANES spectra, EXAFS oscillations, and Fourier transform) are then identified to successive species after checking their chemical meaningfulness, by comparison with spectra of compounds already known in the mixture or as standards, or with plausible models in accordance with the chemistry of the system. Further details about the MCR-ALS method applied to XAS are available in recent publications (Cassinelli *et al.*, 2014; Hong *et al.*, 2015; Lesage *et al.*, 2019). In parallel with the XAS analyses, Raman spectra were measured using a commercial RXN1 Raman spectrometer (Kaiser Optical Systems, Inc.).

## 3.3 Catalytic performance evaluation

### 3.3.1 Materials

Furfural (FF, purity > 99%) was used as substrate in the catalytic tests. The solvents used for the reactions were cyclopentyl methyl ether (CPME, > 99.9%) and 2-butanol (2BuOH, 99.5%). Furfuryl alcohol (FA, > 98%), 2-methylfuran (2MF, > 99%), tetrahydrofurfuryl alcohol (THFA, 99%), 2-methyltetrahydrofuran (2MTHF, > 99%), tetrahydrofuran (THF, > 99.9%), furan (> 99%), cyclopentane (CPA, 98%), cyclopentene (CPE, > 96%), cyclopentanone (CPO, > 99.5%), cyclopentanol (CPOH, > 99%), 1,4-pentanediol (1,4PDO, > 99%), 1,5-pentanediol (1,5PDO, > 97%), levulinic acid (LA, > 98%),  $\gamma$ -valerolactone (GVL, > 99%), 2-butanone (2BTNE, > 99%) were used for peaks identification in the chromatograms and calibration. All products were purchased from Sigma-Aldrich and used as such.

### 3.3.2 Experimental set-up

#### 3.3.2.1 Screening Pressure Reactor (SPR)

A catalyst screening for furfural hydrodeoxygenation (HDO) reaction in the liquid phase was carried out on the REALCAT platform (Paul *et al.*, 2015) in a Screening Pressure Reactor (SPR) from Unchained Labs equipped with 24 parallel stainless-steel batch reactors of 6 mL each (Figure 3.1). The stirring in the reactor vessels is ensured by orbital shaking under controlled pressure and temperature conditions. The SPR runs at temperatures up to 400 °C and pressures up to 50 bar.

The SPR is operated via a computer equipped with Automation Studio and Library Studio software that provide a user interface, hardware to communicate with the SPR system, and operational controls (process control and recording). Automation

Studio protocols were used to control the experiment, while Library Studio was used to collect and store experimental parameters.

Figure 3.1. Screening Pressure Reactor (SPR).



Reference: available at <https://www.unchainedlabs.com/catalyst-screening/>. Accessed on September 11, 2022.

### 3.3.2.2 Parr reactor

Individual tests for each support or catalyst were performed in a 50 mL batch Hastelloy Parr 4590 autoclave set-up equipped with a pressure gauge, a thermocouple, and a mechanical stirring (Figure 3.2). The Parr reactor operates at temperatures up to 500 °C and pressures up to 200 bar.

Figure 3.2. Parr reactor.



Reference: available at <https://www.parrinst.com/reactors-pressure-vessels/>. Accessed on September 11, 2022.

### 3.3.2.3 Description of catalysts activation in H<sub>2</sub>

To remove the passivation layer of Mo carbides before the catalytic tests, the catalysts were treated with pure hydrogen in the SPR.

Firstly, the desired amounts of catalysts were weighted directly in each reactor and then the reactor vessel was hermetically sealed and flushed by gas flow according to the following protocol. The reactors were first purged at room temperature with N<sub>2</sub> (200 mL min<sup>-1</sup> STP) for 10 minutes to eliminate oxygen and then with pure H<sub>2</sub> (200 mL min<sup>-1</sup> STP) for more 10 minutes to eliminate the residual N<sub>2</sub>. After that, the reactor vessel was pressurized up to 30 bar using 500 mL min<sup>-1</sup> STP of H<sub>2</sub>. Then the H<sub>2</sub> flow was reduced to 50 mL min<sup>-1</sup> STP and the system started to be heated up to 400 °C (5 °C min<sup>-1</sup>). This temperature was kept constant for 1 hour. The reactors were then cooled to 30 °C and flushed with pure N<sub>2</sub> (200 mL min<sup>-1</sup> STP) to remove the excess hydrogen. The hermetically sealed reactor vessel was then transferred to a glovebox (MBRAUN), in which the reactivated catalysts were storage.



For the catalytic tests carried out in the SPR, the reactor vessel containing the reactivated catalysts was charged with the reaction mixture without any contact with air inside the glovebox. For each run, 40 mL of reaction mixture containing 0.5 mol L<sup>-1</sup> of furfural in cyclopentyl methyl ether (CPME) or 2-butanol (2BuOH) was prepared and distributed in the reactors (1.5 mL each). Finally, the hermetically sealed reactor vessel was removed from the glovebox and connected to the SPR unit.

For the tests carried out in the Parr reactor, the reactivated catalysts were kept inside the glovebox to avoid re-oxidation, then the reactor vessel was charged with the desired amount of catalyst and 15 mL of reaction mixture containing 0.25 or 0.5 mol L<sup>-1</sup> of furfural in CPME or 2BuOH without exposure to air. After that, the Parr reactor was removed from the glove box and connected to the unit.

### **3.3.2.4 Description of the experimental catalytic tests**

After connecting the reactor vessel to the SPR unit the inlet and outlet valves were opened. The reactors were first purged with N<sub>2</sub> (200 mL min<sup>-1</sup> STP) for 10 minutes and then with pure H<sub>2</sub> (200 mL min<sup>-1</sup> STP) for more 10 minutes at room temperature. Then, the system was pressurized up to 30 bar with 500 mL min<sup>-1</sup> STP of H<sub>2</sub>. When the pressure was reached, the set of reactors was heated to the desired temperature (200 °C) using a heating ramp of 5 °C min<sup>-1</sup>. Only then the agitation of 600 rpm was initiated. The catalysts were tested for 4 hours using a molar ratio of substrate per mol of active phase (R) of 21. At the end of the reaction, the temperature was reduced to 40 °C, the valves of the reactor were opened, and the reactor was flushed with N<sub>2</sub> (200 mL min<sup>-1</sup> STP) for 10 minutes to remove all the gases from the reactor.

For the tests carried out in the Parr reactor, after connecting the reactor vessel, the system was purged 3 times with hydrogen and 30 bar of H<sub>2</sub> was added. The reaction mixture was heated at 5 °C min<sup>-1</sup> from room temperature to 200 °C (45 bar total pressure) and then the stirring was started (600 rpm), at this moment the time was set to zero. After 4 hours of reaction, the stirring was stopped, and the autoclave was cooled in an ice bath until reaching a temperature lower than 30 °C. Around 2 mL was taken from

the liquid mixture and 1 mL of aliquots were analyzed after filtration to separate the catalyst.

### 3.3.3 Analytical methods

The liquid samples collected after reaction were analyzed by gas chromatography and a flame-ionization detector (Shimadzu GC-2010 Plus) using a ZB-5MS column (30 m x 0.25 mm x 0.25  $\mu$ m) and the identification of the compounds was done according to the method described in Table 3.1.

Table 3.1. GC analytical methods parameters.

<b>Injection</b>	Injection mode	Split ratio 400
	Temperature	250 °C
	Carrier gas	H <sub>2</sub>
	Pressure	62.8 kPa
	Total flow	704.6 mL min <sup>-1</sup>
	Column flow	1.75 mL min <sup>-1</sup>
<b>Oven</b>	Initial Temperature, T <sub>0</sub>	27 °C / 4 min
	T <sub>1</sub> (rate)	170 °C (25 °C min <sup>-1</sup> )
	T <sub>2</sub> (rate)	240 °C (50 °C min <sup>-1</sup> ) / 11 min
	Equilibration time	0.5 min
	Total program time	22.11 min
	Final temperature, T <sub>F</sub>	240 °C
<b>Detector</b>	FID	
	Temperature	250 °C
	H <sub>2</sub> flow	40 mL min <sup>-1</sup>
	Air flow	400 mL min <sup>-1</sup>

Reference: own author (2023)

Furfural (FF), furfuryl alcohol (FA), 2-methylfuran (2MF), tetrahydrofurfuryl alcohol (THFA), 2-methyltetrahydrofuran (2MTHF), tetrahydrofuran (THF), furan (F), cyclopentane (CPA), cyclopentene (CPE), cyclopentanone (CPO), cyclopentanol (CPOH), 1,4-pentanediol (1,4PDO), 1,5-pentanediol (1,5PDO), levulinic acid (LA),

$\gamma$ -valerolactone (GVL), 2-butanone (2BTNE) were used for GC calibration. For the other compounds, not commercially available, identified by mass spectrometry such as 2-(sec-butoxymethyl)furan (SBMF), 2-(dibutoxymethyl)furan (FDA), 2,5-bis(furan-2-methyl)furan (BFMF), 1,2-di-2-furyl-1,2-ethanediol (DFE), 2-(furan-2-methyl)-5-methylfuran (FMMF), 2,2-(1,2-ethenediyl)bis-furan (EBF), 5-hydroxy-2-pentanone (HPTE) and sec-butyl 4-oxopentanoate (SBOP), the Effective Carbon Number (ECN) concept was used for calibration. Details of the calibration can be seen in Annex A.

The conversion of furfural ( $X_{FF}$ ), product yield (Y), and carbon balance (CB) were calculated using Equations 3.2 - 3.4.

$$X_{FF} (\%) = \frac{[mmol FF]_0 - [mmol FF]_t}{[mmol FF]_0} \times 100 \quad \text{Equation 3.2}$$

$$Y (\%) = \frac{[mmol P]}{[mmol FF]_0} \times \frac{C_P}{C_{FF}} \quad \text{Equation 3.3}$$

$$CB (\%) = \left( \sum_{i=0}^n Y_i + \frac{[mmol FF]_t}{[mmol FF]_0} \right) \times 100 \quad \text{Equation 3.4}$$

where

0 corresponds to the beginning of the reaction and t at any time,

P is the product,

n is the total number of products,

C is the number of carbons in the product.

### 3.4 References

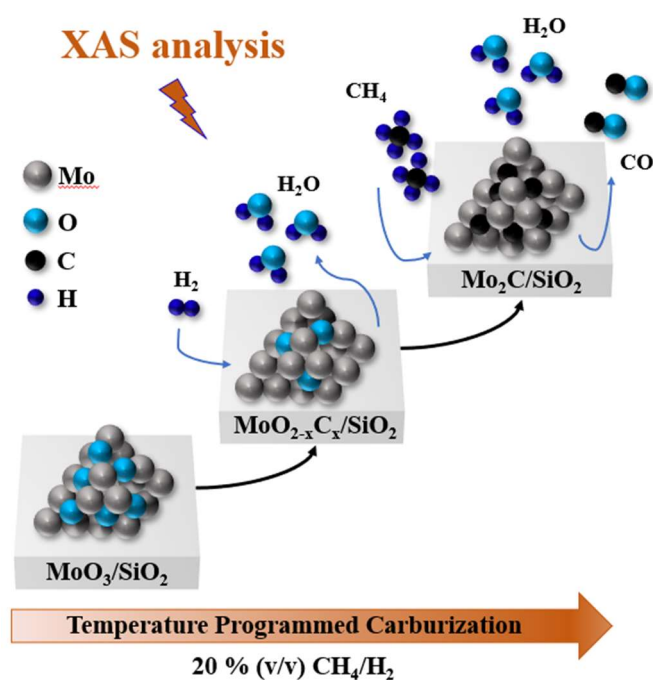
- Briois, V., La Fontaine, C., Belin, S., Barthe, L., Moreno, T., Pinty, V., Carcy, A., Girardot, R., Fonda, E., 2016. ROCK: the new Quick-EXAFS beamline at SOLEIL. *J. Phys.: Conf. Ser.* 712, 012149. <https://doi.org/10.1088/1742-6596/712/1/012149>
- Cassinelli, W.H., Martins, L., Passos, A.R., Pulcinelli, S.H., Santilli, C.V., Rochet, A., Briois, V., 2014. Multivariate curve resolution analysis applied to time-resolved synchrotron X-ray Absorption Spectroscopy monitoring of the activation of copper alumina catalyst. *Catalysis Today* 229, 114–122. <https://doi.org/10.1016/j.cattod.2013.10.077>
- Chen, M., Hao, W., Ma, R., Ma, X., Yang, L., Yan, F., Cui, K., Chen, H., Li, Y., 2017. Catalytic ethanolysis of Kraft lignin to small-molecular liquid products over an alumina supported molybdenum nitride catalyst. *Catalysis Today* 298, 9–15. <https://doi.org/10.1016/j.cattod.2017.08.012>
- Hong, J., Marceau, E., Khodakov, A.Y., Gaberová, L., Griboval-Constant, A., Girardon, J.-S., Fontaine, C.L., Briois, V., 2015. Speciation of Ruthenium as a Reduction Promoter of Silica-Supported Co Catalysts: A Time-Resolved in Situ XAS Investigation. *ACS Catal.* 5, 1273–1282. <https://doi.org/10.1021/cs501799p>
- Jaumot, J., de Juan, A., Tauler, R., 2015. MCR-ALS GUI 2.0: New features and applications. *Chemometrics and Intelligent Laboratory Systems* 140, 1–12. <https://doi.org/10.1016/j.chemolab.2014.10.003>
- La Fontaine, C., Barthe, L., Rochet, A., Briois, V., 2013. X-ray absorption spectroscopy and heterogeneous catalysis: Performances at the SOLEIL's SAMBA beamline. *Catalysis Today* 205, 148–158. <https://doi.org/10.1016/j.cattod.2012.09.032>
- Lesage, C., Devers, E., Legens, C., Fernandes, G., Roudenko, O., Briois, V., 2019. High pressure cell for edge jumping X-ray absorption spectroscopy: Applications to industrial liquid sulfidation of hydrotreatment catalysts. *Catalysis Today* 336, 63–73. <https://doi.org/10.1016/j.cattod.2019.01.081>

Newville, M., 2001. *IFEFFIT*: interactive XAFS analysis and *FEFF* fitting. *J Synchrotron Rad* 8, 322–324. <https://doi.org/10.1107/S0909049500016964>

Paul, S., Heyte, S., Katryniok, B., Garcia-Sancho, C., Maireles-Torres, P., Dumeignil, F., 2015. REALCAT: A New Platform to Bring Catalysis to the Lightspeed. *Oil Gas Sci. Technol. – Rev. IFP Energies nouvelles* 70, 455–462. <https://doi.org/10.2516/ogst/2014052>

Sousa, L.A., Zotin, J.L., Teixeira da Silva, V., 2012. Hydrotreatment of sunflower oil using supported molybdenum carbide. *Applied Catalysis A: General* 449, 105–111. <https://doi.org/10.1016/j.apcata.2012.09.030>

# CHAPTER 4. CHARACTERIZATION OF UNSUPPORTED AND SiO<sub>2</sub>-SUPPORTED Mo<sub>2</sub>C AND METAL-PROMOTED Mo CARBIDES BY *IN SITU* X-RAY ABSORPTION SPECTROSCOPY, TEMPERATURE-PROGRAMMED CARBURIZATION, AND X-RAY DIFFRACTION.



## Abstract

The synthesis of different Mo carbides, including an unsupported Mo<sub>2</sub>C and SiO<sub>2</sub>-supported carbide catalysts, promoted or not with Ni or Cu, under 20% (v/v) CH<sub>4</sub>/H<sub>2</sub>, was investigated by *in situ* X-ray spectroscopy (XAS) and temperature-programmed carburization (TPC). XAS experiments were performed to get more insight into the effect of the promoters during the synthesis of the Mo carbides. The results showed that the presence of a second metal promotes the first step of reduction, and it is related to the crystallinity of the mixed molybdates in the initial promoter species, but it does not assist the carburizing step.

## 4. INTRODUCTION

Temperature-programmed carburization (TPC) is the most widely used technique to synthesize transition metal carbides (TMC). In this methodology, a metal oxide is heated at a specific rate in a carburizing atmosphere containing CO or a hydrocarbon ( $\text{CH}_4$ ,  $\text{C}_2\text{H}_6$ ,  $\text{C}_3\text{H}_8$ ,  $\text{C}_4\text{H}_{10}$ ) used as a carbon source, co-fed or not with hydrogen (Pang *et al.*, 2019). In general, when a mixture of  $\text{CH}_4/\text{H}_2$  is used in the TPC, the synthesis is monitored by mass spectroscopy and the signals of water ( $m/z = 18$ ) and CO ( $m/z = 28$ ) related to the reduction of the metal oxide and formation of the carbide, respectively, are accompanied (Lee, 1987). The profiles obtained give an idea of the temperature ranges in which the transformations take place, but it is difficult to make inferences about the chemical changes of the species, especially in more complex systems such as for bimetallic carbides.

The use of bimetallic carbides is advantageous because they exhibit higher catalytic activity than monometallic carbides (Jung *et al.*, 2004b; Ma *et al.*, 2014c, 2014b; Zhang *et al.*, 2011; Zou *et al.*, 2016). In addition, the presence of a second metal (Pt, Pd, Ni, Co, Cu) added to  $\text{MoO}_3$  is reported to lower the first stage of reduction ( $\text{MoO}_3$  to  $\text{MoO}_2$  or an oxycarbide) by 100 - 250 °C during the carburization under a  $\text{CH}_4/\text{H}_2$  atmosphere, which is caused by the ability of the metals in activating hydrogen (Jung *et al.*, 2004b).

In this sense, X-ray absorption spectroscopy (XAS) is a powerful technique that allows the monitoring of the species formed during *in situ* carburization. To the best of your knowledge, XAS analysis has been used to investigate Ni-Mo/Cu-Mo bimetallic carbides only after their synthesis (Smirnov *et al.* 2019; Schaidle *et al.*, 2012) and not during carburization.

Taking this into account, the main goal of this chapter is to investigate the *in situ* carburization of monometallic and bimetallic  $\text{SiO}_2$ -supported Mo carbides promoted with Ni or Cu by XAS and correlate with the results of TPC.

## 4.1 Results and discussions

### 4.1.1 Characterization

The formation of the supported phases was followed by *in situ* XAS, carried out at Mo, Ni, and Cu K-edges, with further input from Raman spectra recorded on the initial calcined samples.

The XAS data at the Mo K-edge related to the calcined precursors of Mo<sub>2</sub>C/SiO<sub>2</sub>, Ni-Mo<sub>x</sub>C<sub>y</sub>/SiO<sub>2</sub>, and Cu-Mo<sub>x</sub>C<sub>y</sub>/SiO<sub>2</sub> are presented in Figures 4.1 - 4.3. The shape of the XANES spectra and position in energy are similar to those of the MoO<sub>3</sub> standard, especially for Mo<sub>2</sub>C/SiO<sub>2</sub> (Figure 4.1). For the two promoted catalysts, the only significant difference is the increase of intensity of the second feature after the edge, at 20040 eV, also well visible on a spectrum reported in the literature for  $\gamma$ -CuMoO<sub>4</sub> (Jonane *et al.*, 2018).

Raman spectroscopy confirms that MoO<sub>3</sub> is present in the three samples, (bands at 994, 819, and 665 cm<sup>-1</sup> (Mo *et al.*, 2016b), Figure 4.4), in a well-crystallized form for the precursors of Mo<sub>2</sub>C/SiO<sub>2</sub> and Ni-Mo<sub>x</sub>C<sub>y</sub>/SiO<sub>2</sub>, in a more poorly organized form for the precursor of Cu-Mo<sub>x</sub>C<sub>y</sub>/SiO<sub>2</sub>, as evidenced by the low intensity of these bands. Raman spectroscopy also reveals the existence of a second phase on the oxide precursor of Ni-Mo<sub>x</sub>C<sub>y</sub>/SiO<sub>2</sub>. The weak but well-defined band at 961 cm<sup>-1</sup> is unambiguously assigned to  $\alpha$ -NiMoO<sub>4</sub> (Abdel-Dayem, 2007; Ehrenberg *et al.*, 1995), a mixed oxide in which octahedral groups of [NiO<sub>6</sub>] and [MoO<sub>6</sub>] alternate. Some weak bands are also visible for the precursor of Cu-Mo<sub>x</sub>C<sub>y</sub>/SiO<sub>2</sub>. The band at 960 cm<sup>-1</sup> may be attributed to CuMoO<sub>4</sub> (Joseph *et al.*, 2016; Tan and Luan, 2020), but the broad band at 930 cm<sup>-1</sup>, which is expected to be thin and poorly intense for crystalline CuMoO<sub>4</sub> (Joseph *et al.*, 2016; Tan and Luan, 2020), can rather arise from molybdates with a higher degree of condensation of the molybdate units, such as in Cu<sub>3</sub>Mo<sub>2</sub>O<sub>9</sub> (Saravanakumar *et al.*, 2019).

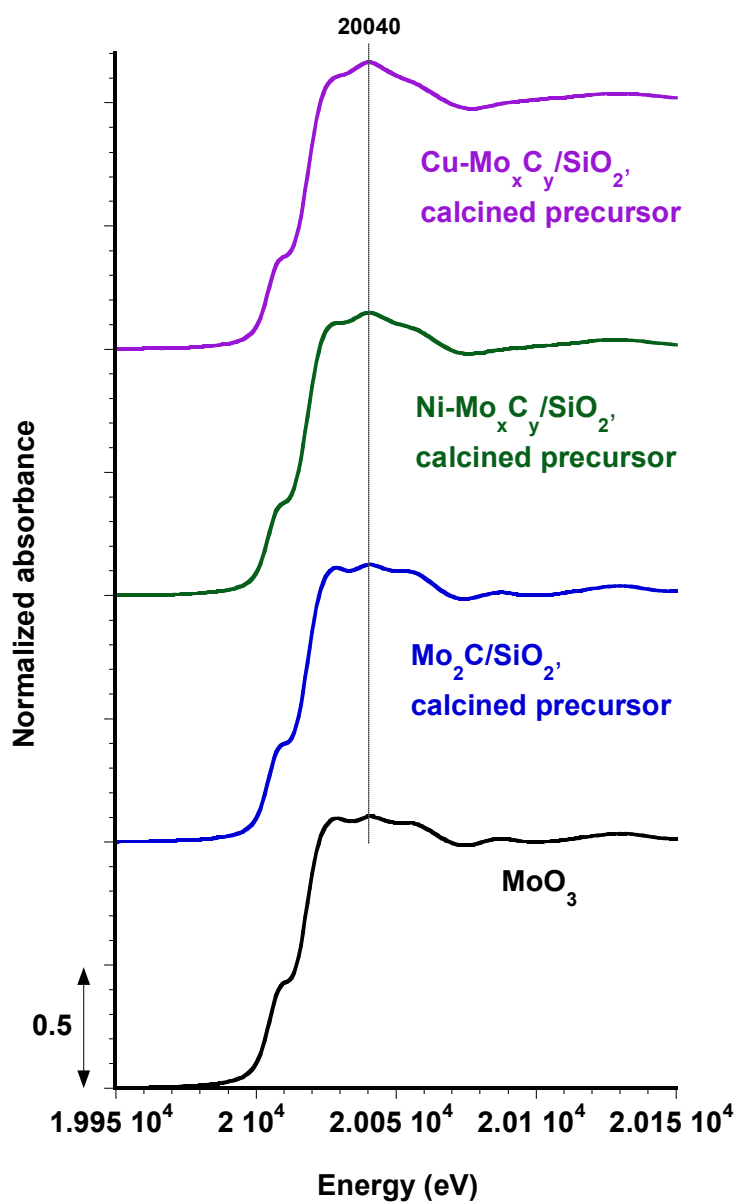
X-ray diffraction (Figure 4.5) done in ambient conditions accordingly confirms the presence of MoO<sub>3</sub> (JCPDS 05-0508) for all materials, while NiMoO<sub>4</sub>



(JCPDS 45-0142) and  $\text{CuMoO}_4$  (JCPDS 22-0242) and  $\text{Cu}_3\text{Mo}_2\text{O}_9$  (JCPDS 34-0637) phases were observed for the calcined precursors of  $\text{Ni-Mo}_x\text{C}_y/\text{SiO}_2$  and  $\text{Cu-Mo}_x\text{C}_y/\text{SiO}_2$ , respectively. However, the diffractogram of the latter also presented other diffraction lines that could not be identified.

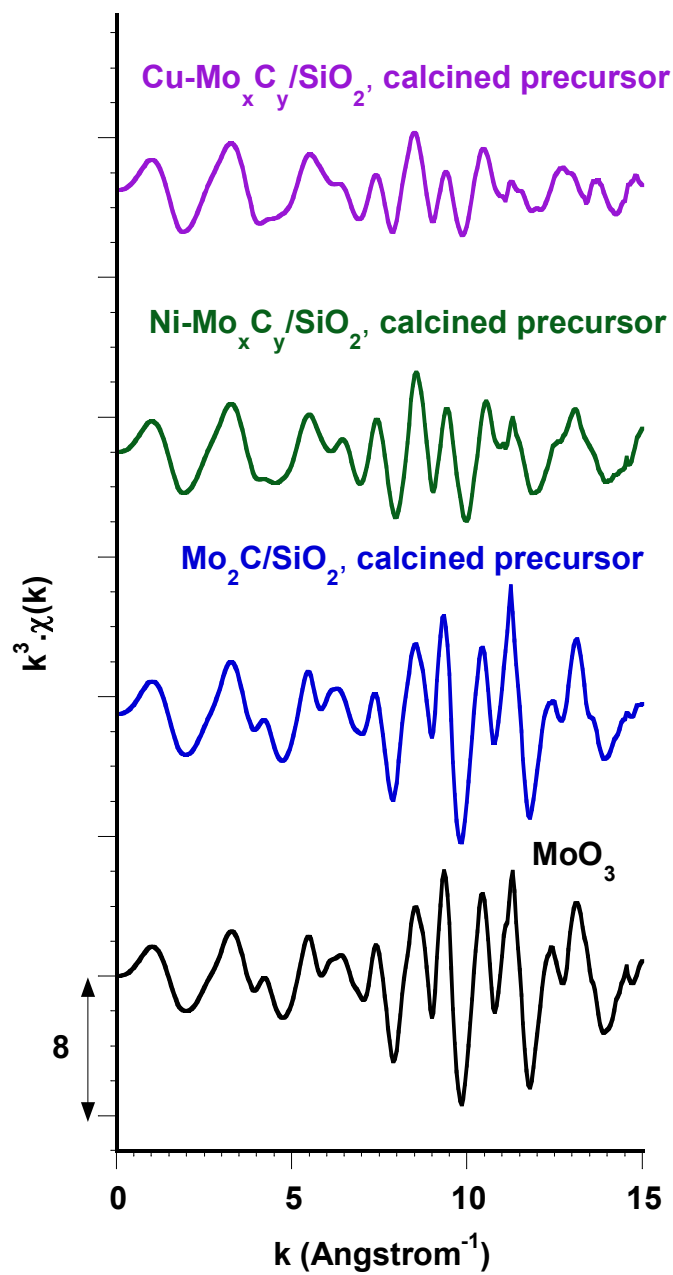
The feature at 20040 eV (Figure 4.1), the differences in the structure of the EXAFS oscillations (Figure 4.2), and the differences in the shape of the peaks on the associated Fourier transforms for the promoted systems (Figure 4.3) are thus linked to the presence of a mixture of  $\text{MoO}_3$  and Ni/Cu molybdates, more crystallized in the case of  $\text{Ni-Mo}_x\text{C}_y/\text{SiO}_2$ , and less for  $\text{Cu-Mo}_x\text{C}_y/\text{SiO}_2$ . Due to the complexity of the typical oxidic environment of Mo(VI) ions (several different Mo-O distances ranging between 1.6 and 2.2 Å) and the existence of mixtures in the bimetallic systems, it was not attempted to perform EXAFS fits for the calcined precursors at the Mo K-edge.

Figure 4.1. XANES spectra recorded at the Mo K-edge for the calcined precursors. Comparison with reference MoO<sub>3</sub>.



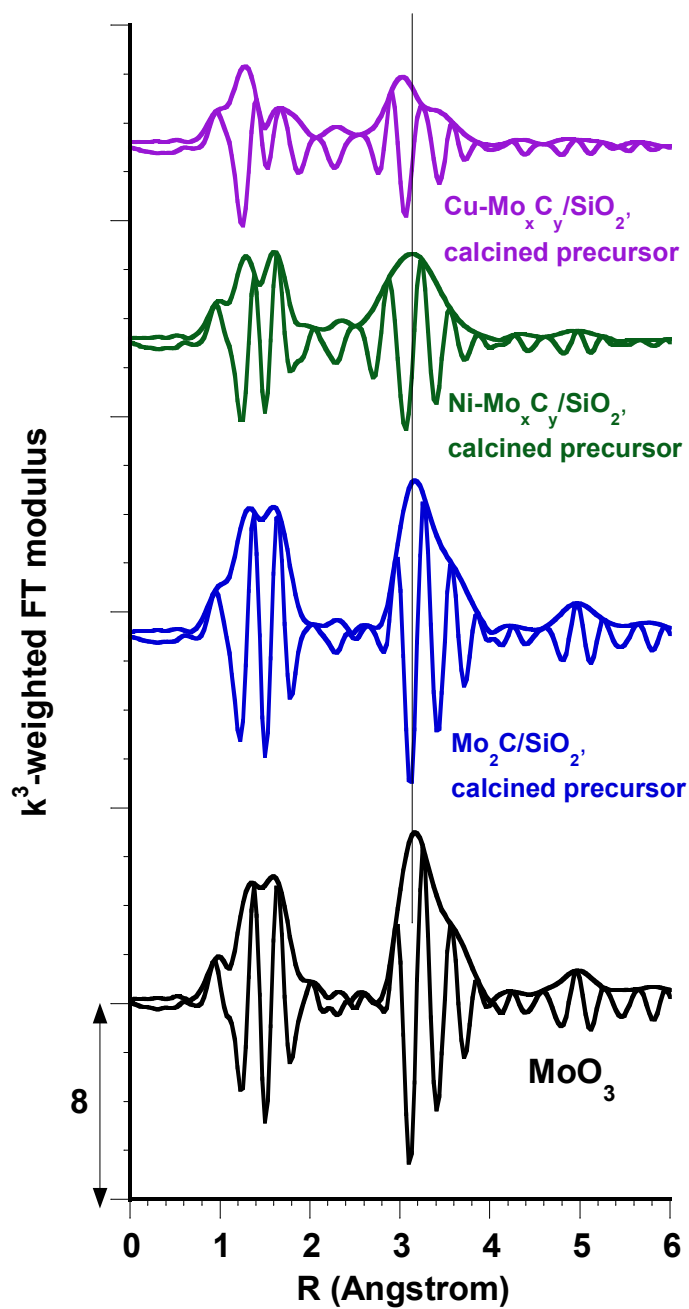
Reference: own author (2023)

Figure 4.2. EXAFS signals recorded at the Mo K-edge for the calcined precursors. Comparison with reference MoO<sub>3</sub>.



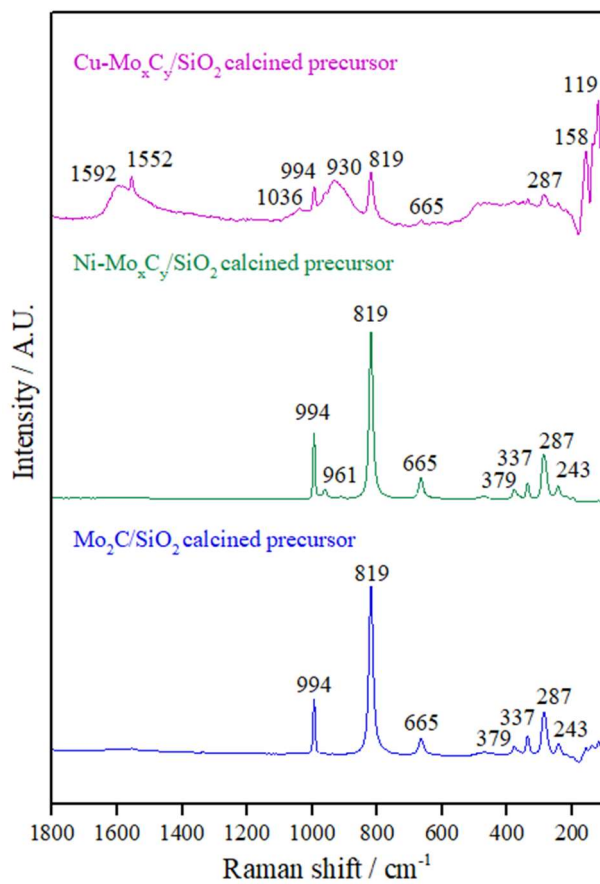
Reference: own author (2023)

Figure 4.3. Fourier transforms of the EXAFS signals recorded at the Mo K-edge for the calcined precursors ( $k = 3.5 - 15 \text{ \AA}^{-1}$ ). Comparison with reference  $\text{MoO}_3$ .



Reference: own author (2023)

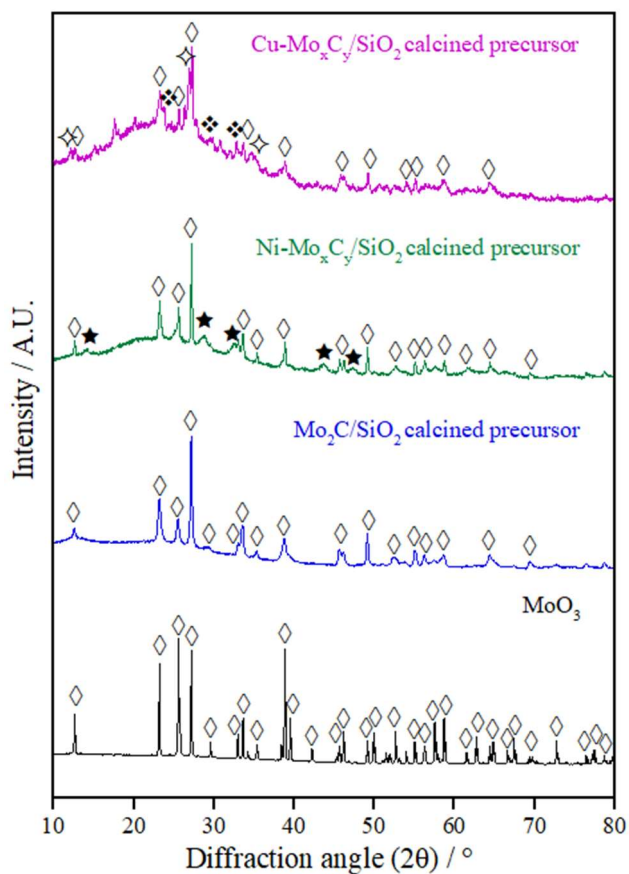
Figure 4.4. Raman spectra for the calcined precursors of Cu-Mo<sub>x</sub>C<sub>y</sub>/SiO<sub>2</sub>, Ni-Mo<sub>x</sub>C<sub>y</sub>/SiO<sub>2</sub>, and Mo<sub>2</sub>C/SiO<sub>2</sub> (recorded at room temperature).



Reference: own author (2023)

Figure 4.5. Diffractograms of the calcined precursors of unsupported and SiO<sub>2</sub>-supported Mo carbides.

◇ MoO<sub>3</sub>, ★ NiMoO<sub>4</sub>, ❖ CuMoO<sub>4</sub>, ◇ Cu<sub>3</sub>Mo<sub>2</sub>O<sub>9</sub>.

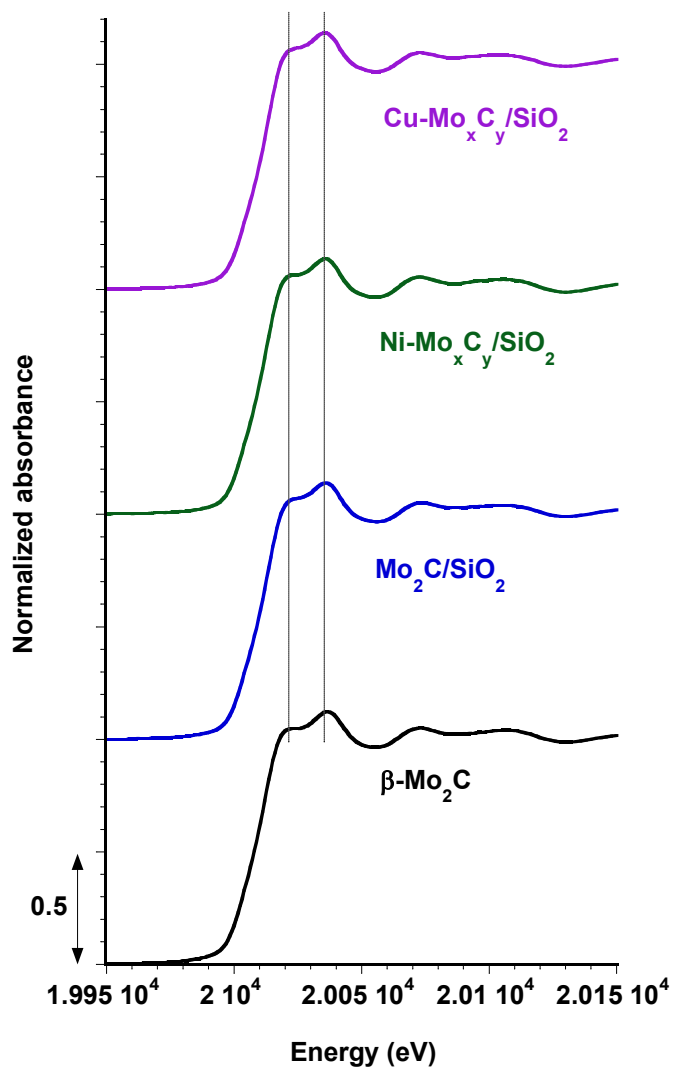


Reference: own author (2023)

Before analyzing the carburization process up to 650 °C, the state of Mo after carburization will be investigated here. The XAS analysis was performed on spectra recorded after cooling to room temperature (RT), still under a CH<sub>4</sub>/H<sub>2</sub> atmosphere.

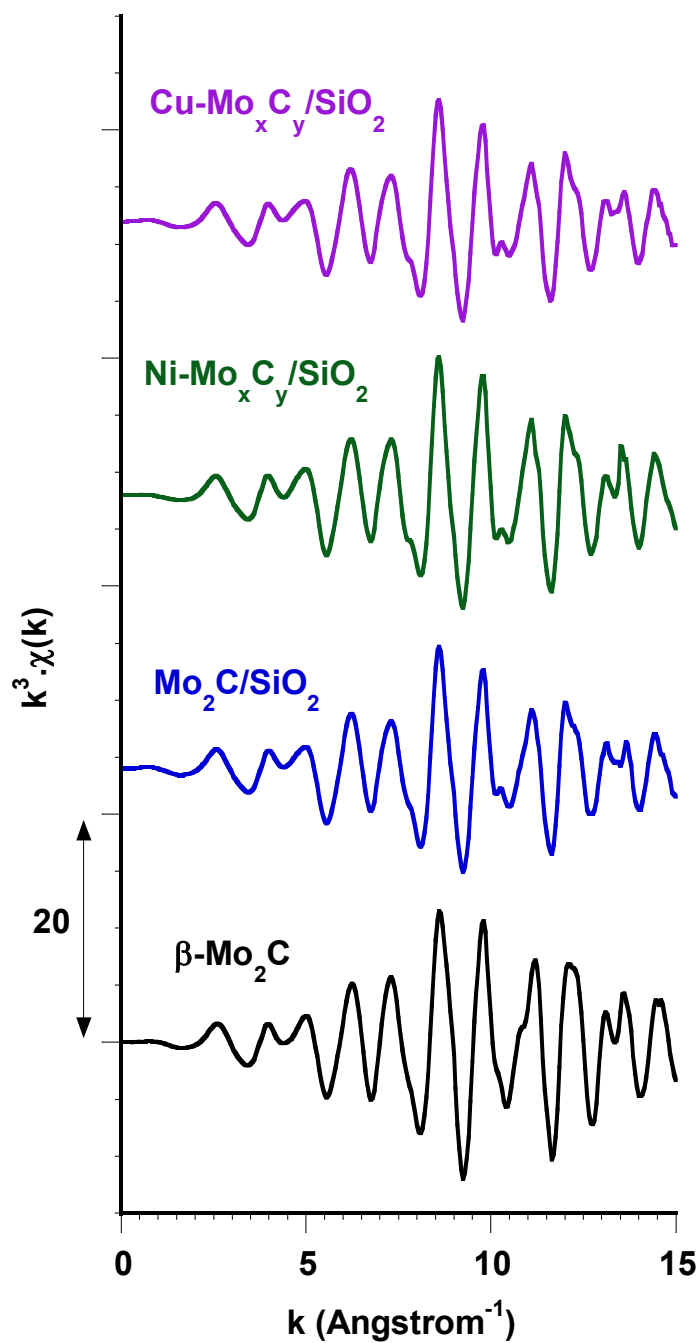
After carburization, the XANES spectra, EXAFS oscillations and Fourier transforms of Mo<sub>2</sub>C/SiO<sub>2</sub>, Ni-Mo<sub>x</sub>C<sub>y</sub>/SiO<sub>2</sub>, and Cu-Mo<sub>x</sub>C<sub>y</sub>/SiO<sub>2</sub> are very similar, and resemble that of reference bulk β-Mo<sub>2</sub>C (an unsupported sample whose structure was identified by XRD after passivation, and that was reactivated under H<sub>2</sub> at 400 °C before recording the XAS spectrum) (Figures 4.6 - 4.8).

Figure 4.6. XANES spectra recorded at the Mo K-edge for the carburized catalysts (spectra recorded at room temperature). Comparison with reference  $\beta$ -Mo<sub>2</sub>C.



Reference: own author (2023)

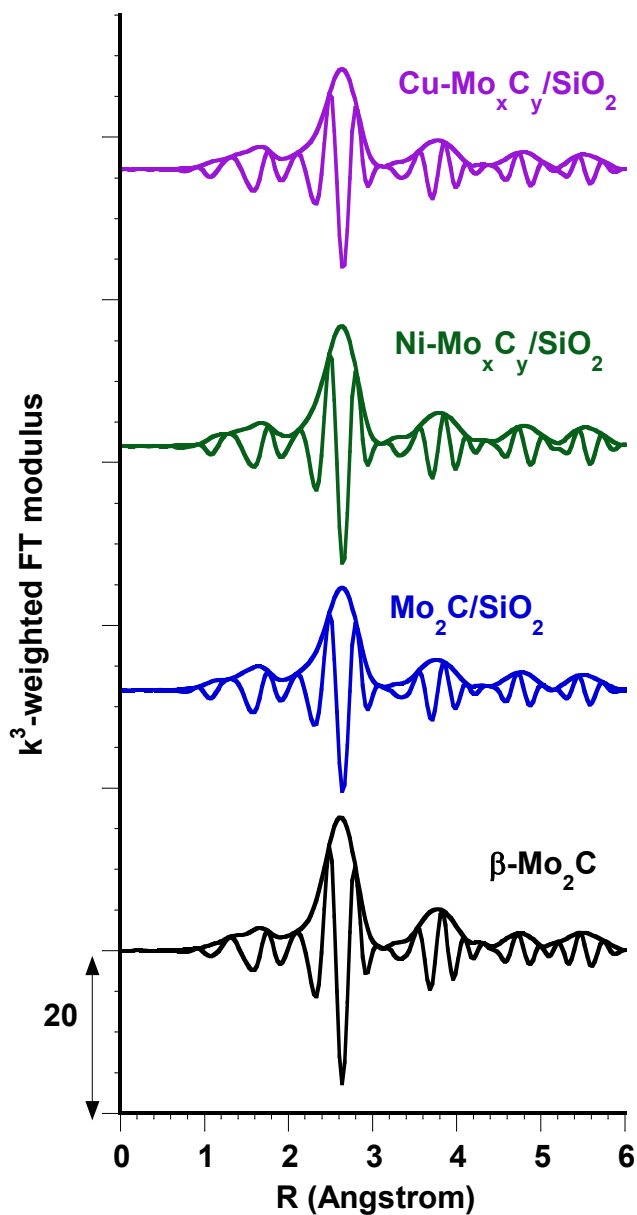
Figure 4.7. EXAFS signals recorded at the Mo K-edge for the carburized catalysts (spectra recorded at room temperature). Comparison with reference  $\beta$ -Mo<sub>2</sub>C.



Reference: own author (2023)



Figure 4.8. Fourier transforms of the EXAFS signals recorded at the Mo K-edge for the carburized catalysts (spectra recorded at room temperature,  $k = 3.5 - 15 \text{ \AA}^{-1}$ ). Comparison with reference  $\beta\text{-Mo}_2\text{C}$ .



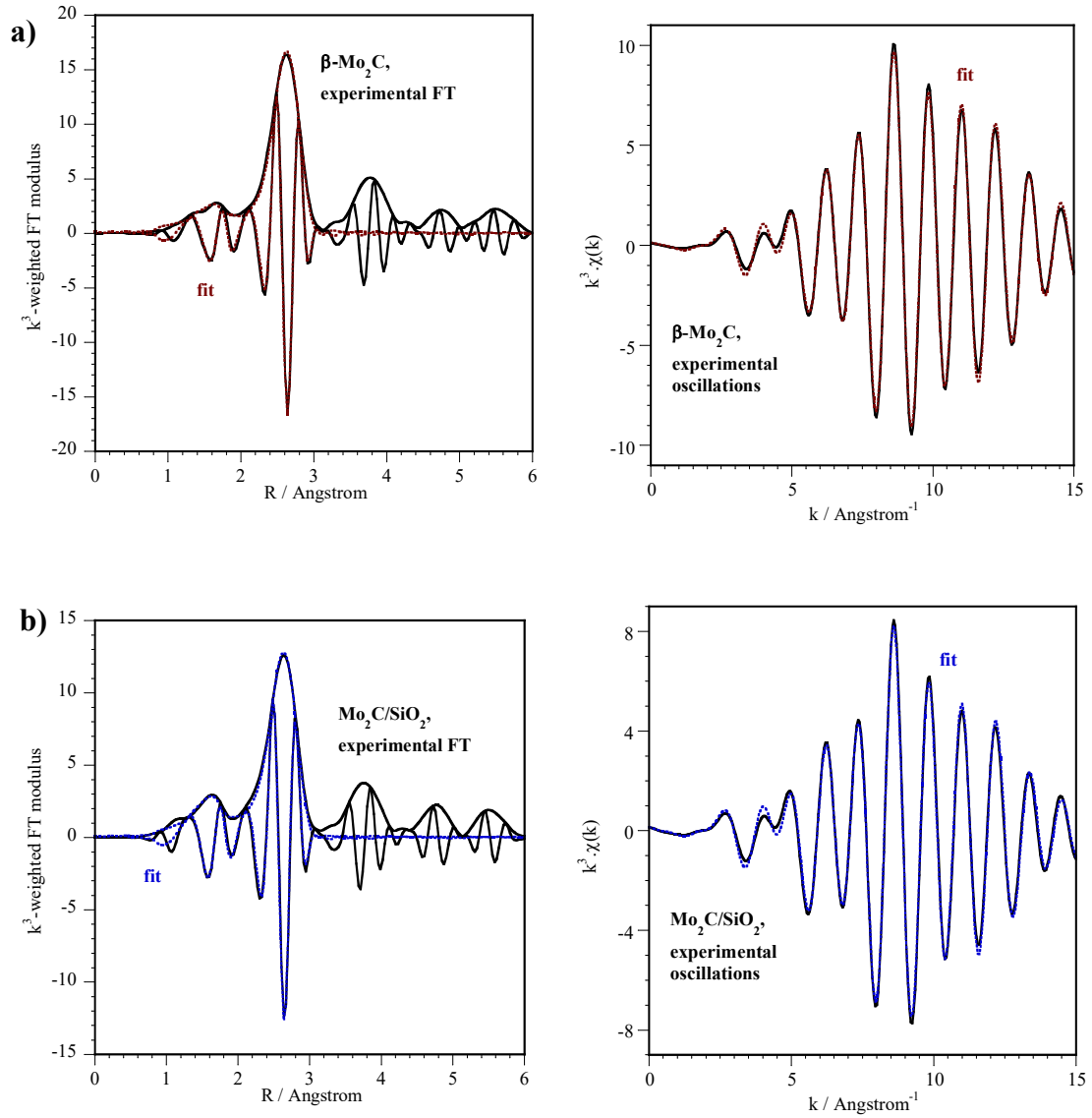
Reference: own author (2023)

The results of the fits for the first two shells of neighbors (C and Mo atoms) are presented in Figures 4.9 and 4.10, and Table 4.1. They are consistent with the formation of Mo carbides. Given the limited number of independent parameters allowed for the fit, it was chosen to fit each shell with a single contribution of C and Mo. This does not preclude the existence of several interatomic Mo-C or Mo-Mo distances in the structure

of the carbide, and the distribution of Mo-C distances can explain the larger error bar for the Debye-Waller parameter obtained by fitting the C shell. It can be added that the possible presence of O atoms in the first shell was always rejected by the fits.

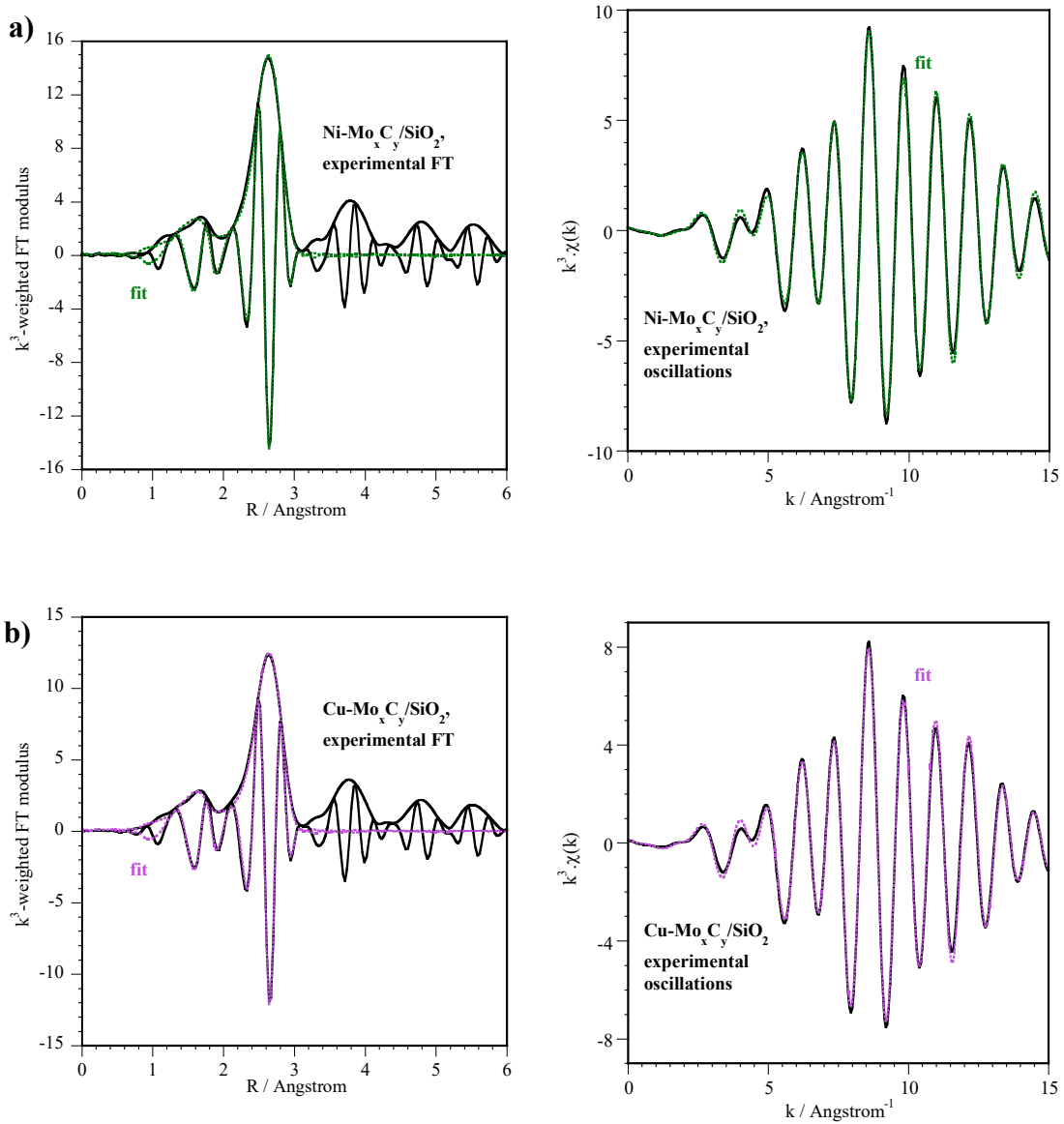
The number of C atoms around Mo is found to be larger in the supported systems than in unsupported  $\beta$ -Mo<sub>2</sub>C. However, it must be remembered that the number of neighboring atoms (N) and the Debye-Waller parameter ( $\sigma^2$ ) are correlated, and here increase concomitantly. The increase of N(C) can thus be interpreted either as the sign of a C enrichment around Mo in the carbide or as an over-estimation of N by the fit, compensating for a high value of  $\sigma^2$ . A second feature that would allow favoring the hypothesis of a carbon enrichment on the supported systems is linked to the Mo-C and Mo-Mo average interatomic distances, longer by 0.012 to 0.020 Å than those found for the  $\beta$ -Mo<sub>2</sub>C standard.

Figure 4.9. XAS data at the Mo K-edge after carburization of a)  $\beta$ -Mo<sub>2</sub>C after reactivation in H<sub>2</sub> at 400 °C, and b) Mo<sub>2</sub>C/SiO<sub>2</sub> (spectra recorded at room temperature). Fit of the first and second shells of neighbors: Fourier transform (left) and EXAFS oscillations (right).  $k = 3.5 - 15 \text{ \AA}^{-1}$ .



Reference: own author (2023)

Figure 4.10. XAS data at the Mo K-edge after carburization of a) Ni-Mo<sub>x</sub>C<sub>y</sub>/SiO<sub>2</sub> and b) Cu-Mo<sub>x</sub>C<sub>y</sub>/SiO<sub>2</sub> (spectra recorded at room temperature). Fit of the first and second shells of neighbors: Fourier transform (left) and EXAFS oscillations (right).  $k = 3.5 - 15 \text{ \AA}^{-1}$ .



Reference: own author (2023)

Table 4.1. Fitted parameters at the Mo K-edge ( $E_0 = 20013$  eV,  $S02 = 0.98$ ) determined from the EXAFS analysis of spectra recorded at room temperature on carburized catalysts.  $k = 3.5 - 15 \text{ \AA}^{-1}$ . Fit of the first peaks from the Fourier transform between 1 and 3  $\text{\AA}$ .

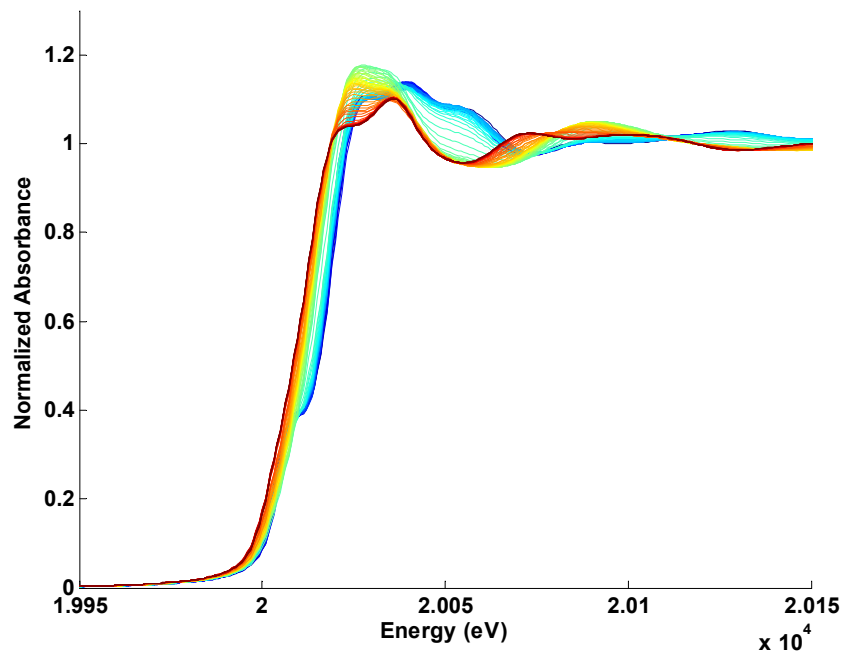
Catalyst	Backscatter	N	$\sigma^2 (\text{\AA}^2) \times 10^3$	R ( $\text{\AA}$ )
$\beta\text{-Mo}_2\text{C}^a$	C	$2.7 \pm 0.9$	$4.1 \pm 0.3$	$2.08 \pm 0.02$
	Mo	$7.3 \pm 0.8$	$5.7 \pm 0.5$	$2.966 \pm 0.005$
	$\Delta E_0 = -5.5$ eV, r-factor = 0.01575, $\chi^2 = 592$ , $N_{\text{ind}} = 13$ , $N_{\text{var}} = 7$			
$\beta\text{-Mo}_2\text{C}/\text{SiO}_2$	C	$3.5 \pm 0.9$	$6 \pm 2$	$2.10 \pm 0.01$
	Mo	$7.3 \pm 0.8$	$7.3 \pm 0.6$	$2.978 \pm 0.005$
	$\Delta E_0 = -3.8$ eV, r-factor = 0.01462, $\chi^2 = 441$ , $N_{\text{ind}} = 13$ , $N_{\text{var}} = 7$			
$\text{Ni-Mo}_x\text{C}_y/\text{SiO}_2$	C	$4 \pm 1$	$6 \pm 2$	$2.10 \pm 0.01$
	Mo	$7.5 \pm 0.8$	$6.7 \pm 0.5$	$2.979 \pm 0.004$
	$\Delta E_0 = -4.5$ eV, r-factor = 0.01232, $\chi^2 = 301$ , $N_{\text{ind}} = 13$ , $N_{\text{var}} = 7$			
$\text{Cu-Mo}_x\text{C}_y/\text{SiO}_2$	C	$3.5 \pm 0.9$	$6 \pm 2$	$2.10 \pm 0.01$
	Mo	$7.1 \pm 0.8$	$7.2 \pm 0.6$	$2.981 \pm 0.005$
	$\Delta E_0 = -4.2$ eV, r-factor = 0.01481, $\chi^2 = 425$ , $N_{\text{ind}} = 13$ , $N_{\text{var}} = 7$			

<sup>a</sup> (after reactivation in  $\text{H}_2$  at 400  $^\circ\text{C}$ )

Reference: own author (2023)

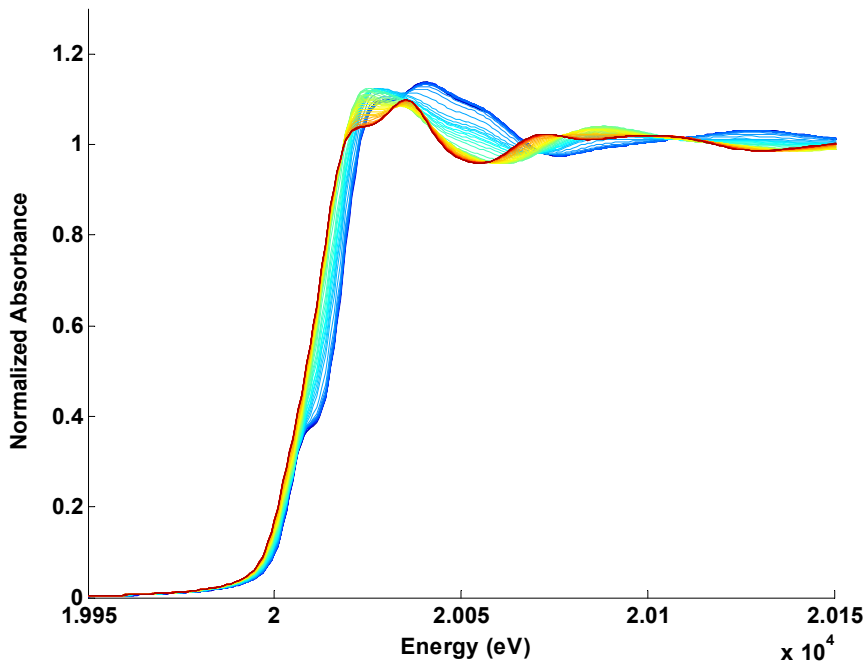
The evolution of the XAS spectra at the Mo K-edge during carburization is presented in Figures 4.11 - 4.13. The color gradient from blue to red is related to the increase in temperature, from 30 to 650  $^\circ\text{C}$ . It is seen that molybdenum is transformed almost continuously during the temperature ramp under  $\text{CH}_4/\text{H}_2$ , till the Mo carbide is ultimately formed. Qualitatively speaking, one can observe that the first strong shift of the spectra to lower energies (first stage of Mo reduction), along with the appearance of a poorly intense white line at 20020 eV, occurs in a lower temperature range for  $\text{Cu-Mo}_x\text{C}_y/\text{SiO}_2$  (light blue color) than for  $\text{Mo}_2\text{C}/\text{SiO}_2$  and  $\text{Ni-Mo}_x\text{C}_y/\text{SiO}_2$  (green color).

Figure 4.11. Evolution of the XAS spectra of Mo<sub>2</sub>C/SiO<sub>2</sub> at the Mo K-edge upon carburization (from room temperature, dark blue, to 650 °C, red). For the sake of clarity, every 8<sup>th</sup> spectrum is shown only.



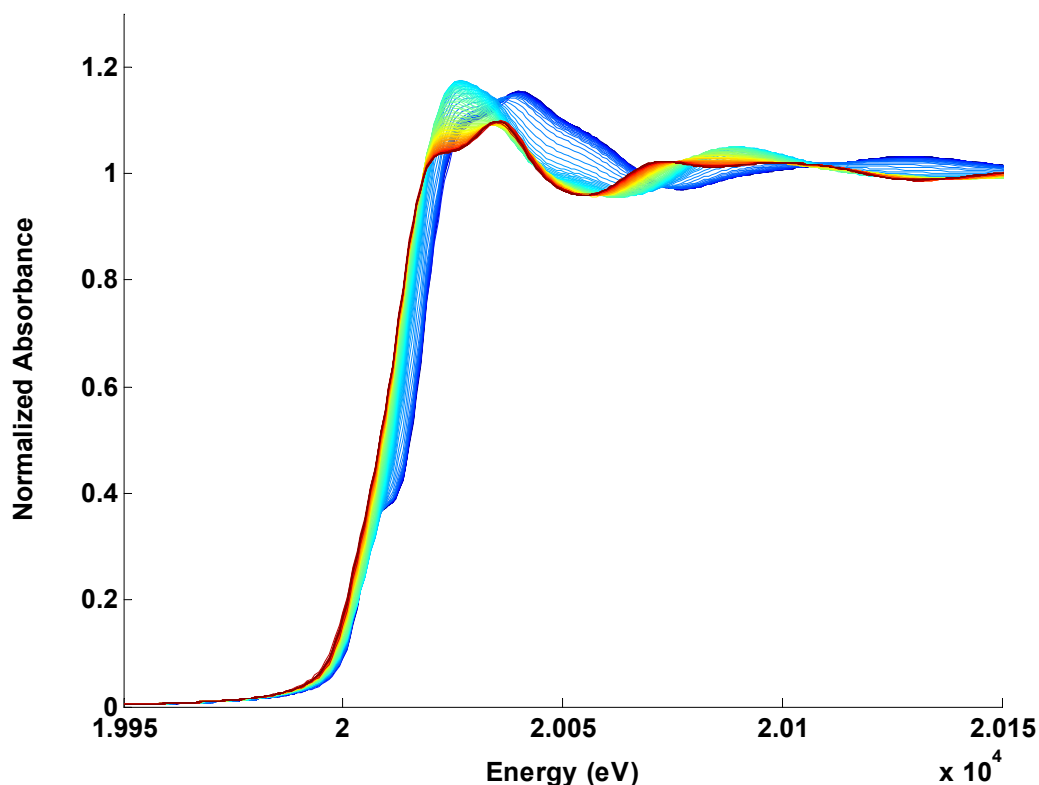
Reference: own author (2023)

Figure 4.12. Evolution of the XAS spectra of Ni-Mo<sub>x</sub>C<sub>y</sub>/SiO<sub>2</sub> at the Mo K-edge upon carburization (from room temperature, dark blue, to 650 °C, red). For the sake of clarity, every 2<sup>nd</sup> spectrum is shown only.



Reference: own author (2023)

Figure 4.13. Evolution of the XAS spectra of Cu-Mo<sub>x</sub>C<sub>y</sub>/SiO<sub>2</sub> at the Mo K-edge upon carburization (from room temperature, dark blue, to 650 °C, red). For the sake of clarity, every 2<sup>nd</sup> spectrum is shown only.



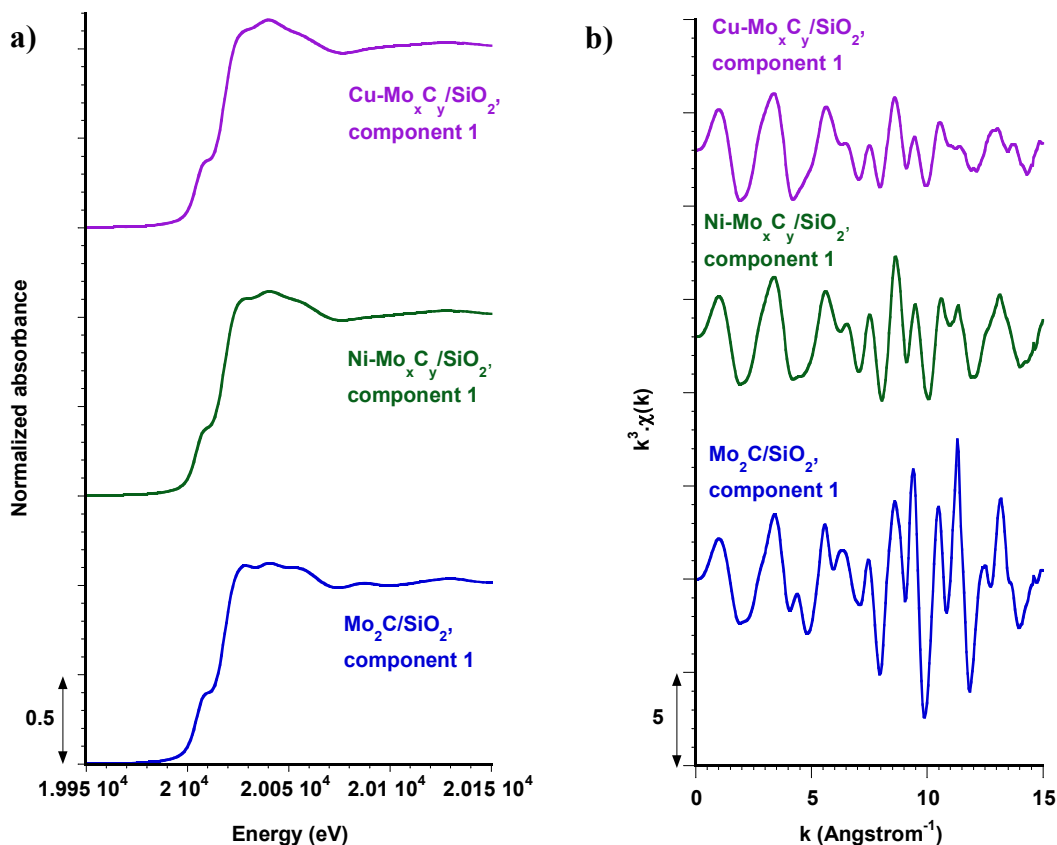
Reference: own author (2023)

An analysis of the evolution of Mo speciation was carried out using an MCR-ALS procedure. Each experimental spectrum in the series is considered to be a linear combination of a set of independent, successive spectral components, and the MCR-ALS algorithm extracts both the matrix of spectral components and a matrix of associated “concentrations” evolving with the rising temperature. The spectral components are analyzed using the XAS toolbox, to identify the chemical species (if the spectral component is characteristic of a known species), or, as will also be the case here, to obtain spectroscopic or structural footprints of the successive species involved in the carburization process (if the spectral component cannot be associated with a recognizable chemical species, or corresponds to a mixture).

The MCR-ALS procedure could evidence four distinct spectral components in each of the three carburization processes. The first of them corresponds to the spectrum of the initial, calcined precursor (Figure 4.14), representing MoO<sub>3</sub> for Mo<sub>2</sub>C/SiO<sub>2</sub>, and a

mixture of  $\text{MoO}_3$  and Ni/Cu-Mo(VI) molybdates for Ni- $\text{Mo}_x\text{C}_y/\text{SiO}_2$  and Cu- $\text{Mo}_x\text{C}_y/\text{SiO}_2$ . This component will be denoted as representing “Mo(VI) oxides” collectively.

Figure 4.14. MCR-ALS analysis at the Mo-K edge of the carburization ramp: characteristics of the first spectral components. a) XANES spectra, b) EXAFS oscillations.



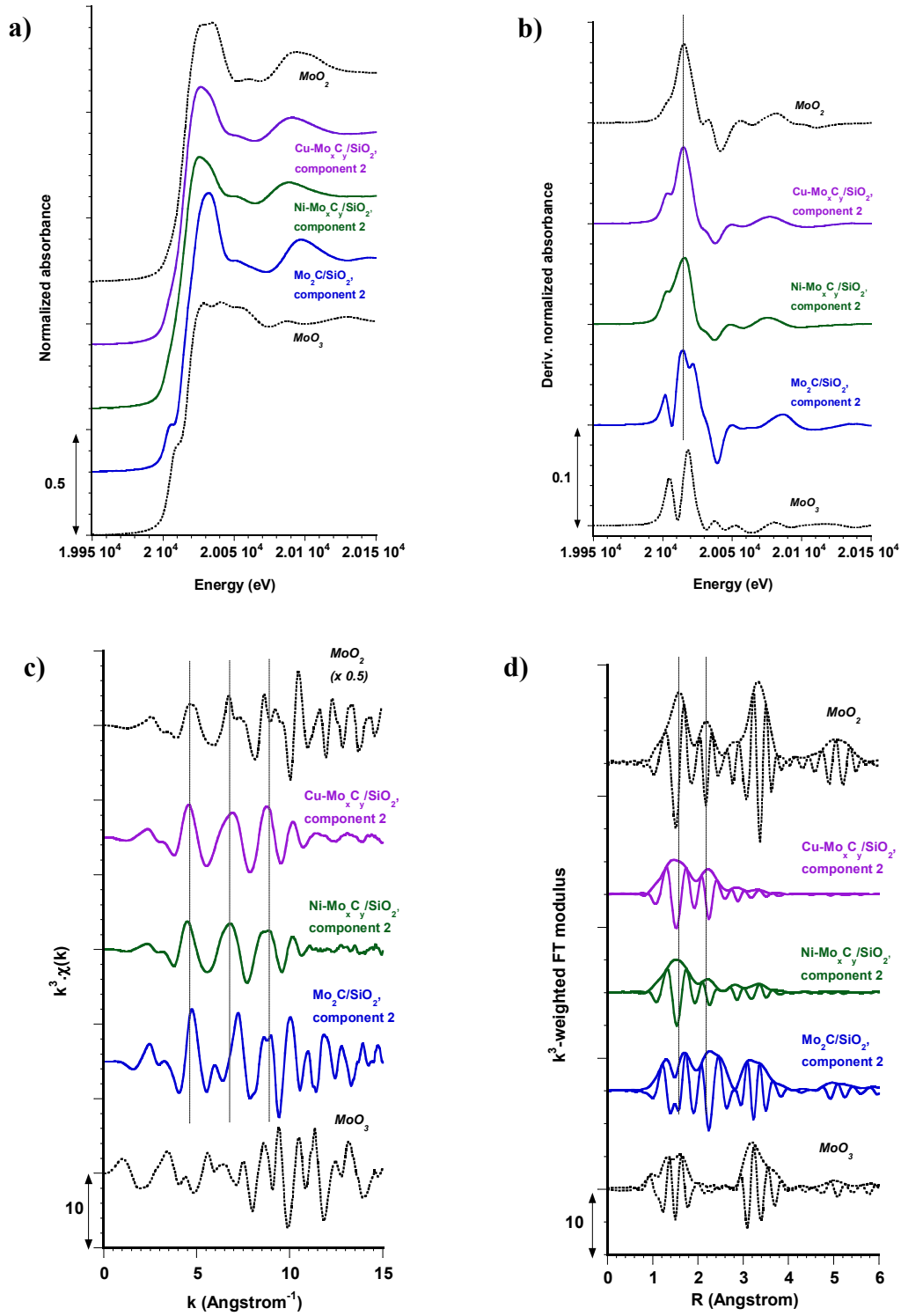
Reference: own author (2023)

For the three samples, the second spectral component () is characterized by a significant shift of the edge toward lower energies compared with  $\text{MoO}_3$ , implying a decrease in the average oxidation state of Mo. This shift can be better observed when plotting the derivative of the absorbance as a function of the energy (b). However, the spectral components for the promoted systems differ from that extracted for  $\text{Mo}_2\text{C}/\text{SiO}_2$ . The latter still presents a pre-edge (a), as is also seen on the spectrum reported in the literature for  $\text{Mo}_4\text{O}_{11}$ , an oxide in which two Mo atoms have been reduced to Mo(V)



(Ressler *et al.*, 2000). The presence of two maxima in the derivative (b), close to those of the MoO<sub>3</sub> and MoO<sub>2</sub> standards, suggests the presence of several oxidation states in the oxide. In contrast, the derivatives calculated for Ni-Mo<sub>x</sub>C<sub>y</sub>/SiO<sub>2</sub> and Cu-Mo<sub>x</sub>C<sub>y</sub>/SiO<sub>2</sub> resemble more that of Mo(IV)-containing MoO<sub>2</sub>, in line with the position of the first three EXAFS oscillations (c), and with the position of the peaks on the Fourier transform (d). The second spectral component thus reflects the formation of Mo suboxides (average oxidation state comprised between Mo(IV) and Mo(V) formed by reduction of Mo(VI)).

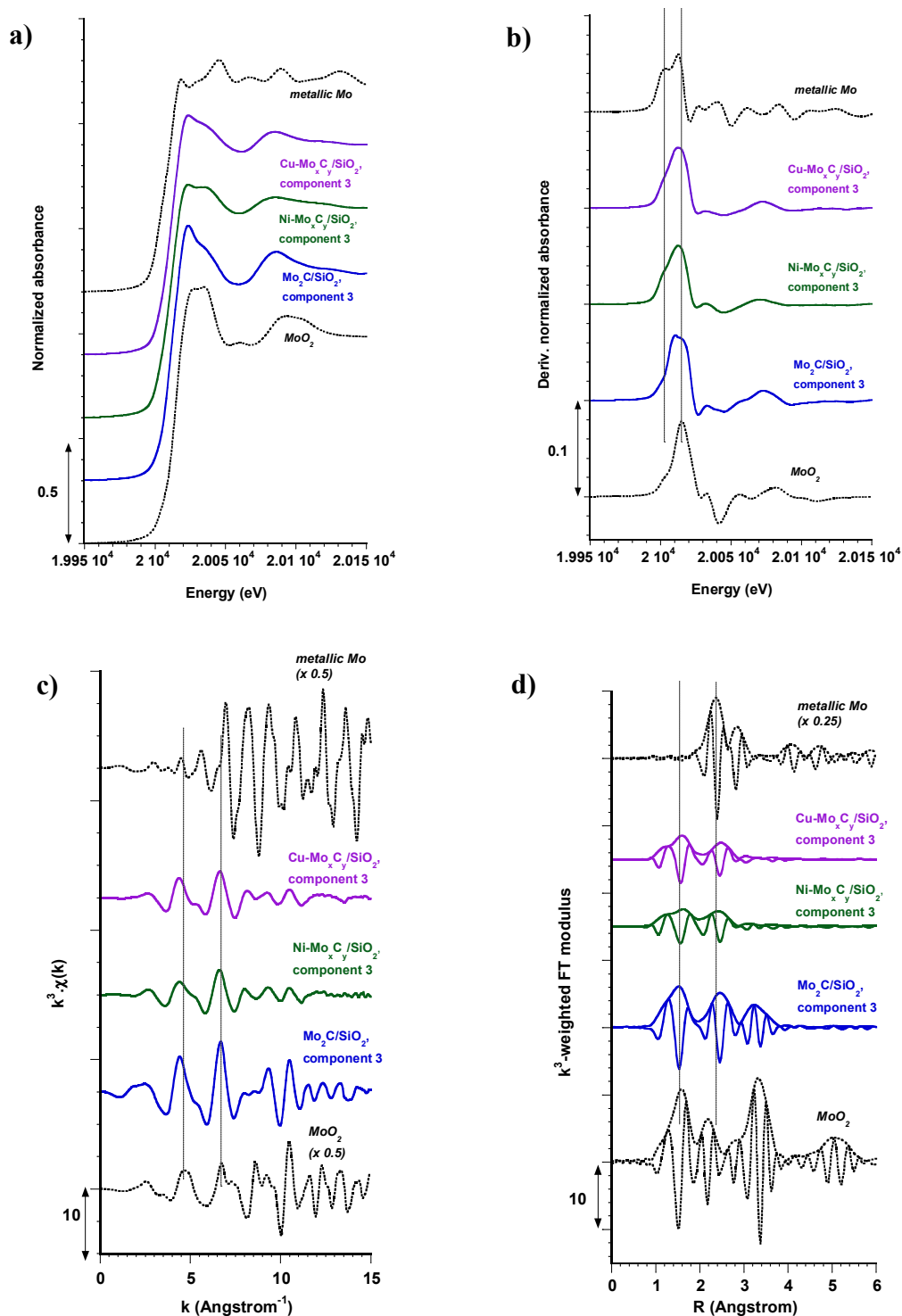
Figure 4.15. MCR-ALS analysis at the Mo-K edge of the carburization ramp: characteristics of the second components. a) XANES spectra and b) derivatives, c) EXAFS oscillations, d) Fourier transforms ( $k = 3.5 - 15 \text{ \AA}^{-1}$ ). Comparison with references  $\text{MoO}_3$  and  $\text{MoO}_2$ .



Reference: own author (2023)

The third spectral components (Figure 4.16) share two common characteristics: the shape of the XANES spectrum, displaying on the white line a first feature more intense than the second one, similar to the spectra recently assigned to a Mo oxycarbide intermediate (Kurlov *et al.*, 2020; Zheng *et al.*, 2019) (Figure 4.16a); and a further decrease of the average oxidation state of Mo, with one maximum of the derivative of the XANES spectrum remaining close to that of MoO<sub>2</sub>, and a shoulder at lower energy close to that of metallic Mo (Figure 4.16b). This composite aspect is also found in the examination of the EXAFS oscillations. The position of the first oscillations roughly corresponds to those found for MoO<sub>2</sub>, but the next ones are different (Figure 4.16c). Finally, if the first peak in the Fourier transform is found at the position expected for a O shell, like in MoO<sub>2</sub>, the second peak does not correspond to the Mo shell from MoO<sub>2</sub> and is located at a slightly larger distance than the first peak of Mo neighbors in metallic Mo (Figure 4.16d).

Figure 4.16. MCR-ALS analysis at the Mo-K edge of the carburization ramp: characteristics of the third components. a) XANES spectra and b) derivatives, c) EXAFS oscillations, d) Fourier transforms ( $k = 3.5 - 15 \text{ \AA}^{-1}$ ). Comparison with references  $\text{MoO}_2$  and Mo foil.



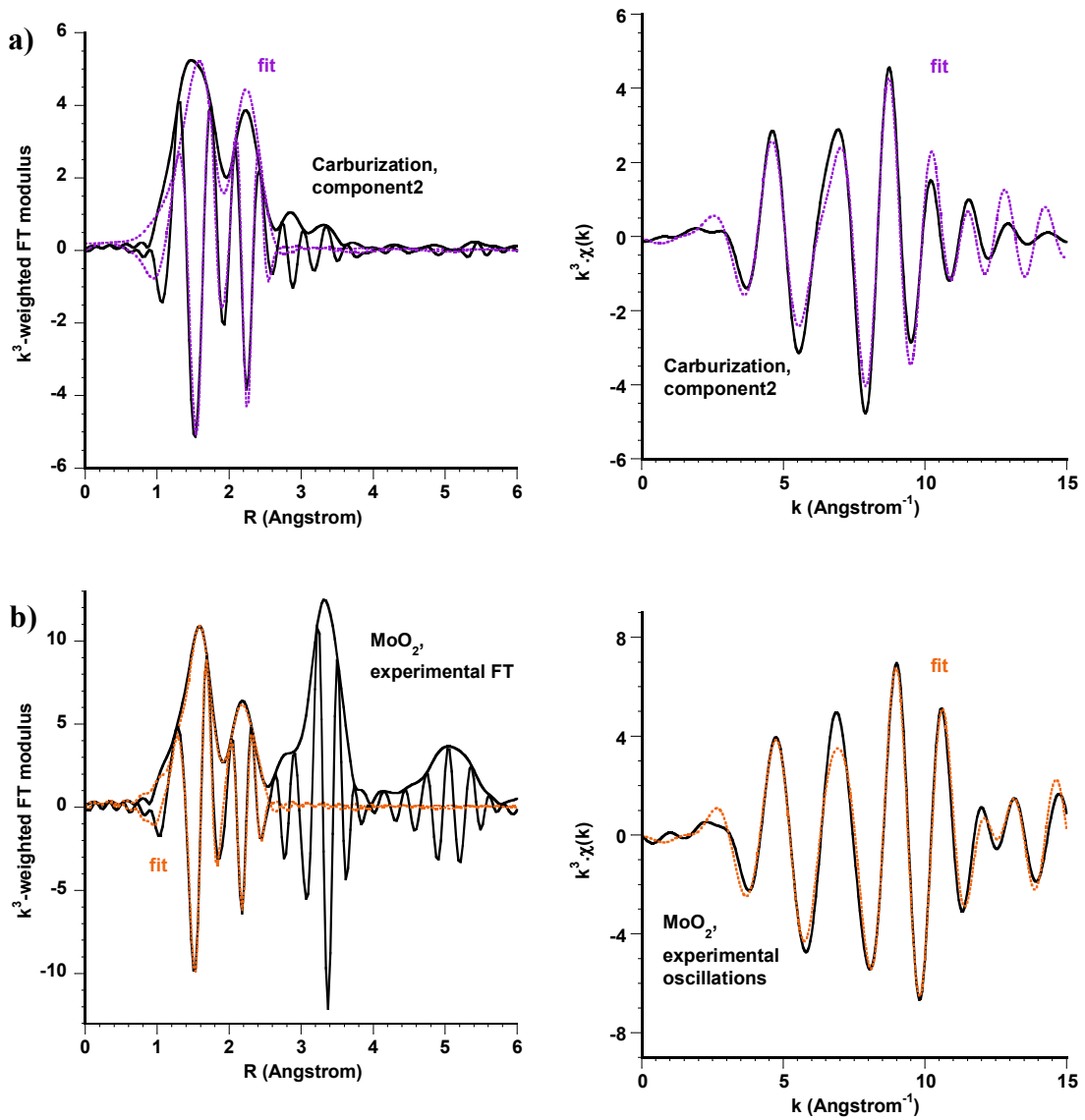
Reference: own author (2023)

To obtain more precise structural information on these intermediate species, the second and third spectral components extracted for Cu-Mo<sub>x</sub>C<sub>y</sub>/SiO<sub>2</sub> were selected for EXAFS fitting. This system was chosen because it is the one for which the intermediate spectral components appear most sequentially, and are more likely to represent distinct species.

The identification of a MoO<sub>2</sub>-like phase is confirmed for the second spectral component, by comparison with a fit done on the spectrum of MoO<sub>2</sub> using the same number of parameters (Table 4.2, Figure 4.17). The only difference is a Mo-Mo interatomic distance longer by 0.07 Å.

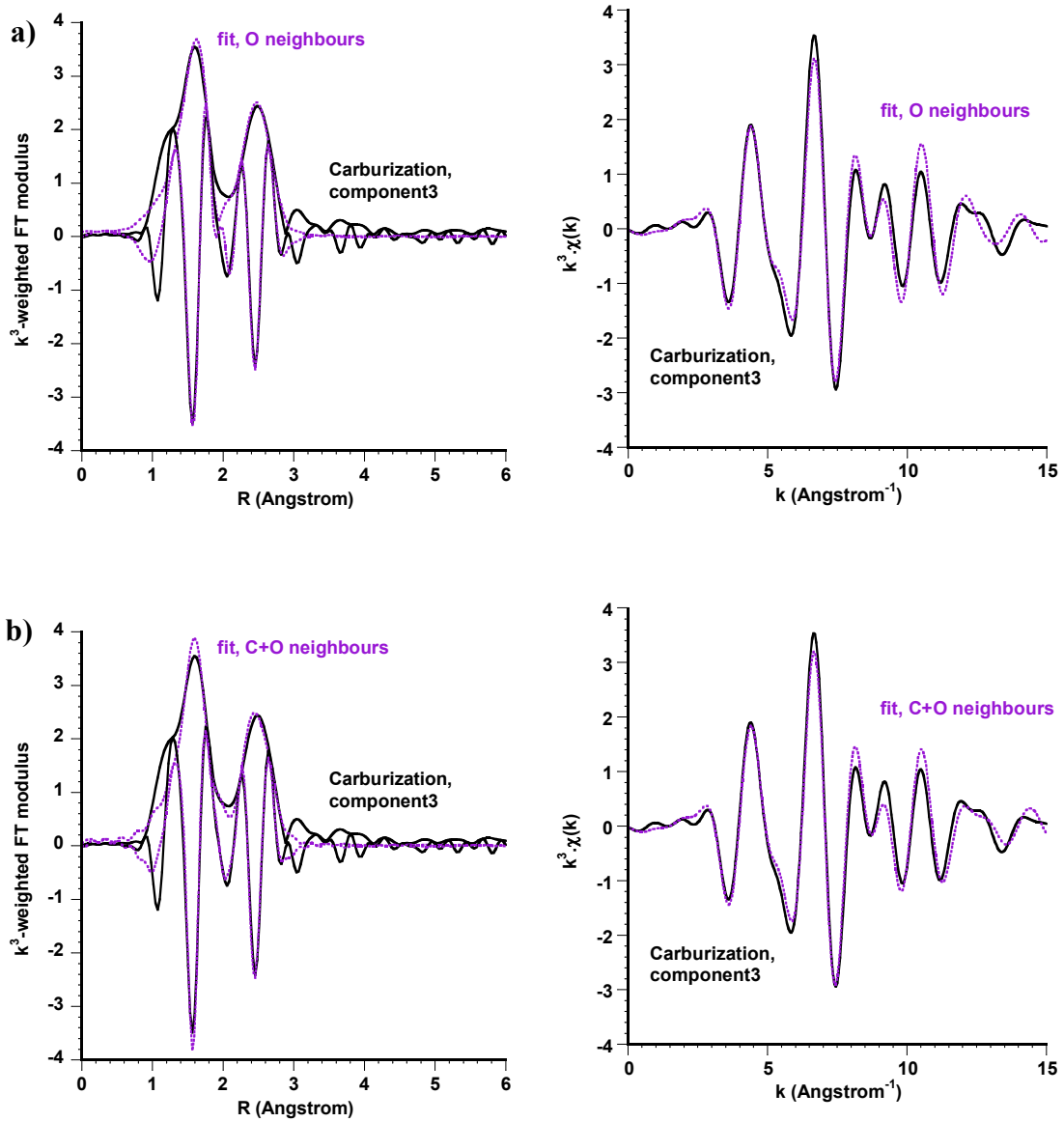
A precise assignment is more difficult to establish for the third spectral component (Table 4.2, Figure 4.7). The first peak in the Fourier transform is found to arise from a shell of O atoms. A fit using both C and O atoms appears less plausible because it results in an extremely low Debye-Waller parameter, lower than that found when fitting the EXAFS signal of a well-organized oxide like MoO<sub>2</sub> at RT. The second peak corresponds to Mo neighbors at an interatomic distance of 2.80 Å, which is both larger than the Mo-Mo distance in metallic Mo (2.72 Å), and smaller than the distances evaluated in the carburized catalysts (Table 4.1; approximately 2.97 Å), or in the crystalline oxycarbide phases whose structure was described in detail by (Bouchy *et al.* 2000) (2.90 - 2.96 Å). The high Debye-Waller factor for the second shell can be explained by a thermal effect (as will be seen below, the third component is prominent at about 400 °C) or by a structural disorder around Mo.

Figure 4.17. MCR-ALS analysis at the Mo K-edge of the carburization of Cu-Mo<sub>x</sub>C<sub>y</sub>/SiO<sub>2</sub>. Fit of the first and second shells of neighbors for the second spectral component (a) compared with reference monoclinic MoO<sub>2</sub> (b): Fourier transform ( $k = 3.5 - 15 \text{ \AA}^{-1}$ , left) and EXAFS oscillations (right). See Table 4.2.



Reference: own author (2023)

Figure 4.18. MCR-ALS analysis at the Mo K-edge of the carburization of Cu-Mo<sub>x</sub>C<sub>y</sub>/SiO<sub>2</sub>. Fit of the first and second shells of neighbors for the second spectral component (a) compared with reference monoclinic MoO<sub>2</sub> (b): Fourier transform ( $k = 3.5 - 15 \text{ \AA}^{-1}$ , left) and EXAFS oscillations (right). See Table 4.2.



Reference: own author (2023)

Table 4.2. Fitted parameters at the Mo K-edge ( $E_0 = 20013$  eV,  $S02 = 0.98$ ) determined from the EXAFS analysis of the second and third components extracted by MCR-ALS procedure during the carburization of  $\text{Cu-Mo}_x\text{C}_y/\text{SiO}_2$ .  $k = 3.5 - 14 \text{ \AA}^{-1}$ .

Catalyst	Backscatter	N	$\sigma^2 (\text{\AA}^2) \times 10^3$	R ( $\text{\AA}$ )
MoO <sub>2</sub>	O	$5.1 \pm 0.9$	$3 \pm 2$	$2.00 \pm 0.02$
	Mo	$1.0 \pm 0.3$	$3 \pm 2$	$2.52 \pm 0.02$
	$\Delta E_0 = 0.5$ eV, R = 1 - 2.7 $\text{\AA}$ , r-factor = 0.04759, $\chi^2 = 1248$ , $N_{\text{ind}} = 12$ , $N_{\text{var}} = 6$			
Mo foil	Mo	$8.0 \pm 0.4$	$3.8 \pm 0.3$	$2.721 \pm 0.003$
	Mo	$6.0 \pm 0.4$	$3.8 \pm 0.3$	$3.136 \pm 0.004$
	$\Delta E_0 = -5.1$ eV, R = 1 - 3 $\text{\AA}$ , r-factor = 0.00356, $\chi^2 = 274$ , $N_{\text{ind}} = 13$ , $N_{\text{var}} = 5$			
Cu-Mo <sub>x</sub> C <sub>y</sub> /SiO <sub>2</sub> second component	O	$4 \pm 1$	$7 \pm 3$	$2.03 \pm 0.02$
	Mo	$1.6 \pm 0.8$	$7 \pm 3$	$2.59 \pm 0.02$
	$\Delta E_0 = -0.5$ eV, R = 1 - 2.7 $\text{\AA}$ , r-factor = 0.07985, $\chi^2 = 1645$ , $N_{\text{ind}} = 12$ , $N_{\text{var}} = 6$			
Cu-Mo <sub>x</sub> C <sub>y</sub> /SiO <sub>2</sub> third component Hyp.: 1 <sup>st</sup> shell of O	O	$4.8 \pm 0.8$	$5 \pm 2$	$2.06 \pm 0.01$
	Mo	$5 \pm 2$	$16 \pm 3$	$2.80 \pm 0.02$
	$\Delta E_0 = 1.2$ eV, R = 1 - 3 $\text{\AA}$ , r-factor = 0.03512, $\chi^2 = 309$ , $N_{\text{ind}} = 14$ , $N_{\text{var}} = 7$			
Cu-Mo <sub>x</sub> C <sub>y</sub> /SiO <sub>2</sub> third component Hyp.: 1 <sup>st</sup> shell of C/O	O	$1.3 \pm 0.5$	$2 \pm 2$	$2.02 \pm 0.03$
	C	$1.3 \pm 0.5$	$2 \pm 2$	$2.18 \pm 0.02$
	Mo	$5 \pm 2$	$16 \pm 3$	$2.80 \pm 0.02$
$\Delta E_0 = -0.4$ eV, R = 1 - 3 $\text{\AA}$ , r-factor = 0.02936, $\chi^2 = 339$ , $N_{\text{ind}} = 14$ , $N_{\text{var}} = 7$				

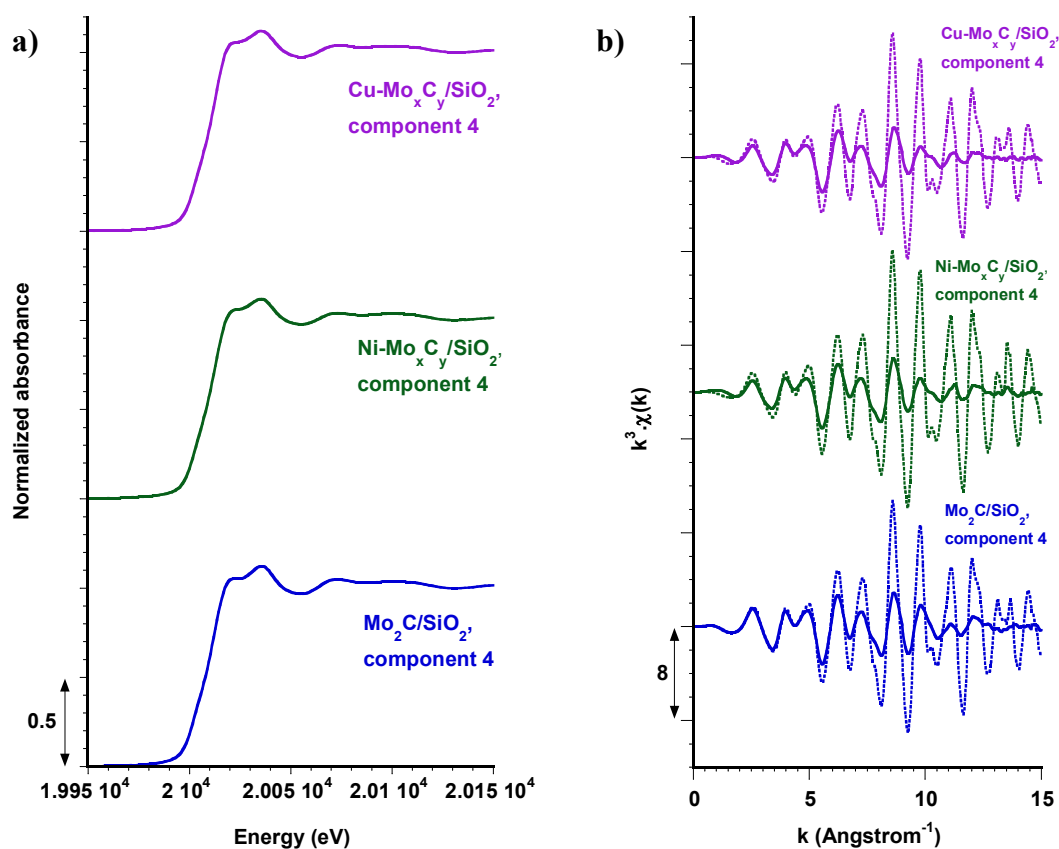
Reference: own author (2023)

In conclusion, a comparison with the spectra presented in the literature points to phases mentioned as oxycarbides  $\text{MoO}_x\text{C}_y$ . But the impossibility to fit the first shell with a combination of C and O atoms, and the Mo-Mo interatomic distance, which significantly differs from those reported either in organized oxycarbide crystals or metallic Mo, also suggests the formation of a heterogeneous, mostly oxidic, system, in which only a fraction of Mo has pursued its reduction, or is initiating its carburization. It will be seen in the section dedicated to temperature-programmed carburization that the degree of carburization of this species may not be the same for the three systems.



Finally, the fourth spectral component extracted by the MCR-ALS procedure is identical to that of the final Mo carbide, as confirmed by a comparison of the position of the oscillations with those recorded after cooling under CH<sub>4</sub>/H<sub>2</sub> to RT (Figure 4.19). The damping is due to thermal effects.

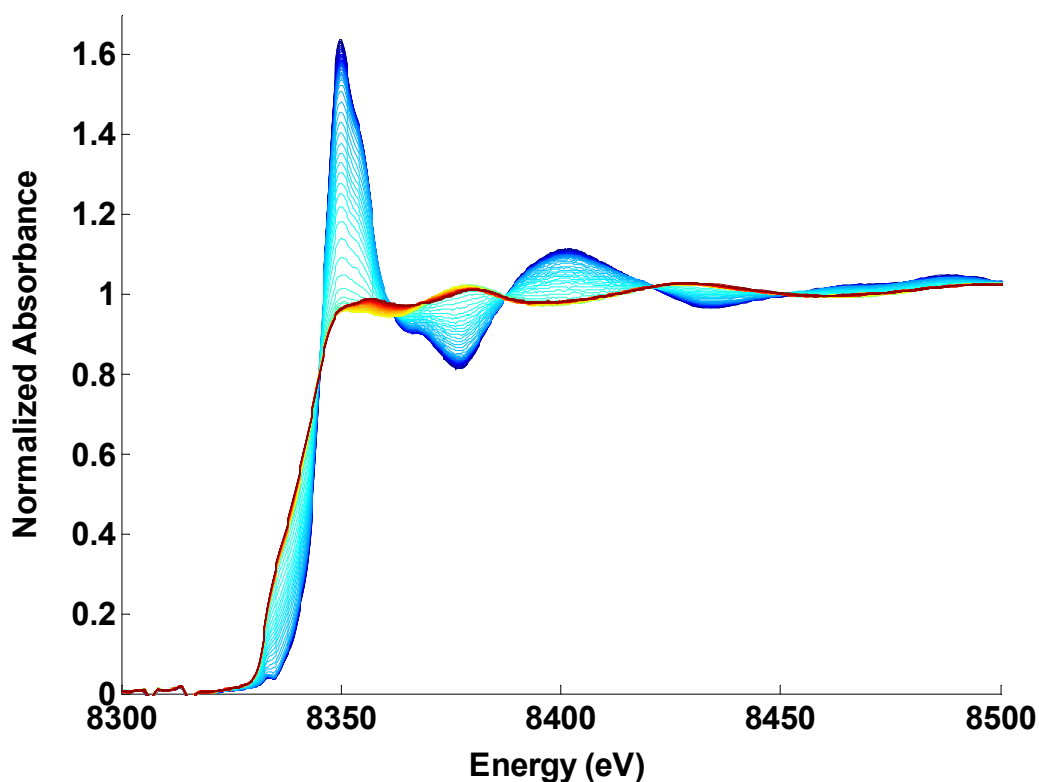
Figure 4.19. MCR-ALS analysis at the Mo-K edge of the carburization ramp: characteristics of the fourth components. a) XANES spectra, b) EXAFS oscillations. Dotted lines: EXAFS oscillations of the carburized catalysts recorded at room temperature.



Reference: own author (2023)

The evolution of the spectra recorded during the carburization of Ni-Mo<sub>x</sub>C<sub>y</sub>/SiO<sub>2</sub> at the Ni K-edge is presented in Figure 4.20. The initial intense white line is characteristic of Ni<sup>2+</sup>, and its disappearance indicates that nickel is reduced to the metallic state during the first half of the ramp. But even after reduction, some changes in the spectra are visible (yellow-red spectra).

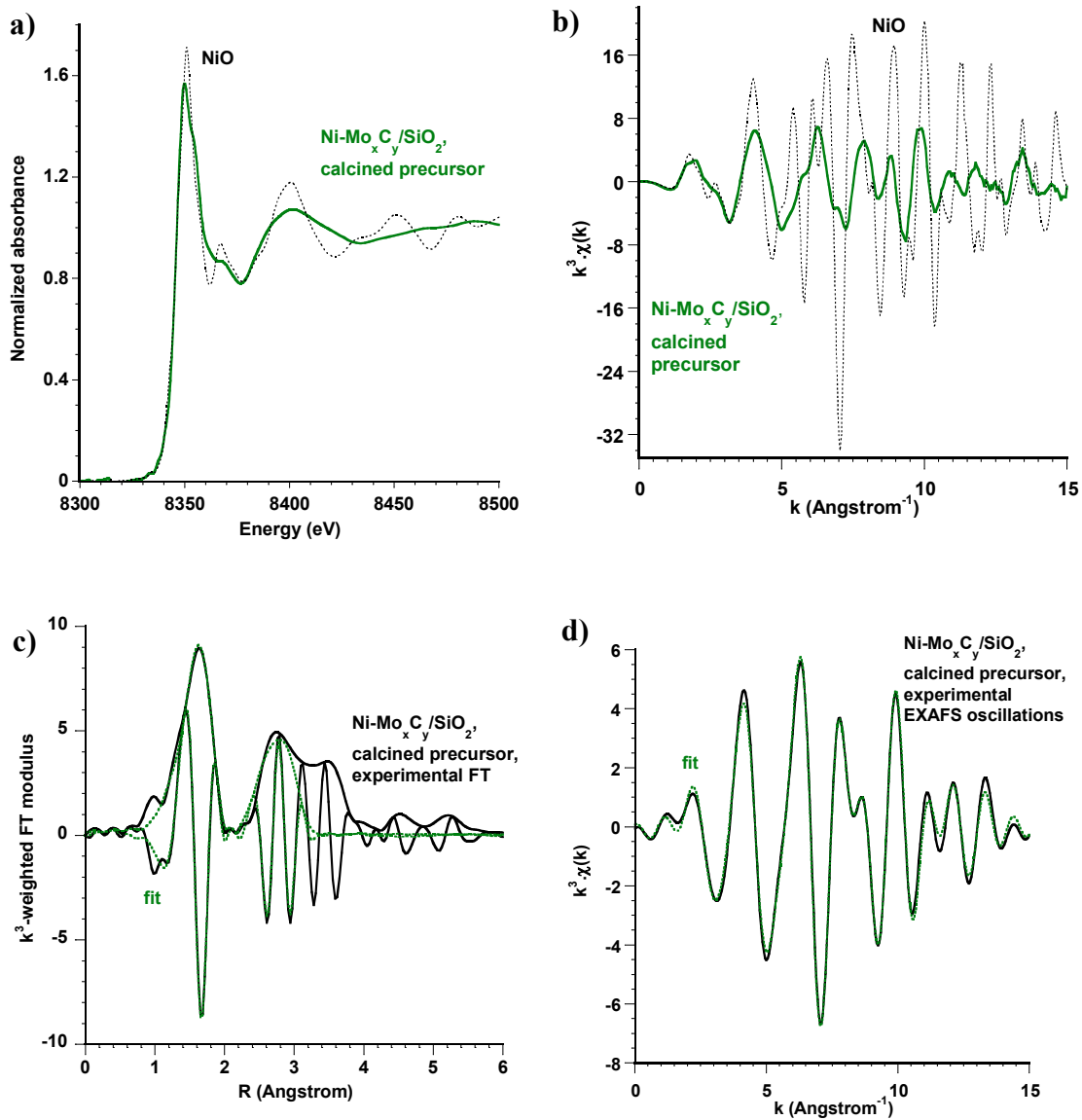
Figure 4.20. Evolution of the XAS spectra of Ni-Mo<sub>x</sub>C<sub>y</sub>/SiO<sub>2</sub> at the Ni K-edge upon carburization (from room temperature, dark blue, to 650 °C, red).



Reference: own author (2023)

EXAFS confirms that in the calcined precursor, Ni<sup>2+</sup> is present in the  $\alpha$ -NiMoO<sub>4</sub> phase detected by Raman spectroscopy; NiO would provide very different oscillations (Figure 4.21). The expected number of neighbors and interatomic distances in the crystal structure are 6 O atoms at  $R = 2.018 - 2.140 \text{ \AA}$ , 2 Ni atoms at  $R = 3.027 \text{ \AA}$ , and 2 Mo atoms at  $R = 3.207 \text{ \AA}$ , and correspond to those determined by fitting (Table 4.3). The fit was not attempted at longer distances owing to the superimposition of more than 10 multiple scattering paths between 3.4 and 4  $\text{\AA}$ .

Figure 4.21. XAS data at the Ni K-edge of the Ni-Mo<sub>x</sub>C<sub>y</sub>/SiO<sub>2</sub> calcined precursor. a) XANES spectrum and b) EXAFS oscillations, comparison with reference NiO. Fit of the first and second shells of neighbors: c) Fourier transform and d) EXAFS oscillations,  $k = 3 - 13 \text{ \AA}^{-1}$ .



Reference: own author (2023)

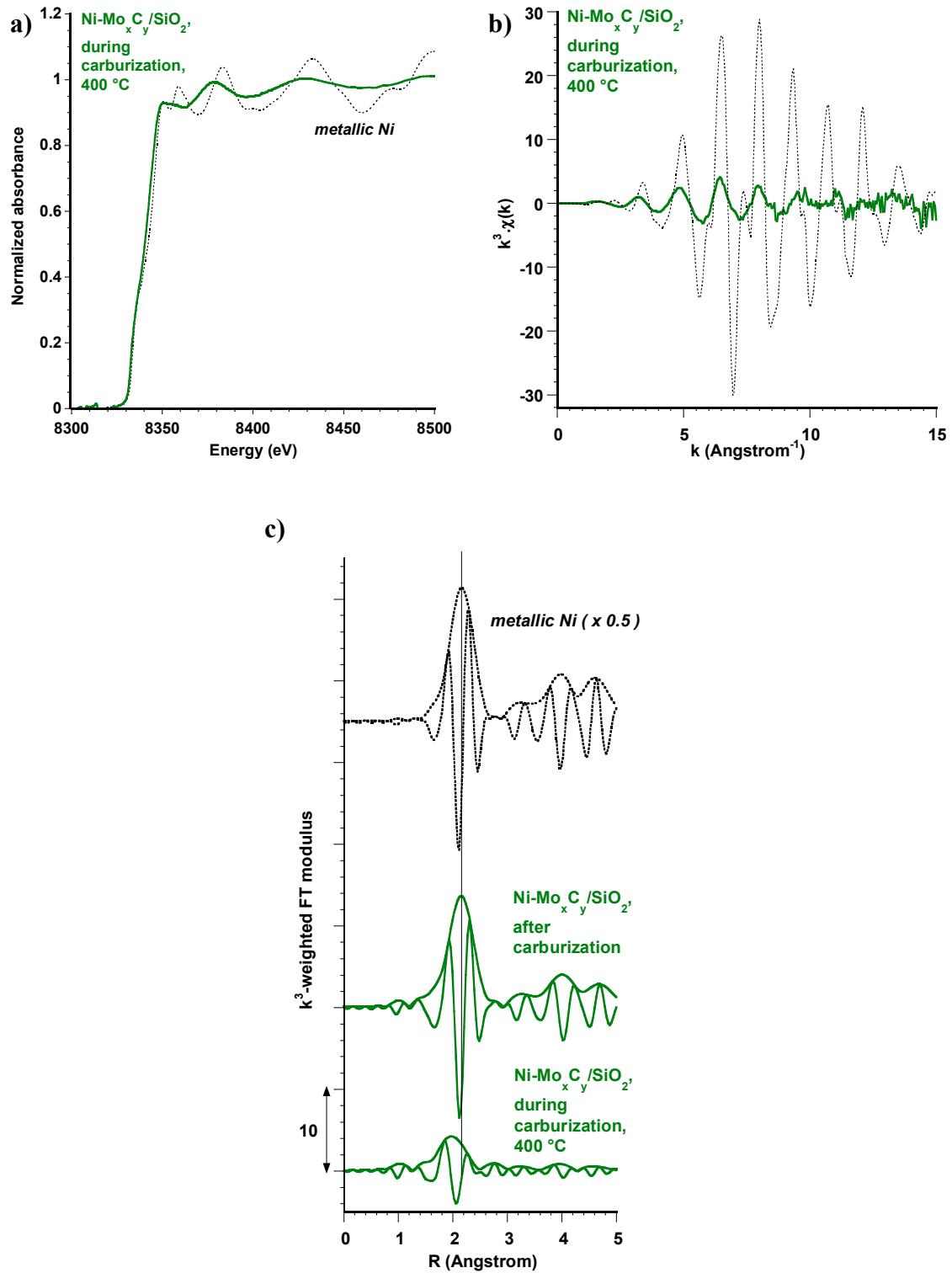
Table 4.3. Fitted parameters at the Ni K-edge ( $E_0 = 8339 \pm 2$  eV,  $S02 = 0.80$ ) or at the Cu K-edge ( $E_0 = 8987 \pm 4$  eV,  $S02 = 0.91$ ) determined from the EXAFS analysis of spectra recorded at room temperature.  $k = 3 - 13 \text{ \AA}^{-1}$  at the Ni K-edge,  $k = 3.5 - 14 \text{ \AA}^{-1}$  at the Cu K-edge. Fit of the first peak(s) from the Fourier transform between 1 and 3  $\text{\AA}$ .

Catalyst	Backscatter	N	$\sigma^2 (\text{\AA}^2) \times 10^3$	R ( $\text{\AA}$ )
Ni-Mo <sub>x</sub> C <sub>y</sub> /SiO <sub>2</sub> calcined	O	6.4 ± 0.7	6 ± 2	2.030 ± 0.009
	Ni	1.4 ± 0.6	6 ± 2	2.97 ± 0.03
	Mo	1.6 ± 0.9	6 ± 2	3.17 ± 0.03
r-factor = 0.01766, $\chi^2 = 365$ , $N_{\text{ind}} = 12$ , $N_{\text{var}} = 8$				
Ni-Mo <sub>x</sub> C <sub>y</sub> /SiO <sub>2</sub> carburized	Ni	6.8 ± 0.5	8.3 ± 0.6	2.494 ± 0.004
	r-factor = 0.00473, $\chi^2 = 427$ , $N_{\text{ind}} = 12$ , $N_{\text{var}} = 4$			
Cu-Mo <sub>x</sub> C <sub>y</sub> /SiO <sub>2</sub> calcined	O	4.9 ± 0.3	4.9 ± 0.6	1.941 ± 0.004
	r-factor = 0.00791, $\chi^2 = 41$ , $N_{\text{ind}} = 13$ , $N_{\text{var}} = 4$			
Cu-Mo <sub>x</sub> C <sub>y</sub> /SiO <sub>2</sub> carburized	Cu	9.0 ± 0.7	9.6 ± 0.6	2.544 ± 0.005
	r-factor = 0.00598, $\chi^2 = 148$ , $N_{\text{ind}} = 13$ , $N_{\text{var}} = 4$			

Reference: own author (2023)

A spectrum recorded during carburization at 400 °C is presented in Figure 4.22a. As was anticipated from Figure 4.20, Ni is now in a reduced, metallic state (comparison of the edge position with Ni foil, position in energy of the main oscillations, Figure 4.22a and b). But the shape of the spectrum just past the edge is quite different from that of bulk Ni metal, with a complete absence of structuration around 8350 eV. The peak of nearest neighbors on the Fourier transform is also located at a significantly shorter distance than in metallic Ni (Figure 4.22c), which may indicate that small groups of Ni atoms, which one can presume are stabilized by an underlying phase, have not formed well-organized metal particles yet.

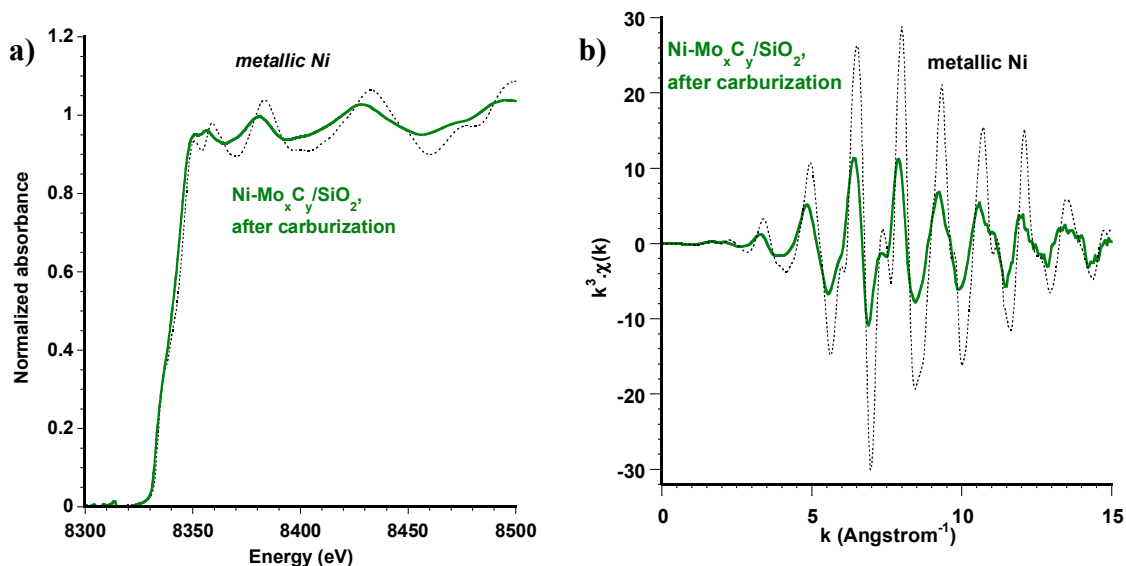
Figure 4.22. XAS data at the Ni K-edge of the Ni-Mo<sub>x</sub>C<sub>y</sub>/SiO<sub>2</sub> catalyst, recorded during carburization, at 400 °C. a) XANES spectrum and b) EXAFS oscillations, comparison with reference Ni foil. c) Comparison of the Fourier transforms, k = 3 - 13 Å<sup>-1</sup>.



Reference: own author (2023)

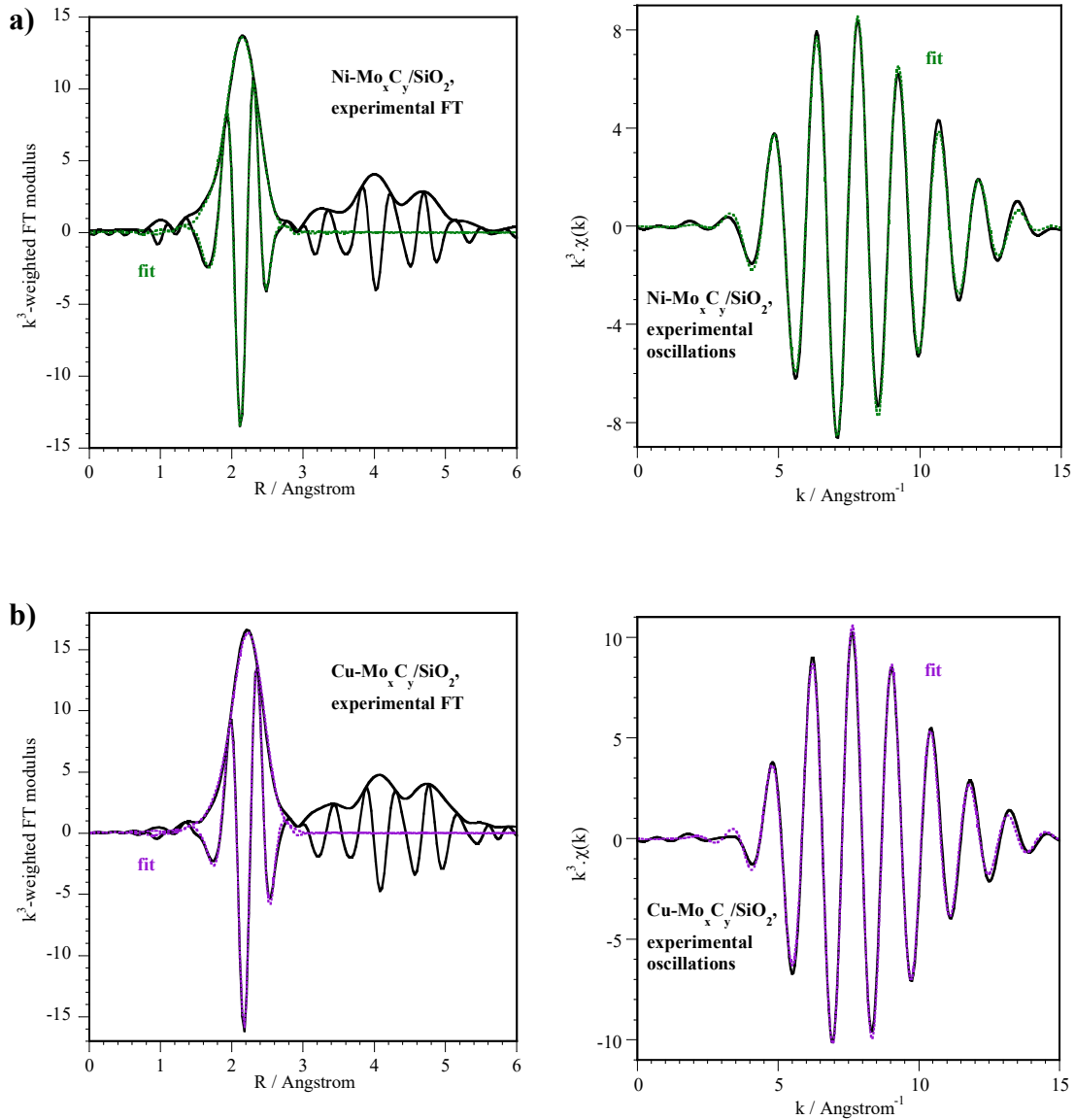
In contrast, after carburization has been completed and cooling to RT has taken place (Figures 4.23 and 4.24), face-centered (fcc) cubic Ni is detected. The number of nearest neighbors is far below the value of 12 in bulk Ni (Table 4.3). A value of 6.8, as found here, can be linked to small Ni particles, whose size would be close to 1 nm (Patterson and Abela, 2010), a highly dispersed state for reduced Ni. The interatomic distance (2.494 Å) corresponds to that in metallic Ni, and the hypothesis of a Ni carbide, in which distances are longer, can be excluded (a Ni - Ni distance of 2.63 Å was reported for Ni<sub>3</sub>C by Struis *et al.*, 2009).

Figure 4.23. XAS data at the Ni K-edge of the Ni-Mo<sub>x</sub>C<sub>y</sub>/SiO<sub>2</sub> catalyst after carburization. a) XANES spectrum and b) EXAFS oscillations, comparison with reference NiO. Spectra recorded at room temperature.



Reference: own author (2023)

Figure 4.24. XAS data a) of Ni-Mo<sub>x</sub>C<sub>y</sub>/SiO<sub>2</sub> at the Ni K-edge and b) of Cu-Mo<sub>x</sub>C<sub>y</sub>/SiO<sub>2</sub> at the Cu K-edge, after carburization (spectra recorded at room temperature). Fit of the first shell of neighbors: Fourier transform (left) and EXAFS oscillations (right),  $k = 3 - 13 \text{ \AA}^{-1}$  at the Ni K-edge,  $k = 3.5 - 14 \text{ \AA}^{-1}$  at the Cu K-edge.

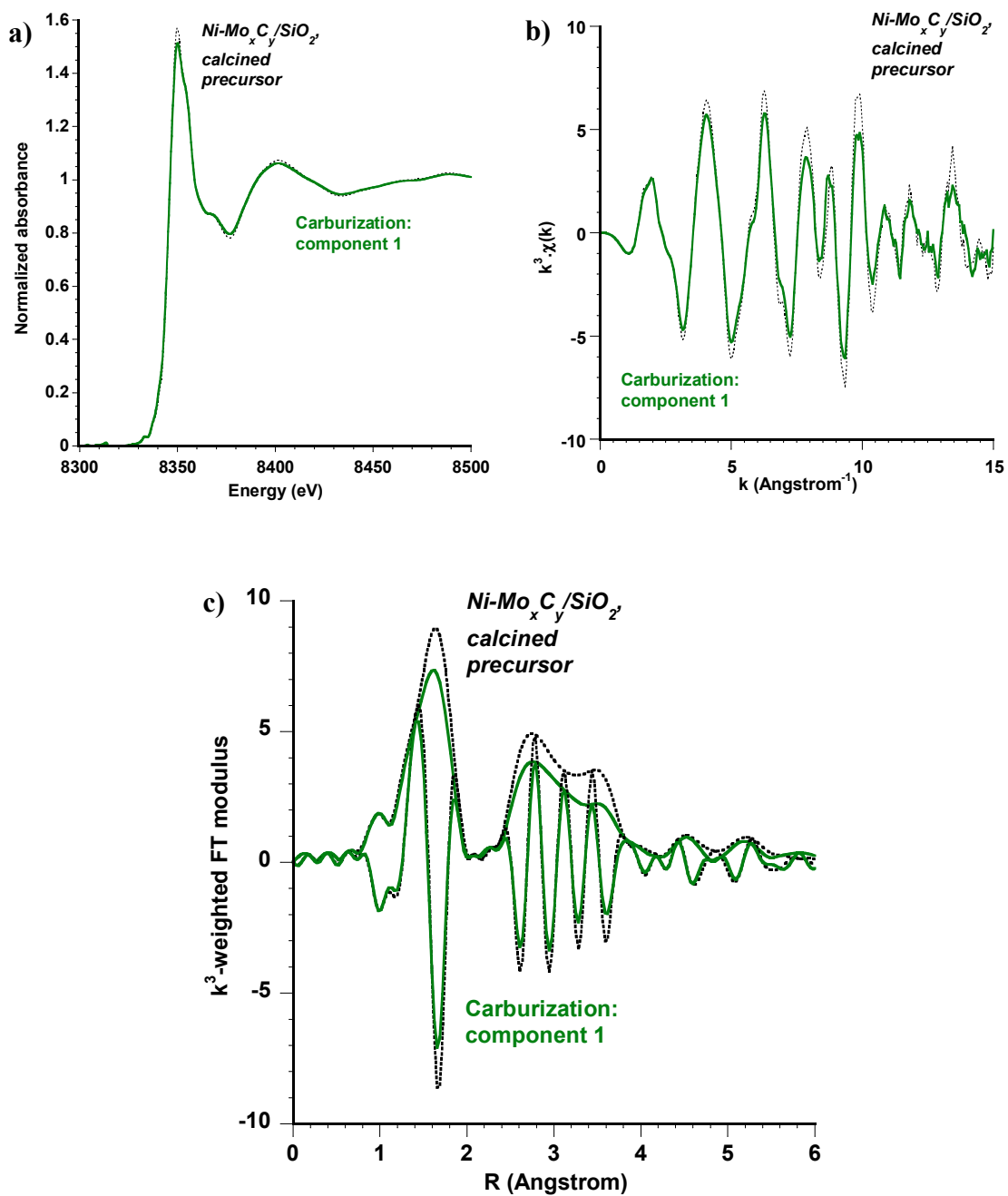


Reference: own author (2023)

The MCR-ALS analysis of the carburization of Ni-Mo/SiO<sub>2</sub> at the Ni K-edge extracts three spectral components (Figures 4.25 - 4.27). The first one corresponds to NiMoO<sub>4</sub>, the second one is identical to the spectrum recorded at 400 °C (small groups

of Ni atoms), and the third one to fcc Ni nanoparticles, with EXAFS oscillations damped because of a strong thermal effect in the last part of the temperature ramp.

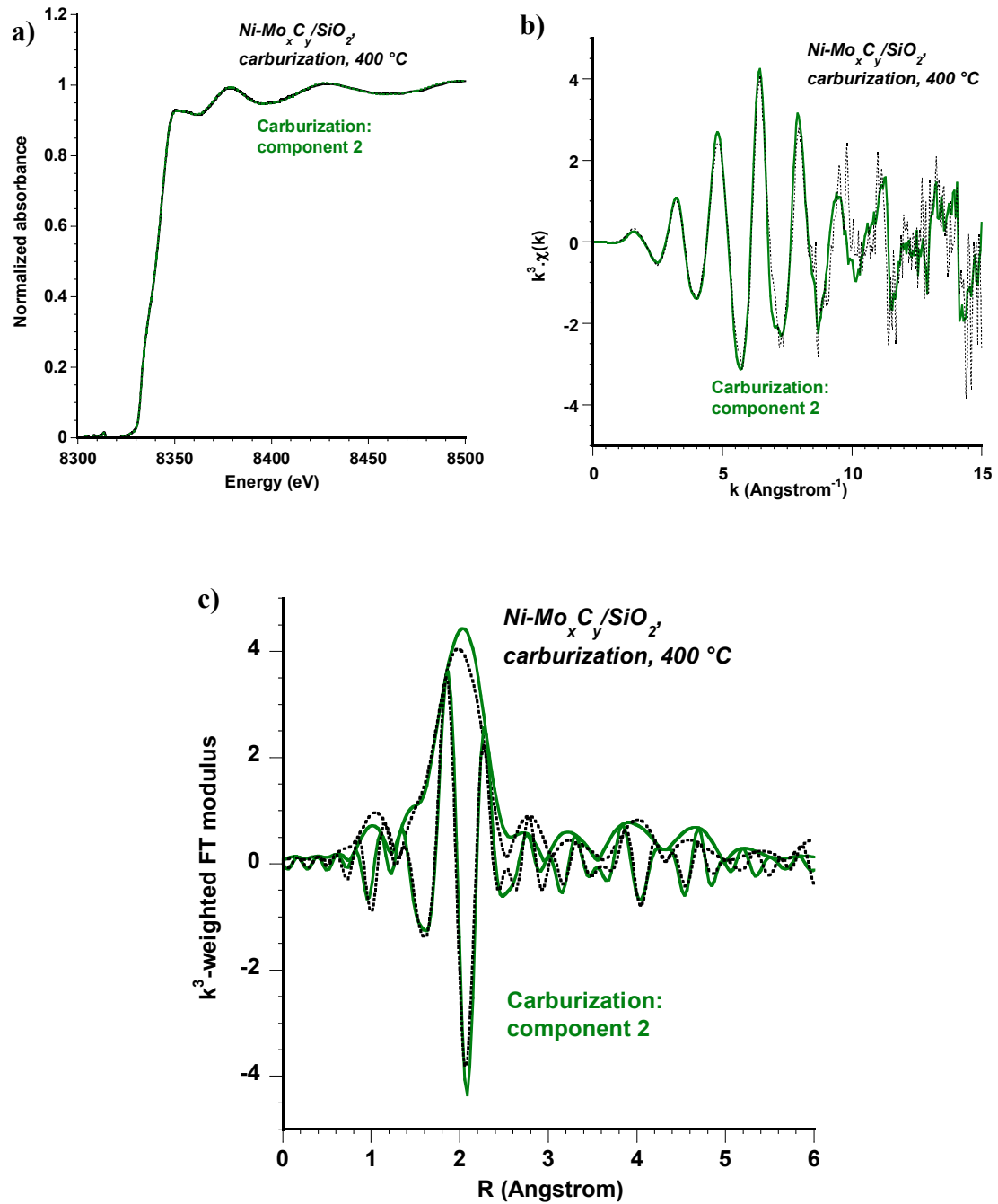
Figure 4.25. MCR-ALS analysis at the Ni-K edge of the carburization of Ni-Mo<sub>x</sub>C<sub>y</sub>/SiO<sub>2</sub>: comparison of the first component with the calcined precursor. a) XANES spectrum, b) EXAFS oscillations, c) Fourier transform,  $k = 3 - 13 \text{ \AA}^{-1}$ .



Reference: own author (2023)

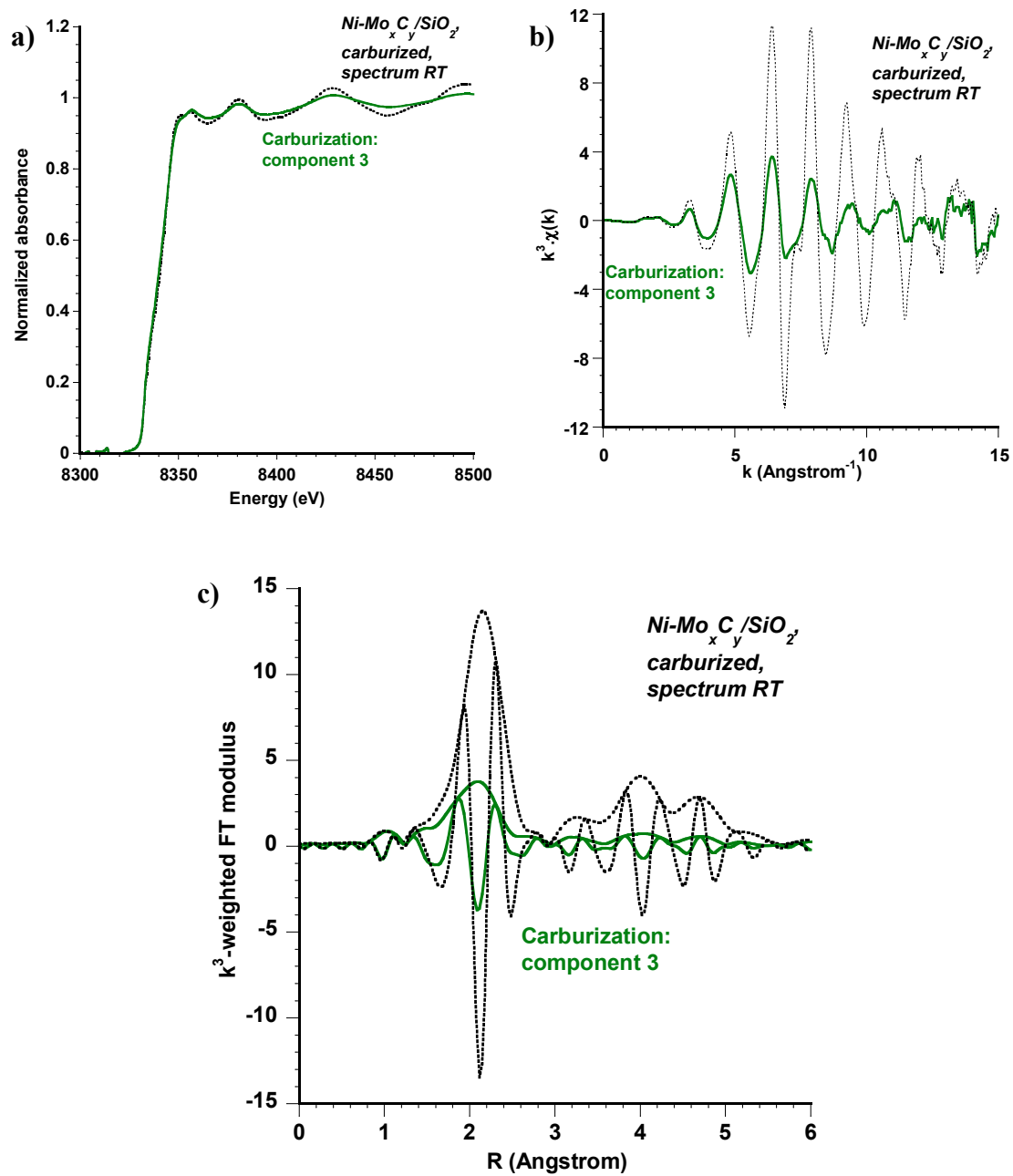


Figure 4.26. MCR-ALS analysis at the Ni-K edge of the carburization of Ni-Mo<sub>x</sub>C<sub>y</sub>/SiO<sub>2</sub>: comparison of the second component with the spectrum recorded at 400 °C during carburization. a) XANES spectrum, b) EXAFS oscillations, c) Fourier transform, k = 3 - 13 Å<sup>-1</sup>.



Reference: own author (2023)

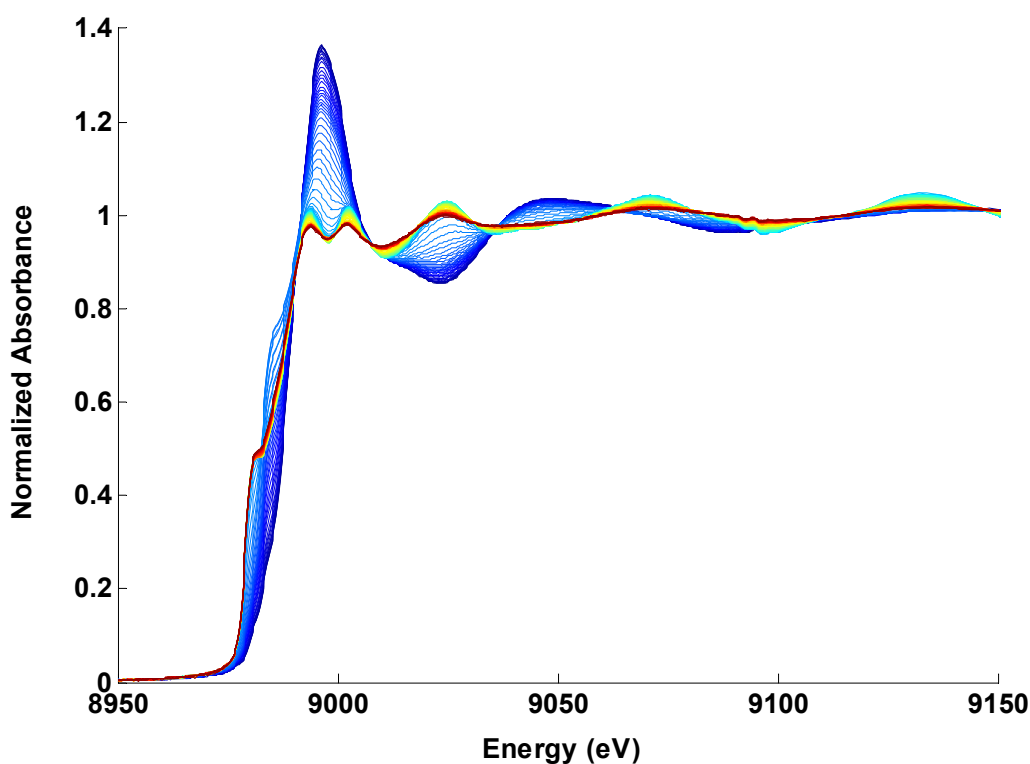
Figure 4.27. MCR-ALS analysis at the Ni-K edge of the carburization of Ni-Mo<sub>x</sub>C<sub>y</sub>/SiO<sub>2</sub>: comparison of the third component with the spectrum recorded after carburization at room temperature. a) XANES spectrum, b) EXAFS oscillations, c) Fourier transform,  $k = 3 - 13 \text{ \AA}^{-1}$ .



Reference: own author (2023)

The evolution of the spectra recorded during the carburization of Cu-Mo<sub>x</sub>C<sub>y</sub>/SiO<sub>2</sub> at the Cu K-edge is presented in Figure 4.28. The reduction of Cu<sup>2+</sup>, characterized by the intense white line, takes place at a low temperature. An intermediate species then contributes to a well-visible pre-edge feature, distinct from that of metallic Cu and more intense, before the typical spectrum of metallic Cu appears.

Figure 4.28. Evolution of the XAS spectra of Cu-Mo<sub>x</sub>C<sub>y</sub>/SiO<sub>2</sub> at the Cu K-edge upon carburization (from room temperature, dark blue, to 650 °C, red).

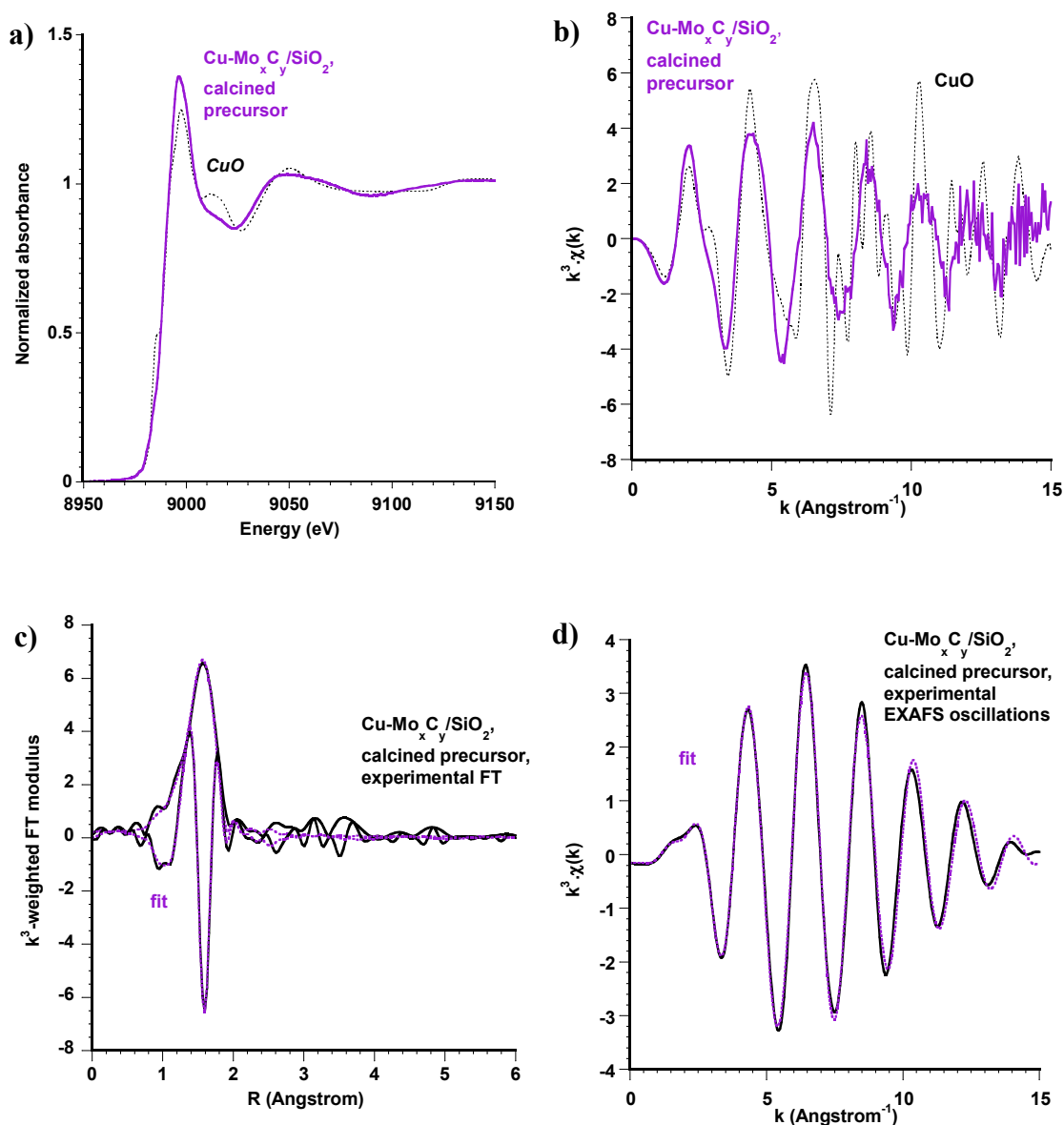


Reference: own author (2023)

The analysis of the XAS data is much less informative than at the Ni K-edge. The position in the energy of the XANES spectrum recorded on the calcined system (Figure 4.29) is similar to that of standard CuO, which indicates that Cu is present in the Cu<sup>2+</sup> state, but the spectrum is different: for example, no pre-edge feature is present. This absence of a pre-edge feature was also reported in the literature for  $\gamma$ -CuMoO<sub>4</sub> (Jonane *et al.*, 2018). The fit of the EXAFS data only reveals a shell of O atoms around

$\text{Cu}^{2+}$ , which explains why the EXAFS oscillations are seen at approximately the same energies as in  $\text{CuO}$  (Table 4.3). These observations remain consistent with the hypothesis of poorly organized  $\text{Cu}^{2+}$  molybdates suggested by Raman spectroscopy.

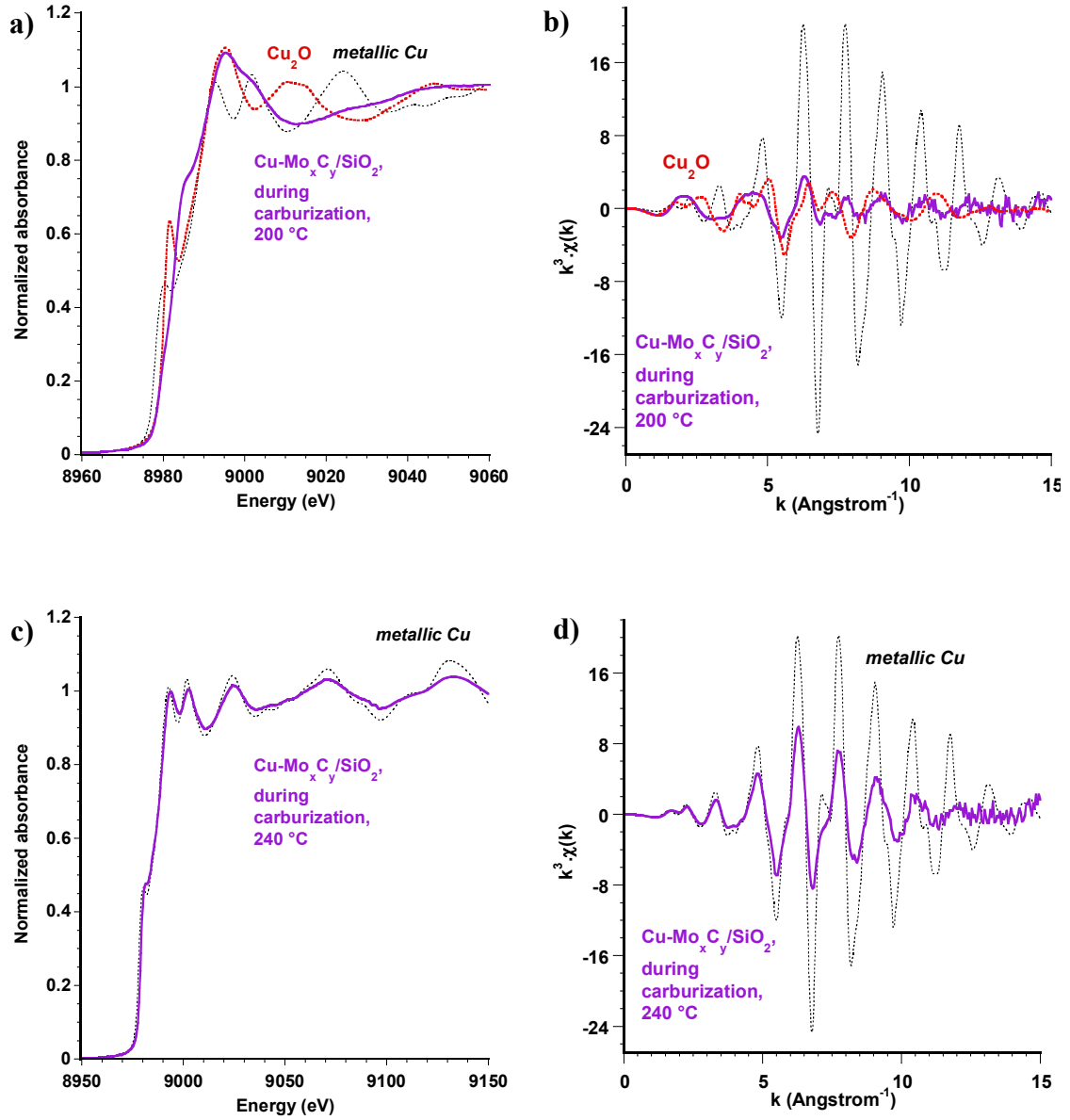
Figure 4.29. XAS data at the Cu K-edge of the  $\text{Cu-Mo}_x\text{C}_y/\text{SiO}_2$  calcined precursor. a) XANES spectrum and b) EXAFS oscillations, comparison with reference  $\text{CuO}$ . Fit of the first shell of neighbors: c) Fourier transform and d) EXAFS oscillations,  $k = 3.5 - 14 \text{ \AA}^{-1}$ .



Reference: own author (2023)

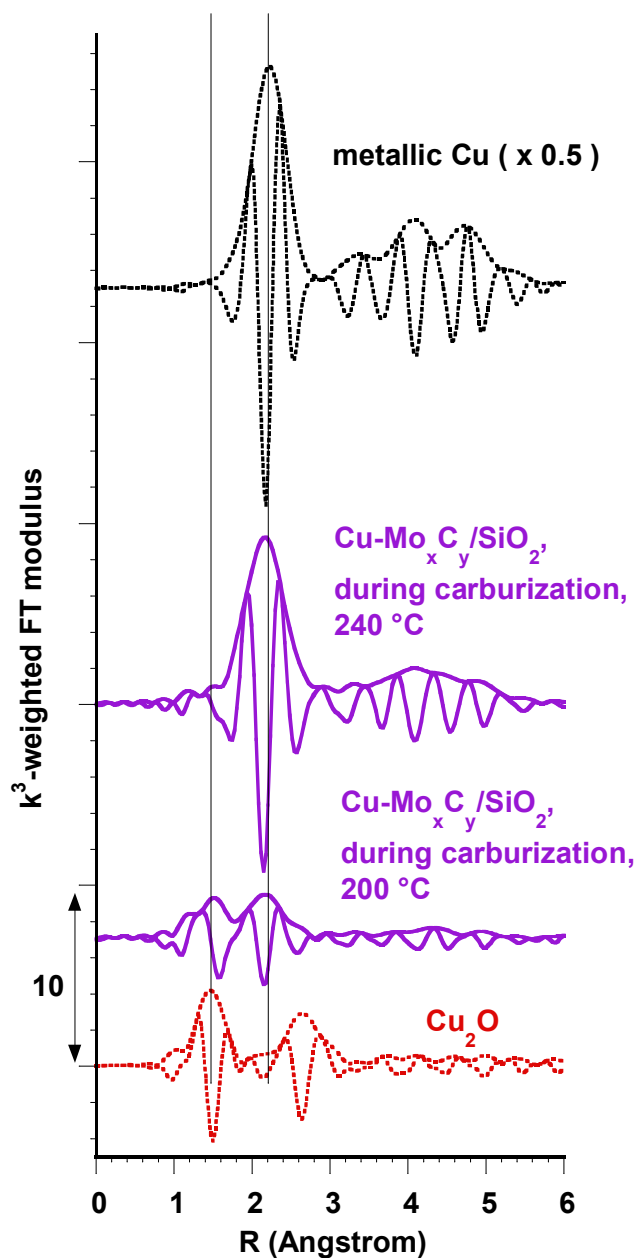
Figure 4.30 presents two spectra recorded at 200 and 240 °C. At 200 °C, the position of the edge is intermediate between that of CuO and Cu<sub>2</sub>O. However, the intense pre-edge feature and the EXAFS oscillations are quite different from those of these standards. In contrast, the species detected at 240 °C is metallic Cu. This is confirmed by the Fourier transform that shows the four successive peaks characteristic of the face-centered cubic metal (Figure 4.31). At 200 °C, the Fourier transform presents two peaks: one at the position of O nearest-neighbors, like in Cu<sub>2</sub>O; the second one at the position of Cu nearest-neighbors in the metal, and not in Cu<sub>2</sub>O. XANES spectra found in the literature that display the same shape have been interpreted either as Cu<sub>2</sub>O clusters, small partly oxidized Cu clusters, or metallic Cu clusters stabilized by ligands or by an oxidic matrix (Dubale *et al.*, 2015; Halder *et al.*, 2021; Huseyinova *et al.*, 2016; Liu *et al.*, 2019; Mammen *et al.*, 2019, 2018; Nayak *et al.*, 2018; Oyanagi *et al.*, 2012; Zandkarimi *et al.*, 2020). The position of the peaks on the Fourier transform favors the latter interpretation.

Figure 4.30. XAS data at the Cu K-edge of the Cu-Mo<sub>x</sub>C<sub>y</sub>/SiO<sub>2</sub> catalyst, recorded during carburization, at 200 °C: a) XANES spectrum and b) EXAFS oscillations; and at 240 °C: c) XANES spectrum and d) EXAFS oscillations. Comparison with references Cu foil and Cu<sub>2</sub>O.



Reference: own author (2023)

Figure 4.31. Comparison of the Fourier transforms at the Cu-K edge of catalyst  $\text{Cu-Mo}_x\text{C}_y/\text{SiO}_2$  at two stages of carburization (200 and 240 °C), and reference metallic Cu foil and  $\text{Cu}_2\text{O}$  (FT shifted along the vertical axis).  $k = 3.5 - 14 \text{ \AA}^{-1}$ .

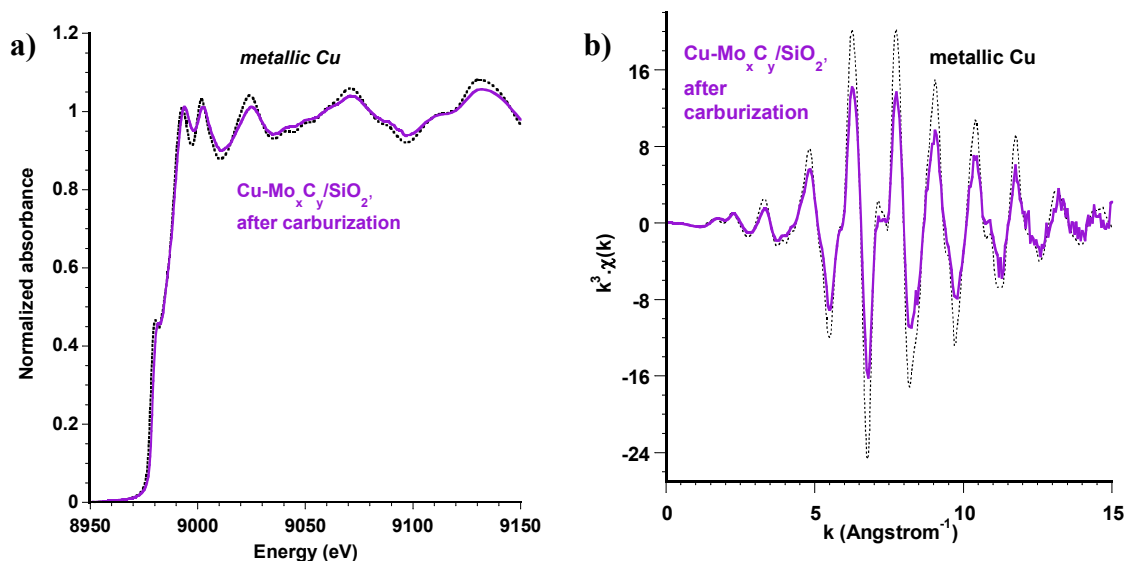


Reference: own author (2023)

After carburization and cooling to RT, Cu is unambiguously present as fcc Cu nanoparticles (Figures 4.24b and 4.32). The number of nearest neighbors, 9 (Table 4.3),

shows that these nanoparticles are larger than the Ni nanoparticles detected after the carburization of Ni-Mo<sub>x</sub>C<sub>y</sub>/SiO<sub>2</sub>.

Figure 4.32. XAS data at the Cu K-edge of the Cu-Mo<sub>x</sub>C<sub>y</sub>/SiO<sub>2</sub> catalyst after carburization (spectrum recorded at room temperature). a) XANES spectrum and b) EXAFS oscillations, comparison with reference Cu foil.

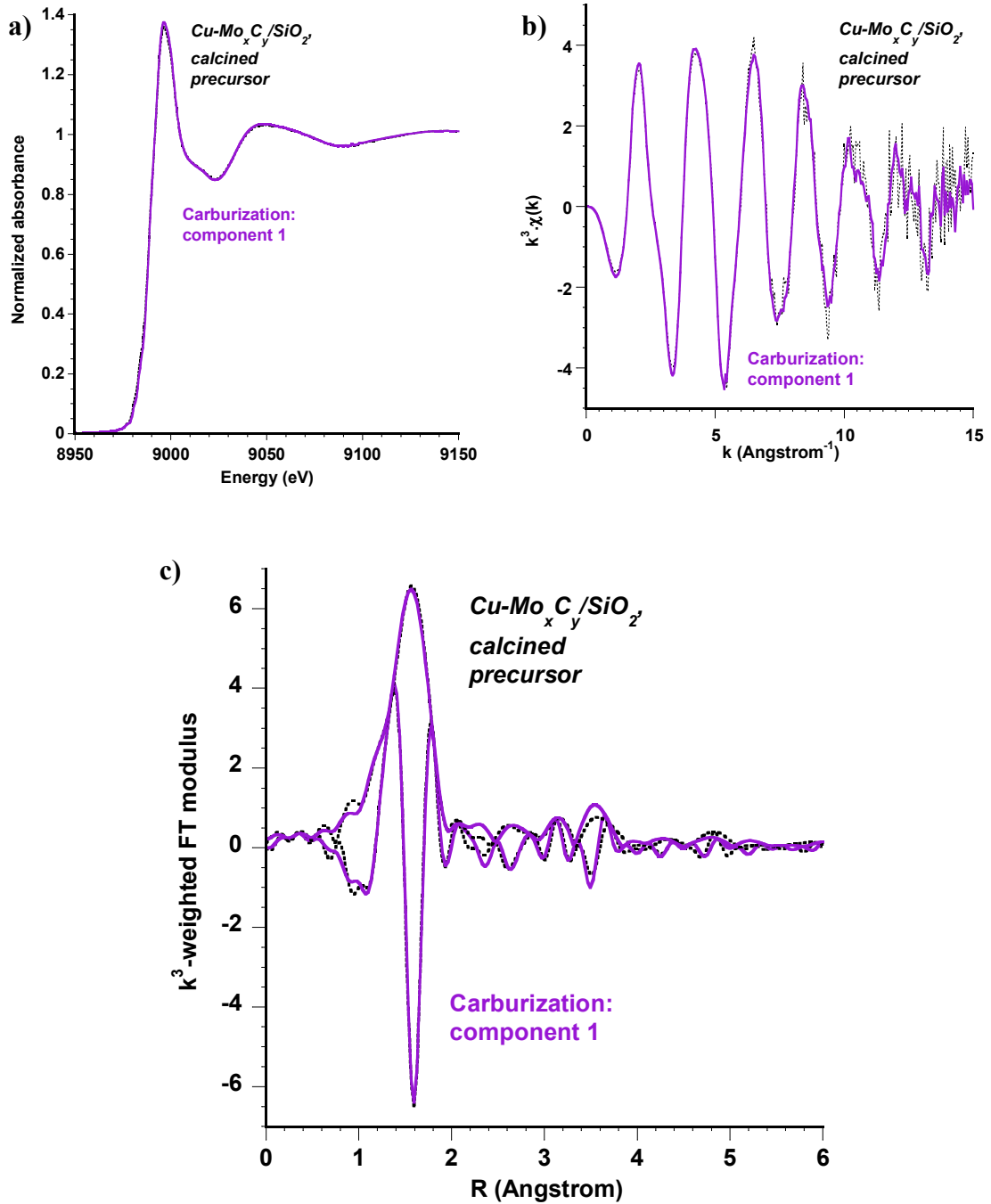


Reference: own author (2023)

The MCR-ALS analysis of the carburization ramp at the Cu K-edge provides four spectral components (Figures 4.33 - 4.36): Cu<sup>2+</sup> in the initial copper molybdates; the Cu clusters in contact with an oxidic matrix; metallic fcc Cu nanoparticles; and a fourth component also representing metallic Cu (XANES spectrum), but whose Fourier transform is shifted to lower distances compared with the metal standard. Spectra recorded during the cooling of the sample show that this contribution reverts to the third spectral component in a linear way concerning temperature. One can thus surmise that the fourth contribution comes from a reversible thermally-induced distortion of the spectrum of Cu nanoparticles. The third and fourth contributions will thus be treated as a single species, fcc Cu, in the following.

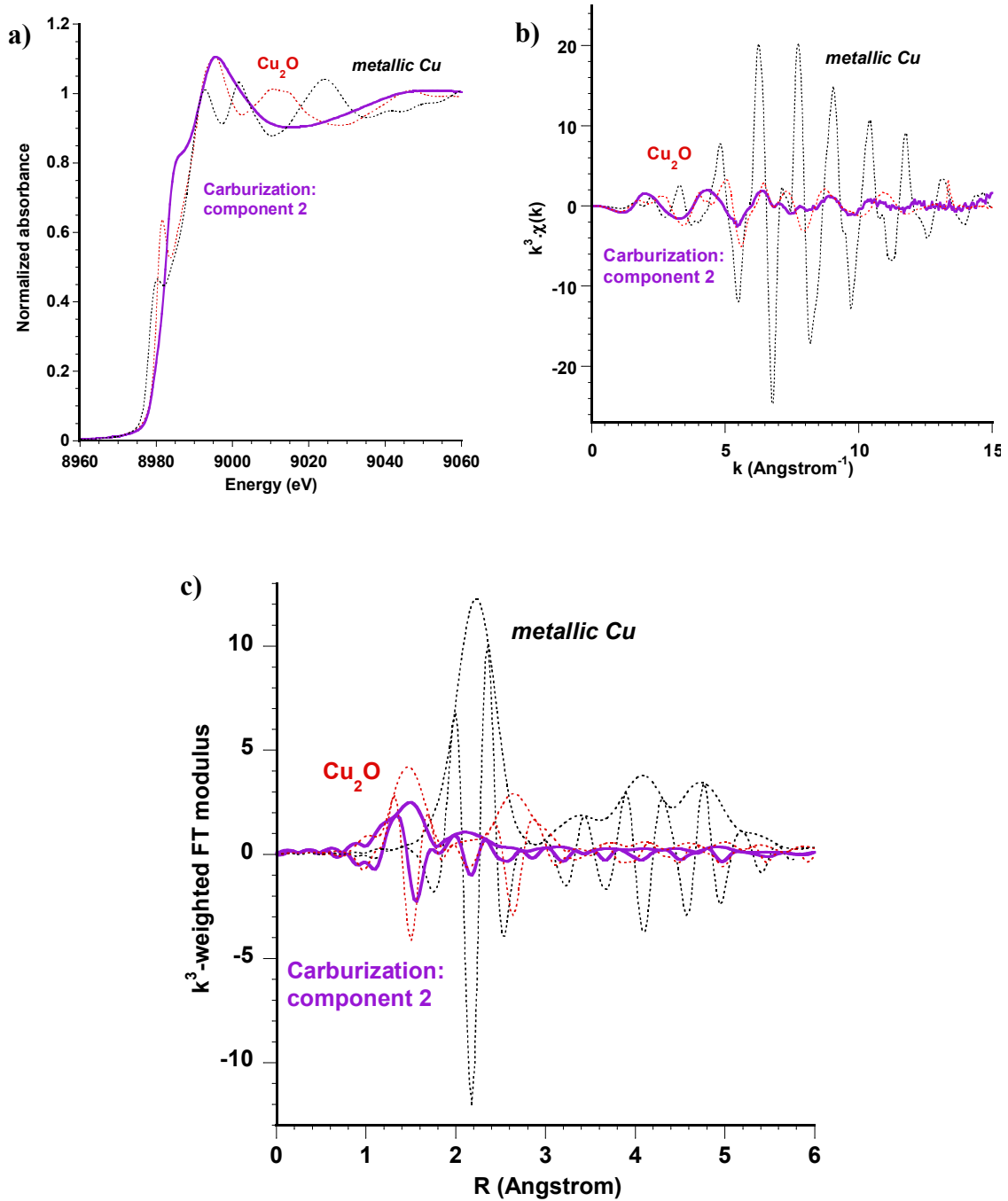


Figure 4.33. MCR-ALS analysis at the Cu-K edge of the carburization of  $\text{Cu-Mo}_x\text{C}_y/\text{SiO}_2$ : comparison of the first component with the calcined precursor. a) XANES spectrum, b) EXAFS oscillations, c) Fourier transform,  $k = 3.5 - 14 \text{ \AA}^{-1}$ .



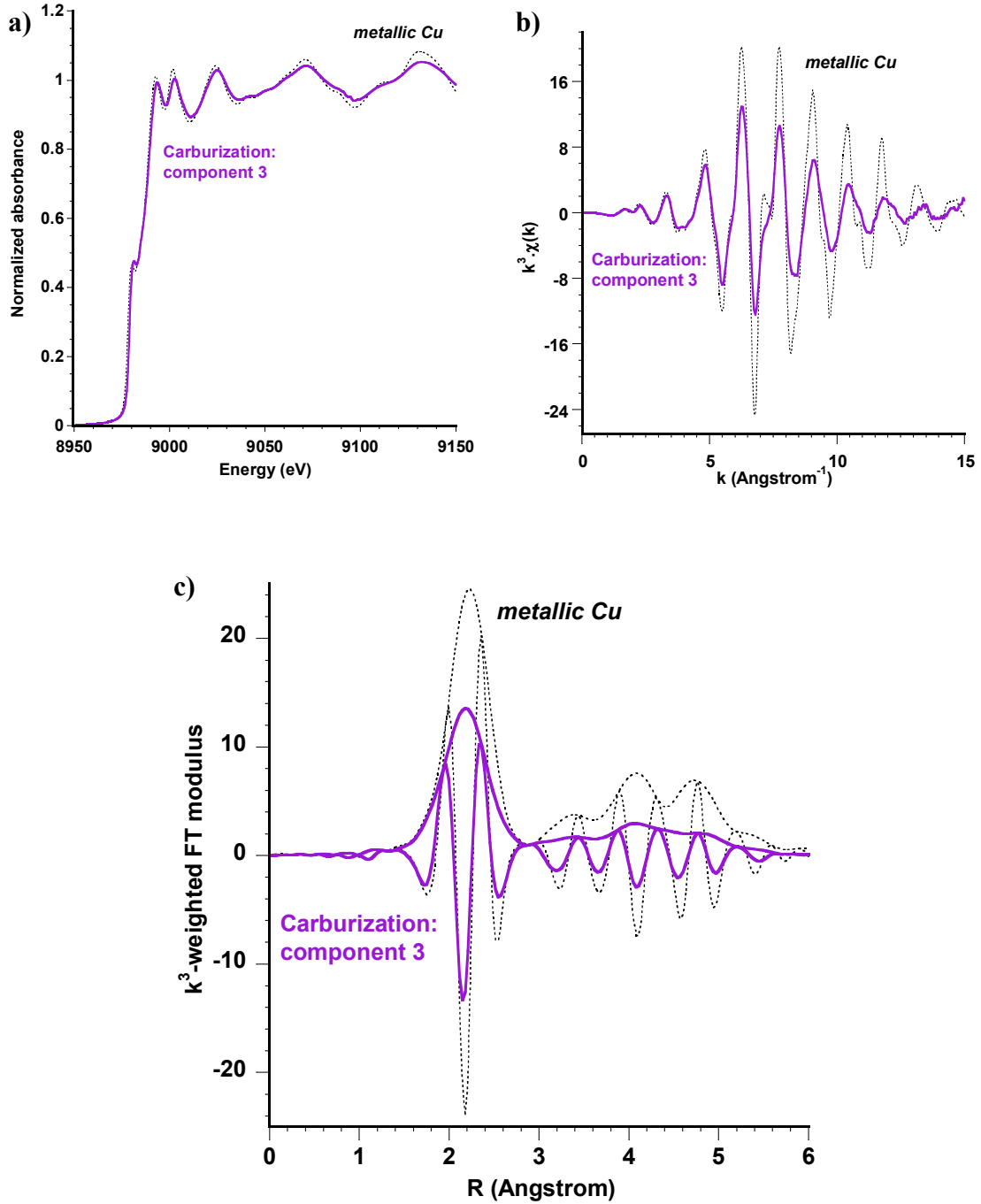
Reference: own author (2023)

Figure 4.34. MCR-ALS analysis at the Cu-K edge of the carburization of Cu-Mo<sub>x</sub>C<sub>y</sub>/SiO<sub>2</sub>: comparison of the second component with references Cu foil and Cu<sub>2</sub>O. a) XANES spectrum, b) EXAFS oscillations, c) Fourier transform,  $k = 3.5 - 14 \text{ \AA}^{-1}$ .



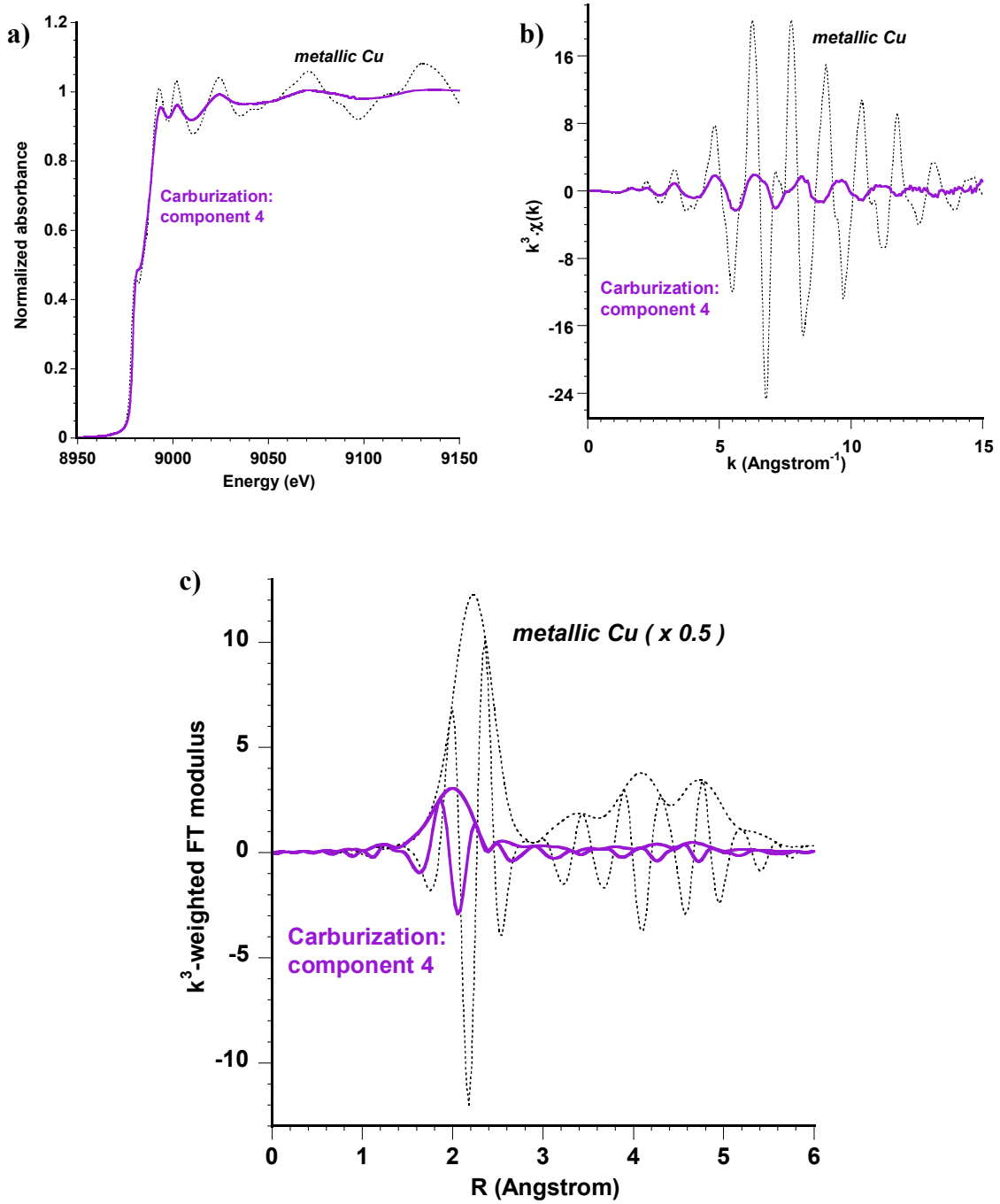
Reference: own author (2023)

Figure 4.35. MCR-ALS analysis at the Cu-K edge of the carburization of Cu-Mo<sub>x</sub>C<sub>y</sub>/SiO<sub>2</sub>: comparison of the third component with reference Cu foil. a) XANES spectrum, b) EXAFS oscillations, c) Fourier transform,  $k = 3.5 - 14 \text{ \AA}^{-1}$ .



Reference: own author (2023)

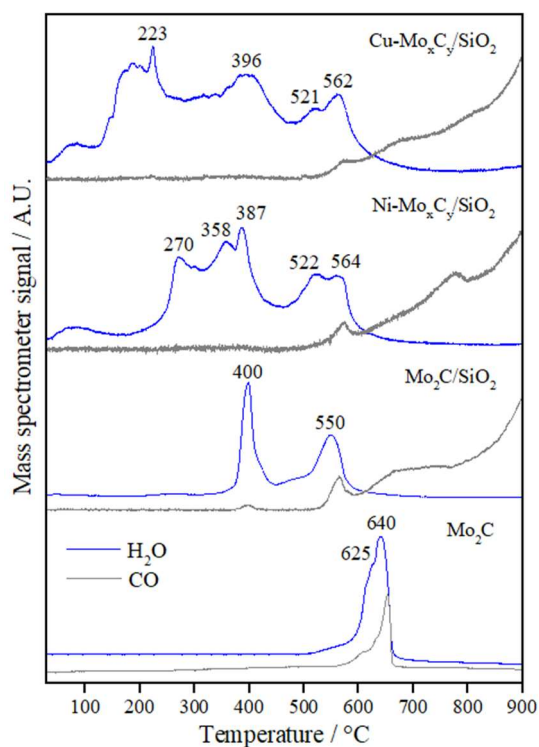
Figure 4.36. MCR-ALS analysis at the Cu-K edge of the carburization of Cu-Mo<sub>x</sub>C<sub>y</sub>/SiO<sub>2</sub>: comparison of the fourth component with reference Cu foil. a) XANES spectrum, b) EXAFS oscillations, c) Fourier transform,  $k = 3.5 - 14 \text{ \AA}^{-1}$ .



Reference: own author (2023)

The reduction of Mo oxides and the formation of Mo carbides during carburization with CH<sub>4</sub> and H<sub>2</sub> mixture was followed by temperature-programmed carburization in a parallel experiment (Figure 4.37), which revealed the associated production of water and CO.

Figure 4.37. Water and CO formation profiles during temperature-programmed carburization of the calcined precursors of Cu-Mo<sub>x</sub>C<sub>y</sub>/SiO<sub>2</sub>, Ni-Mo<sub>x</sub>C<sub>y</sub>/SiO<sub>2</sub>, Mo<sub>2</sub>C/SiO<sub>2</sub>, and Mo<sub>2</sub>C.

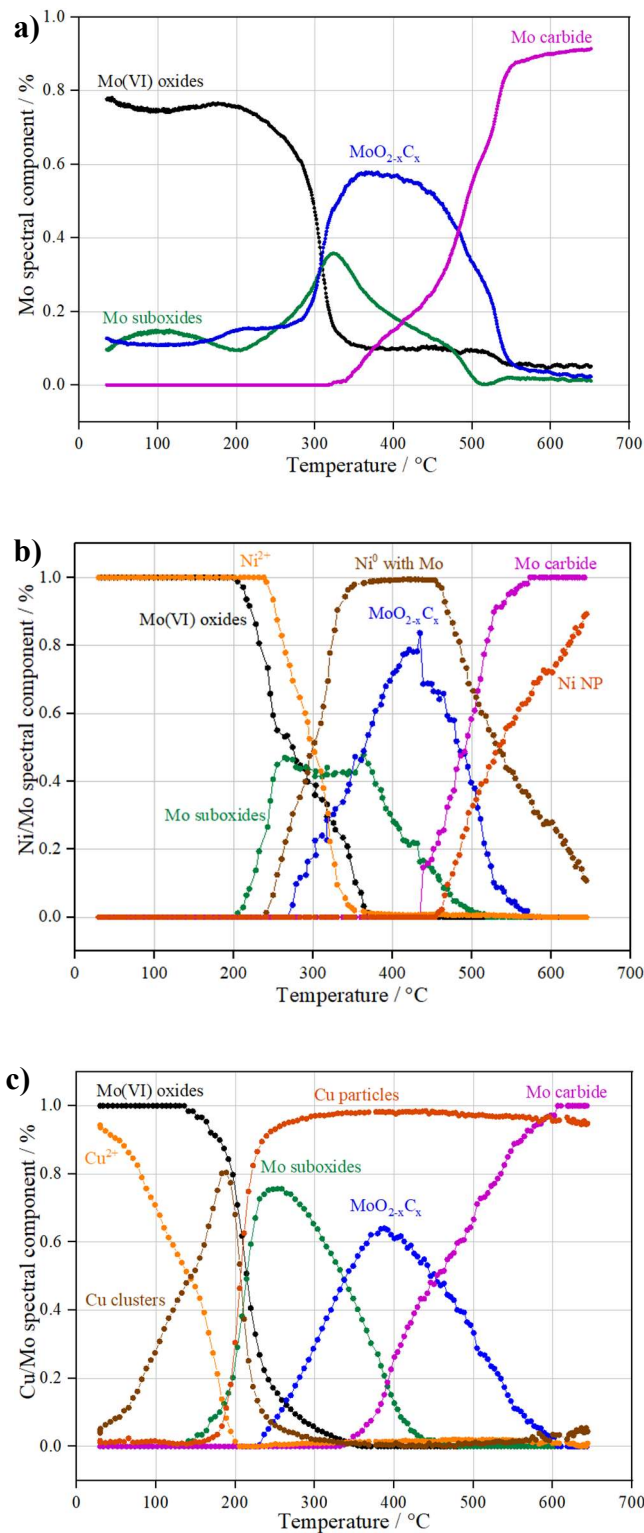


Reference: own author (2023)

The water signal during the carburization of the unsupported Mo<sub>2</sub>C catalyst showed a maximum at 640 °C with a shoulder at 625 °C (Figure 4.37). According to the literature, for the MoO<sub>3</sub> carburization taking place in an atmosphere of CH<sub>4</sub>/H<sub>2</sub>, the latter peak is ascribed to the reduction of MoO<sub>3</sub> to MoO<sub>2</sub>, while the former corresponds to the carburization of MoO<sub>2</sub> and formation of the Mo carbide (β-Mo<sub>2</sub>C), which is followed by the consumption of methane and production of CO (Hanif *et al.*, 2002; Lee, 1987; Oshikawa *et al.*, 2001; Xu *et al.*, 2015).

The thermograms of the supported catalysts, in special the bimetallic carbides, are way more complex and difficult to interpret, but the MCR-ALS analysis of the *in situ* XAS experiments sheds light on the changes of Mo, Ni and Cu speciation taking place during the ramp. The weights of each spectral component deduced from the MCR-ALS analysis are presented as a function of temperature in . Each curve corresponding to the disappearance of a species, by reduction or carburization, exhibits an inflection point (maximum rate of consumption), that should correspond to a peak of water or CO production on the thermograms, allowing identification of the various stages of reaction.

Figure 4.38. Concentrations profiles of Mo, Ni, and Cu species during TPC of the calcined precursors of a) Mo<sub>2</sub>C/SiO<sub>2</sub>, b) Ni-Mo<sub>x</sub>C<sub>y</sub>/SiO<sub>2</sub>, and c) Cu-Mo<sub>x</sub>C<sub>y</sub>/SiO<sub>2</sub> from MCR-ALS analysis of the Mo, Ni, and Cu K-edge data.



Reference: own author (2023)

By supporting the carbide on silica ( $\text{Mo}_2\text{C}/\text{SiO}_2$  catalyst), the transformations occur at clearly lower temperatures than for the bulk carbide. The main two peaks are shifted to 400 and 550 °C. XAS suggests that the very small production of water around 300 °C corresponds to the reduction by  $\text{H}_2$  of  $\text{MoO}_3$  to a Mo suboxide. The very low degree of reduction could validate the hypothesis of a reduction to  $\text{Mo}_4\text{O}_{11}$ , in which the reduction of Mo(VI) to Mo(V) concerns a minor number of Mo ions. Given the overlapping domains of the predominance of the second and third components, the exact attribution of the peak at 400 °C is more difficult. It could be associated with a further reduction of  $\text{Mo}_4\text{O}_{11}$  to the species providing the third spectral component, and minor concomitant production of CO could be linked to the starting carburization of a Mo fraction. The water production and onset of CO production at 550 °C correspond to the formation of the Mo carbide.

For the  $\text{Ni-Mo}_x\text{C}_y/\text{SiO}_2$  catalyst, the peaks at 270 and 358 °C are associated with the reduction of  $\text{MoO}_3$  and  $\text{NiMoO}_4$ , to  $\text{MoO}_2$  and groups of reduced Ni atoms. The reduction of  $\text{NiMoO}_4$  was indeed reported to occur in the 250 - 400 °C range in the literature (Silva *et al.*, 2019). Because of the slightly delayed reduction of  $\text{Ni}^{2+}$  concerning Mo(VI), which was checked not to be an analysis artifact by comparing the experimental spectra at the Mo and Ni K-edges in the 220 - 250 °C range,  $\text{NiMoO}_4$  seems to reduce after the reduction of  $\text{MoO}_3$  has started. Compared with  $\text{Mo}_2\text{C}/\text{SiO}_2$ , there is a significant gain in reduction temperature. The peak at 387 °C can be assigned to the reduction of  $\text{MoO}_2$  to the partly reduced oxide represented by the third spectral component. In this case, the reaction is not accompanied by a release of CO and the oxide may not exhibit carburization. As was the case for  $\text{Mo}_2\text{C}/\text{SiO}_2$ , the final Mo carburization takes place above 500 °C, in two stages that the MCR-ALS analysis cannot explain. It is accompanied by the formation of the fcc Ni nanoparticles (NP).

For the  $\text{Cu-Mo}_x\text{C}_y/\text{SiO}_2$  catalyst, the intensity of the water signal starts to increase at 120 °C and exhibits a maximum at 223 °C with several shoulders. These peaks are associated with the reduction of  $\text{Cu}^{2+}$  in the copper molybdate phases, followed by the rapid reduction of Mo(VI) oxides to  $\text{MoO}_2$ . Compared with the former systems, the gain in temperature for this reduction step is relevant. It may be associated with the poorly crystalline nature of the Cu molybdates and with the subsequent activation of  $\text{H}_2$  on the newly-formed Cu nanoparticles in the 200 - 225 °C range. The



next pronounced peak at 396 °C refers to the reduction of MoO<sub>2</sub> to the partly reduced oxide represented by the third spectral component, here again without the production of CO, and the final stages of carburization take place above 500 °C.

In conclusion, both the TPC profiles and MCR-ALS diagrams indicate that the last steps of reduction and carburization occur in the same temperature range for the three supported catalysts. The main gain upon the addition of a promoter concerns the initial reduction of Mo(VI) oxides and can be linked to the crystallinity of the mixed molybdates, and to the temperature at which metal particles able to activate H<sub>2</sub> are formed.

This effect was observed before by (Jung *et al.*, 2004b) during the carburization of MoO<sub>3</sub> promoted with Ni, Cu, Co, Pd, and Pt under CH<sub>4</sub>/H<sub>2</sub>. The presence of a promoter decreased the starting temperature of the initial reduction for all materials. Similarly, (Zhang *et al.*, 2011) observed by temperature-programmed reduction of NiO, MoO<sub>3</sub>, and NiMoO<sub>x</sub> in H<sub>2</sub> that Ni species in NiMoO<sub>x</sub> were more difficult to reduce than in NiO, while the Mo species were easily reduced in comparison with MoO<sub>3</sub>.

On the other hand, the presence of Ni and Cu as promoters has been reported to favor the carburization process because this metal causes the activation and dissociation of CH<sub>4</sub> into carbon and hydrogen at lower temperatures compared with non-promoted carbides (Jung *et al.*, 2004b; Zou *et al.*, 2016), but this is not observed in the present work.

It was also demonstrated that after completion of carburization, Ni and Cu are both present as metal nanoparticles, probably in strong stabilizing interaction with the underlying Mo carbide given their small size, but bimetallic NiMo or CuMo carbide phases were not formed. Ni nanoparticles appear more dispersed than Cu nanoparticles, and no Ni carbide is evidenced after carburization.

## 4.2 Conclusion

The carburization of a monometallic (Mo<sub>2</sub>C/SiO<sub>2</sub>) and bimetallic Mo carbides (Ni-Mo<sub>x</sub>C<sub>y</sub>/SiO<sub>2</sub> and Cu-Mo<sub>x</sub>C<sub>y</sub>/SiO<sub>2</sub>) under a CH<sub>4</sub>/H<sub>2</sub> mixture was investigated by

XAS and multivariate analysis of the spectra as a function of temperature. It was demonstrated that four successive groups of Mo species were involved in the carburization process: (i)  $\text{MoO}_3$  for  $\text{Mo}_2\text{C}/\text{SiO}_2$ , and a mixture of  $\text{MoO}_3$  and Ni/Cu-Mo(VI) molybdates for Ni- $\text{Mo}_x\text{C}_y/\text{SiO}_2$  and Cu- $\text{Mo}_x\text{C}_y/\text{SiO}_2$ , representing the Mo(VI) oxides present on the calcined precursors; (ii)  $\text{Mo}_4\text{O}_{11}$  ( $\text{Mo}_2\text{C}/\text{SiO}_2$ ) and  $\text{MoO}_2$  (Ni- $\text{Mo}_x\text{C}_y/\text{SiO}_2$  and Cu- $\text{Mo}_x\text{C}_y/\text{SiO}_2$ ) for Mo suboxides (oxidation state between IV and VI) formed by reduction of the Mo(VI) oxides; (iii)  $\text{MoO}_{2-x}\text{C}_x$  formed by reduction of the Mo suboxides and characterized by a limited degree of carburization (low production of CO); (iv)  $\text{Mo}_2\text{C}$  formed by the full carburization of  $\text{MoO}_{2-x}\text{C}_x$  (important production of CO).

TPC analysis was performed and compared to the XAS experiments. The synthesis of the monometallic carbide ( $\text{Mo}_2\text{C}/\text{SiO}_2$ ) proceeded by the reduction of  $\text{MoO}_3$  species present in the calcined precursor in the range of 300 to 400 °C and the final carbide was formed above 500 °C.

Regarding the bimetallic carbides, the results showed that the reduction of the Cu molybdates present in the calcined precursor of the Cu- $\text{Mo}_x\text{C}_y/\text{SiO}_2$  catalyst started at lower temperatures in comparison with Mo species in the monometallic carbide. The produced metallic Cu particles assisted the initial reduction of the Mo species in the Cu-promoted Mo carbide by providing more hydrogen.

On the other hand, Ni molybdates found in the calcined precursor of the Ni- $\text{Mo}_x\text{C}_y/\text{SiO}_2$  catalyst were reduced at higher temperatures than the Mo species and did not contribute to the first step of reduction. No bimetallic NiMo or CuMo carbide phases were formed and Ni and Cu were found only as nanoparticles in contact with the carbide phase. Finally, both metals did not assist in the formation of the Mo carbide at higher temperatures, which occurred at the same range of temperature as observed for the monometallic  $\text{Mo}_2\text{C}/\text{SiO}_2$  catalyst.

### 4.3 References

- Abdel-Dayem, H.M., 2007. Dynamic Phenomena during Reduction of  $\alpha$ -NiMoO<sub>4</sub> in Different Atmospheres: In-Situ Thermo-Raman Spectroscopy Study. *Ind. Eng. Chem. Res.* 46, 2466–2472. <https://doi.org/10.1021/ie0613467>
- Bouchy, C., Hamid, S. B. D-A., Derouane, E. G., 2000. Metastable fcc  $\alpha$ -MoC supported on HZSM5 - Preparation and catalytic performance for the non-oxidative conversion of methane to aromatic compounds. *Chem. Commun.*, 125-126.
- Dubale, A.A., Pan, C.-J., Tamirat, A.G., Chen, H.-M., Su, W.-N., Chen, C.-H., Rick, J., Ayele, D.W., Aragaw, B.A., Lee, J.-F., Yang, Y.-W., Hwang, B.-J., 2015. Heterostructured Cu<sub>2</sub>O/CuO decorated with nickel as a highly efficient photocathode for photoelectrochemical water reduction. *J. Mater. Chem. A* 3, 12482–12499. <https://doi.org/10.1039/C5TA01961C>
- Ehrenberg, H., Svoboda, I., Wltschek, G., Wiesmann, M., Trouw, F., Weitzel, H., Fuess, H., 1995. Crystal and magnetic structure of  $\alpha$ -NiMoO<sub>4</sub>. *J. Magn. Magn. Mater.* 150, 371-376.
- Halder, A., Lenardi, C., Timoshenko, J., Mravak, A., Yang, B., Kolipaka, L.K., Piazzoni, C., Seifert, S., Bonačić-Koutecký, V., Frenkel, A.I., Milani, P., Vajda, S., 2021. CO<sub>2</sub> Methanation on Cu-Cluster Decorated Zirconia Supports with Different Morphology: A Combined Experimental In Situ GIXANES/GISAXS, Ex Situ XPS and Theoretical DFT Study. *ACS Catal.* 11, 6210–6224. <https://doi.org/10.1021/acscatal.0c05029>
- Hanif, A., Xiao, T., York, A.P.E., Sloan, J., Green, M.L.H., 2002. Study on the Structure and Formation Mechanism of Molybdenum Carbides. *Chem. Mater.* 14, 1009–1015. <https://doi.org/10.1021/cm011096e>
- Huseyinova, S., Blanco, J., Requejo, F.G., Ramallo-López, J.M., Blanco, M.C., Buceta, D., López-Quintela, M.A., 2016. Synthesis of Highly Stable Surfactant-free Cu<sub>5</sub> Clusters in Water. *J. Phys. Chem. C* 120, 15902–15908. <https://doi.org/10.1021/acs.jpcc.5b12227>

- Jonane, I., Cintins, A., Kalinko, A., Chernikov, R., Kuzmin, A., 2018. X-ray absorption near edge spectroscopy of thermochromic phase transition in  $\text{CuMoO}_4$ . *Low Temperature Physics* 44, 434–437. <https://doi.org/10.1063/1.5034155>
- Joseph, N., Varghese, J., Siponkoski, T., Teirikangas, M., Sebastian, M.T., Jantunen, H., 2016. Glass-Free  $\text{CuMoO}_4$  Ceramic with Excellent Dielectric and Thermal Properties for Ultralow Temperature Cofired Ceramic Applications. *ACS Sustainable Chem. Eng.* 4, 5632–5639. <https://doi.org/10.1021/acssuschemeng.6b01537>
- Jung, K.T., Kim, W.B., Rhee, C.H., Lee, J.S., 2004. Effects of Transition Metal Addition on the Solid-State Transformation of Molybdenum Trioxide to Molybdenum Carbides. *Chem. Mater.* 16, 307–314. <https://doi.org/10.1021/cm030395w>
- Kurlov, A., Huang, X., Deeva, E.B., Abdala, P.M., Fedorov, A., Müller, C.R., 2020. Molybdenum carbide and oxycarbide from carbon-supported  $\text{MoO}_3$  nanosheets: phase evolution and DRM catalytic activity assessed by TEM and *in situ* XANES/XRD methods. *Nanoscale* 12, 13086–13094. <https://doi.org/10.1039/D0NR02908D>
- Lee, J., 1987. Molybdenum carbide catalysts I. Synthesis of unsupported powders. *Journal of Catalysis* 106, 125–133. [https://doi.org/10.1016/0021-9517\(87\)90218-1](https://doi.org/10.1016/0021-9517(87)90218-1)
- Liu, Yang, Marcella, N., Timoshenko, J., Halder, A., Yang, B., Kolipaka, L., Pellin, Michael.J., Seifert, S., Vajda, S., Liu, P., Frenkel, A.I., 2019. Mapping XANES spectra on structural descriptors of copper oxide clusters using supervised machine learning. *J. Chem. Phys.* 151, 164201. <https://doi.org/10.1063/1.5126597>
- Ma, Y., Guan, G., Phanthong, P., Hao, X., Huang, W., Tsutsumi, A., Kusakabe, K., Abudula, A., 2014a. Catalytic Activity and Stability of Nickel-Modified Molybdenum Carbide Catalysts for Steam Reforming of Methanol. *J. Phys. Chem. C* 118, 9485–9496. <https://doi.org/10.1021/jp501021t>
- Ma, Y., Guan, G., Shi, C., Zhu, A., Hao, X., Wang, Z., Kusakabe, K., Abudula, A., 2014b. Low-temperature steam reforming of methanol to produce hydrogen over various metal-doped molybdenum carbide catalysts. *International Journal of Hydrogen Energy* 39, 258–266. <https://doi.org/10.1016/j.ijhydene.2013.09.150>
- Mammen, N., Spanu, L., Tyo, E.C., Yang, B., Halder, A., Seifert, S., Pellin, M.J., Vajda, S., Narasimhan, S., 2019. Using first principles calculations to interpret XANES

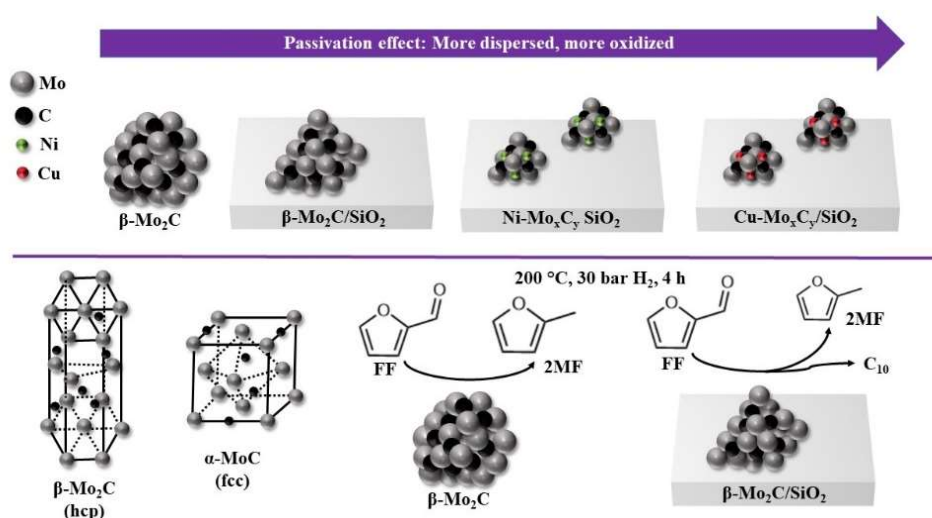
- experiments: extracting the size-dependence of the ( $p$ ,  $T$ ) phase diagram of sub-nanometer Cu clusters in an O<sub>2</sub> environment. *J. Phys.: Condens. Matter* 31, 144002. <https://doi.org/10.1088/1361-648X/aafcf9>
- Mammen, N., Spanu, L., Tyo, E.C., Yang, B., Halder, A., Seifert, S., Pellin, M.J., Vajda, S., Narasimhan, S., 2018. Reversing Size-Dependent Trends in the Oxidation of Copper Clusters through Support Effects. *Eur. J. Inorg. Chem.* 2018, 16–22. <https://doi.org/10.1002/ejic.201701355>
- Mo, T., Xu, J., Yang, Y., Li, Y., 2016. Effect of carburization protocols on molybdenum carbide synthesis and study on its performance in CO hydrogenation. *Catalysis Today* 261, 101–115. <https://doi.org/10.1016/j.cattod.2015.07.014>
- Nayak, C., Bhattacharyya, D., Jha, S.N., Sahoo, N.K., 2018. In Situ XAS Study on Growth of PVP-Stabilized Cu Nanoparticles. *ChemistrySelect* 3, 7370–7377. <https://doi.org/10.1002/slct.201801358>
- Oshikawa, K., Nagai, M., Omi, S., 2001. Characterization of Molybdenum Carbides for Methane Reforming by TPR, XRD, and XPS. *J. Phys. Chem. B* 105, 9124–9131. <https://doi.org/10.1021/jp0111867>
- Oyanagi, H., Sun, Z.H., Jiang, Y., Uehara, M., Nakamura, H., Yamashita, K., Orimoto, Y., Zhang, L., Lee, C., Fukano, A., Maeda, H., 2012. Small copper clusters studied by x-ray absorption near-edge structure. *Journal of Applied Physics* 111, 084315. <https://doi.org/10.1063/1.3700346>
- Patterson, B.D., Abela, R., 2010. Novel opportunities for time-resolved absorption spectroscopy at the X-ray free electron laser. *Phys. Chem. Chem. Phys.* 12, 5647. <https://doi.org/10.1039/c003406a>
- Ressler, T., Jentoft, R.E., Wienold, J., Günter, M.M., Timpe, O., 2000. In Situ XAS and XRD Studies on the Formation of Mo Suboxides during Reduction of MoO<sub>3</sub>. *J. Phys. Chem. B* 104, 6360–6370. <https://doi.org/10.1021/jp000690t>
- Saravanakumar, B., Ravi, G., Yuvakkumar, R., Ganesh, V., Guduru, R.K., 2019. Synthesis of polyoxometalates, copper molybdate (Cu<sub>3</sub>Mo<sub>2</sub>O<sub>9</sub>) nanopowders, for energy storage applications. *Materials Science in Semiconductor Processing* 93, 164–172. <https://doi.org/10.1016/j.mssp.2019.01.002>

- Schaidle, J.A., Schweitzer, N.M., Ajenifujah, O.T., Thompson, L.T., 2012. On the preparation of molybdenum carbide-supported metal catalysts. *Journal of Catalysis* 289, 210–217. <https://doi.org/10.1016/j.jcat.2012.02.012>
- Silva, C.G., Passos, F.B., da Silva, V.T., 2019. Influence of the support on the activity of a supported nickel-promoted molybdenum carbide catalyst for dry reforming of methane. *Journal of Catalysis* 375, 507–518. <https://doi.org/10.1016/j.jcat.2019.05.024>
- Smirnov, A. A., Shilov, I. N., Saraev, A. A., Kauchev, V. V., Bulavchenko, O. A., Zavarukhin, S. G., Yakovlev, V. A., 2019. Hydrogenation of Furfural to 2-Methylfuran over Ni-Mo<sub>2</sub>C- $\gamma$ -Al<sub>2</sub>O<sub>3</sub> catalyst. *WSEAS Trans. Environ. Dev.* 15, 189-196.
- Struis, R.P.W.J., Bachelin, D., Ludwig, C., Wokaun, A., 2009. Studying the Formation of Ni<sub>3</sub>C from CO and Metallic Ni at  $T = 265$  °C in Situ Using Ni K-Edge X-ray Absorption Spectroscopy. *J. Phys. Chem. C* 113, 2443–2451. <https://doi.org/10.1021/jp809409c>
- Tan, W., Luan, J., 2020. Investigation into the synthesis conditions of CuMoO<sub>4</sub> by an *in situ* method and its photocatalytic properties under visible light irradiation. *RSC Adv.* 10, 9745–9759. <https://doi.org/10.1039/D0RA00496K>
- Xu, W., Ramírez, P.J., Stacchiola, D., Brito, J.L., Rodriguez, J.A., 2015. The Carburation of Transition Metal Molybdates (MxMoO<sub>4</sub>, M = Cu, Ni or Co) and the Generation of Highly Active Metal/Carbide Catalysts for CO<sub>2</sub> Hydrogenation. *Catal Lett* 145, 1365–1373. <https://doi.org/10.1007/s10562-015-1540-5>
- Zandkarimi, B., Sun, G., Halder, A., Seifert, S., Vajda, S., Sautet, P., Alexandrova, A.N., 2020. Interpreting the Operando XANES of Surface-Supported Subnanometer Clusters: When Fluxionality, Oxidation State, and Size Effect Fight. *J. Phys. Chem. C* 124, 10057–10066. <https://doi.org/10.1021/acs.jpcc.0c02823>
- Zhang, A., Zhu, A., Chen, B., Zhang, S., Au, C., Shi, C., 2011. In-situ synthesis of nickel modified molybdenum carbide catalyst for dry reforming of methane. *Catalysis Communications* 12, 803–807. <https://doi.org/10.1016/j.catcom.2011.01.019>
- Zheng, Y., Tang, Y., Gallagher, J.R., Gao, J., Miller, J.T., Wachs, I.E., Podkolzin, S.G., 2019. Molybdenum Oxide, Oxycarbide, and Carbide: Controlling the Dynamic

Composition, Size, and Catalytic Activity of Zeolite-Supported Nanostructures. *J. Phys. Chem. C* 123, 22281–22292. <https://doi.org/10.1021/acs.jpcc.9b05449>

Zou, H., Chen, S., Huang, J., Zhao, Z., 2016. Effect of additives on the properties of nickel molybdenum carbides for the tri-reforming of methane. *International Journal of Hydrogen Energy* 41, 16842–16850. <https://doi.org/10.1016/j.ijhydene.2016.07.108>

# CHAPTER 5. HYDRODEOXYGENATION OF FURFURAL OVER UNSUPPORTED AND SiO<sub>2</sub>-SUPPORTED Mo<sub>2</sub>C AND METAL-PROMOTED Mo CARBIDES. TUNNING THE SELECTIVITY BETWEEN 2-METHYLFURAN AND C<sub>10</sub> FUROINS DIESEL PRECURSORS



## Abstract

The hydrodeoxygenation of furfural (FF) over Mo carbides in liquid phase at 200 °C, 30 bar of H<sub>2</sub> for 4 h in 2-butanol was investigated. Unsupported and SiO<sub>2</sub>-supported Mo-carbide with different crystallographic phases ( $\beta\text{-Mo}_2\text{C}/\text{SiO}_2$  and  $\alpha\text{-MoC}/\text{SiO}_2$ ), and in the presence of Cu or Ni as promoters were studied. The reactivation effect under H<sub>2</sub> atmosphere of the passivated Mo carbides was investigated by XAS. The results show that Mo is present as more or less oxidized in the passivated catalysts, with a more severe oxidation in the bimetallic systems. In these cases, the original carbides are not restored after reactivation. The product distribution for the HDO of furfural depended on catalyst oxidation degree. In the less oxidized Mo carbide ( $\beta\text{-Mo}_2\text{C}$ ), a higher yield to 2-methylfuran is obtained, while C<sub>10</sub> condensation products are formed in the more oxidized catalysts.



## 5. INTRODUCTION

As demonstrated in Chapter 2, the HDO of furfural has been reported to occur mainly over Cu (Gong *et al.*, 2018b, 2017; Seemala *et al.*, 2018), Ni (Jaatinen *et al.*, 2016; Yantao Wang *et al.*, 2018) and bimetallic catalysts (Fu *et al.*, 2017; Kalong *et al.*, 2021b; Srivastava *et al.*, 2017) and many catalysts tested for the HDO of furfural are based on noble metals such as Re (Chuseang *et al.*, 2021; Toledo *et al.*, 2019; Zhou *et al.*, 2020b), Ru (Panagiotopoulou *et al.*, 2014; Panagiotopoulou and Vlachos, 2014; Wang *et al.*, 2017), Ir (Date *et al.*, 2018), Pt (Dohade and Dhepe, 2018) and Pd (Antunes *et al.*, 2018).

In general, Cu-based catalysts are selective in breaking C-O bonds, because they adsorb furfural in the  $\eta^1$ -(O) configuration via the aldehyde function (Chen *et al.*, 2018), but they exhibit poor ability to dissociate hydrogen and hence led to low activity. In contrast, Ni-based catalysts readily dissociate hydrogen (Pozzo and Alfè, 2009), but it is poorly selective as it can hydrogenate the aromatic furan ring of furfural due to its adsorption in the  $\eta^2$ -(C,O)-aldehyde mode, leading the catalyst to interact with both the aldehyde group and the furan ring (Chen *et al.*, 2018).

Transition metal carbides proved to be quite selective in breaking C=O, C-OH, and C-O-C bonds in HDO reactions (Smith, 2020; Sullivan *et al.*, 2016; Zhou *et al.*, 2021). The catalytic activity of carbides has already been considered comparable to that of noble metals (Levy and Boudart, 1973; Xiong *et al.*, 2014). The thermodynamically stable hexagonal close-packed (hcp)  $\beta$ -Mo<sub>2</sub>C and metastable face-centered cubic (fcc)  $\alpha$ -MoC structures are the most common phases of Mo carbides (Xu *et al.*, 2014). Knowing the crystallographic phase of the carbide is important because this causes them to perform differently depending on the reaction. For example,  $\beta$ -Mo<sub>2</sub>C was more active than  $\alpha$ -MoC in the hydrogenation of 1,3-butadiene (Yang *et al.*, 2022), CO<sub>2</sub> hydrogenation (Xu *et al.*, 2014), dehydrogenation of benzyl alcohol (Z. Li *et al.*, 2014), HDO of thiophene (Mccrea *et al.*, 1997), hydrogenolysis of n-butane (Lee, 1990). On the other hand,  $\alpha$ -MoC was more active than  $\beta$ -Mo<sub>2</sub>C in the HDO of stearic acid (Souza Macedo *et al.*, 2019), and in the reforming of CH<sub>4</sub> (Tsuji *et al.*, 2000).

The addition of metals such as Ni (Cheng and Huang, 2010; Ma *et al.*, 2014b; Zou *et al.*, 2016), Pt (Ma *et al.*, 2014c), Co (Lin *et al.*, 2018) has been reported to enhance the catalytic performance of Mo carbides by either promoting hydrogen activation or removal of graphitic carbon deposited on the catalyst surface at the end of their synthesis (Jung *et al.*, 2004a; Ma *et al.*, 2014b, 2014c; Zhang *et al.*, 2011; Zou *et al.*, 2016). As a consequence, the use of promoters can enhance the activity of Mo carbides catalysts as observed in many reactions such as steam reforming of methanol (Ma *et al.*, 2014b, 2014c), steam reforming of CH<sub>4</sub> (Cheng and Huang, 2010; Zou *et al.*, 2016), and water-gas shift reaction (Nagai *et al.*, 2006).

Another important point concerning the use of carbides, especially in liquid phase reactions, is related to the necessity of performing an oxidative passivation treatment of the materials due to their pyrophoric nature (Hanif *et al.*, 2002; Lee, 1987). For this reason, the performance of the catalysts relies on the efficiency of the reactivation under H<sub>2</sub> needed to remove the oxidized layers from the carbides before exposure to reactants. Although there are some studies on passivation methodologies using different gases (Bogatin *et al.*, 1991; Mehdad *et al.*, 2017; Wu *et al.*, 2004), only a few studies in the literature focus on the reactivation of the passivated carbides and their final state prior to reaction (Leary *et al.*, 1987; Leclercq *et al.*, 1995; Mehdad *et al.*, 2017; Shou *et al.*, 2012; Zhu *et al.*, 2020). The composition of the reactivated phases is important for catalysis since the presence of oxygen is reported to add acidic properties to the carbides and modify the selectivity to the products (Lee *et al.*, 2014; Sullivan *et al.*, 2016).

Therefore, the aim of this chapter was to investigate the performance of Mo carbides for the HDO of furfural in liquid phase. Unsupported and SiO<sub>2</sub>-supported Mo carbides catalysts were compared and the effect of the Mo carbide crystallographic phases on supported catalysts ( $\beta$ -Mo<sub>2</sub>C/SiO<sub>2</sub> and  $\alpha$ -MoC/SiO<sub>2</sub>) was also evaluated. Furthermore, the addition of Cu or Ni, two metals widely used in the HDO of furfural (Khemthong *et al.*, 2021; Natsir and Shimazu, 2020), was also studied. The reactivation of these catalysts under pure hydrogen was studied by X-ray absorption analysis (XAS) in order to establish a relationship between catalyst structure and performance.

## 5.1 Results and discussions

### 5.1.1 Characterization

Elemental analysis and ICP-OES were performed to estimate the content of Mo, Cu, Ni, and C species in the passivated catalysts (Table 5.1). The results show that after passivation, the C/Mo molar ratio is lower than expected from the given chemical formula of the carbide: 0.36 - 0.45 for the  $\beta$ -Mo<sub>2</sub>C catalysts (instead of 0.50) and 0.5 for  $\alpha$ -MoC (instead of 1).

The textural properties of SiO<sub>2</sub> and passivated catalysts determined by N<sub>2</sub> physisorption are reported in Table 5.1. A decrease in the specific surface area (SSA) and pore volume (P<sub>v</sub>) was observed after the synthesis of supported carbides compared to the bare support, consistent with the formation of 20 wt.% Mo<sub>2</sub>C, which is a nonporous material with a very low surface area. The N<sub>2</sub> adsorption-desorption isotherms are displayed in Figure 5.1. All supported catalysts showed a profile similar to that of bare SiO<sub>2</sub>, which, according to IUPAC classification, corresponds to a type II isotherm, with an H3 hysteresis loop (Thommes *et al.*, 2015).

Table 5.1. Chemical composition and textural properties of SiO<sub>2</sub> and passivated catalysts, and crystallite diameter (Dc) of Mo carbide phase calculated from XRD.

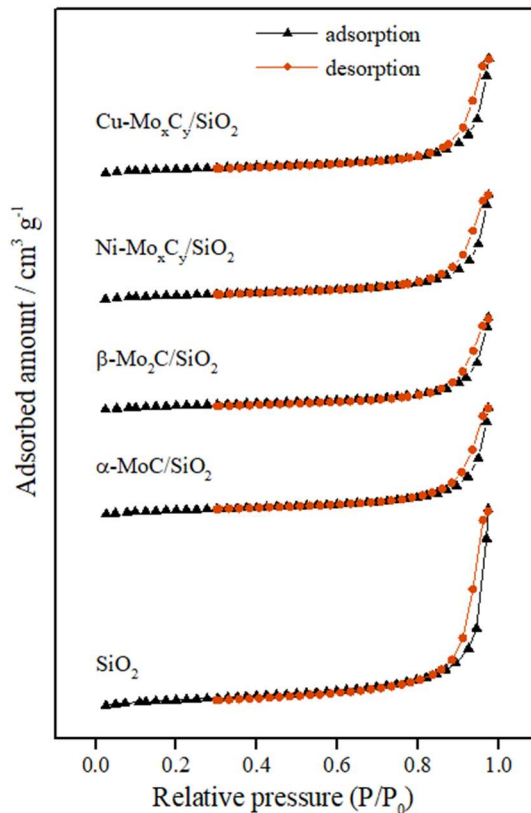
Material	Content (wt. %)					SSA <sup>a</sup> (m <sup>2</sup> g <sup>-1</sup> )	P <sub>v</sub> <sup>b</sup> (cm <sup>3</sup> g <sup>-1</sup> )	Dc (nm)
	Mo	C	Ni	Cu	active phase			
SiO <sub>2</sub>	-	-	-	-	-	198	1.13	-
β-Mo <sub>2</sub> C	-	-	-	-	-	13	0.01	9
β-Mo <sub>2</sub> C/SiO <sub>2</sub>	17.6	0.8	-	-	18.4	140	0.53	5
α-MoC/SiO <sub>2</sub>	17.7	1.1	-	-	18.8	140	0.61	4
Ni-Mo <sub>x</sub> C <sub>y</sub> /SiO <sub>2</sub>	16.0	0.9	2.8	-	19.7	142	0.60	3
Cu-Mo <sub>x</sub> C <sub>y</sub> /SiO <sub>2</sub>	14.9	0.8	-	2.0	17.7	137	0.66	3
Ni/SiO <sub>2</sub>	-	-	2.6	-	2.6	187	1.07	14
Cu/SiO <sub>2</sub>	-	-	-	2.1	2.1	185	0.70	40

<sup>a</sup> Determined by the BET method

<sup>b</sup> Determined by the BJH method

Reference: own author (2023)

Figure 5.1. N<sub>2</sub> adsorption-desorption isotherms of SiO<sub>2</sub> and passivated catalysts.



Reference: own author (2023)

After passivation (Figure 5.2), the diffractograms of unsupported and supported monometallic carbides prepared by direct carburization exhibited the characteristic diffraction lines of the hexagonal  $\beta$ -Mo<sub>2</sub>C phase (JCPDS 35-0787) at  $2\theta = 34.4^\circ, 37.8^\circ, 39.4^\circ, 61.5^\circ,$  and  $74.6^\circ$ . For the catalyst that was first nitrated and then carburized, a typical pattern of the  $\alpha$ -MoC phase was observed (Wan *et al.*, 2014; Yang *et al.*, 2021). The broad peak at  $2\theta = 21.9^\circ$  corresponds to a classical pattern of amorphous SiO<sub>2</sub> (JCPDS 39-1425).

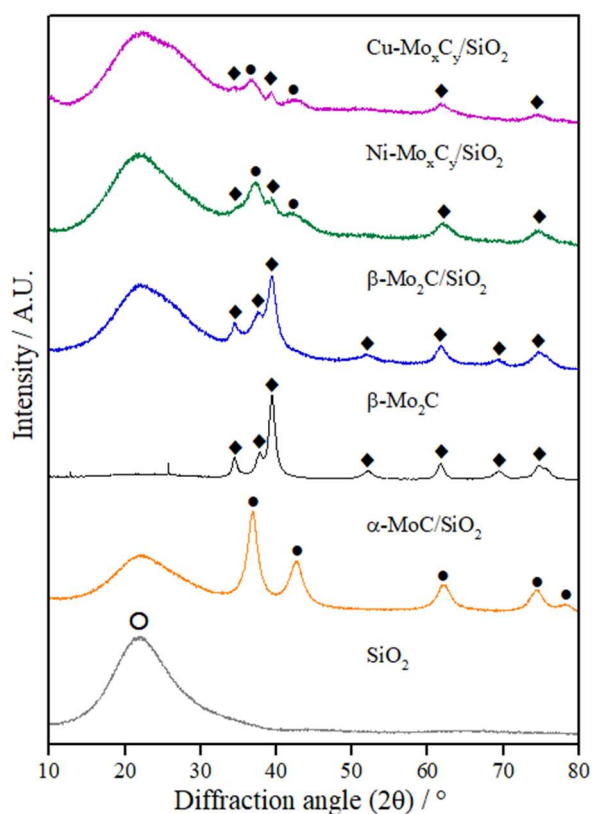
For the passivated Ni- or Cu- promoted carbides, poorly crystalline  $\beta$ -Mo<sub>2</sub>C and  $\alpha$ -MoC carbide phases were detected, although the preparation and passivation methodology were the same as for the monometallic carbide. No phases containing Ni and Cu, including bimetallic carbides, were observed. The presence of bimetallic carbides is commonly observed when sulphates are used as precursors during the preparation of the catalysts; when nitrate precursors are employed, metallic Ni on top of  $\beta$ -Mo<sub>2</sub>C has been observed for Ni-Mo catalysts after carburization (Xu *et al.*, 2015). This result is also in agreement with the results presented in Chapter 4, in which we observed by XAS the formation of Ni nanoparticles in strong interaction with  $\beta$ -Mo<sub>2</sub>C after carburization of Ni-Mo<sub>x</sub>C<sub>y</sub>/SiO<sub>2</sub> catalyst.

The presence of the  $\alpha$ -MoC phase has been observed before for carbides promoted with Ni (Smirnov *et al.* 2019; Jung *et al.*, 2004b) and Cu (Liu *et al.*, 2016; Ma *et al.*, 2014a) metals, but it seems that the formation of this phase is not easily predictable. The formation of cubic  $\alpha$ -MoC in Cu-promoted Mo carbides was related to the increase of Cu loading from the Cu/Mo molar ratio of 1.6/98.4 to 10/90, while a further increase to 15/85 and 25/75 led to the decrease and near disappearance of  $\alpha$ -MoC, respectively (Ma *et al.*, 2014a).

In another work, however, the  $\alpha$ -MoC formation was only observed for unsupported Mo carbides promoted with Ni, Pd, and Pt, which were able to promote the hydrogen and methane activation at lower temperatures during temperature-programmed carburization compared to Cu and Co metals (Jung *et al.*, 2004b). Despite this, several Ni-promoted Mo carbides exhibited only the formation of the  $\beta$ -Mo<sub>2</sub>C phase (A. Dantas *et al.*, 2018; Barbosa *et al.*, 2021; Ma *et al.*, 2014b, 2014c; Silva *et al.*, 2019; T. Zhang *et al.*, 2018).

The mean crystallite diameter ( $D_c$ ) of the carbide phase was estimated by the Scherrer equation and the results are reported in Table 5.1. The unsupported  $\beta$ - $\text{Mo}_2\text{C}$  showed the largest crystallite diameter (9 nm).  $D_c$  is smaller on the monometallic supported catalysts, between 4 - 5 nm, indicating that supporting the Mo carbide phase increased its dispersion. Finally, the bimetallic catalysts showed the lowest value of  $D_c$  (3 nm).

Figure 5.2. Diffractograms of  $\text{SiO}_2$  and passivated Mo carbides.  $\blacklozenge$   $\beta$ - $\text{Mo}_2\text{C}$ ,  $\bullet$   $\alpha$ - $\text{MoC}$ ,  $\circ$   $\text{SiO}_2$ .



Reference: own author (2023)

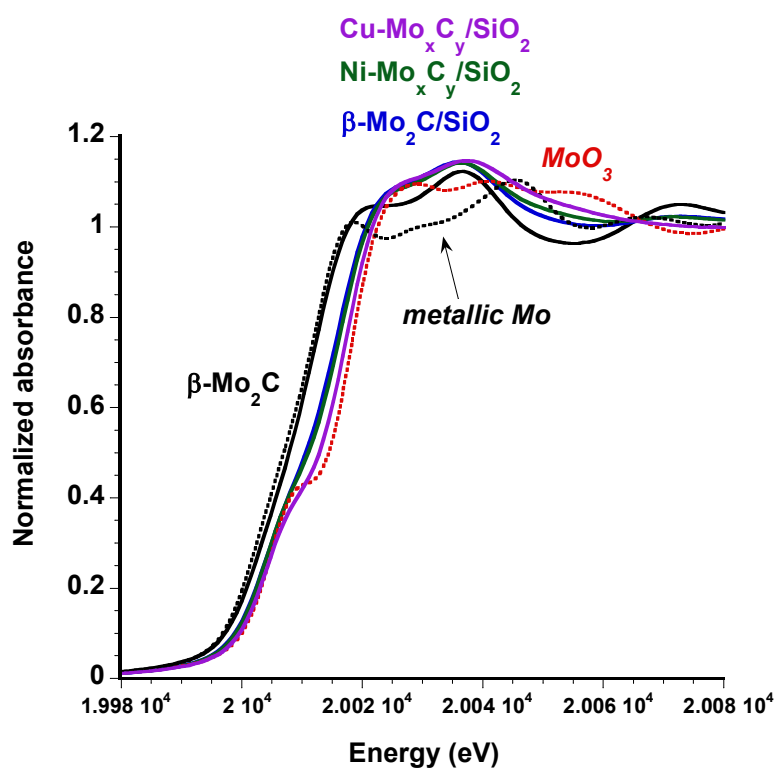
Information on the *in situ* formation of the Mo carbides on  $\beta$ - $\text{Mo}_2\text{C}/\text{SiO}_2$ ,  $\text{Ni-Mo}_x\text{C}_y/\text{SiO}_2$ , and  $\text{Cu-Mo}_x\text{C}_y/\text{SiO}_2$  followed by X-ray absorption spectroscopy, multivariate analysis of the spectra as a function of temperature and, temperature-programmed carburization can be found in Chapter 4. It was found that the carburization process involved four successive groups of Mo species: (i) Mo(VI) oxides

present on the calcined precursors; (ii) Mo suboxides (oxidation state between IV and VI) formed by reduction of the Mo(VI) oxides; (iii) a species denoted as  $\text{MoO}_{2-x}\text{C}_x$  formed by reduction of the Mo suboxides and characterized by a limited degree of carburization (low production of CO); (iv) the final Mo carbide formed by the full carburization of  $\text{MoO}_{2-x}\text{C}_x$  (important production of CO). Only well-crystallized Mo carbide was detected by *in situ* XAS at the end of the carburization step.

Additionally, on the bimetallic catalysts, Ni appeared after carburization as highly dispersed metallic particles (about 1 nm) in strong interaction with the Mo carbide, and Cu as metallic particles formed at a lower temperature and larger in size than Ni.

The passivation of the supported catalysts by diluted  $\text{O}_2$  is expected to strongly alter the nature of the phases, and X-ray diffraction only gives access to the carbide phases that conserve a long-range order. Figure 5.3 compares the XANES spectra of the supported passivated catalysts at the Mo K-edge with that of metallic Mo,  $\text{MoO}_3$ , and standard unsupported passivated  $\beta\text{-Mo}_2\text{C}$ . While the bulk carbide is only slightly oxidized, the XANES spectra of the supported catalysts significantly shift towards higher energies, not far from the position of the Mo(VI) edge in  $\text{MoO}_3$ , especially for the Cu- $\text{Mo}_x\text{C}_y/\text{SiO}_2$  catalyst. This pronounced oxidation can be linked to the more dispersed state of the Mo carbide particles on  $\text{SiO}_2$ , compared with the bulk carbide that is only superficially oxidized. The EXAFS signals are also significantly changed (Figure 5.4). The oscillations at low energy (those most influenced by light atoms such as O) resemble those recorded on  $\text{MoO}_3$  for the most oxidized catalyst. The Fourier transforms (Figure 5.5) still present the strong peak related to Mo next-nearest neighbors in Mo carbides though with low intensity, but the peak of nearest neighbors (the C shell in the carbide) has changed noticeably, in particular for the most oxidized catalyst, Cu- $\text{Mo}_x\text{C}_y/\text{SiO}_2$ .

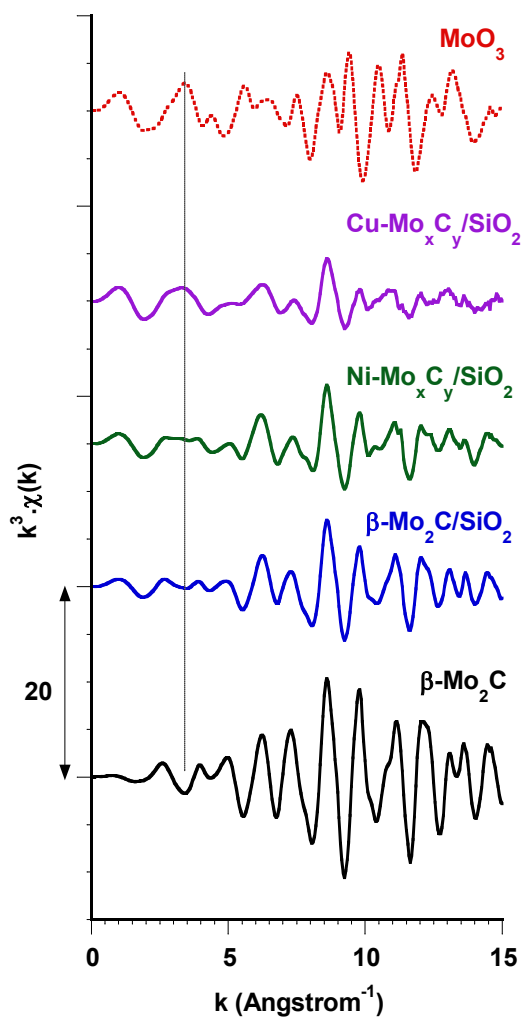
Figure 5.3. XANES spectra recorded at the Mo K-edge for the passivated catalysts (spectra recorded at room temperature). Comparison with references MoO<sub>3</sub> and metallic Mo (dotted lines).



Reference: own author (2023)

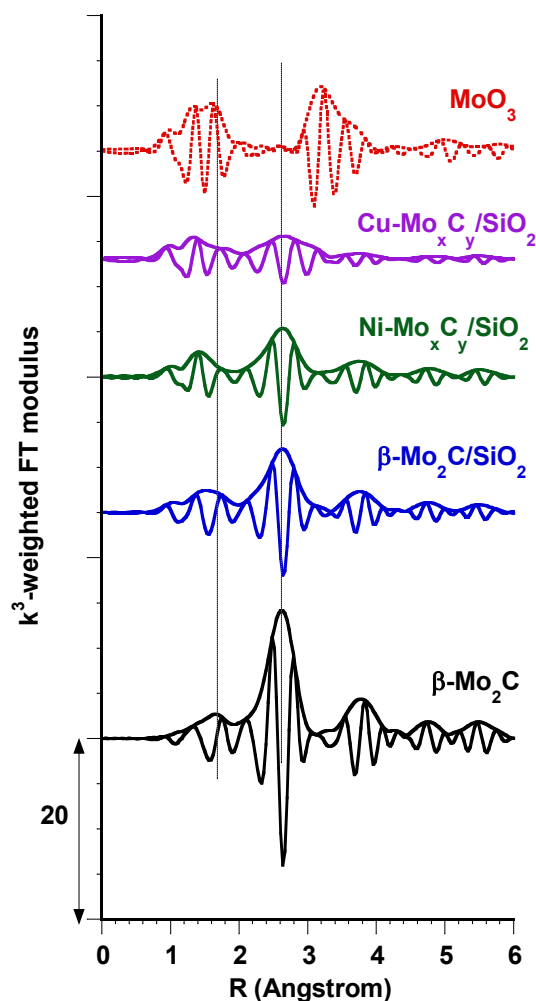


Figure 5.4. EXAFS signals recorded at the Mo K-edge for the passivated catalysts (spectra recorded at room temperature). Comparison with reference  $\text{MoO}_3$ .



Reference: own author (2023)

Figure 5.5. Fourier transforms of the EXAFS signals recorded at the Mo K-edge for the passivated catalysts ( $k = 3.5 - 15 \text{ \AA}^{-1}$ , spectra recorded at room temperature). Comparison with reference  $\text{MoO}_3$ .



Reference: own author (2023)

Attempts to fit this mixture of Mo oxides and carbides with a limited number of parameters did not prove successful, with much information from the EXAFS signals left unexplained. The composition of the passivated catalysts was thus evaluated by comparing the XANES spectra and EXAFS experimental signals with linear combinations of the four spectral components extracted by MCR-ALS analysis during carburization process of the solids: fully oxidized Mo, partly reduced Mo oxide, partly oxidized Mo carbide, and Mo carbide. The validity of this analysis is strengthened by the similarity between the XANES spectrum of  $\text{Mo}_{2-x}\text{C}_x$  and that of oxycarbides recorded during the passivation and reactivation processes of Mo carbides and reported

in the literature (Kurlov *et al.*, 2020; Zheng *et al.*, 2019). The linear combinations were optimized using the Athena software, in the XANES region (edge  $\pm 40$  eV) and on the  $k^3$ -weighted EXAFS oscillations. It should be noted that the limit of this procedure lies in the fact that the EXAFS spectral components from the intermediate species were extracted in the 200 - 400 °C range, while the initial and final spectra were recorded at room temperature, prior to and after carburization. Nevertheless, the fits in the XANES and the EXAFS domains led to similar tendencies, with differences of only  $\pm 3\%$ , and except in one case they will not be reported individually.

Values deduced from the linear combinations are presented in Table 5.2 (first line for each catalyst) and the comparison with the results extracted from the MCR-ALS analysis of the reactivation ramp (second line, in italic). The comparison of the linear combinations with the experimental results is shown in Figures 5.6 and 5.7. A comparison, detailed in the next sections, also gives a very good agreement in most cases.

Unsupported  $\beta$ -Mo<sub>2</sub>C appears as only slightly oxidized to an oxycarbide form, whereas the main contributions for the supported samples are Mo(VI) oxides and Mo carbide. The proportion of Mo(VI) oxides increases in the order:  $\beta$ -Mo<sub>2</sub>C/SiO<sub>2</sub> < Ni-Mo<sub>x</sub>C<sub>y</sub>/SiO<sub>2</sub> < Cu-Mo<sub>x</sub>C<sub>y</sub>/SiO<sub>2</sub>. In particular, more than 60% of Mo appears to have been oxidized by the passivation treatment on the Cu-Mo<sub>x</sub>C<sub>y</sub>/SiO<sub>2</sub> catalyst. The highly dispersed state of the carbide and its pronounced oxidation are both consistent with the poorly intense diffraction lines of the Mo carbides seen by XRD.

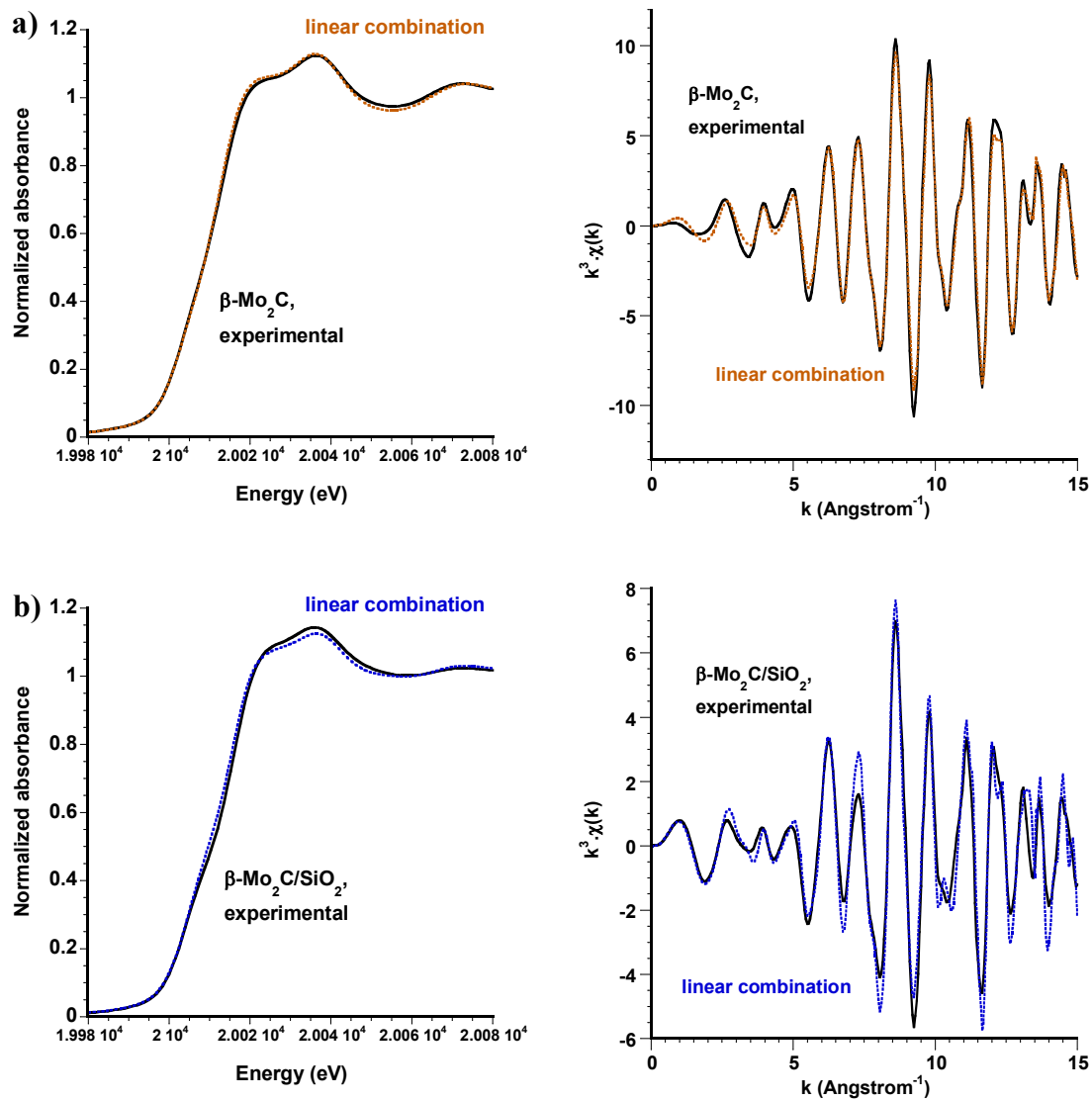
Table 5.2. Composition of the passivated and reactivated catalysts evaluated from the linear combination of standard spectra and MCR-ALS analysis (italics) at the Mo K-edge.

Percentage of each component (%)	Component 1 (Mo(VI) oxides)	Component 2 (Mo suboxides)	Component 3 (Mo <sub>2-x</sub> C <sub>x</sub> )	Component 4 (Mo carbide)
<b><i>Passivated catalysts</i></b>				
$\beta$ -Mo <sub>2</sub> C	0	0	10	90
	<i>0</i>	<i>0</i>	<i>12</i>	<i>88</i>
$\beta$ -Mo <sub>2</sub> C/SiO <sub>2</sub>	27	14	2	57
	<i>28</i>	<i>12</i>	<i>12</i>	<i>48</i>
Ni-Mo <sub>x</sub> C <sub>y</sub> /SiO <sub>2</sub>	41	12	7	40
	<i>49</i>	<i>9</i>	<i>1</i>	<i>41</i>
Cu-Mo <sub>x</sub> C <sub>y</sub> /SiO <sub>2</sub>	62	11	4	23
	<i>65</i>	<i>14</i>	<i>0</i>	<i>21</i>
<b><i>Reactivated catalysts</i></b>				
$\beta$ -Mo <sub>2</sub> C/SiO <sub>2</sub>	0	0	20	80
	<i>1</i>	<i>1</i>	<i>10</i>	<i>88</i>
Ni-Mo <sub>x</sub> C <sub>y</sub> /SiO <sub>2</sub>	0	0	58	42
	<i>0</i>	<i>0</i>	<i>41</i>	<i>59</i>
Cu-Mo <sub>x</sub> C <sub>y</sub> /SiO <sub>2</sub>				
<i>XANES</i>	0	29 <sup>a</sup>	38	33
<i>EXAFS</i>	0	6 <sup>a</sup>	66	28
	<i>0</i>	<i>0</i>	<i>35</i>	<i>65</i>

<sup>a</sup> Metallic Mo

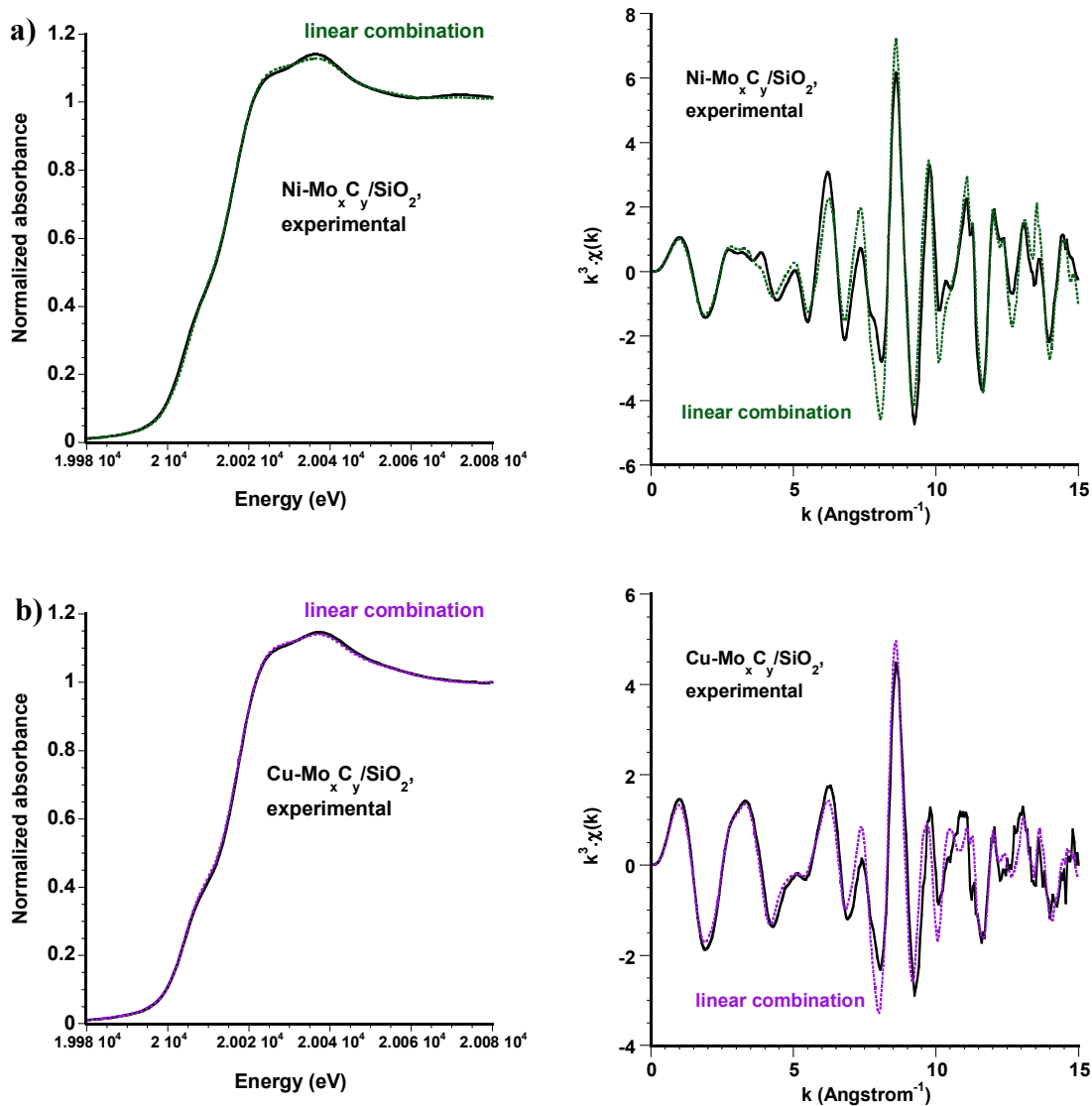
Reference: own author (2023)

Figure 5.6. Analysis of the data recorded at the Mo K-edge for the passivated catalysts (spectra recorded at room temperature), using linear combinations of MCR-ALS components (see Table 5.2). XANES spectrum (left) and EXAFS oscillations (right), a)  $\beta$ -Mo<sub>2</sub>C and b)  $\beta$ -Mo<sub>2</sub>C/SiO<sub>2</sub>.



Reference: own author (2023)

Figure 5.7. Analysis of the data recorded at the Mo K-edge for the passivated catalysts (spectra recorded at room temperature), using linear combinations of MCR-ALS components (see Table 5.2). XANES spectrum (left) and EXAFS oscillations (right), a) Ni-Mo<sub>x</sub>C<sub>y</sub>/SiO<sub>2</sub> and b) Cu-Mo<sub>x</sub>C<sub>y</sub>/SiO<sub>2</sub>.

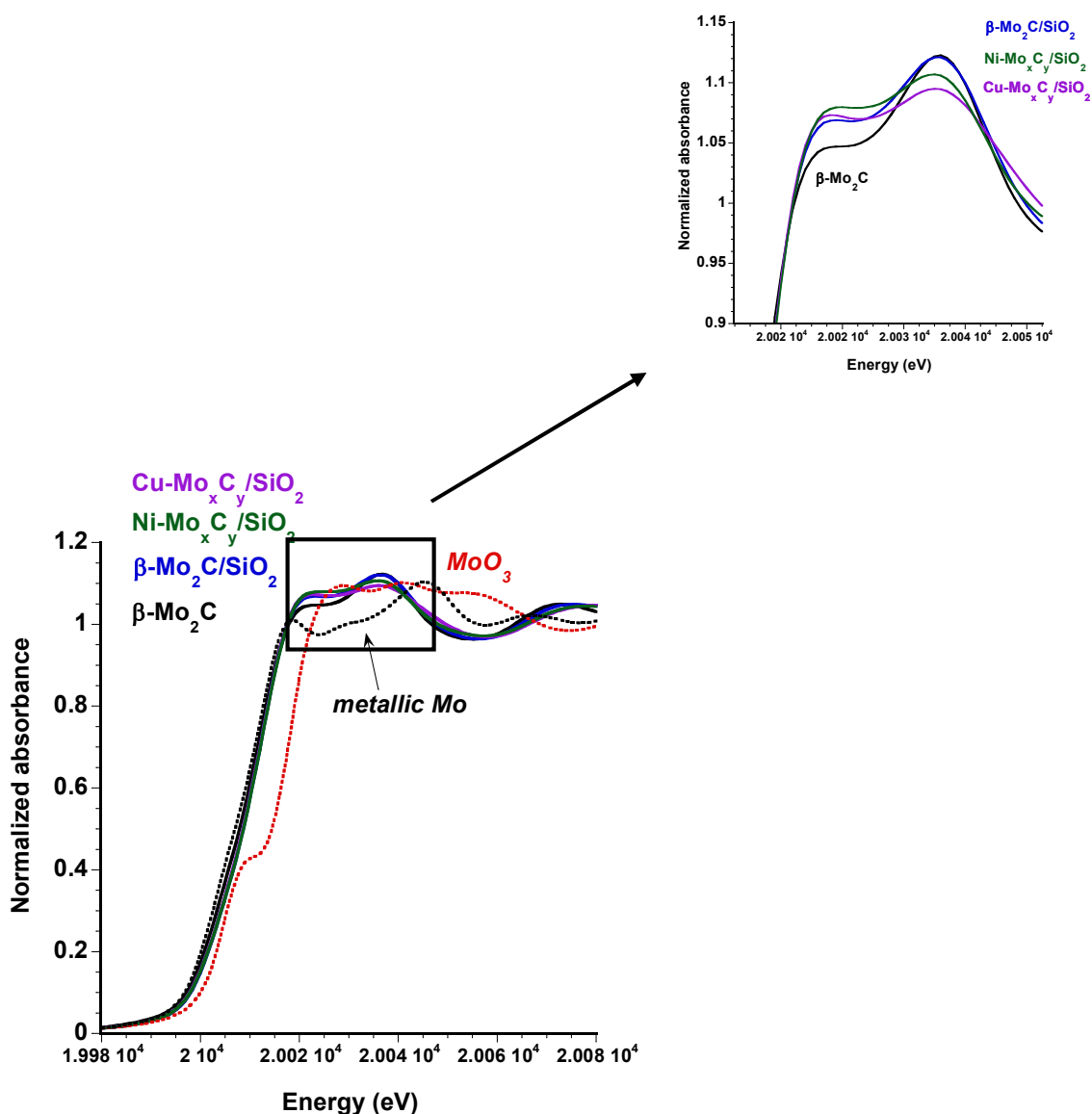


Reference: own author (2023)

Reactivation of the passivated catalysts under pure H<sub>2</sub> up to 400 °C resulted in a shift of the XANES spectra at the Mo K-edge to lower energies, close to the edge of metallic Mo (Figure 5.8, spectra recorded after cooling down to room temperature). But a zoom on the upper part of the spectra shows significant differences. The EXAFS oscillations recorded for the bimetallic catalysts remain very different from those of the

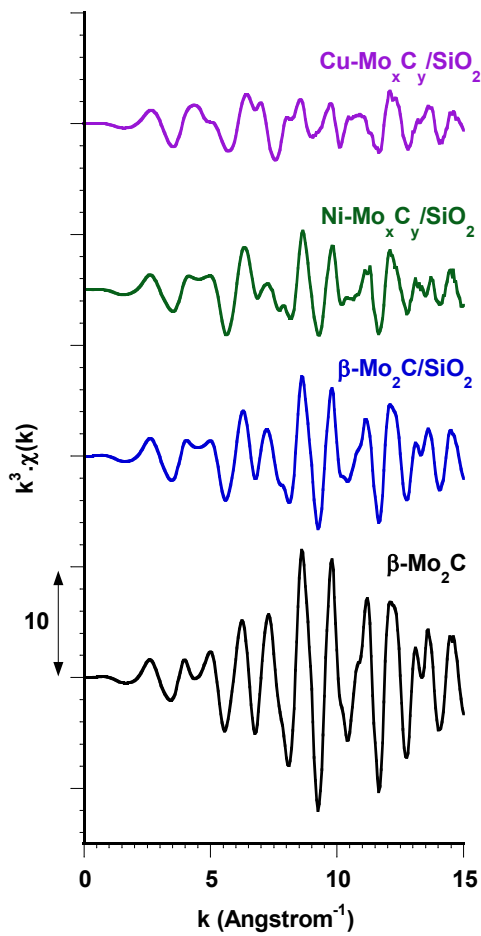
pure carbide (Figure 5.9). The Fourier transform for reduced  $\text{Cu-Mo}_x\text{C}_y/\text{SiO}_2$  is very different from that of the carbide, while the peaks from  $\text{Ni-Mo}_x\text{C}_y/\text{SiO}_2$  present a low intensity (Figure 5.10). The reduction under pure  $\text{H}_2$  after passivation does not restore the supported catalysts to their initial fully carburized state.

Figure 5.8. XANES spectra recorded at the Mo K-edge for the reactivated catalysts (spectra recorded at room temperature). Comparison with references  $\text{MoO}_3$  and metallic Mo (dotted lines).



Reference: own author (2023)

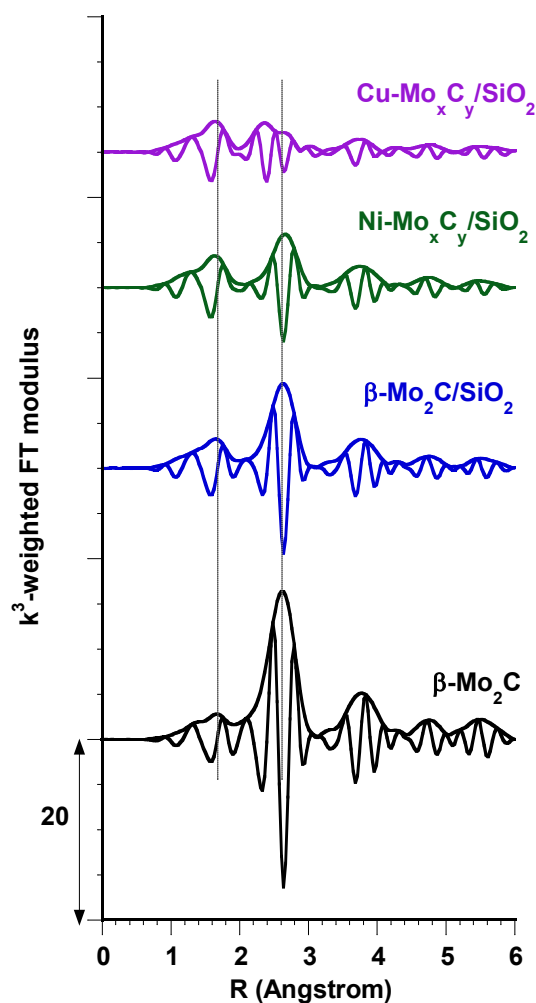
Figure 5.9. EXAFS signals recorded at the Mo K-edge for the passivated catalysts after reactivation (spectra recorded at room temperature). Comparison with reference  $\beta$ - $\text{Mo}_2\text{C}$ .



Reference: own author (2023)



Figure 5.10. Fourier transforms of the EXAFS signals recorded at the Mo K-edge for the passivated catalysts after reactivation ( $k = 3.5 - 15 \text{ \AA}^{-1}$ , spectra recorded at room temperature). Comparison with reference  $\beta\text{-Mo}_2\text{C}$ .

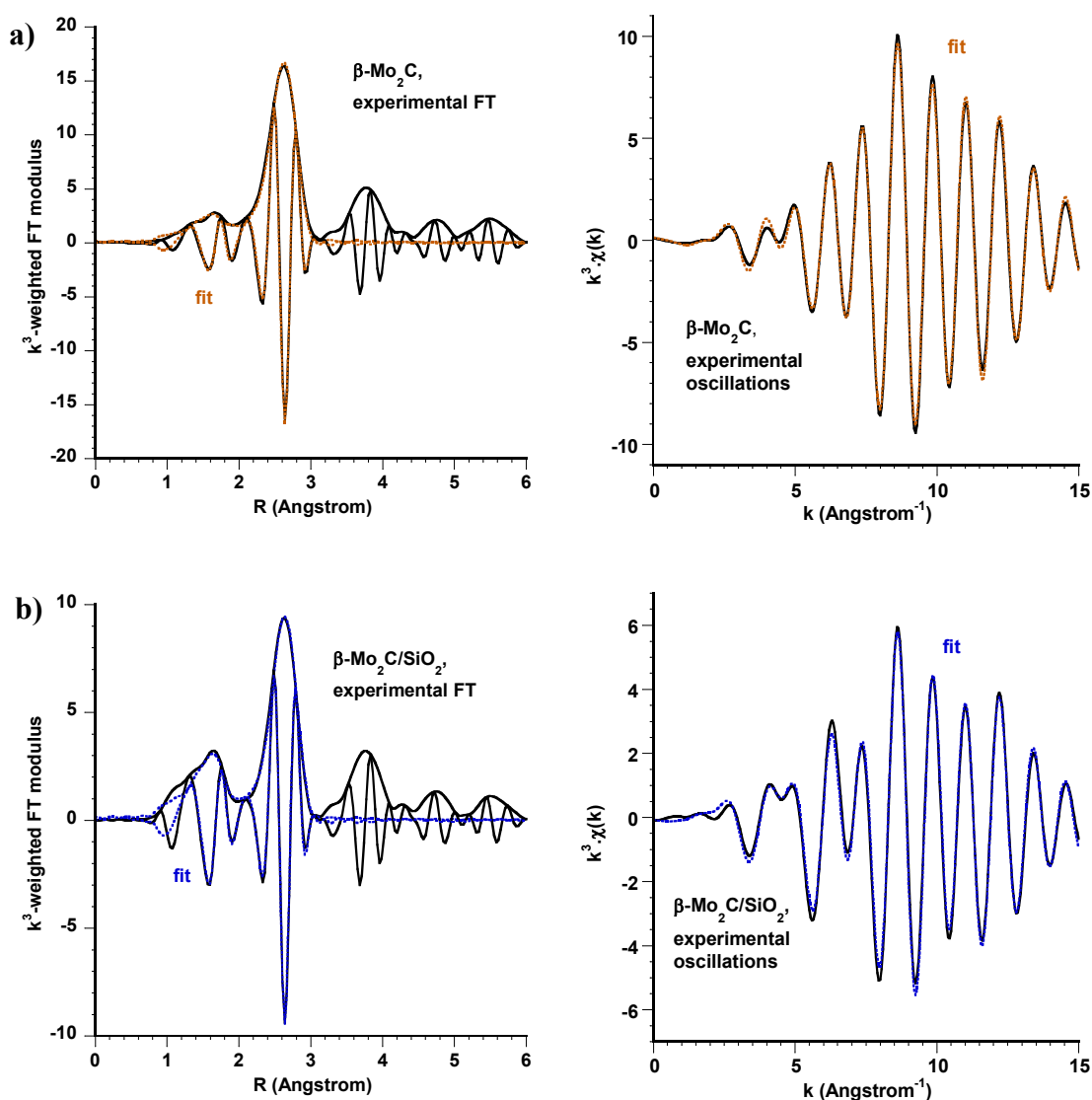


Reference: own author (2023)

The first and second shells from reduced  $\beta\text{-Mo}_2\text{C}/\text{SiO}_2$  could be fitted using the same interatomic distances as after carburization (Figures 5.11 and 5.12, Table 5.3). The major change is a decrease in the number of Mo neighbors in the second shell, which indicates that upon passivation and reactivation, the Mo carbide particles have somewhat lost their structural organization. The Mo carbide hypothesis also allows fitting the EXAFS data from  $\text{Ni-Mo}_x\text{C}_y/\text{SiO}_2$ . But the quality of the fit is poorer, especially between 1 and 2  $\text{\AA}$ . The addition of O atoms in the first shell is rejected by the fit, but the presence of another phase is likely. Finally, the fit for  $\text{Cu-Mo}_x\text{C}_y/\text{SiO}_2$

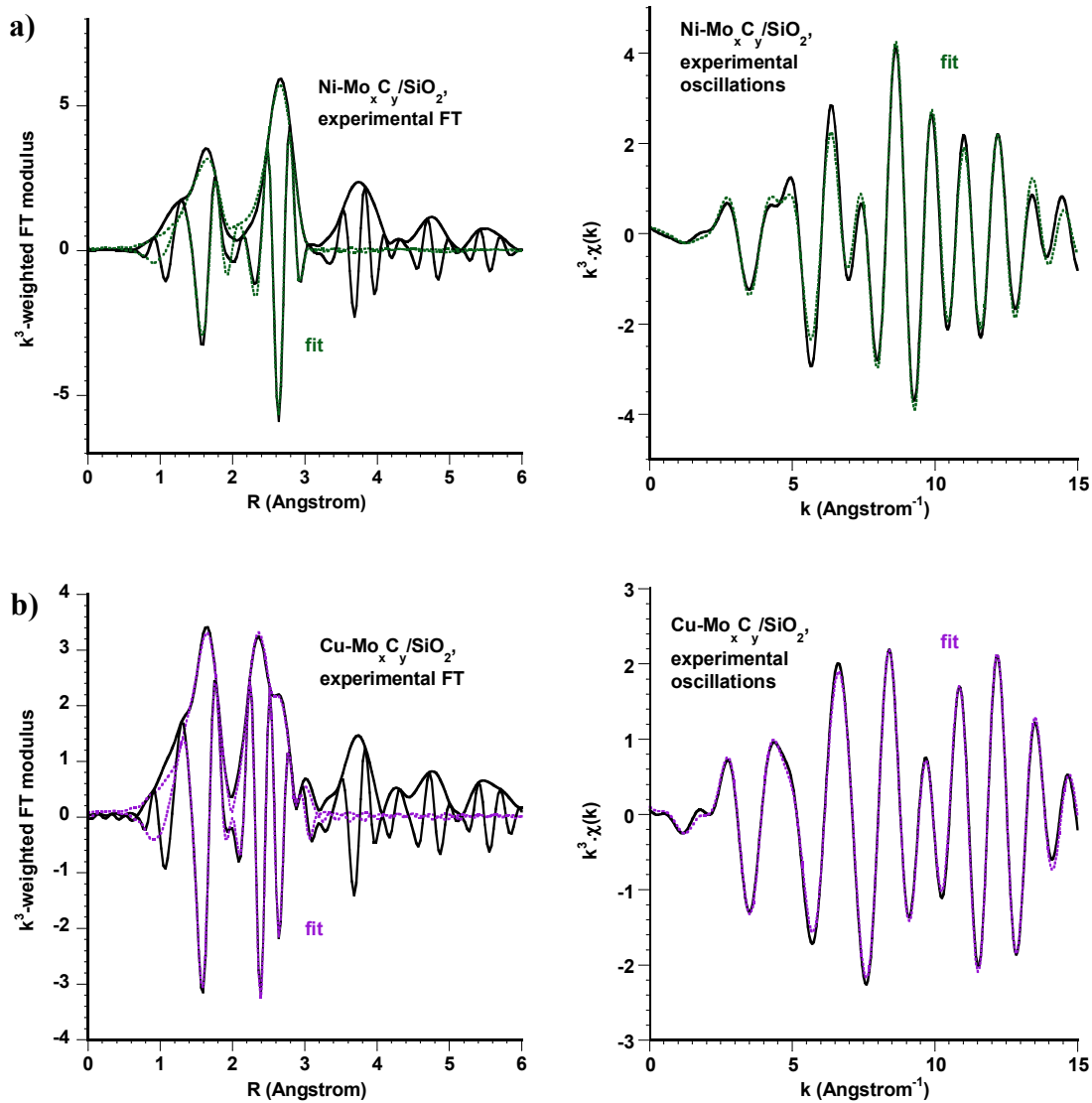
gives satisfactory results, but it is obvious that the second shell of neighbors is very different from that of Mo carbides. The introduction of three Mo-Mo interatomic distances is necessary. A distance at 2.75 Å is consistent with the presence of decarburized metallic Mo; distances at 2.94 and 3.10 Å are consistent with Mo carbides.

Figure 5.11. XAS data at the Mo K-edge of the passivated catalysts after reactivation (spectrum recorded at room temperature). Fit of the first and second shells of neighbors: Fourier transform ( $k = 3.5 - 15 \text{ \AA}^{-1}$ , left) and EXAFS oscillations (right), a)  $\beta\text{-Mo}_2\text{C}$  and b)  $\beta\text{-Mo}_2\text{C}/\text{SiO}_2$ .



Reference: own author (2023)

Figure 5.12. XAS data at the Mo K-edge of the passivated catalysts after reactivation (spectrum recorded at room temperature). Fit of the first and second shells of neighbors: Fourier transform (left) and EXAFS oscillations (right), a) Ni-Mo<sub>x</sub>C<sub>y</sub>/SiO<sub>2</sub> and b) Cu-Mo<sub>x</sub>C<sub>y</sub>/SiO<sub>2</sub>.



Reference: own author (2023)

Table 5.3. Fitted parameters at the Mo K-edge ( $E_0 = 20013$  eV,  $S02 = 0.98$ ) determined from the EXAFS analysis of spectra recorded at room temperature on catalysts after passivation and reactivation in  $H_2$ .  $k = 3.5 - 15.5 \text{ \AA}^{-1}$ . Fit of the first peak(s) from the Fourier transform between 1 and 3  $\text{\AA}$ .

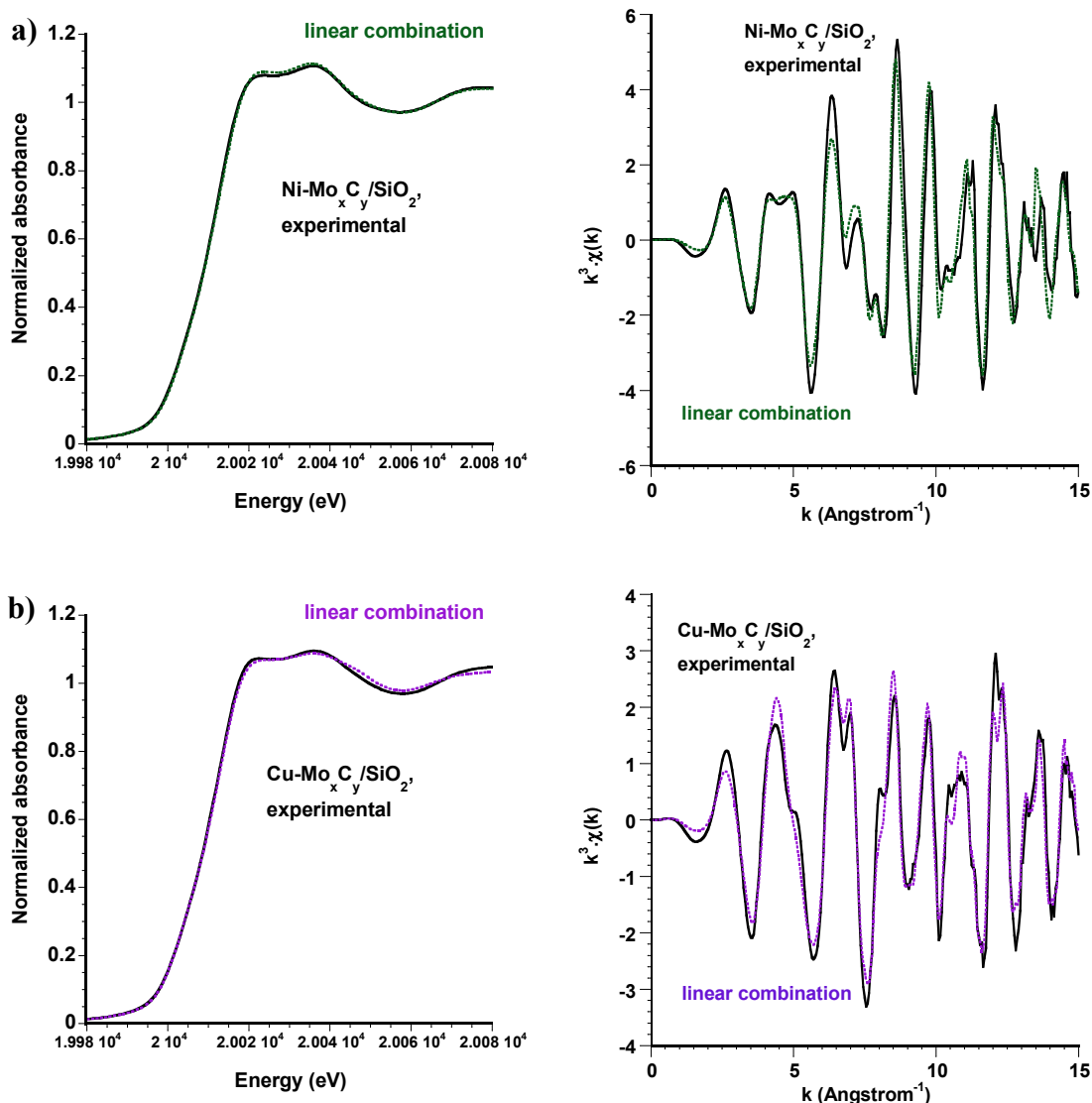
Catalyst	Backscatter	N	$\sigma^2 (\text{\AA}^2) \times 10^3$	R ( $\text{\AA}$ )
$\beta\text{-Mo}_2\text{C}$	C	$2.7 \pm 0.9$	$4.1 \pm 0.3$	$2.08 \pm 0.02$
	Mo	$7.3 \pm 0.8$	$5.7 \pm 0.5$	$2.966 \pm 0.005$
	$\Delta E_0 = -5.5$ eV, r-factor = 0.01575, $\chi^2 = 592$ , $N_{\text{ind}} = 13$ , $N_{\text{var}} = 7$			
$\beta\text{-Mo}_2\text{C}/\text{SiO}_2$	C	$4.1 \pm 0.6$	$6 \pm 1$	$2.105 \pm 0.006$
	Mo	$4.1 \pm 0.4$	$6.1 \pm 0.4$	$2.976 \pm 0.003$
	$\Delta E_0 = -2.7$ eV, r-factor = 0.00717, $\chi^2 = 202$ , $N_{\text{ind}} = 13$ , $N_{\text{var}} = 7$			
Ni-Mo <sub>x</sub> C <sub>y</sub> /SiO <sub>2</sub>	C	$4 \pm 1$	$6 \pm 3$	$2.12 \pm 0.02$
	Mo	$2.9 \pm 0.8$	$7 \pm 2$	$2.976 \pm 0.009$
	$\Delta E_0 = -0.4$ eV, r-factor = 0.03385, $\chi^2 = 615$ , $N_{\text{ind}} = 13$ , $N_{\text{var}} = 7$			
Cu-Mo <sub>x</sub> C <sub>y</sub> /SiO <sub>2</sub>	C	$3.5 \pm 0.6$	$5 \pm 2$	$2.106 \pm 0.009$
	Mo	$2.5 \pm 0.8$	$8 \pm 2$	$2.751 \pm 0.009$
	Mo	$3 \pm 2$	$8 \pm 2$	$2.94 \pm 0.02$
	Mo	$1.3 \pm 0.6$	$8 \pm 2$	$3.10 \pm 0.04$
	$\Delta E_0 = -3.2$ eV, r-factor = 0.00773, $\chi^2 = 366$ , $N_{\text{ind}} = 13$ , $N_{\text{var}} = 11$			

Reference: own author (2023)

A comparison with linear combinations of the carburization spectral components, as was done for the passivated samples, was then attempted (Table 5.2, bottom section, upright characters). After reactivation, the  $\beta\text{-Mo}_2\text{C}/\text{SiO}_2$  catalyst was restored to the carbide state at about 85% with oxycarbide as a minor phase. Results for the reactivated bimetallic catalysts are shown in Figure 5.13. Speciation on Ni-Mo<sub>x</sub>C<sub>y</sub>/SiO<sub>2</sub> fits with the presence of about 50% of remaining oxycarbide. However, for Cu-Mo<sub>x</sub>C<sub>y</sub>/SiO<sub>2</sub>, and in line with the EXAFS analysis, better fits were obtained by combining the spectra from the Mo carbide and oxycarbide with that of the metallic Mo standard. However, the best linear combinations obtained in the XANES and EXAFS domains are based on quite different compositions of the mixture, probably because the intense oscillations of well-crystallized bulk Mo might not be the right standards for EXAFS linear combination. In any case, the bimetallic catalysts appear as significantly de-carburized by the passivation treatment, with consequences in the reactivated state. It will be seen below (analysis at the Ni K-edge) that a fraction of metallic Mo may also

be present on Ni-Mo<sub>x</sub>C<sub>y</sub>/SiO<sub>2</sub>, even if not detected by EXAFS analysis or by performing linear combinations of standard spectra.

Figure 5.13. Analysis of the data recorded at the Mo K-edge for the passivated catalysts after reactivation (spectra recorded at room temperature), using linear combinations of MCR-ALS components (see Table 5.2). XANES spectrum (left) and EXAFS oscillations (right), a) Ni-Mo<sub>x</sub>C<sub>y</sub>/SiO<sub>2</sub> and b) Cu-Mo<sub>x</sub>C<sub>y</sub>/SiO<sub>2</sub>.

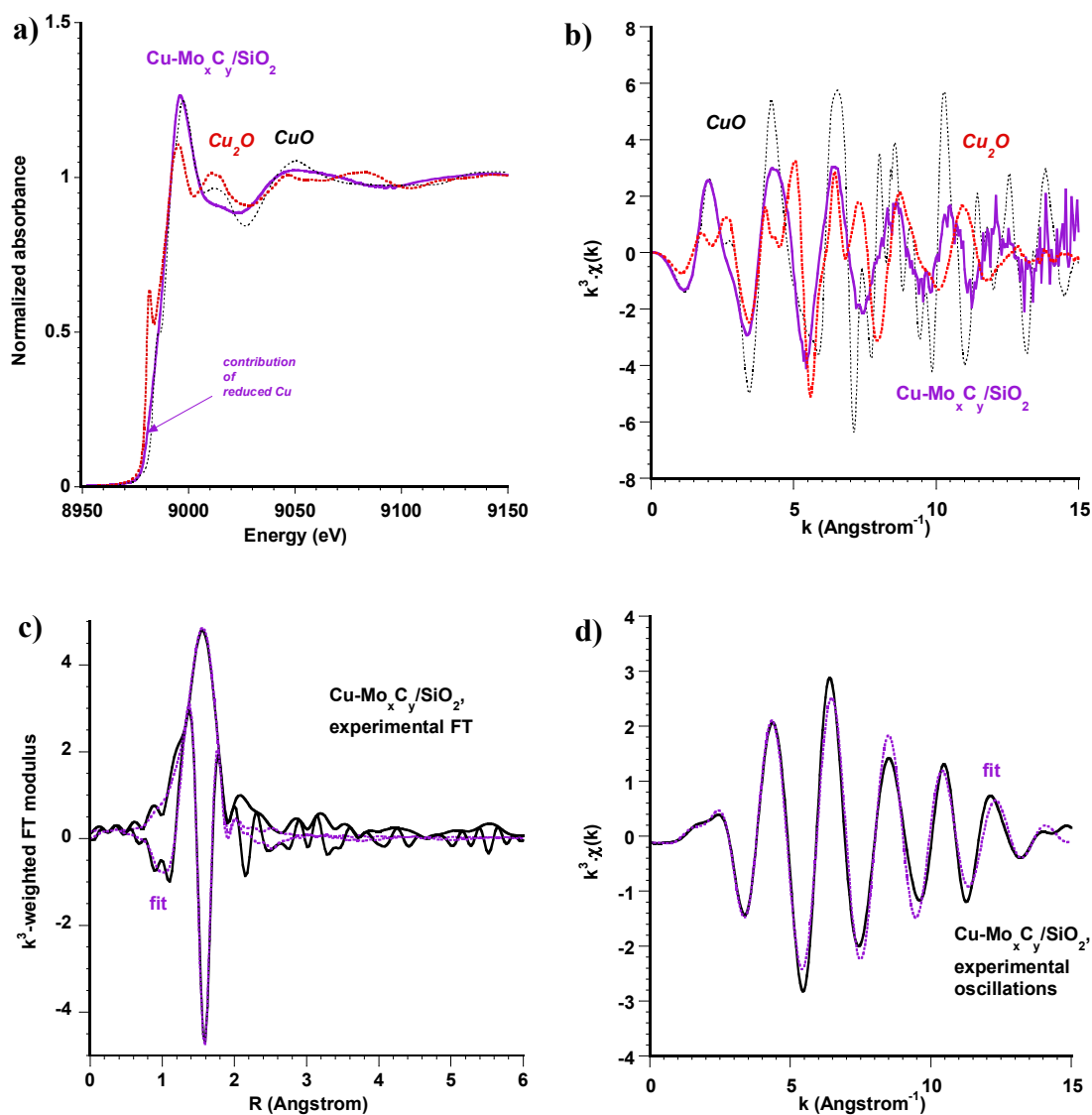


Reference: own author (2023)

XAS at the Cu K-edge is poorly informative about the initial state of Cu in the passivated Cu-Mo<sub>x</sub>C<sub>y</sub>/SiO<sub>2</sub> catalyst, save for its Cu<sup>2+</sup> oxidation state and environment of

O atoms (Figure 5.14, Table 5.4). A small contribution of reduced Cu may be present in the XANES spectrum. Cu fcc nanoparticles are restored upon reactivation (Figure 5.15), with roughly the same number of nearest neighbors as was found after carburization (Table 5.4). No phase associating Cu and Mo was evidenced.

Figure 5.14. XAS data at the Cu K-edge of the  $\text{Cu-Mo}_x\text{C}_y/\text{SiO}_2$  catalyst after passivation. a) XANES spectrum and b) EXAFS oscillations, comparison with references  $\text{CuO}$  and  $\text{Cu}_2\text{O}$ . Fit of the first shell of neighbors: c) Fourier transform and d) EXAFS oscillations.  $k = 3.5 - 14 \text{ \AA}^{-1}$ .



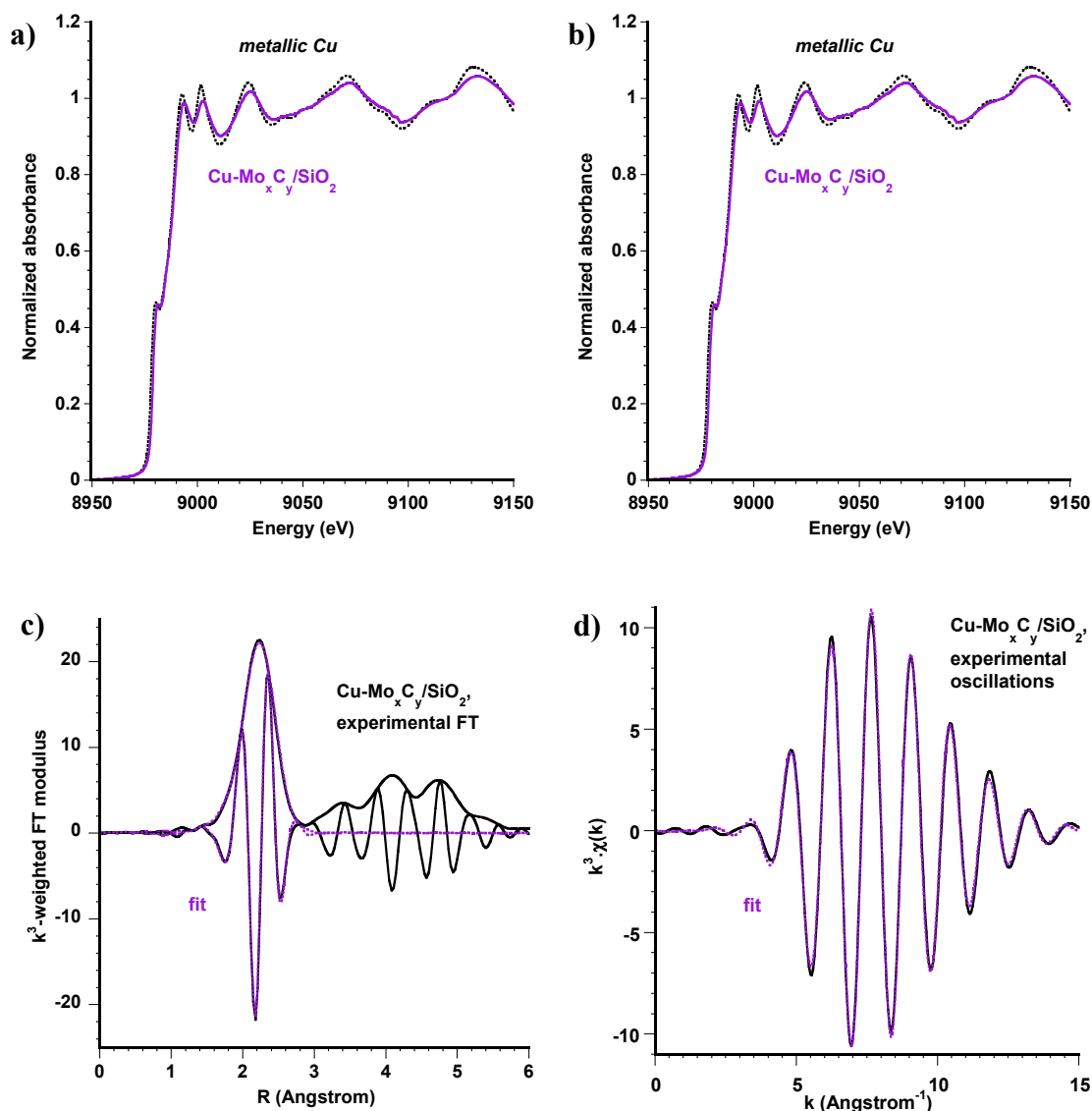
Reference: own author (2023)

Table 5.4. Fitted parameters at the Cu K-edge ( $E_0 = 8987 \pm 4$  eV,  $S02 = 0.91$ ) determined from the EXAFS analysis of spectra recorded at room temperature.  $k = 3.5 - 14 \text{ \AA}^{-1}$ . Fit of the first peak from the Fourier transform between 1 and 3  $\text{\AA}$ .

<b>Catalyst</b>	<b>Backscatter</b>	<b>N</b>	<b><math>\sigma^2</math> (<math>\text{\AA}^2</math>) x <math>10^3</math></b>	<b>R (<math>\text{\AA}</math>)</b>
Cu-Mo <sub>x</sub> C <sub>y</sub> /SiO <sub>2</sub> passivated	O	$4 \pm 1$	$6 \pm 3$	$2.12 \pm 0.02$
	r-factor = 0.02803, $\chi^2 = 211$ , $N_{\text{ind}} = 13$ , $N_{\text{var}} = 4$			
Cu-Mo <sub>x</sub> C <sub>y</sub> /SiO <sub>2</sub> passivated and reactivated	Cu	$9.7 \pm 0.7$	$10.0 \pm 0.6$	$2.538 \pm 0.005$
	r-factor = 0.00555, $\chi^2 = 205$ , $N_{\text{ind}} = 13$ , $N_{\text{var}} = 4$			

Reference: own author (2023)

Figure 5.15. XAS data at the Cu K-edge of the passivated Cu-Mo<sub>x</sub>C<sub>y</sub>/SiO<sub>2</sub> catalyst after reactivation (spectrum recorded at room temperature). a) XANES spectrum and b) EXAFS oscillations, comparison with reference Cu foil. Fit of the first shell of neighbors: c) Fourier transform and d) EXAFS oscillations.  $k = 3.5 - 14 \text{ \AA}^{-1}$ .



Reference: own author (2023)

At the Ni K-edge, the XANES spectrum recorded on the passivated Ni-Mo<sub>x</sub>C<sub>y</sub>/SiO<sub>2</sub> catalyst indicates that Ni appears as Ni<sup>2+</sup> ions, but not in a pure NiO phase (Figure 5.16). The EXAFS oscillations are different, the white line is not as intense as in the pure oxide, and a small feature at low energy betrays the presence of

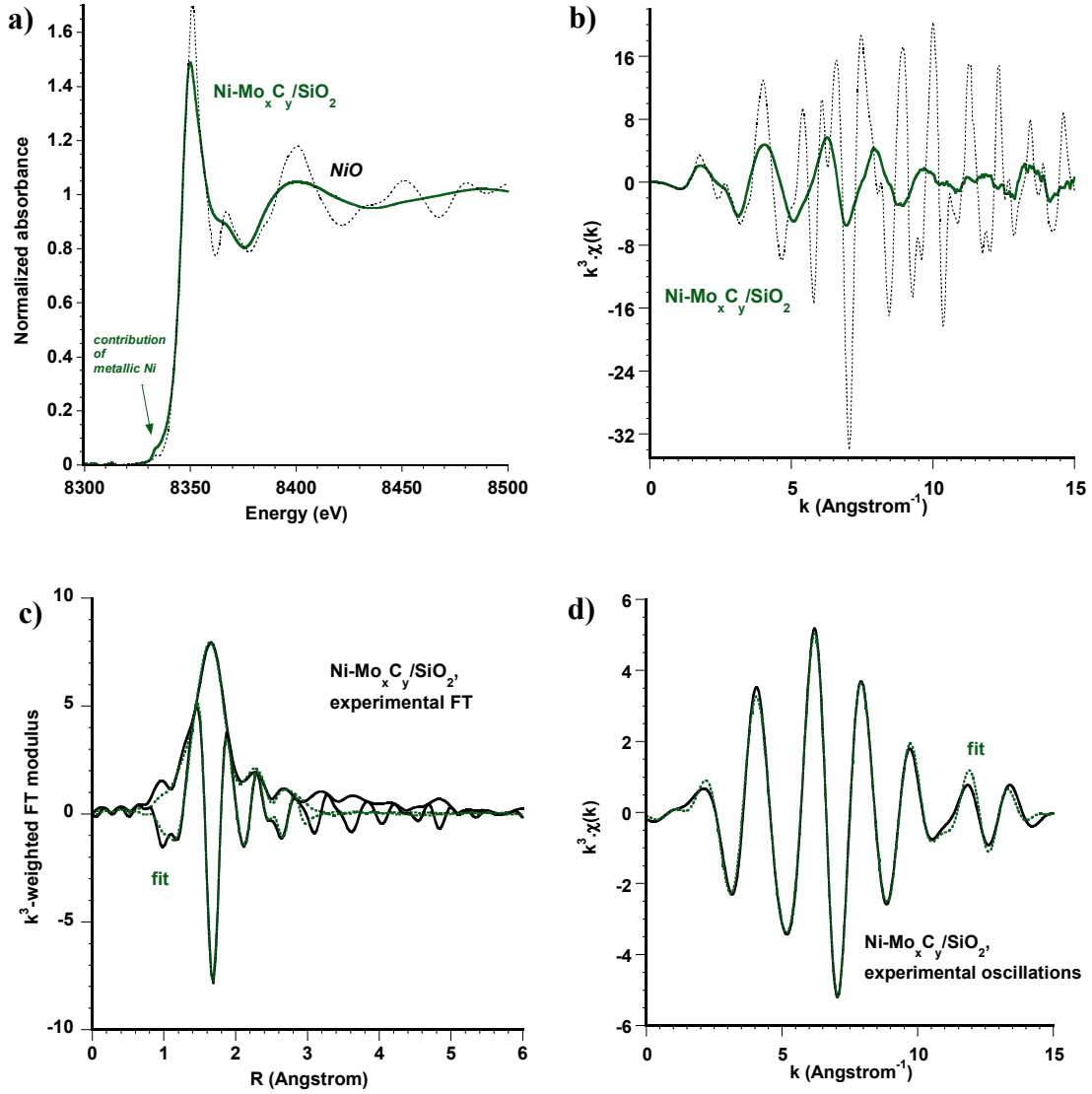


residual reduced Ni. Indeed, the fit shows the presence of O nearest neighbors in the first shell, and Ni<sup>2+</sup> next-nearest neighbors in the second shell ( $R = 3.02 \text{ \AA}$ ), as they are present in NiO, but also metallic Ni atoms at  $2.50 \text{ \AA}$  (Table 5.5). NiMoO<sub>4</sub> is thus not formed during passivation.

After reactivation, and in contrast with Cu, the XANES spectrum does not correspond to that of the fcc Ni particles (Figure 5.17). The spectrum is not modified by cooling back to room temperature; the unusual shape of the XANES spectrum and the low position in  $R$  of the peak of nearest neighbors on the Fourier transform are conserved. This validates the existence of a distinct Ni species and not the consequence of a thermal effect. EXAFS fitting was not possible using Ni atoms only, or a combination of Ni and O atoms. The best fit was obtained by associating Ni atoms and 1 or 2 reduced Mo atoms, at interatomic distances consistent with the different sizes of the atoms - though with a high but acceptable value of  $\sigma^2$  (Table 5.5).

This result tends to indicate that, unlike Cu, highly dispersed Ni-reduced centers are associated to reduced Mo in the reactivated state. The presence of Mo-poor Ni alloys in carburized systems was indeed demonstrated before using X-ray diffraction (Shilov *et al.*, 2018; Smirnov *et al.*, 2017).

Figure 5.16. XAS data at the Ni K-edge of the Ni-Mo<sub>x</sub>C<sub>y</sub>/SiO<sub>2</sub> catalyst after passivation. a) XANES spectrum and b) EXAFS oscillations, comparison with reference NiO. Fit of the first and second shells of neighbors: c) Fourier transform and d) EXAFS oscillations.  $k = 3 - 13 \text{ \AA}^{-1}$ .



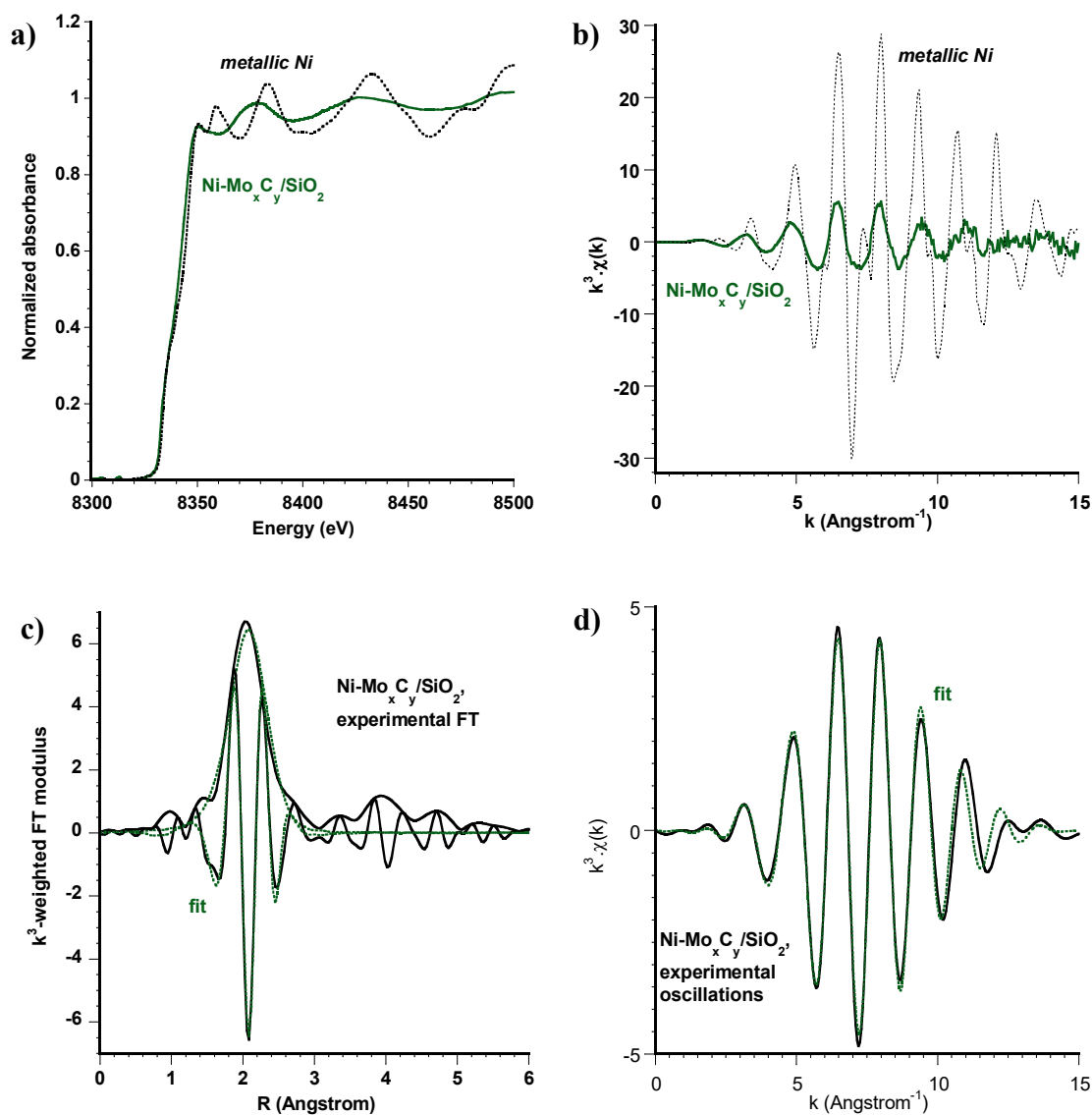
Reference: own author (2023)

Table 5.5. Fitted parameters at the Ni K-edge ( $E_0 = 8339 \pm 2$  eV,  $S02 = 0.80$ ) determined from the EXAFS analysis of spectra recorded at room temperature.  $k = 3 - 13 \text{ \AA}^{-1}$ . Fit of the first peak(s) from the Fourier transform between 1 and 3  $\text{\AA}$ .

<b>Catalyst</b>	<b>Backscatter</b>	<b>N</b>	<b><math>\sigma^2</math> (<math>\text{\AA}^2</math>) x <math>10^3</math></b>	<b>R (<math>\text{\AA}</math>)</b>
Ni-Mo <sub>x</sub> C <sub>y</sub> /SiO <sub>2</sub> passivated	O	$5 \pm 1$	$6 \pm 2$	$2.039 \pm 0.008$
	Ni	$0.7 \pm 0.2$	$6 \pm 2$	$2.50 \pm 0.02$
	Ni	$0.6 \pm 0.3$	$6 \pm 2$	$3.02 \pm 0.03$
r-factor = 0.01766, $\chi^2 = 365$ , $N_{\text{ind}} = 12$ , $N_{\text{var}} = 8$				
Ni-Mo <sub>x</sub> C <sub>y</sub> /SiO <sub>2</sub> passivated and reactivated	Ni	$5.8 \pm 0.8$	$13 \pm 2$	$2.47 \pm 0.01$
	Mo	$1.3 \pm 0.7$	$13 \pm 2$	$2.60 \pm 0.03$
	r-factor = 0.01855, $\chi^2 = 116$ , $N_{\text{ind}} = 12$ , $N_{\text{var}} = 6$			

Reference: own author (2023)

Figure 5.17. XAS data at the Ni K-edge of the passivated Ni-Mo<sub>x</sub>C<sub>y</sub>/SiO<sub>2</sub> catalyst after reactivation (spectrum recorded at room temperature). a) XANES spectrum and b) EXAFS oscillations, comparison with reference Ni foil. Fit of the first shell of neighbors: c) Fourier transform and d) EXAFS oscillations.  $k = 3 - 13 \text{ \AA}^{-1}$ .

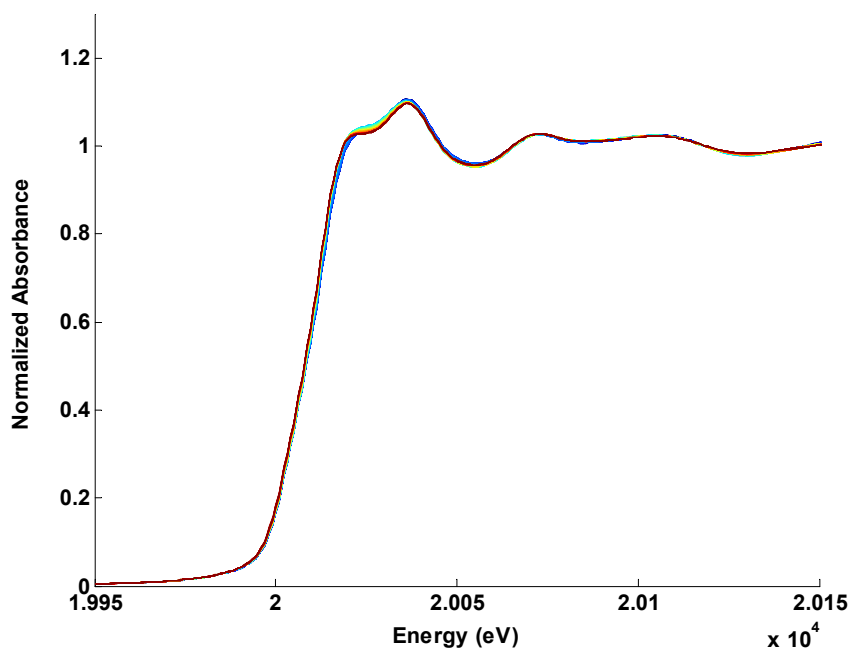


Reference: own author (2023)

Figures 5.18 and 5.26 present the evolution of the spectra and Mo speciation, as deduced from an MCR-ALS analysis of the spectra recorded during the reactivation of unsupported  $\beta$ -Mo<sub>2</sub>C, using the two spectral contributions associated with Mo “oxycarbides” and Mo carbides. The oxycarbide contribution, which one can suppose is

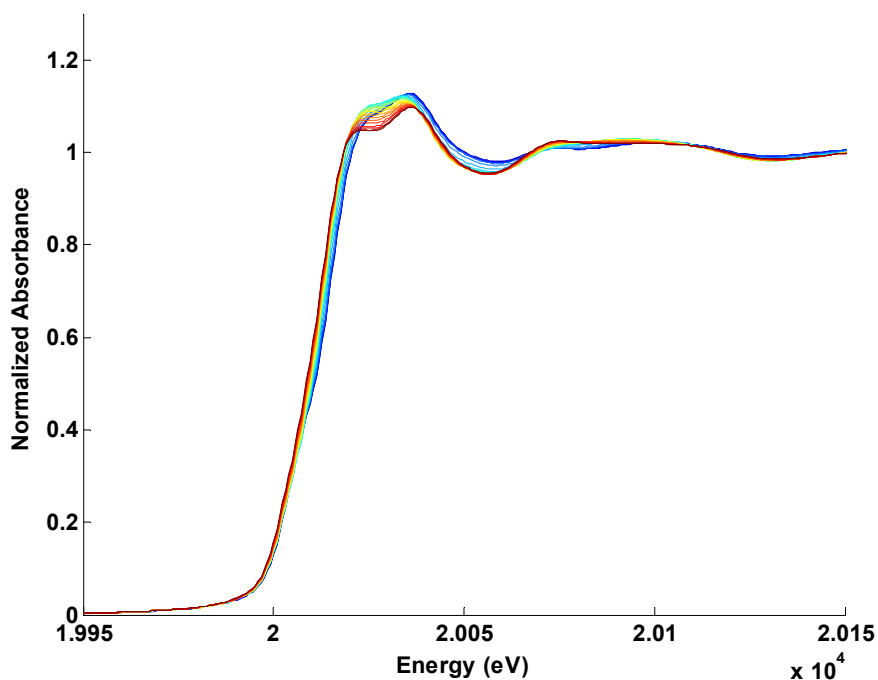
located at the surface of the carbide grains, is progressively reduced between room temperature and 400 °C, and the carbide is quantitatively restored. The same is shown for  $\beta$ -Mo<sub>2</sub>C/SiO<sub>2</sub> in Figures 5.19 and 5.26, this time using four spectral contributions associated to Mo(VI) oxides, Mo suboxides, Mo “oxycarbides” and Mo carbides. The Mo(VI) oxides fraction from  $\beta$ -Mo<sub>2</sub>C/SiO<sub>2</sub> is reduced between room temperature and 150 °C, one can suppose thanks to the hydrogen activated by the remaining carbide fraction, and the resulting suboxide fraction between 150 and 400 °C. According to the MCR-ALS analysis and the linear combinations (Table 5.2), between 80 and 90% of the carbide is restored on  $\beta$ -Mo<sub>2</sub>C/SiO<sub>2</sub> after reactivation.

Figure 5.18. Evolution of the XAS spectra of passivated  $\beta$ -Mo<sub>2</sub>C at the Mo K-edge upon reactivation (from room temperature, dark blue, to 400 °C, red). Every 8<sup>th</sup> spectrum is shown only.



Reference: own author (2023)

Figure 5.19. Evolution of the XAS spectra of passivated  $\beta$ -Mo<sub>2</sub>C/SiO<sub>2</sub> at the Mo K-edge upon reactivation (from room temperature, dark blue, to 400 °C, red). For the sake of clarity, every 8<sup>th</sup> spectrum is shown only.



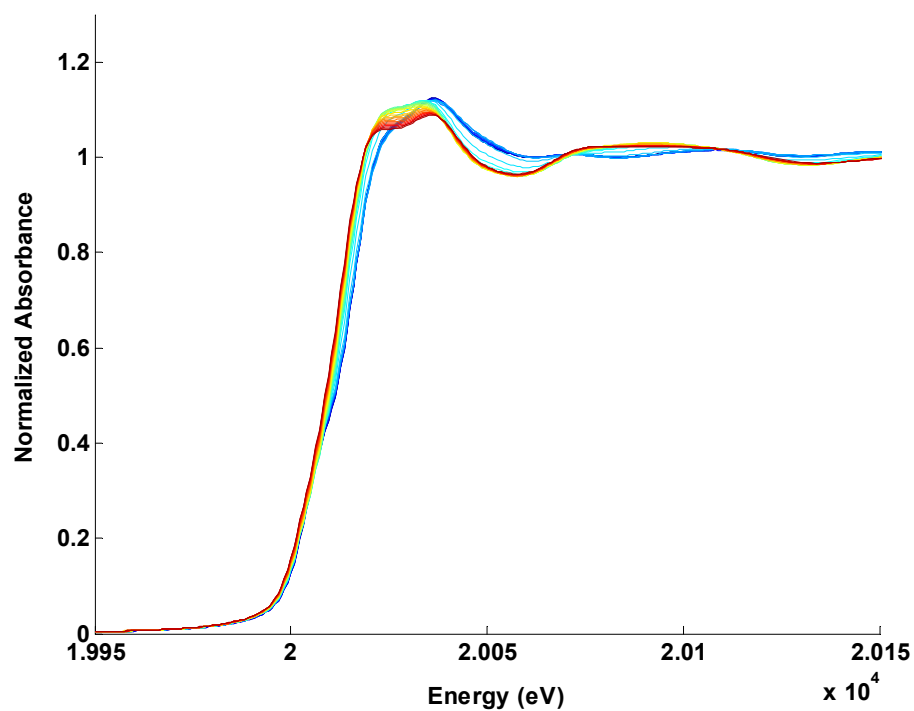
Reference: own author (2023)

For the bimetallic systems, the MCR-ALS analysis at the Mo K-edge must be interpreted with caution. First, it is likely misinterpreting early reductive changes in the Mo(VI) oxides fraction by mobilizing the Mo carbide spectral component. Oddly enough, the fraction of Mo suboxides is seen to decrease at the same time, which is not consistent either. Second, the introduction of the XAS spectrum of metallic Mo in the matrix of spectral components did not lead to a satisfactory analysis (this contribution ended at 0% at the end of the minimization procedure), though it was seen by EXAFS that a fraction of Mo was probably in the metallic state at least in Cu-Mo<sub>x</sub>C<sub>y</sub>/SiO<sub>2</sub>. The figures will only be used to compare the evolution of Mo and that of the metal promoter below 250 °C, as the final process of reactivation only based on Mo oxycarbide and carbide is probably lacunary.

The evolution of the spectra recorded at the Mo K-edge and the Ni K-edge during the reactivation of passivated Ni-Mo<sub>x</sub>C<sub>y</sub>/SiO<sub>2</sub> is shown in Figures 5.20 and 5.21, respectively. The reduction of the oxidized fraction of Mo is well visible, but what is

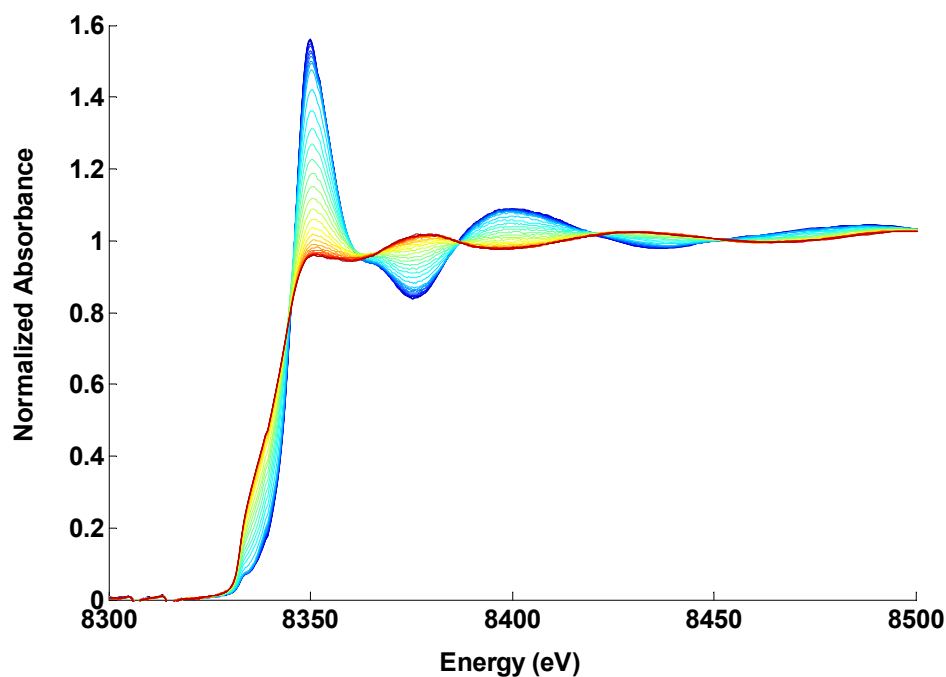
especially striking is the reduction of  $\text{Ni}^{2+}$ , resulting from deep oxidation of the Ni nanoparticles during passivation.

Figure 5.20. Evolution of the XAS spectra of passivated  $\text{Ni-Mo}_x\text{C}_y/\text{SiO}_2$  at the Mo K-edge upon reactivation (from room temperature, dark blue, to 400 °C, red).



Reference: own author (2023)

Figure 5.21. Evolution of the XAS spectra of passivated Ni-Mo<sub>x</sub>C<sub>y</sub>/SiO<sub>2</sub> at the Ni K-edge upon reactivation (from room temperature, dark blue, to 400 °C, red).



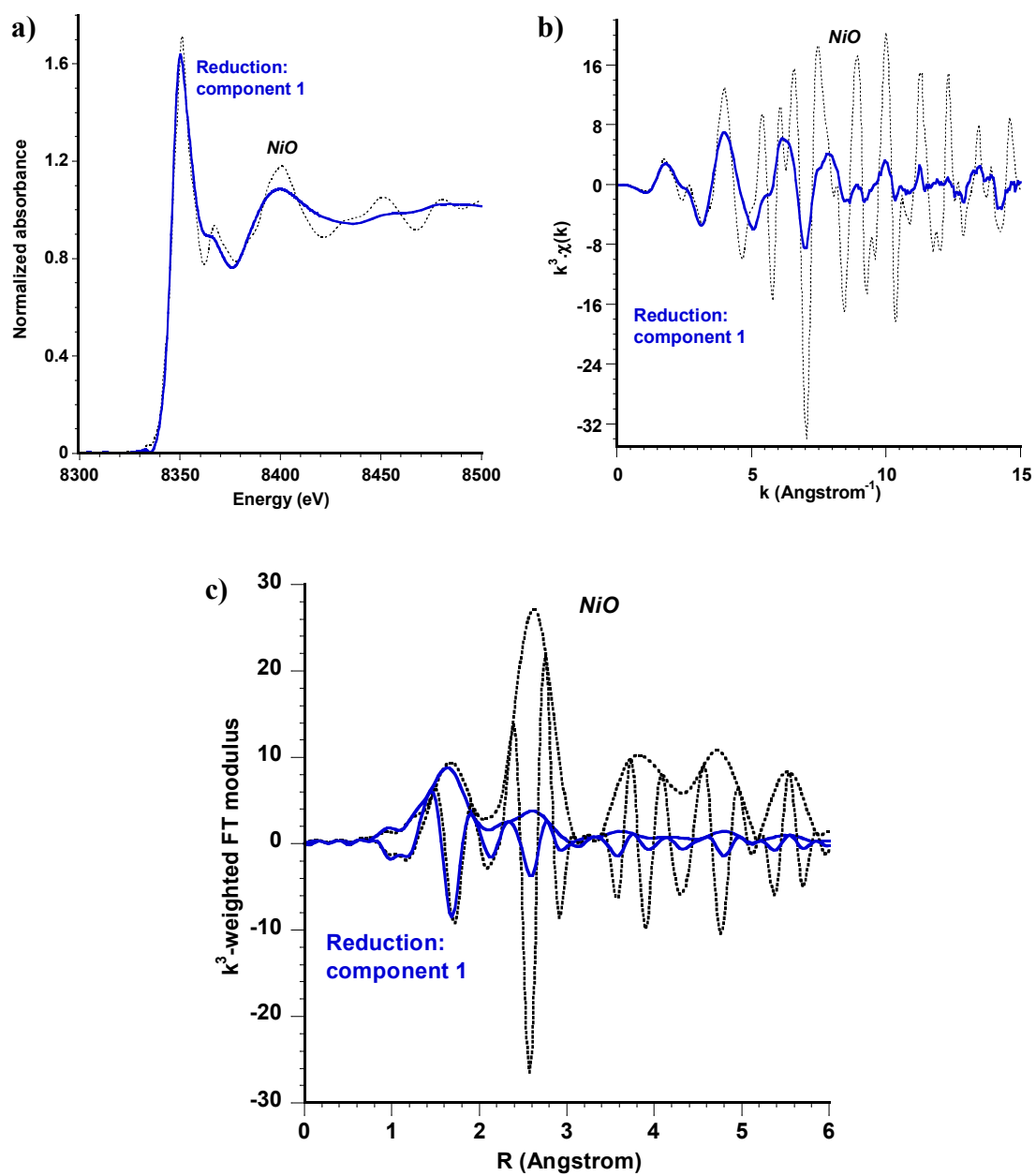
Reference: own author (2023)

The evolution of the Mo and Ni species during reactivation is presented in Figure 5.26. The MCR-ALS analysis of Ni reduction is based on two species only, Ni<sup>2+</sup> and the Ni reduced clusters in interaction with Mo. The characteristics of the two spectral components are shown in Figures 5.22 and 5.23.

The succession of reactions is the following: (1) like for  $\beta$ -Mo<sub>2</sub>C/SiO<sub>2</sub>, the Mo(VI) oxide fraction is reduced to Mo suboxides around 150 °C; (2) between 140 and 300 °C, the oxidized Ni fraction is reduced; (3) above 150 °C, Mo suboxides are also progressively reduced, yielding a fraction of metallic Mo with which the reduced Ni particles interact; (4) the partial restoration of the Mo carbide takes place between 200 and 400 °C.

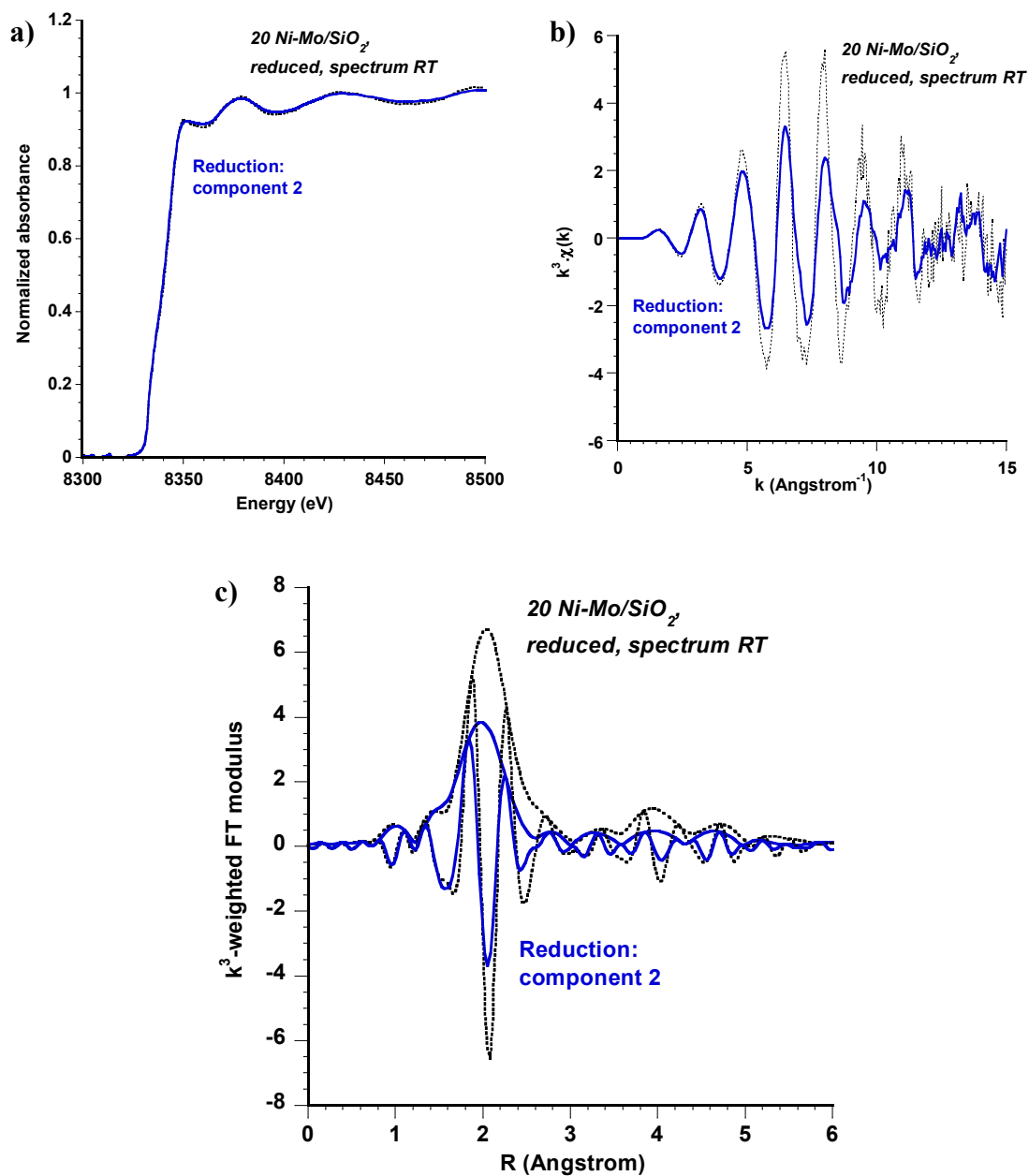


Figure 5.22. MCR-ALS analysis of the reduction of passivated Ni-Mo<sub>x</sub>C<sub>y</sub>/SiO<sub>2</sub>: comparison of the first component with NiO. a) XANES spectrum, b) EXAFS oscillations, c) Fourier transform.  $k = 3 - 13 \text{ \AA}^{-1}$ .



Reference: own author (2023)

Figure 5.23. MCR-ALS analysis of the reduction of passivated Ni-Mo<sub>x</sub>C<sub>y</sub>/SiO<sub>2</sub>: comparison of the second component with the spectrum recorded after reactivation at room temperature. a) XANES spectrum, b) EXAFS oscillations, c) Fourier transform.  $k = 3 - 13 \text{ \AA}^{-1}$ .



Reference: own author (2023)

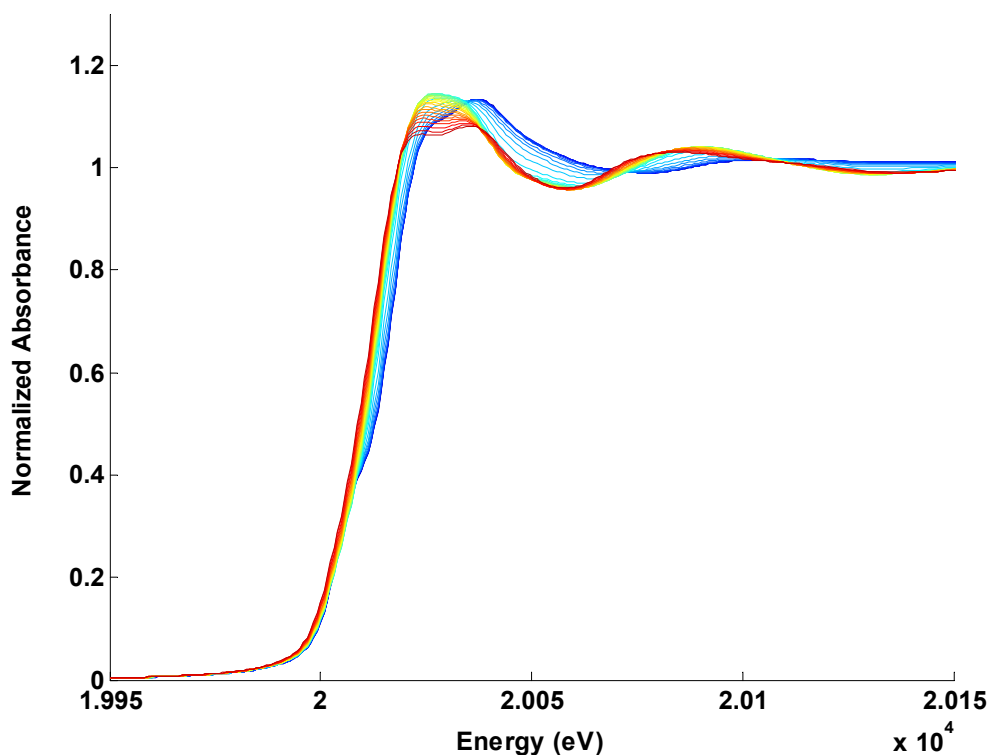
It should be noted that discrepancies between the different strategies of quantification exist for Ni-Mo<sub>x</sub>C<sub>y</sub>/SiO<sub>2</sub>. Concerning the final reduced state, the linear combination and the MCR-ALS procedure led to opposite results in terms of carbide

and a de-carburized fraction (Table 5.2, first and second lines, respectively). Introducing metallic Mo in the linear combination of the EXAFS oscillations did not allow for any correct fitting. Furthermore, the EXAFS fit is clearly dominated by the Mo carbide.

Disregarding the quantitative aspects, it can be concluded that in its reduced state, Ni-Mo<sub>x</sub>C<sub>y</sub>/SiO<sub>2</sub> still contains Mo carbide, but along with a larger fraction of oxycarbide and possibly metal than on β-Mo<sub>2</sub>C/SiO<sub>2</sub>. Highly dispersed Ni nanoparticles, reduced between 150 and 350 °C, are associated with, or stabilized by, reduced Mo atoms in the de-carburized fraction.

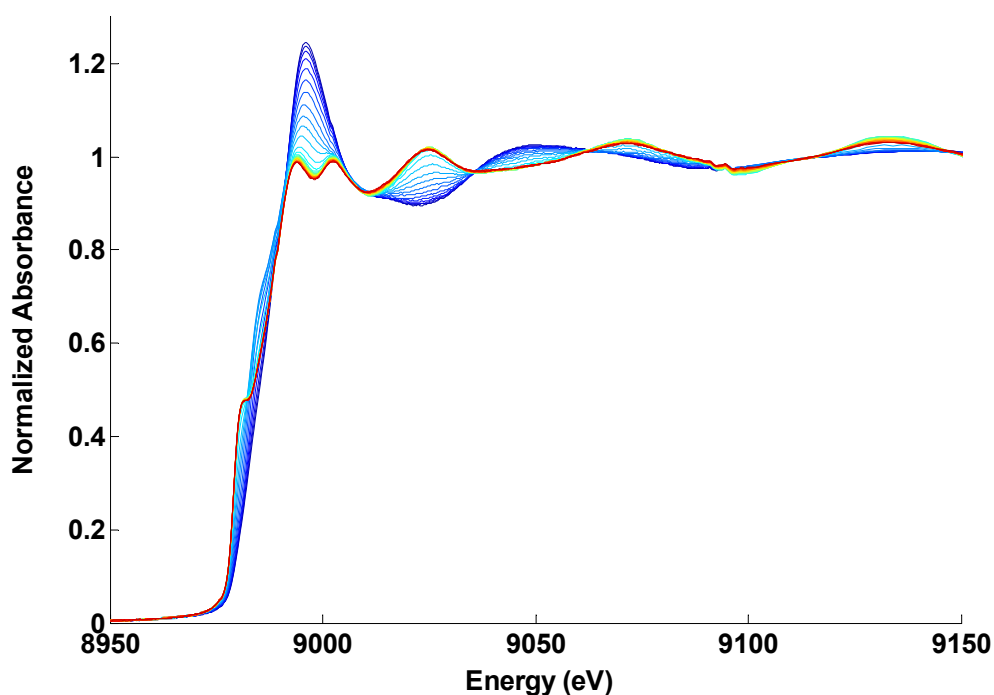
The evolution of the spectra recorded at the Mo K-edge and the Cu K-edge during the reactivation of passivated Cu-Mo<sub>x</sub>C<sub>y</sub>/SiO<sub>2</sub> is shown in Figures 5.24 and 5.25, respectively. The MCR-ALS analysis of Cu reduction was based on the same three spectral contributions that were found during carburization: Cu<sup>2+</sup> ions, Cu clusters in an oxidic environment, and Cu nanoparticles.

Figure 5.24. Evolution of the XAS spectra of passivated Cu-Mo<sub>x</sub>C<sub>y</sub>/SiO<sub>2</sub> at the Mo K-edge upon reactivation (from room temperature, dark blue, to 400 °C, red).



Reference: own author (2023)

Figure 5.25. Evolution of the XAS spectra of passivated Cu-Mo<sub>x</sub>C<sub>y</sub>/SiO<sub>2</sub> at the Cu K-edge upon reactivation (from room temperature, dark blue, to 400 °C, red).

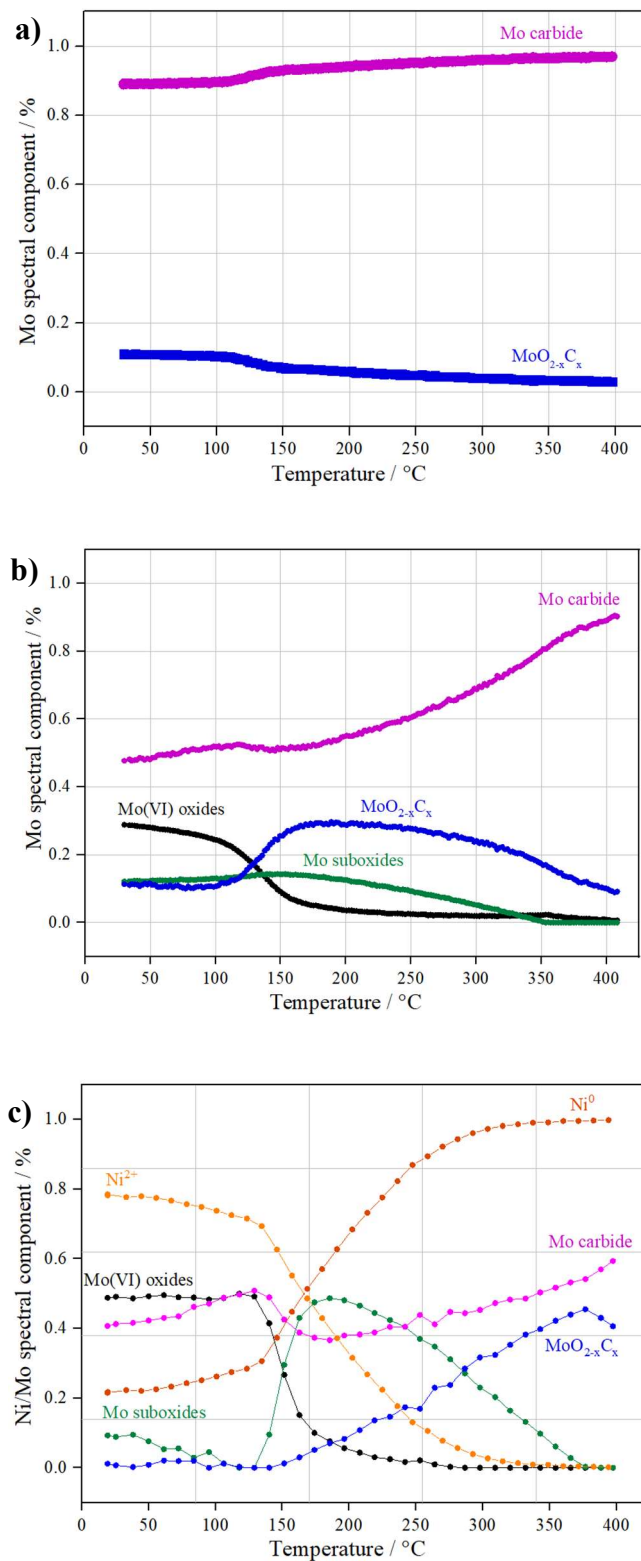


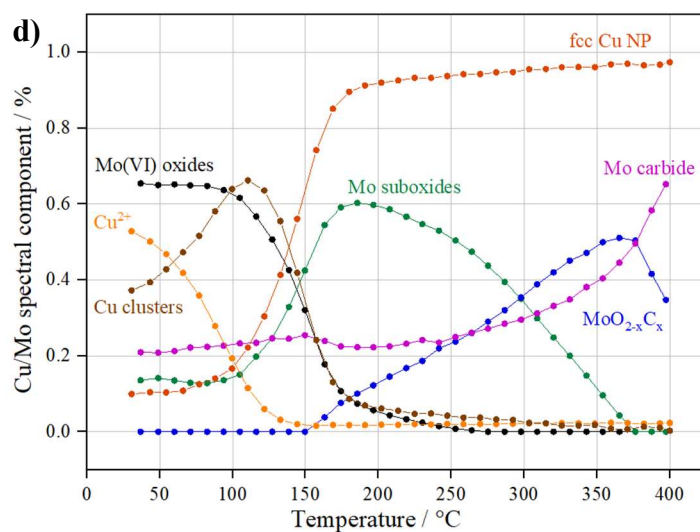
Reference: own author (2023)

The evolution of Mo and Cu speciation is shown in Figure 5.26: (1) initial coexistence of reduced Cu clusters and Cu<sup>2+</sup> ions, reduced below 150 °C; (2) concomitant formation of the Cu nanoparticles (still larger than the Ni particles in the Ni-Mo<sub>x</sub>C<sub>y</sub>/SiO<sub>2</sub> catalyst and without any strong interaction with Mo) and reduction of Mo(VI) oxides to Mo suboxides, between 120 and 250 °C, possibly promoted by the activation of H<sub>2</sub> on Cu; (3) partial reduction of Mo suboxides to Mo between 200 and 350 °C, and restoration of a fraction of Mo carbide above 250 °C.

As was the case for Ni-Mo<sub>x</sub>C<sub>y</sub>/SiO<sub>2</sub>, discrepancies exist in the quantifications of the different fractions (Table 5.2, upright characters for linear combinations, italic characters for MCR-ALS analysis). But in this case, the presence of metallic Mo is ascertained by EXAFS fitting, which suggests a higher degree of de-carburization compared with the two other catalysts, in line with the larger proportion of Mo(VI) oxides detected in the passivated catalyst.

Figure 5.26. Concentrations profiles of Mo, Ni, and Cu species during reactivation in H<sub>2</sub> of the passivated a)  $\beta$ -Mo<sub>2</sub>C, b)  $\beta$ -Mo<sub>2</sub>C/SiO<sub>2</sub>, c) Ni-Mo<sub>x</sub>C<sub>y</sub>/SiO<sub>2</sub>, and d) Cu-Mo<sub>x</sub>C<sub>y</sub>/SiO<sub>2</sub> catalysts from MCR-ALS analysis of the Mo, Ni, and Cu K-edge data.





Reference: own author (2023)

In conclusion, the passivation of the supported catalysts goes deeper than for unsupported  $\beta$ -Mo<sub>2</sub>C. While a fraction of Mo carbide is always present, the proportion of oxidized fraction is larger on the bimetallic catalysts, especially on the Cu-containing one. The ramp under H<sub>2</sub> leads to the reduction of superficially oxidized Mo carbide, and to that of the deeply oxidized fraction to de-carburized metallic Mo. The larger this fraction in the passivated catalyst, like on Cu-Mo<sub>x</sub>C<sub>y</sub>/SiO<sub>2</sub>, the deeper the final de-carburization of the catalyst. After reduction, Cu nanoparticles are restored to their initial state, while the highly dispersed Ni nanoparticles now appear in strong interaction with the reduced Mo fraction.

### 5.1.2 Catalytic results

In the first step of the catalytic evaluation, a screening of the catalysts for the HDO of furfural was performed using 2-butanol as solvent at 200 °C under 30 bar of H<sub>2</sub> for 4 hours. The results are reported in Table 5.6.

Table 5.6. FF conversion and product yields for the HDO of FF over Mo carbide-based catalysts

(Reaction conditions: 200 °C, 30 bar H<sub>2</sub>, 4 hours, R = 21, 0.5 M FF in 2-butanol, SPR).

Material	X <sub>FF</sub> (%)	Yield (%)					CB (%)
		FA	2MF	FMMF	EBF	Other <sup>a</sup>	
Blank	22	5	1	0	0	0	85
SiO <sub>2</sub>	24	6	1	0	0	0	84
β-Mo <sub>2</sub> C	50	7	9	2	3	1	72
β-Mo <sub>2</sub> C/SiO <sub>2</sub>	100	0	26	8	8	2	46
α-MoC/SiO <sub>2</sub>	89	2	10	7	9	1	46
Ni-Mo <sub>x</sub> C <sub>y</sub> /SiO <sub>2</sub>	100	0	35	11	0	7	53
Cu-Mo <sub>x</sub> C <sub>y</sub> /SiO <sub>2</sub>	93	0	16	6	9	4	42

<sup>a</sup> 2-methyltetrahydrofuran (2MTHF), tetrahydrofurfuryl alcohol (THFA), 2-(sec-butoxymethyl)furan (SBMF), 1,4-pentanediol (1,4PDO), levulinic acid (LA), 2-(dibutoxymethyl)furan (FDA), 2,5-bis(furan-2-ylmethyl)furan (BFMF).

Reference: own author (2023)

The FF conversion for the test carried out without catalyst (blank test) and with SiO<sub>2</sub> was approximately the same, indicating that silica support has no activity. A lower FF conversion was observed over the unsupported β-Mo<sub>2</sub>C in comparison with the supported catalyst containing the same carbide phase (β-Mo<sub>2</sub>C/SiO<sub>2</sub>), which suggests that SiO<sub>2</sub> promotes the dispersion of the active phase as revealed by XRD and XAS experiments, which hence improves the activity of the Mo carbide. In addition, different crystallographic phases of Mo carbide on the supported catalysts led to different activities, since β-Mo<sub>2</sub>C was slightly more active than the α-MoC phase (100 and 89%, respectively). Finally, it is difficult to draw any conclusions about the effect of the promoters on Mo carbide regarding the activity, since all three catalysts (β-Mo<sub>2</sub>C/SiO<sub>2</sub>, Ni-Mo<sub>x</sub>C<sub>y</sub>/SiO<sub>2</sub>, Cu-Mo<sub>x</sub>C<sub>y</sub>/SiO<sub>2</sub>) exhibited almost full conversion of furfural.

The main compounds produced using Mo carbides in the presence of 2-butanol were 2-methylfuran (2MF), furfuryl alcohol (FA), 2-(furan-2-methyl)-5-methylfuran (FMMF), and 2,2-(1,2-ethenediyl)bis-furan (EBF). The first two compounds, i.e., FA and 2MF, are commonly observed in the reductive conversion of furfural. The hydrogenation of FF leads to FA, which is deoxygenated to 2MF (Chen *et al.*, 2018; Mariscal *et al.*, 2016). In contrast, the latter two are not usually produced.

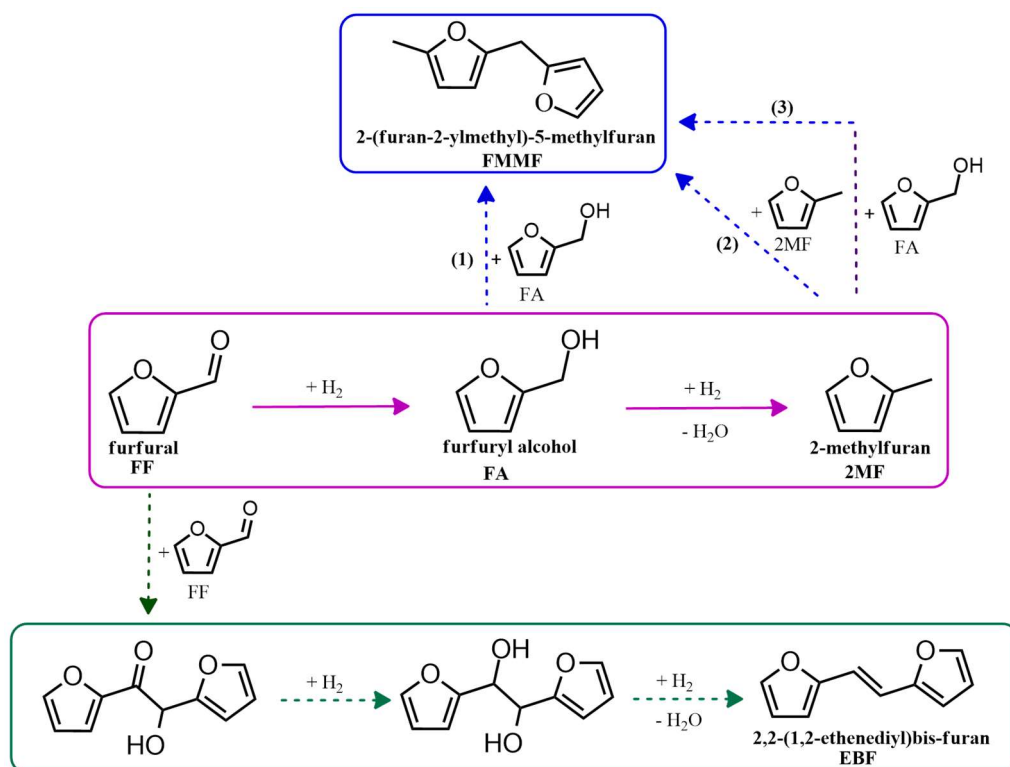
EBF is a C<sub>10</sub> compound generated by the dimerization of two FF molecules, followed by hydrogenation and dehydration reactions (Deng *et al.*, 2018; Huang *et al.*, 2012). The formation of EBF and its intermediates has been reported to occur in the presence of metals via pinacolic coupling in both aqueous and basic solutions under mild conditions (Huang *et al.*, 2012). More recently, EBF was observed as a by-product in the HDO reaction of furfural over unsupported Mo carbides (Deng *et al.*, 2018).

The formation of FMMF can occur by three different reaction pathways (Panagiotopoulou and Vlachos, 2014): (i) FA dimerization, (ii) hydroxyalkylation/alkylation of 2MF, and (iii) reaction of FA with 2MF. The FMMF production in furfural conversion reactions has been observed in a few works in the presence of noble-metal-based catalysts such as Ru (Panagiotopoulou *et al.*, 2014; Panagiotopoulou and Vlachos, 2014), Pt (Dohade and Dhepe, 2018) and Re (Zhou *et al.*, 2020b) in the liquid phase and over unsupported Mo carbides in gas phase (Lee *et al.*, 2014; Xiong *et al.*, 2014).

In any case, these two C<sub>10</sub> compounds formed as by-products in the HDO of furfural have the potential to be used as an alkane mixture suitable to be mixed with commercial diesel fuel after HDO reactions under more severe conditions (Corma *et al.*, 2012, 2011b, 2011a). The possible routes for the formation of the main products are reported in Scheme 5.1.



Scheme 5.1. Main reaction routes for the HDO of FF over unsupported and SiO<sub>2</sub>-supported Mo carbides catalysts.



Reference: own author (2023)

The comparison of the product distribution obtained on the different catalysts will not be made at this stage, since most of them exhibit full conversion of furfural, which can compromise the evaluation and lead to incorrect conclusions. Therefore, to carry out a more in-depth comparative study, the catalysts were tested individually in a larger volume reactor to achieve lower conversions and the results are presented in Table 5.7. For the tests performed in this reactor, a furfural concentration of 0.25 M was selected and compared with the concentration of 0.5 M, employed before for the reactions in the SPR using  $\alpha$ -MoC/SiO<sub>2</sub> as catalyst. The preliminary results (entries 4 and 17) showed that neither the conversion nor the product yields were affected by the concentration of the substrate, then the lowest concentration was used for further experiments.

Table 5.7. FF conversion and product yields for the HDO of FF over unsupported and SiO<sub>2</sub>-supported Mo carbides catalysts

(Reaction conditions: 200 °C, 30 bar of H<sub>2</sub>, 4 hours, 0.25 M FF in 2-butanol, Parr reactor).

Ent.	Material	R	X <sub>FF</sub> (%)	Yield (%)					CB (%)
				FA	2MF	FMMF	EBF	Other <sup>a</sup>	
1	SiO <sub>2</sub>	32	2	1	0	0	0	2	100
2	β-Mo <sub>2</sub> C	32	56	13	24	1	7	0	91
3	β-Mo <sub>2</sub> C/SiO <sub>2</sub>	32	77	5	16	6	18	2	69
4	α-MoC/SiO <sub>2</sub>	32	44	6	6	3	10	5	86
5	Ni-Mo <sub>x</sub> C <sub>y</sub> /SiO <sub>2</sub>	32	99	5	40	8	10	2	66
6	Cu-Mo <sub>x</sub> C <sub>y</sub> /SiO <sub>2</sub>	32	35	3	4	2	6	4	85
7	Ni/SiO <sub>2</sub>	32	49	42	1	0	0	4	97
8	Cu/SiO <sub>2</sub>	32	6	1	0	0	0	3	98
9	MoO <sub>3</sub> /SiO <sub>2</sub>	32	16	0	0	4	3	5	96
10	β-Mo <sub>2</sub> C	19	76	9	40	2	9	1	85
11	β-Mo <sub>2</sub> C/SiO <sub>2</sub>	19	100	0	34	7	11	4	57
12	β-Mo <sub>2</sub> C/SiO <sub>2</sub>	48	62	7	12	4	14	0	76
13	β-Mo <sub>2</sub> C/SiO <sub>2</sub>	127	30	7	2	1	8	2	91
14	α-MoC/SiO <sub>2</sub>	10	87	1	25	6	19	1	66
15	α-MoC/SiO <sub>2</sub>	16	72	4	15	6	15	3	72
16	α-MoC/SiO <sub>2</sub>	64	27	7	2	1	4	7	95
17 <sup>b</sup>	α-MoC/SiO <sub>2</sub>	64	30	7	2	1	10	1	91
18	Ni-Mo <sub>x</sub> C <sub>y</sub> /SiO <sub>2</sub>	48	84	14	27	6	13	1	77
19	Ni-Mo <sub>x</sub> C <sub>y</sub> /SiO <sub>2</sub>	76	69	17	17	3	13	2	83
20	Ni-Mo <sub>x</sub> C <sub>y</sub> /SiO <sub>2</sub>	191	39	10	5	1	10	5	92

<sup>a</sup> Tetrahydrofurfuryl alcohol (THFA), 2-(sec-butoxymethyl)furan (SBMF), 2-(dibutoxymethyl)furan (FDA), 1,2-di-2-furyl-1,2-ethanediol (DFE)

<sup>b</sup> Reaction carried out using 0.5 M FF

Reference: own author (2023)

At first, all catalysts were compared at the same furfural/active phase molar ratio (R = 32). SiO<sub>2</sub> support does not show any significant activity for the HDO reaction of furfural, but it promotes the activity of the active phase (β-Mo<sub>2</sub>C) when comparing the unsupported and supported monometallic molybdenum carbide. The FF conversion increased from 56% for unsupported β-Mo<sub>2</sub>C to 77% for the supported β-Mo<sub>2</sub>C (entries 2 and 3). The same result was observed for experiments performed in the SPR. This

result is due to the larger crystallite size of unsupported  $\beta$ -Mo<sub>2</sub>C in comparison to the supported catalyst (Table 5.1).

The activity of catalysts containing the different Mo carbide phases was also compared (entries 3 and 4). Despite having similar dispersions, as estimated by XRD, the  $\beta$ -phase was more active than the  $\alpha$ -phase in the hydrodeoxygenation of furfural. The same tendency was observed in other reactions such as the hydrogenation of 1,3-butadiene (Yang *et al.*, 2022), dehydrogenation of benzyl alcohol (Z. Li *et al.*, 2014), and hydrogenolysis of n-butane (Lee, 1990). In our case, this is likely due to the higher electron density on the  $\beta$ -phase surface or the presence of more coordinatively unsaturated Mo sites (Yang *et al.*, 2022).

An opposite trend was observed by Deng *et al.*, (2018) when using unsupported  $\beta$ -Mo<sub>2</sub>C and  $\alpha$ -MoC catalysts for the HDO of furfural reaction. According to the authors, the higher activity of  $\alpha$ -MoC in the HDO of FF was mainly due to the stronger bonding of the solvent (2-butanol) to the  $\beta$ -phase, which makes it less accessible to the reagents. Our results suggest that when supporting Mo carbides on SiO<sub>2</sub> a change in the active phase arrangement occurs, which causes the solvent to interact less with the Mo carbide when it is supported. The other possibility would be that in the work of Deng *et al.*, (2018) the same mass of catalyst was used to compare both phases and since they have different molecular weights the  $\beta$ -Mo<sub>2</sub>C will have a lower number of mols than  $\alpha$ -MoC, i.e., the comparison was done at a different R.

The effect of adding promoters to Mo carbide (entries 5 and 6) shows that the use of 3 wt.% Ni favors the activity of the catalyst when compared to the unpromoted ones ( $\beta$ -Mo<sub>2</sub>C/SiO<sub>2</sub> and  $\alpha$ -MoC/SiO<sub>2</sub>). This effect has already been observed for Ni-promoted Mo carbides for the HDO of furfural (Smirnov *et al.* 2019) and the transfer hydrogenation of lignin (Wu *et al.*, 2019). In the first case, it was associated with the ability of Ni in activating hydrogen, which made more hydrogen available in the reaction medium. In the second case, it was attributed to the synergistic effect of the  $\alpha/\beta$ -phases of Mo carbide in comparison with the catalysts containing only one of the phases, which showed lower activity.

In contrast, a negative effect on the catalytic activity (conversion of 35%) was observed when Cu was added to Mo carbide. Among the supported catalysts,

Cu-Mo<sub>x</sub>C<sub>y</sub>/SiO<sub>2</sub> was the one that showed the highest degree of oxidation after passivation, which was associated with the higher dispersion of Mo carbide due to the poor organization of copper molybdates in the calcined precursor. As observed by XAS, around 60% of Mo was still oxidized after reactivation. In addition, the test carried out with the reference catalyst Cu/SiO<sub>2</sub> (entry 8) also showed that the catalyst containing this metal is not active for the HDO of furfural since its conversion is very similar to the bare support SiO<sub>2</sub> (entry 1).

To evaluate the product distribution, all catalysts were compared at similar conversion (entries 3, 10, 15, and 19) by modification of the furfural and active phase molar ratio. For unsupported  $\beta$ -Mo<sub>2</sub>C, a much higher yield of 2MF (40%) was observed compared to  $\beta$ -Mo<sub>2</sub>C/SiO<sub>2</sub> (16%), which is likely due to the lower formation of condensation products, such as FMMF and EBF over the former catalyst (entries 3 and 10). Although unsupported  $\beta$ -Mo<sub>2</sub>C was less active than the supported ones, it was more selective to 2MF than the others. Since SiO<sub>2</sub> used as support in this work proved to be inactive for FF conversion, this change in the product distribution was attributed to the different degrees of oxidation of the catalysts after reactivation, as seen by XAS experiments.

The surface and structure modification of carbides by oxygen has been reported before (Chen and Bhan, 2017; Lee *et al.*, 2014; Sullivan *et al.*, 2015). The treatment of unsupported Mo<sub>2</sub>C with O<sub>2</sub> before the catalytic tests led to the formation of unidentified C<sub>6</sub><sup>+</sup> hydrocarbons and a 10-fold decrease in toluene production rate during the HDO of m-cresol in comparison with the untreated Mo<sub>2</sub>C catalyst (Chen and Bhan, 2017). Meanwhile, the exposure to oxygen created Bronsted acid sites on the Mo<sub>2</sub>C surface in the isopropanol dehydration (Sullivan *et al.*, 2016). Similarly, Lee *et al.*, (2014) associated the formation of C<sub>10</sub><sup>+</sup> compounds, including FMMF, in the HDO of FF in gas phase with the presence of acid sites in Mo<sub>2</sub>C catalysts caused by passivation.

In our case, the higher formation of condensation products over the  $\beta$ -Mo<sub>2</sub>C/SiO<sub>2</sub> catalyst is due to the presence of Mo oxycarbide species that catalyze alkylation reactions (Smith, 2020). For unsupported  $\beta$ -Mo<sub>2</sub>C, a lower formation of condensation occurs because this catalyst is less oxidized as observed by XAS. To prove this hypothesis, a reaction with a MoO<sub>3</sub>/SiO<sub>2</sub> catalyst was performed (entry 9). The result

showed that only EBF, FFMF, and 2-(sec-butoxymethyl)furan (SMBF), which is an ether formed by the condensation of FA with the solvent 2-butanol were produced. This result show that the degree of oxidation of Mo carbide phase strongly affects the selectivity to deoxygenated products for HDO of FF reaction. Therefore, Mo oxycarbides favors the formation of  $C_{10}^+$  compounds whereas Mo carbide promotes the production of 2MF.

The effect of passivation and activation was studied by Zhu *et al.*, (2020) by comparing the activity of a non-passivated, passivated, and activated Mo carbide for the hydrogenation of  $CO_2$ . The authors observed that the passivated catalyst was significantly less active than the non-passivated one. Even after activation at 550 °C for 1 hour in a 10% vol. hydrogen flow ( $50 \text{ mL min}^{-1}$ ), the activated catalysts were still less active than the non-passivated catalyst, which was associated with the surface Mo oxidation degree determined by XPS analysis (passivated > passivated-activated > non-passivated).

In another work, Kumar and Bhan, (2019) investigated the passivation of  $Mo_2C$  catalyst under 1%  $O_2/He$  at different temperatures (23, 70, 150 °C) for 0.5 hour and compared the performance of the catalysts in the HDO of anisole at 150 °C. The non-passivated Mo carbide formed benzene with 97% of selectivity while the increasing oxygen content in  $Mo_2C$ , obtained at different temperatures of passivation, decreased anisole conversion, aromatic reaction rate, and selectivity. However, a treatment with hydrogen at 450 °C of the oxygen-modified  $Mo_2C$  was reported to restore these parameters returning to similar values obtained over the non-passivated Mo carbide. All these works, demonstrate that passivation changes the nature of the carbides and that adequate reactivation of the catalyst is necessary before reaction.

The catalysts containing different phases of Mo carbide (entries 3 and 15) showed similar product yields, regardless of the crystalline phase, indicating that the same type of catalytic sites is involved in the reaction. The same observation was made by Souza Macedo *et al.*, (2019) when using  $\beta$ - $Mo_2C$  and  $\alpha$ - $MoC$  supported on carbon nanofibers (CNF) for the HDO reaction of stearic acid.

Although the addition of Ni favored the activity of  $\beta$ - $Mo_2C/SiO_2$  catalyst and increased the FA yield, its presence did not promote the yield to 2MF but contributed to

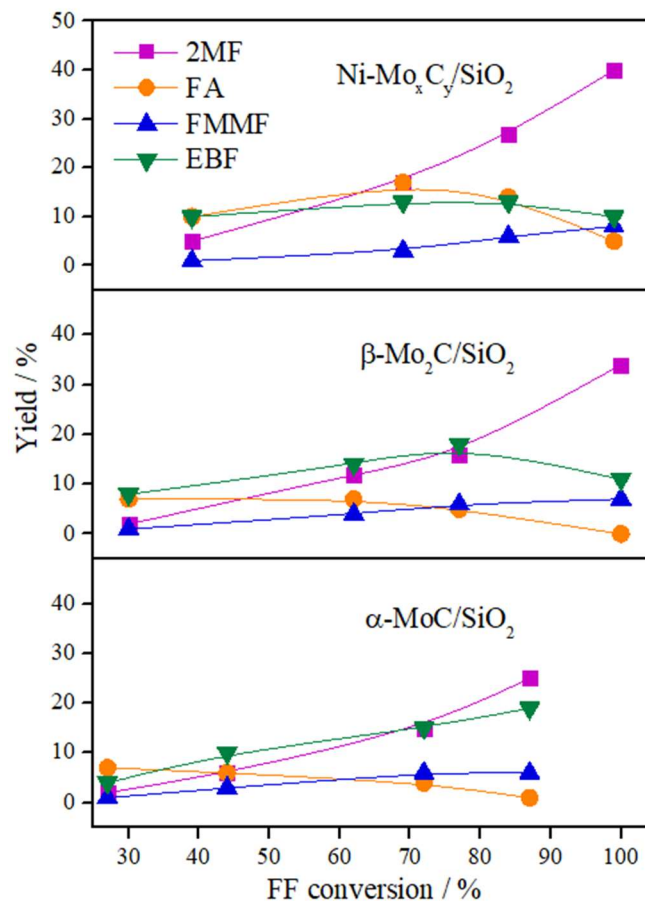
the reduction in the formation of condensation products (FMMF and EBF) (entries 3 and 19). In this case, instead of the reaction of furfural with other FF molecule to produce EBF, it is preferentially converted into FA, which decreases the formation of EBF. Furthermore, the production of FMMF formed by the reaction of 2MF with FA was also reduced. This indicates that the Ni-Mo<sub>x</sub>C<sub>y</sub>/SiO<sub>2</sub> catalyst has a higher initial conversion rate of FF compared to the β-Mo<sub>2</sub>C/SiO<sub>2</sub> catalyst.

A test performed with Ni/SiO<sub>2</sub> catalyst (entry 7) elucidated these observations since it produced mainly FA (yield of 42%) confirming that Ni has a limited activity to generate 2MF and that the Mo carbide is the active phase responsible for deoxygenation of FA to 2MF. In addition, a bimetallic carbide was not formed, in agreement with the XAS results.

The variation in the yield of products as a function of the FF conversion was evaluated for the β-Mo<sub>2</sub>C/SiO<sub>2</sub>, α-MoC/SiO<sub>2</sub>, and Ni-Mo<sub>x</sub>C<sub>y</sub>/SiO<sub>2</sub> catalysts (Figure 5.27). Increasing FF conversion, favored the yield to 2MF, which increase was accompanied by a reduction in the FA yield for all catalysts, confirming that the latter is a reaction intermediate. In general, a similar trend related to the evolution of all products was observed for the β-Mo<sub>2</sub>C/SiO<sub>2</sub> and Ni-Mo<sub>x</sub>C<sub>y</sub>/SiO<sub>2</sub> catalysts, while the EBF yield increases with the conversion for the α-MoC/SiO<sub>2</sub> catalyst. The FMMF yield remained below 10% for all catalysts.

Figure 5.27. Product yields versus FF conversion for Ni-Mo<sub>x</sub>C<sub>y</sub>/SiO<sub>2</sub>, β-Mo<sub>2</sub>C/SiO<sub>2</sub>, and α-MoC/SiO<sub>2</sub> catalysts

(Reaction conditions: 200 °C, 30 bar of H<sub>2</sub>, 4 hours, 0.25 M FF in 2-butanol, Parr reactor).



Reference: own author (2023)

### 5.1.3 Conclusions

The effect of supporting the Mo carbide phase (unsupported and SiO<sub>2</sub>-supported β-Mo<sub>2</sub>C), the Mo carbide phase type (β-Mo<sub>2</sub>C and α-MoC) and the addition of Ni and Cu promoters (Ni-Mo<sub>x</sub>C<sub>y</sub>/SiO<sub>2</sub> and Cu-Mo<sub>x</sub>C<sub>y</sub>/SiO<sub>2</sub>) were evaluated for the HDO of furfural in liquid phase at 200 °C, 30 bar of H<sub>2</sub> for 4 hours using 2-butanol as solvent. The passivation after synthesis and activation of the carbides with pure hydrogen before the catalytic tests were investigated using XAS analysis. The supported catalysts exhibited higher degrees of oxidation in comparison with the unsupported one. This

effect was more pronounced for the bimetallic Mo carbides, in special for the one promoted with Cu, which showed more disordered species that were more easily oxidized. The reactivation at 400 °C under pure H<sub>2</sub> did not restore the original carbides. For the unsupported  $\beta$ -Mo<sub>2</sub>C and monometallic  $\beta$ -Mo<sub>2</sub>C/SiO<sub>2</sub>, MoO<sub>3</sub> and Mo suboxides species were reduced during the whole range of temperature, and 80 - 90% of the carbide phase was restored. The reactivation of passivated Ni-Mo<sub>x</sub>C<sub>y</sub>/SiO<sub>2</sub> produced, besides the Mo carbide, reduced Mo species in strong interaction with Ni. Finally, metallic Mo was formed after reactivation of Cu-Mo<sub>x</sub>C<sub>y</sub>/SiO<sub>2</sub>, and Cu nanoparticles similar to those obtained after carburization were produced.

The use of SiO<sub>2</sub> as support promoted the activity of  $\beta$ -Mo<sub>2</sub>C by improving its dispersion. This, however, led to higher oxidation of the carbide phase in the supported catalyst ( $\beta$ -Mo<sub>2</sub>C/SiO<sub>2</sub>) after passivation causing the reduction of the 2MF yield in comparison with the unsupported one. The presence of oxycarbide species promoted condensation reactions and the formation of C<sub>10</sub> compounds, which can be used as diesel precursors. On the other hand, the Mo carbide phase favored the formation of 2MF. The comparison of the different crystalline phases of supported Mo carbides showed that  $\beta$ -Mo<sub>2</sub>C is more active than  $\alpha$ -MoC for the HDO of furfural. However, in similar conversions, the same product distribution is observed regardless of the Mo carbide phase.

Finally, the use of Ni as promoter for the  $\beta$ -Mo<sub>2</sub>C/SiO<sub>2</sub> increased the activity of the catalyst but did not improve the yield to 2MF. In contrast, the carbide promoted with Cu exhibited a lower activity than that of the monometallic one, which was attributed to the deep oxidation of the Cu-Mo<sub>x</sub>C<sub>y</sub>/SiO<sub>2</sub> catalyst. Therefore, the Mo carbides proved to be very active in converting FF, but their deoxygenating ability is widely affected by the degree of oxidation of the catalyst.



## 5.2 References

- A. Dantas, S.L., Lopes-Moriyama, A.L., Souza, C.P., 2018. Synthesis and characterization of molybdenum carbide doped with nickel. *Mater. Chem. Phys.* 216, 243–249. <https://doi.org/10.1016/j.matchemphys.2018.05.074>
- Antunes, M.M., Lima, S., Fernandes, A., Ribeiro, M.F., Chadwick, D., Hellgardt, K., Pillinger, M., Valente, A.A., 2018. One-pot hydrogen production and cascade reaction of furfural to bioproducts over bimetallic Pd-Ni TUD-1 type mesoporous catalysts. *Appl. Catal. B Environ.* 237, 521–537. <https://doi.org/10.1016/j.apcatb.2018.06.004>
- Barbosa, R.D., Baldanza, M.A.S., de Resende, N.S., Passos, F.B., da Silva, V.L. dos S.T., 2021. Nickel-Promoted Molybdenum or Tungsten Carbides as Catalysts in Dry Reforming of Methane: Effects of Variation in CH<sub>4</sub>/CO<sub>2</sub> Molar Ratio. *Catal. Lett.* 151, 1578–1591. <https://doi.org/10.1007/s10562-020-03420-8>
- Bogatin, Y., Robinson, M., Ormerod, J., 1991. Water milling and gas passivation method for production of corrosion resistant Nd-Fe-B-N/C powder and magnets. *J. Appl. Phys.* 70, 6594–6596. <https://doi.org/10.1063/1.349868>
- Chen, C.-J., Bhan, A., 2017. Mo<sub>2</sub>C Modification by CO<sub>2</sub>, H<sub>2</sub>O, and O<sub>2</sub>: Effects of Oxygen Content and Oxygen Source on Rates and Selectivity of *m*-Cresol Hydrodeoxygenation. *ACS Catal.* 7, 1113–1122. <https://doi.org/10.1021/acscatal.6b02762>
- Chen, S., Wojcieszak, R., Dumeignil, F., Marceau, E., Royer, S., 2018. How Catalysts and Experimental Conditions Determine the Selective Hydroconversion of Furfural and 5-Hydroxymethylfurfural. *Chem. Rev.* 118, 11023–11117. <https://doi.org/10.1021/acs.chemrev.8b00134>
- Cheng, J., Huang, W., 2010. Effect of cobalt (nickel) content on the catalytic performance of molybdenum carbides in dry-methane reforming. *Fuel Process. Technol.* 91, 185–193. <https://doi.org/10.1016/j.fuproc.2009.09.011>
- Chuseang, J., Nakwachara, R., Kalong, M., Ratchahat, S., Koo-amornpattana, W., Klysubun, W., Khemthong, P., Faungnawakij, K., Assabumrungrat, S., Itthibenchapong,

- V., Srifa, A., 2021. Selective hydrogenolysis of furfural into fuel-additive 2-methylfuran over a rhenium-promoted copper catalyst. *Sustain. Energy Fuels* 5, 1379–1393. <https://doi.org/10.1039/D1SE00036E>
- Corma, A., de la Torre, O., Renz, M., 2012. Production of high quality diesel from cellulose and hemicellulose by the Sylvan process: catalysts and process variables. *Energy Environ. Sci.* 5, 6328. <https://doi.org/10.1039/c2ee02778j>
- Corma, A., de la Torre, O., Renz, M., 2011a. High-Quality Diesel from Hexose- and Pentose-Derived Biomass Platform Molecules. *ChemSusChem* 4, 1574–1577. <https://doi.org/10.1002/cssc.201100296>
- Corma, A., de la Torre, O., Renz, M., Villandier, N., 2011b. Production of High-Quality Diesel from Biomass Waste Products. *Angew. Chem. Int. Ed.* 50, 2375–2378. <https://doi.org/10.1002/anie.201007508>
- Date, N.S., Hengne, A.M., Huang, K.-W., Chikate, R.C., Rode, C.V., 2018. Single pot selective hydrogenation of furfural to 2-methylfuran over carbon supported iridium catalysts. *Green Chem.* 20, 2027–2037. <https://doi.org/10.1039/C8GC00284C>
- Deng, Y., Gao, R., Lin, L., Liu, T., Wen, X.-D., Wang, S., Ma, D., 2018. Solvent Tunes the Selectivity of Hydrogenation Reaction over  $\alpha$ -MoC Catalyst. *J. Am. Chem. Soc.* 140, 14481–14489. <https://doi.org/10.1021/jacs.8b09310>
- Dohade, M.G., Dhepe, P.L., 2018. One pot conversion of furfural to 2-methylfuran in the presence of PtCo bimetallic catalyst. *Clean Technol. Environ. Policy* 20, 703–713. <https://doi.org/10.1007/s10098-017-1408-z>
- Fu, Z., Wang, Z., Lin, W., Song, W., Li, S., 2017. High efficient conversion of furfural to 2-methylfuran over Ni-Cu/Al<sub>2</sub>O<sub>3</sub> catalyst with formic acid as a hydrogen donor. *Appl. Catal. Gen.* 547, 248–255. <https://doi.org/10.1016/j.apcata.2017.09.011>
- Gong, W., Chen, C., Fan, R., Zhang, H., Wang, G., Zhao, H., 2018. Transfer-hydrogenation of furfural and levulinic acid over supported copper catalyst. *Fuel* 231, 165–171. <https://doi.org/10.1016/j.fuel.2018.05.075>
- Gong, W., Chen, C., Zhang, H., Wang, G., Zhao, H., 2017. Efficient Synthesis of 2-Methylfuran from Bio-Derived Furfural over Supported Copper Catalyst: The

Synergistic Effect of  $\text{CuO}_x$  and Cu. *ChemistrySelect* 2, 9984–9991. <https://doi.org/10.1002/slct.201702206>

Hanif, A., Xiao, T., York, A.P.E., Sloan, J., Green, M.L.H., 2002. Study on the Structure and Formation Mechanism of Molybdenum Carbides. *Chem. Mater.* 14, 1009–1015. <https://doi.org/10.1021/cm011096e>

Huang, Y.-B., Yang, Z., Dai, J.-J., Guo, Q.-X., Fu, Y., 2012. Production of high quality fuels from lignocellulose-derived chemicals: a convenient C–C bond formation of furfural, 5-methylfurfural and aromatic aldehyde. *RSC Adv.* 2, 11211. <https://doi.org/10.1039/c2ra22008c>

Jaatinen, S.K., Karinen, R.S., Lehtonen, J.S., 2016. Liquid Phase Furfural Hydrotreatment to 2-Methylfuran on Carbon Supported Nickel Catalyst - Effect of Process Conditions. *ChemistrySelect* 1, 5363–5373. <https://doi.org/10.1002/slct.201601333>

Jung, K.T., Kim, W.B., Rhee, C.H., Lee, J.S., 2004a. Effects of Transition Metal Addition on the Solid-State Transformation of Molybdenum Trioxide to Molybdenum Carbides. *Chem. Mater.* 16, 307–314. <https://doi.org/10.1021/cm030395w>

Jung, K.T., Kim, W.B., Rhee, C.H., Lee, J.S., 2004b. Effects of Transition Metal Addition on the Solid-State Transformation of Molybdenum Trioxide to Molybdenum Carbides. *Chem. Mater.* 16, 307–314. <https://doi.org/10.1021/cm030395w>

Kalong, M., Hongmanorom, P., Ratchahat, S., Koo-amornpattana, W., Faungnawakij, K., Assabumrungrat, S., Srifa, A., Kawi, S., 2021. Hydrogen-free hydrogenation of furfural to furfuryl alcohol and 2-methylfuran over Ni and Co-promoted  $\text{Cu}/\gamma\text{-Al}_2\text{O}_3$  catalysts. *Fuel Process. Technol.* 214, 106721. <https://doi.org/10.1016/j.fuproc.2020.106721>

Khemthong, P., Yimsukanan, C., Narkkun, T., Srifa, A., Witoon, T., Pongchaiphol, S., Kiatphuengporn, S., Faungnawakij, K., 2021. Advances in catalytic production of value-added biochemicals and biofuels via furfural platform derived lignocellulosic biomass. *Biomass Bioenergy* 148, 106033. <https://doi.org/10.1016/j.biombioe.2021.106033>

- Kumar, A., Bhan, A., 2019. Oxygen content as a variable to control product selectivity in hydrodeoxygenation reactions on molybdenum carbide catalysts. *Chem. Eng. Sci.* 197, 371–378. <https://doi.org/10.1016/j.ces.2018.12.027>
- Kurlov, A., Huang, X., Deeva, E.B., Abdala, P.M., Fedorov, A., Müller, C.R., 2020. Molybdenum carbide and oxycarbide from carbon-supported MoO<sub>3</sub> nanosheets: phase evolution and DRM catalytic activity assessed by TEM and *in situ* XANES/XRD methods. *Nanoscale* 12, 13086–13094. <https://doi.org/10.1039/D0NR02908D>
- Leary, K. J., Michaels, J. N., Stacy, A. M., 1987. The use of TPD and TPR to study subsurface mobility - Diffusion of oxygen in Mo<sub>2</sub>C. *J. Catal.* 107, 393-406.
- Leclercq, G., Kamal, M., Lamonier, J.-F., Feigenbaum, L., Malfoy, P., Leclercq, L., 1995. Treatment of bulk group VI transition metal carbides with hydrogen and oxygen. *Appl. Catal. Gen.* 121, 169–190. [https://doi.org/10.1016/0926-860X\(94\)00203-7](https://doi.org/10.1016/0926-860X(94)00203-7)
- Lee, J., 1990. Molybdenum carbide catalysts 3. Turnover rates for the hydrogenolysis of n-butane. *J. Catal.* 125, 157–170. [https://doi.org/10.1016/0021-9517\(90\)90086-Y](https://doi.org/10.1016/0021-9517(90)90086-Y)
- Lee, J., 1987. Molybdenum carbide catalysts I. Synthesis of unsupported powders. *J. Catal.* 106, 125–133. [https://doi.org/10.1016/0021-9517\(87\)90218-1](https://doi.org/10.1016/0021-9517(87)90218-1)
- Lee, W.-S., Wang, Z., Zheng, W., Vlachos, D.G., Bhan, A., 2014. Vapor phase hydrodeoxygenation of furfural to 2-methylfuran on molybdenum carbide catalysts. *Catal. Sci. Technol.* 4, 2340. <https://doi.org/10.1039/c4cy00286e>
- Levy, R.B., Boudart, M., 1973. Platinum-Like Behavior of Tungsten Carbide in Surface Catalysis. *Science* 181, 547–549. <https://doi.org/10.1126/science.181.4099.547>
- Li, Z., Chen, C., Zhan, E., Ta, N., Li, Y., Shen, W., 2014. Crystal-phase control of molybdenum carbide nanobelts for dehydrogenation of benzyl alcohol. *Chem. Commun.* 50, 4469. <https://doi.org/10.1039/c4cc00242c>
- Lin, Z., Wan, W., Yao, S., Chen, J.G., 2018. Cobalt-modified molybdenum carbide as a selective catalyst for hydrodeoxygenation of furfural. *Appl. Catal. B Environ.* 233, 160–166. <https://doi.org/10.1016/j.apcatb.2018.03.113>

- Liu, X., Song, Y., Geng, W., Li, H., Xiao, L., Wu, W., 2016. Cu-Mo<sub>2</sub>C/MCM-41: An Efficient Catalyst for the Selective Synthesis of Methanol from CO<sub>2</sub>. *Catalysts* 6, 75. <https://doi.org/10.3390/catal6050075>
- Ma, Y., Guan, G., Hao, X., Zuo, Z., Huang, W., Phanthong, P., Kusakabe, K., Abudula, A., 2014a. Highly-efficient steam reforming of methanol over copper modified molybdenum carbide. *RSC Adv* 4, 44175–44184. <https://doi.org/10.1039/C4RA05673F>
- Ma, Y., Guan, G., Phanthong, P., Hao, X., Huang, W., Tsutsumi, A., Kusakabe, K., Abudula, A., 2014b. Catalytic Activity and Stability of Nickel-Modified Molybdenum Carbide Catalysts for Steam Reforming of Methanol. *J. Phys. Chem. C* 118, 9485–9496. <https://doi.org/10.1021/jp501021t>
- Ma, Y., Guan, G., Shi, C., Zhu, A., Hao, X., Wang, Z., Kusakabe, K., Abudula, A., 2014c. Low-temperature steam reforming of methanol to produce hydrogen over various metal-doped molybdenum carbide catalysts. *Int. J. Hydrog. Energy* 39, 258–266. <https://doi.org/10.1016/j.ijhydene.2013.09.150>
- Mariscal, R., Maireles-Torres, P., Ojeda, M., Sádaba, I., López Granados, M., 2016. Furfural: a renewable and versatile platform molecule for the synthesis of chemicals and fuels. *Energy Environ. Sci.* 9, 1144–1189. <https://doi.org/10.1039/C5EE02666K>
- McCrea, K. R., Logan, J. W., Tarbuck, T. L., Heiser, J. L., Bussell, M. E., 1997. Thiophene Hydrodesulfurization over Alumina-Supported Molybdenum Carbide and Nitride Catalysts - Effect of Mo loading and phase. *J. Catal.* 171, 255–267.
- Mehdad, A., Jentoft, R.E., Jentoft, F.C., 2017. Passivation agents and conditions for Mo<sub>2</sub>C and W<sub>2</sub>C: Effect on catalytic activity for toluene hydrogenation. *J. Catal.* 347, 89–101. <https://doi.org/10.1016/j.jcat.2017.01.002>
- Nagai, M., Zahidul, A.Md., Matsuda, K., 2006. Nano-structured nickel–molybdenum carbide catalyst for low-temperature water-gas shift reaction. *Appl. Catal. Gen.* 313, 137–145. <https://doi.org/10.1016/j.apcata.2006.07.006>
- Natsir, T.A., Shimazu, S., 2020. Fuels and fuel additives from furfural derivatives via etherification and formation of methylfurans. *Fuel Process. Technol.* 200, 106308. <https://doi.org/10.1016/j.fuproc.2019.106308>

- Panagiotopoulou, P., Martin, N., Vlachos, D.G., 2014. Effect of hydrogen donor on liquid phase catalytic transfer hydrogenation of furfural over a Ru/RuO<sub>2</sub>/C catalyst. *J. Mol. Catal. Chem.* 392, 223–228. <https://doi.org/10.1016/j.molcata.2014.05.016>
- Panagiotopoulou, P., Vlachos, D.G., 2014. Liquid phase catalytic transfer hydrogenation of furfural over a Ru/C catalyst. *Appl. Catal. Gen.* 480, 17–24. <https://doi.org/10.1016/j.apcata.2014.04.018>
- Pozzo, M., Alfè, D., 2009. Hydrogen dissociation and diffusion on transition metal (=Ti, Zr, V, Fe, Ru, Co, Rh, Ni, Pd, Cu, Ag)-doped Mg(0001) surfaces. *Int. J. Hydrog. Energy* 34, 1922–1930. <https://doi.org/10.1016/j.ijhydene.2008.11.109>
- Seemala, B., Cai, C.M., Kumar, R., Wyman, C.E., Christopher, P., 2018. Effects of Cu–Ni Bimetallic Catalyst Composition and Support on Activity, Selectivity, and Stability for Furfural Conversion to 2-Methylfuran. *ACS Sustain. Chem. Eng.* 6, 2152–2161. <https://doi.org/10.1021/acssuschemeng.7b03572>
- Shilov, I., Smirnov, A., Bulavchenko, O., Yakovlev, V., 2018. Effect of Ni–Mo Carbide Catalyst Formation on Furfural Hydrogenation. *Catalysts* 8, 560. <https://doi.org/10.3390/catal8110560>
- Shou, H., Ferrari, D., Barton, D.G., Jones, C.W., Davis, R.J., 2012. Influence of Passivation on the Reactivity of Unpromoted and Rb-Promoted Mo<sub>2</sub>C Nanoparticles for CO Hydrogenation. *ACS Catal.* 2, 1408–1416. <https://doi.org/10.1021/cs300083b>
- Silva, C.G., Passos, F.B., da Silva, V.T., 2019. Influence of the support on the activity of a supported nickel-promoted molybdenum carbide catalyst for dry reforming of methane. *J. Catal.* 375, 507–518. <https://doi.org/10.1016/j.jcat.2019.05.024>
- Smirnov, A. A., Shilov, I. N., Saraev, A. A., Kauchev, V. V., Bulavchenko, O. A., Zavarukhin, S. G., Yakovlev, V. A., 2019. Hydrogenation of Furfural to 2-Methylfuran over Ni-Mo<sub>2</sub>C\_γ-Al<sub>2</sub>O<sub>3</sub> catalyst. *WSEAS Trans. Environ. Dev.* 15, 189-196.
- Smirnov, A.A., Geng, Zh., Khromova, S.A., Zavarukhin, S.G., Bulavchenko, O.A., Saraev, A.A., Kaichev, V.V., Ermakov, D.Yu., Yakovlev, V.A., 2017. Nickel molybdenum carbides: Synthesis, characterization, and catalytic activity in hydrodeoxygenation of anisole and ethyl caprate. *J. Catal.* 354, 61–77. <https://doi.org/10.1016/j.jcat.2017.07.009>

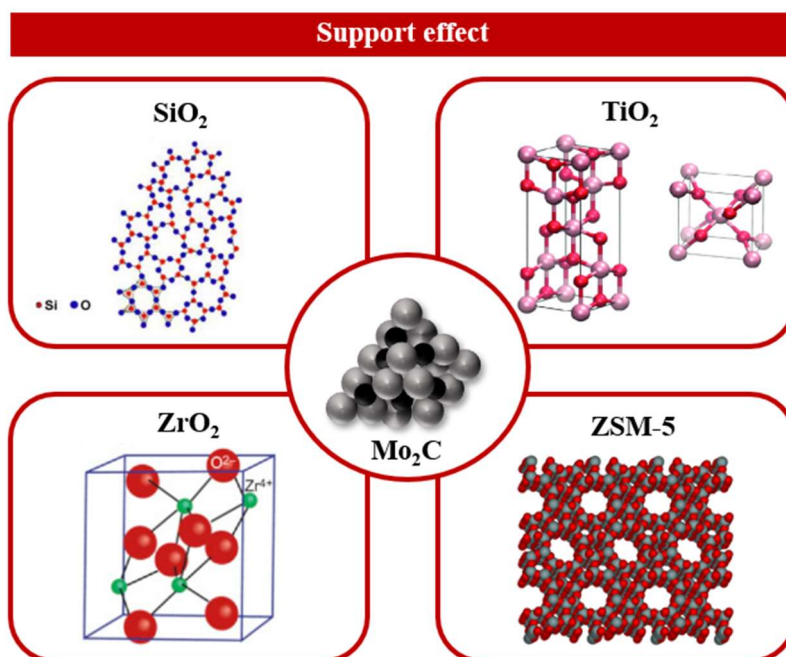
- Smith, K.J., 2020. Metal carbides, phosphides, and nitrides for biomass conversion. *Curr. Opin. Green Sustain. Chem.* 22, 47–53. <https://doi.org/10.1016/j.cogsc.2019.11.008>
- Souza Macedo, L., Oliveira, R.R., van Haasterecht, T., Teixeira da Silva, V., Bitter, H., 2019. Influence of synthesis method on molybdenum carbide crystal structure and catalytic performance in stearic acid hydrodeoxygenation. *Appl. Catal. B Environ.* 241, 81–88. <https://doi.org/10.1016/j.apcatb.2018.09.020>
- Srivastava, S., Jadeja, G.C., Parikh, J., 2017. Synergism studies on alumina-supported copper-nickel catalysts towards furfural and 5-hydroxymethylfurfural hydrogenation. *J. Mol. Catal. Chem.* 426, 244–256. <https://doi.org/10.1016/j.molcata.2016.11.023>
- Sullivan, M. M., Held, J. T., Bhan, A., 2015. Structure and site evolution of molybdenum carbide catalysts upon exposure to oxygen. *J. Catal.* 326, 82–91.
- Sullivan, M.M., Chen, C.-J., Bhan, A., 2016. Catalytic deoxygenation on transition metal carbide catalysts. *Catal. Sci. Technol.* 6, 602–616. <https://doi.org/10.1039/C5CY01665G>
- Thommes, M., Kaneko, K., Neimark, A.V., Olivier, J.P., Rodriguez-Reinoso, F., Rouquerol, J., Sing, K.S.W., 2015. Physisorption of gases, with special reference to the evaluation of surface area and pore size distribution (IUPAC Technical Report). *Pure and Applied Chemistry* 87, 1051–1069. <https://doi.org/10.1515/pac-2014-1117>
- Toledo, F., Ghampson, I.T., Sepúlveda, C., García, R., Fierro, J.L.G., Videla, A., Serpell, R., Escalona, N., 2019. Effect of Re content and support in the liquid phase conversion of furfural to furfuryl alcohol and 2-methyl furan over ReOx catalysts. *Fuel* 242, 532–544. <https://doi.org/10.1016/j.fuel.2019.01.090>
- Tsuji, M., Miyao, T., Naito, S., 2000. Remarkable support effect of ZrO<sub>2</sub> upon the CO<sub>2</sub> reforming of CH<sub>4</sub> over supported Mo carbide catalysts. *Catal. Lett.* 69, 195–198.
- Wan, C., Regmi, Y.N., Leonard, B.M., 2014. Multiple Phases of Molybdenum Carbide as Electrocatalysts for the Hydrogen Evolution Reaction. *Angew. Chem.* 126, 6525–6528. <https://doi.org/10.1002/ange.201402998>

- Wang, B., Li, C., He, B., Qi, J., Liang, C., 2017. Highly stable and selective Ru/NiFe<sub>2</sub>O<sub>4</sub> catalysts for transfer hydrogenation of biomass-derived furfural to 2-methylfuran. *J. Energy Chem.* 26, 799–807. <https://doi.org/10.1016/j.jechem.2017.04.008>
- Wang, Y., Prinsen, P., Triantafyllidis, K.S., Karakoulia, S.A., Trikalitis, P.N., Yopez, A., Len, C., Luque, R., 2018. Comparative Study of Supported Monometallic Catalysts in the Liquid-Phase Hydrogenation of Furfural: Batch Versus Continuous Flow. *ACS Sustain. Chem. Eng.* 6, 9831–9844. <https://doi.org/10.1021/acssuschemeng.8b00984>
- Wu, K., Yang, C., Zhu, Y., Wang, J., Wang, X., Liu, C., Liu, Y., Lu, H., Liang, B., Li, Y., 2019. Synthesis-Controlled  $\alpha$ - and  $\beta$ -Molybdenum Carbide for Base-Promoted Transfer Hydrogenation of Lignin to Aromatic Monomers in Ethanol. *Ind. Eng. Chem. Res.* 58, 20270–20281. <https://doi.org/10.1021/acs.iecr.9b04910>
- Wu, W., Wu, Z., Liang, C., Ying, P., Feng, Z., Li, C., 2004. An IR study on the surface passivation of Mo<sub>2</sub>C/Al<sub>2</sub>O<sub>3</sub> catalyst with O<sub>2</sub>, H<sub>2</sub>O and CO<sub>2</sub>. *Phys. Chem. Chem. Phys.* 6, 5603. <https://doi.org/10.1039/b411849a>
- Xiong, K., Lee, W.-S., Bhan, A., Chen, J.G., 2014. Molybdenum Carbide as a Highly Selective Deoxygenation Catalyst for Converting Furfural to 2-Methylfuran. *ChemSusChem* 7, 2146–2149. <https://doi.org/10.1002/cssc.201402033>
- Xu, W., Ramírez, P.J., Stacchiola, D., Brito, J.L., Rodriguez, J.A., 2015. The Carburization of Transition Metal Molybdates (MxMoO<sub>4</sub>, M = Cu, Ni or Co) and the Generation of Highly Active Metal/Carbide Catalysts for CO<sub>2</sub> Hydrogenation. *Catal. Lett.* 145, 1365–1373. <https://doi.org/10.1007/s10562-015-1540-5>
- Xu, W., Ramirez, P.J., Stacchiola, D., Rodriguez, J.A., 2014. Synthesis of  $\alpha$ -MoC<sub>1-x</sub> and  $\beta$ -MoC<sub>y</sub> Catalysts for CO<sub>2</sub> Hydrogenation by Thermal Carburization of Mo-oxide in Hydrocarbon and Hydrogen Mixtures. *Catal. Lett.* 144, 1418–1424. <https://doi.org/10.1007/s10562-014-1278-5>
- Yang, Q., Sun, K., Xu, Y., Ding, Z., Hou, R., 2022. Tuning crystal phase of molybdenum carbide catalyst to induce the different selective hydrogenation performance. *Appl. Catal. Gen.* 630, 118455. <https://doi.org/10.1016/j.apcata.2021.118455>



- Yang, Y., Liu, X., Xu, Y., Gao, X., Dai, Y., Tang, Y., 2021. Palladium-Incorporated  $\alpha$ -MoC Mesoporous Composites for Enhanced Direct Hydrodeoxygenation of Anisole. *Catalysts* 11, 370. <https://doi.org/10.3390/catal11030370>
- Zhang, A., Zhu, A., Chen, B., Zhang, S., Au, C., Shi, C., 2011. In-situ synthesis of nickel modified molybdenum carbide catalyst for dry reforming of methane. *Catal. Commun.* 12, 803–807. <https://doi.org/10.1016/j.catcom.2011.01.019>
- Zhang, T., Guo, X., Zhao, Z., 2018. Glucose-Assisted Preparation of a Nickel–Molybdenum Carbide Bimetallic Catalyst for Chemoselective Hydrogenation of Nitroaromatics and Hydrodeoxygenation of *m*-Cresol. *ACS Appl. Nano Mater.* 1, 3579–3589. <https://doi.org/10.1021/acsanm.8b00735>
- Zheng, Y., Tang, Y., Gallagher, J.R., Gao, J., Miller, J.T., Wachs, I.E., Podkolzin, S.G., 2019. Molybdenum Oxide, Oxycarbide, and Carbide: Controlling the Dynamic Composition, Size, and Catalytic Activity of Zeolite-Supported Nanostructures. *J. Phys. Chem. C* 123, 22281–22292. <https://doi.org/10.1021/acs.jpcc.9b05449>
- Zhou, K., Chen, J., Cheng, Y., Chen, Z., Kang, S., Cai, Z., Xu, Y., Wei, J., 2020. Enhanced Catalytic Transfer Hydrogenation of Biomass-Based Furfural into 2-Methylfuran over Multifunctional Cu–Re Bimetallic Catalysts. *ACS Sustain. Chem. Eng.* 8, 16624–16636. <https://doi.org/10.1021/acssuschemeng.0c06026>
- Zhou, M., Doan, H.A., Curtiss, L.A., Assary, R.S., 2021. Identification of Active Metal Carbide and Nitride Catalytic Facets for Hydrodeoxygenation Reactions. *J. Phys. Chem. C* 125, 8630–8637. <https://doi.org/10.1021/acs.jpcc.1c02387>
- Zhu, J., Uslamin, E.A., Kosinov, N., Hensen, E.J.M., 2020. Tuning the reactivity of molybdenum (oxy)carbide catalysts by the carburization degree: CO<sub>2</sub> reduction and anisole hydrodeoxygenation. *Catal. Sci. Technol.* 10, 3635–3645. <https://doi.org/10.1039/D0CY00484G>
- Zou, H., Chen, S., Huang, J., Zhao, Z., 2016. Effect of additives on the properties of nickel molybdenum carbides for the tri-reforming of methane. *Int. J. Hydrog. Energy* 41, 16842–16850. <https://doi.org/10.1016/j.ijhydene.2016.07.108>

## CHAPTER 6. HYDRODEOXYGENATION OF FURFURAL TO 2-METHYLFURAN USING SUPPORTED Mo CARBIDES. STUDY OF THE SUPPORT EFFECT.



### Abstract

The hydrodeoxygenation of furfural (FF) in liquid phase at 200 °C, 30 bar of H<sub>2</sub> for 4 hours in 2-butanol and cyclopentyl methyl ether was investigated over Mo carbides supported on different materials (SiO<sub>2</sub>, TiO<sub>2</sub>, ZrO<sub>2</sub>, and ZSM-5). The carburization, passivation, and reactivation under H<sub>2</sub> atmosphere was investigated by XAS analysis. The Mo<sub>2</sub>C/TiO<sub>2</sub> catalyst was the most affected by these treatments presenting smaller and more disorganized particles after carburization and reactivation, respectively. The less de-carburized catalyst, Mo<sub>2</sub>C/SiO<sub>2</sub>, was the most active to convert furfural. The effect of the supports was observed in the first step of the reaction and related to Lewis acidic and basic sites. Their nature was also relevant to the final state of the Mo carbides after carburization, passivation, and reactivation. The Mo carbide supported in both SiO<sub>2</sub> and TiO<sub>2</sub> are suitable catalysts to produce a mixture containing 2-methylfuran and C<sub>10</sub> compounds.

## 6. INTRODUCTION

According to the literature, two types of active sites, metallic and Lewis acidic sites, are required to promote the hydrodeoxygenation of FF to 2MF (Gong *et al.*, 2017; Liu *et al.*, 2020; Tuan Hoang and Viet Pham, 2021). The Lewis acidic sites attract and weaken the C=O bond in FF, which is hydrogenated by hydrogen species provided by the metallic sites.

Metallic species are easily obtained by the total reduction of metal oxides. On the other hand, in general, Lewis acidic sites are coordinatively unsaturated cations found in metals that are not fully reduced. Their presence and amount can be varied by controlling parameters related to the synthesis of the materials, such as the preparation method, calcination temperature and reduction conditions. The drawback of these methodologies, however, lies on the possible function loss of these species if the metal becomes totally reduced. To overcome this, Lewis acidic oxides can be used as supports for metal particles, which allows one to take advantage of the functionalities of a catalyst that is not too susceptible to physicochemical changes.

Up to now, the relationship between the properties of the support and the product distribution for the HDO of furfural is still not clear. The production of 2MF has been directly related to the amount of Lewis acidic sites in the supports (SiO<sub>2</sub>, TiO<sub>2</sub>, Al<sub>2</sub>O<sub>3</sub>, and CeO<sub>2</sub>) for Co-based catalysts exhibiting similar metal dispersion (Liu *et al.*, 2020). On the other hand, the formation of 2MF was not influenced by the nature of the support for ReO<sub>x</sub> catalysts supported on SiO<sub>2</sub>, Al<sub>2</sub>O<sub>3</sub>, and SiO<sub>2</sub>-Al<sub>2</sub>O<sub>3</sub> (Toledo *et al.*, 2019) or bimetallic catalysts containing Cu and Pd supported on SiO<sub>2</sub>, TiO<sub>2</sub>, ZrO<sub>2</sub> and Al<sub>2</sub>O<sub>3</sub> (Chang *et al.*, 2016).

Nevertheless, it is well known that the electronic effect of the supports can modify the arrangement and dispersion of the metals and consequently the adsorption/desorption of the reactants and products. This effect was observed for Cu/Ni catalysts supported on TiO<sub>2</sub> and Al<sub>2</sub>O<sub>3</sub> (Seemala *et al.*, 2018) and bimetallic Cu-Co catalysts supported on SiO<sub>2</sub>, Al<sub>2</sub>O<sub>3</sub>, and ZSM-5 (Srivastava *et al.*, 2016).

The nature of the support is even more relevant when the reaction is performed in the absence of external hydrogen. Higher yields to 2MF were observed over Cu-Pd catalysts supported on ZrO<sub>2</sub> and TiO<sub>2</sub> in comparison with SiO<sub>2</sub> and Al<sub>2</sub>O<sub>3</sub>, which was associated with the acid-base sites of the former materials, which assisted the adsorption and dissociation of the alcohols to produce hydrogen in catalytic transfer hydrogenation (CTH) reactions (Chang *et al.*, 2016).

Aiming to get more insight about the support effect, this chapter studies the performance of Mo carbides supported on SiO<sub>2</sub>, TiO<sub>2</sub>, ZrO<sub>2</sub> and ZSM-5 for the HDO of furfural. Therefore, the acidic properties of the materials, such as the total amount of the acidic sites was considered. Silica has scarcely acidic properties, while TiO<sub>2</sub> and ZrO<sub>2</sub> exhibit Lewis acidic sites and ZSM-5 possesses both Lewis and Brønsted acidic sites. In addition, the use of a protic solvent such as 2-butanol (2BuOH) and an aprotic solvent as cyclopentyl methyl ether (CPME), pointed as a potential green solvent to be used in biomass conversion reactions (de Gonzalo *et al.*, 2019; Molina, 2012), will also be evaluated.

## 6.1 Results and discussions

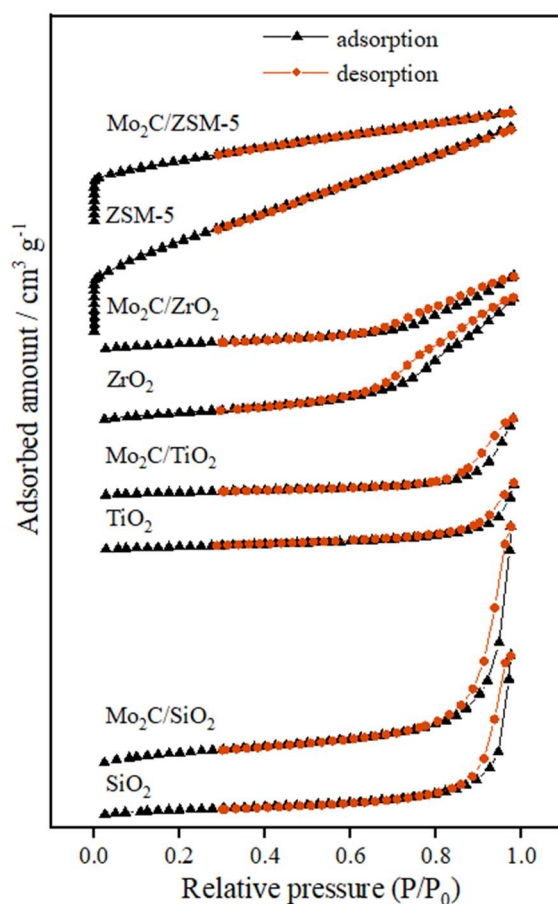
### 6.1.1 Characterization

The content of Mo and C species in the passivated catalysts estimated by ICP-OES and elemental analysis is reported in Table 6.1. The theoretical value of the C/Mo molar ratio is 0.5 according to the chemical formula of the carbide (Mo<sub>2</sub>C). The values obtained for the Mo<sub>2</sub>C/SiO<sub>2</sub> (0.41) and Mo<sub>2</sub>C/TiO<sub>2</sub> (0.52) catalysts were close to the expected value, while an excess of carbon was observed for both Mo<sub>2</sub>C/ZrO<sub>2</sub> (0.60) and Mo<sub>2</sub>C/ZSM-5 (0.61) catalysts.

All catalysts showed similar N<sub>2</sub> adsorption-desorption isotherms to their respective supports (Figure 6.1). According to the IUPAC classification, the adsorption curves on SiO<sub>2</sub> and Mo<sub>2</sub>C/SiO<sub>2</sub> corresponded to a type II isotherm, with an H3

hysteresis loop (Thommas *et al.*, 2015). The Mo<sub>2</sub>C/TiO<sub>2</sub> and Mo<sub>2</sub>C/ZrO<sub>2</sub> catalysts and their respective supports exhibited a type IV isotherm with an H3 hysteresis loop, which is associated with the capillary condensation in meso and micropores (Wang *et al.*, 2013; Juan *et al.* 2022). Finally, ZSM-5 and Mo<sub>2</sub>C/ZSM-5 materials exhibited type I isotherms, typical of microporous materials, in which there is a rapid increase in the adsorbed amount and a long and nearly flat region at higher pressures (Wang, 2013).

Figure 6.1. N<sub>2</sub> adsorption-desorption isotherms of the passivated Mo carbides and respective supports.



Reference: own author (2023)

The textural properties of the supports and passivated catalysts determined by N<sub>2</sub> physisorption are shown in Table 6.1. Except for Mo<sub>2</sub>C/TiO<sub>2</sub> catalyst, a decrease in the specific surface area (SSA) and pore volume (P<sub>v</sub>) was observed for all materials after

the synthesis of carbides in comparison with the bare supports, which is consistent with the formation of 20 wt.% Mo<sub>2</sub>C, a nonporous material with low surface area.

Table 6.1. Chemical composition and textural properties of the supports and Mo carbides catalysts.

Material	Content (wt. %)			SSA <sup>a</sup> (m <sup>2</sup> g <sup>-1</sup> )	P <sub>v</sub> <sup>b</sup> (cm <sup>3</sup> g <sup>-1</sup> )	D <sub>c</sub> (nm)
	Mo	C	Mo <sub>2</sub> C			
SiO <sub>2</sub>	-	-	-	198	1.13	-
TiO <sub>2</sub>	-	-	-	41	0.15	-
ZrO <sub>2</sub>	-	-	-	98	0.29	-
ZSM-5	-	-	-	515	0.32	-
Mo <sub>2</sub> C/SiO <sub>2</sub>	17.6	0.8	18.4	140	0.53	5
Mo <sub>2</sub> C/TiO <sub>2</sub>	18.4	1.1	19.5	44	0.17	-
Mo <sub>2</sub> C/ZrO <sub>2</sub>	17.3	1.4	18.7	70	0.18	-
Mo <sub>2</sub> C/ZSM-5	17.1	1.3	18.4	318	0.04 <sup>c</sup>	5

<sup>a</sup> estimated by the BET method

<sup>b</sup> estimated by the BJH method

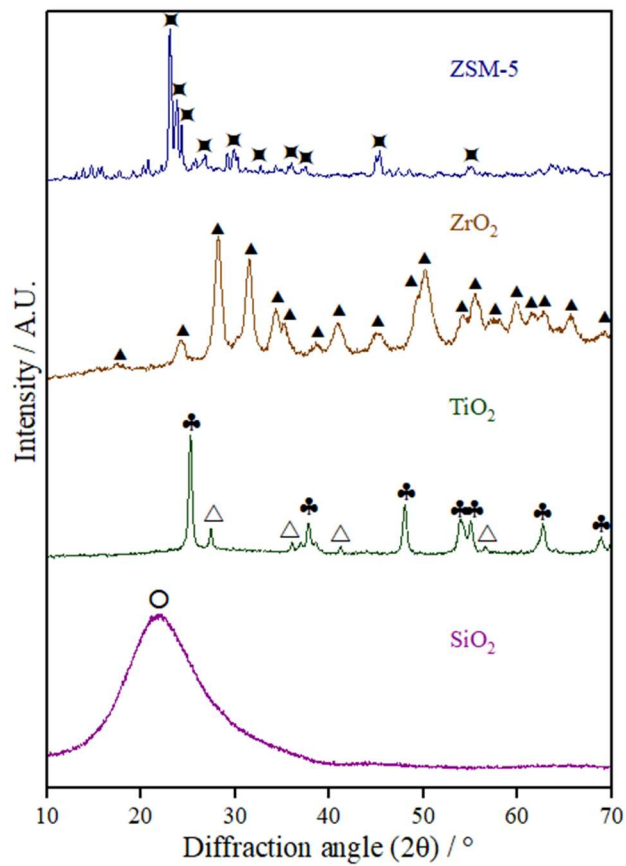
<sup>c</sup> estimated by the t-plot method

Reference: own author (2023)

Figures 6.2 and 6.3 displays the diffractograms of the different supports and calcined precursors of the Mo carbides, respectively. The broad peak at  $2\theta = 21.9^\circ$  corresponds to the classical pattern of amorphous SiO<sub>2</sub> (JCPDS 39-1425). For titania P25, two crystalline phases could be identified: anatase (a-TiO<sub>2</sub>, JCPDS 21-1272) and rutile (r-TiO<sub>2</sub>, JCPDS 21-1276). The zirconia diffractogram exhibits the monoclinic phase (m-ZrO<sub>2</sub>, JCPDS 37-1484) and the diffraction pattern that matches the ZSM-5 diffractogram is JCPDS 44-0002. The molybdenum species formed in all catalysts after calcination corresponds to the MoO<sub>3</sub> phase (JCPDS 05-0508).

Figure 6.2. Diffractograms of the different supports for the Mo carbides.

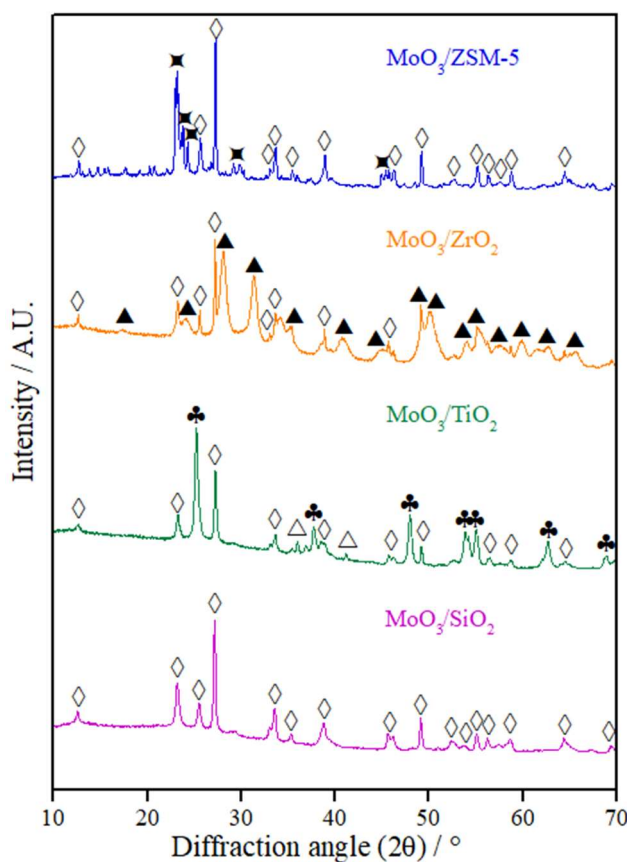
✦ ZSM-5, ▲ m-ZrO<sub>2</sub>, ♣ a-TiO<sub>2</sub>, △ r-TiO<sub>2</sub>



Reference: own author (2023)

Figure 6.3. Diffractograms of the calcined precursors of Mo carbides supported on different materials.  $\diamond$

$\text{MoO}_3$ ,  $\blacktriangleright$  ZSM-5,  $\blacktriangle$  m-ZrO<sub>2</sub>,  $\clubsuit$  a-TiO<sub>2</sub>,  $\triangle$  r-TiO<sub>2</sub>

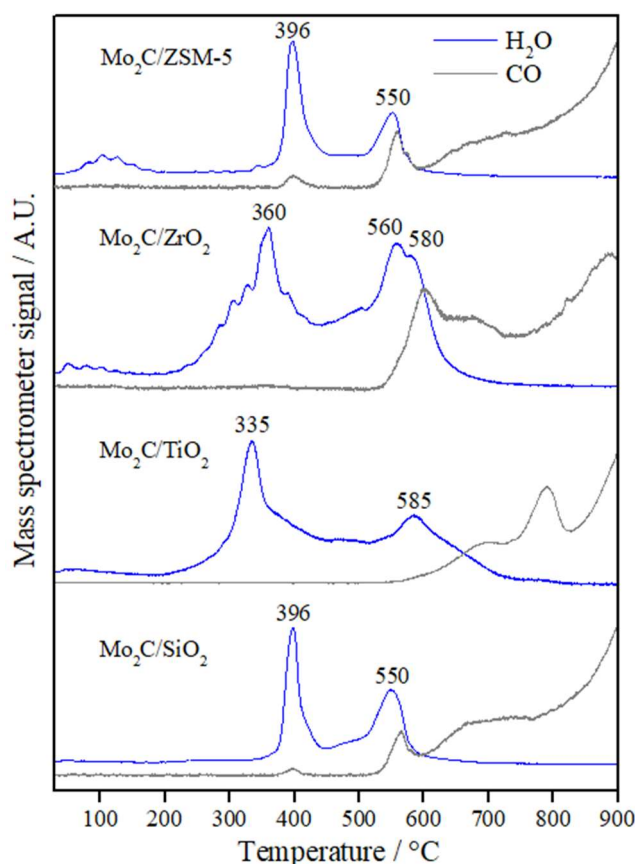


Reference: own author (2023)

To better understand the formation of the carbides, the carburization process was accompanied by water and CO formation during TPC (Figure 6.4). The profiles of all catalysts showed two main regions in the range between 300 - 400 °C and 500 - 600 °C. In Chapter 4, we followed the *in situ* carburization of the Mo<sub>2</sub>C/SiO<sub>2</sub> catalyst by XAS. The results showed that the synthesis of the carbide is initiated by the reduction of the MoO<sub>3</sub> to suboxides, such as Mo<sub>4</sub>O<sub>11</sub>, followed by the incorporation of carbon and formation of a phase with a limited degree of carburization (MoO<sub>2-x</sub>C<sub>x</sub>). These transformations take place in the lower temperature region, while the formation of the final Mo carbide occurs above 450 °C and it is accompanied by an important production of CO.



Figure 6.4. Water and CO formation profiles during TPC of the calcined precursors of Mo<sub>2</sub>C/SiO<sub>2</sub>, Mo<sub>2</sub>C/TiO<sub>2</sub>, Mo<sub>2</sub>C/ZrO<sub>2</sub>, and Mo<sub>2</sub>C/ZSM-5.



Reference: own author (2023)

The carburization process of the catalysts supported on SiO<sub>2</sub> and ZSM-5 are rather similar with two main peaks at 396 °C and 550 °C. In comparison with the literature, a similar profile was observed during the carburization of 10MoO<sub>x</sub>/HZSM-5 with the transformations occurring at higher temperatures in a mixture containing more diluted methane (10% CH<sub>4</sub>/H<sub>2</sub>) (Rahman *et al.*, 2019).

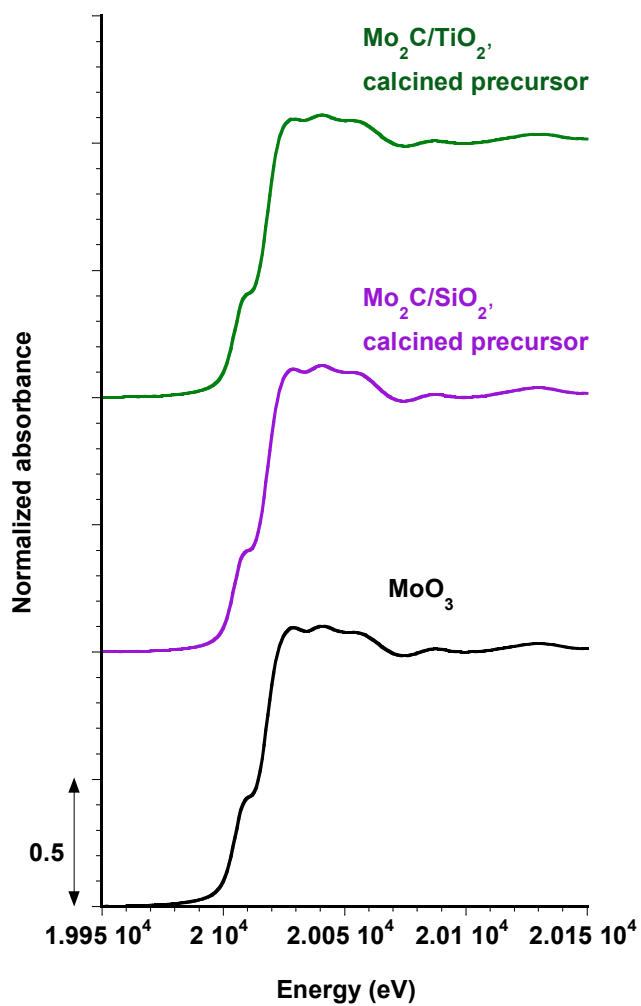
For the Mo<sub>2</sub>C/TiO<sub>2</sub> and Mo<sub>2</sub>C/ZrO<sub>2</sub> catalysts, the first step corresponding to the reduction of Mo oxides takes place at 335 and 360 °C, respectively, i.e., at lower temperatures in comparison with the Mo carbides supported on SiO<sub>2</sub> and ZSM-5. This could indicate a weaker interaction of the Mo species with these supports, which favours the reduction of the Mo oxides. In addition, the several shoulders near the main peak at 360 °C for the Mo<sub>2</sub>C/ZrO<sub>2</sub> catalyst might be related to the reduction of MoO<sub>3</sub> particles

of various sizes. On the contrary, the carburization occurred at higher temperatures for these catalysts in comparison with the ones supported on SiO<sub>2</sub> and ZSM-5.

The molybdenum transformations during the synthesis of the Mo<sub>2</sub>C/TiO<sub>2</sub> catalyst were also investigated by Raman and XAS analyses and compared to the ones of the Mo<sub>2</sub>C/SiO<sub>2</sub> catalyst.

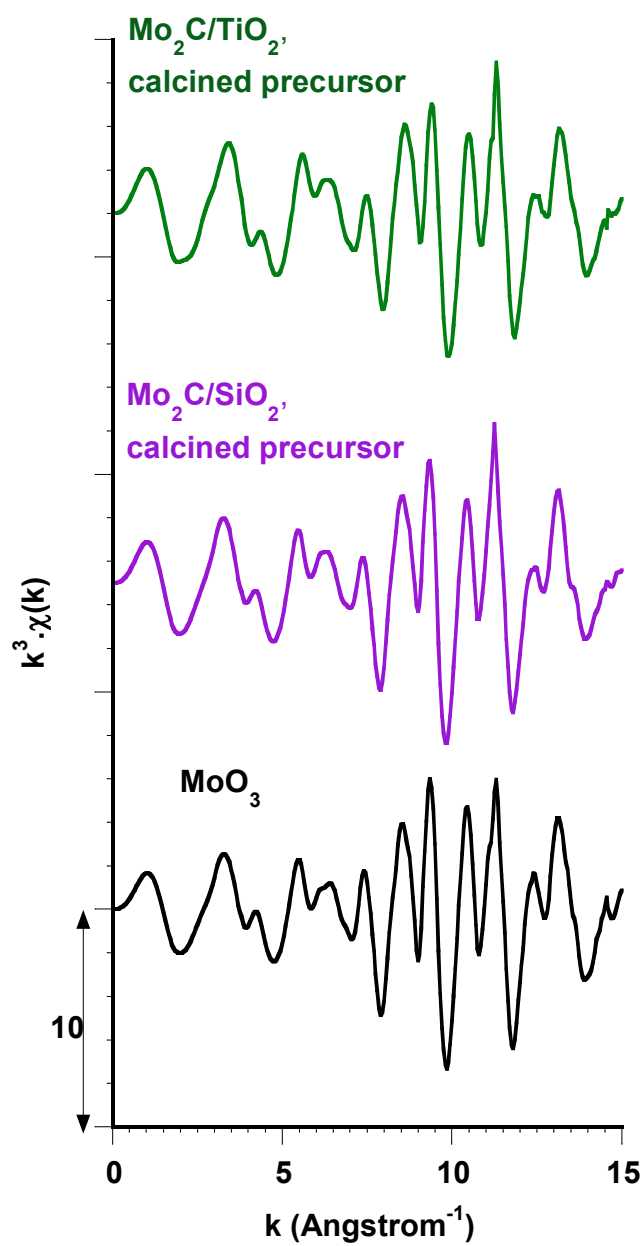
XAS analysis at the Mo K-edge performed for the calcined precursors of Mo<sub>2</sub>C/SiO<sub>2</sub> and Mo<sub>2</sub>C/TiO<sub>2</sub> catalysts are presented in Figures 6.5 - 6.7. For both precursors, the shape of the XANES spectra and position in energy are similar to those of the MoO<sub>3</sub> standard (Figure 6.5). Bands at 994, 819 and 665 cm<sup>-1</sup> in the Raman spectra of the calcined precursors (Figure 6.8) confirm the presence of MoO<sub>3</sub> (Mo *et al.*, 2016b) in a well-crystallized form, which is in agreement with the XRD results. In addition, in the spectrum of the precursor of the Mo<sub>2</sub>C/TiO<sub>2</sub> catalyst, the bands at 636, 514, and 397 cm<sup>-1</sup> are ascribed to the anatase phase of the TiO<sub>2</sub> support (Abou Hamdan *et al.*, 2019).

Figure 6.5. XANES spectra recorded at the Mo K-edge for the calcined precursors of Mo<sub>2</sub>C/SiO<sub>2</sub> and Mo<sub>2</sub>C/TiO<sub>2</sub>. Comparison with reference MoO<sub>3</sub>.



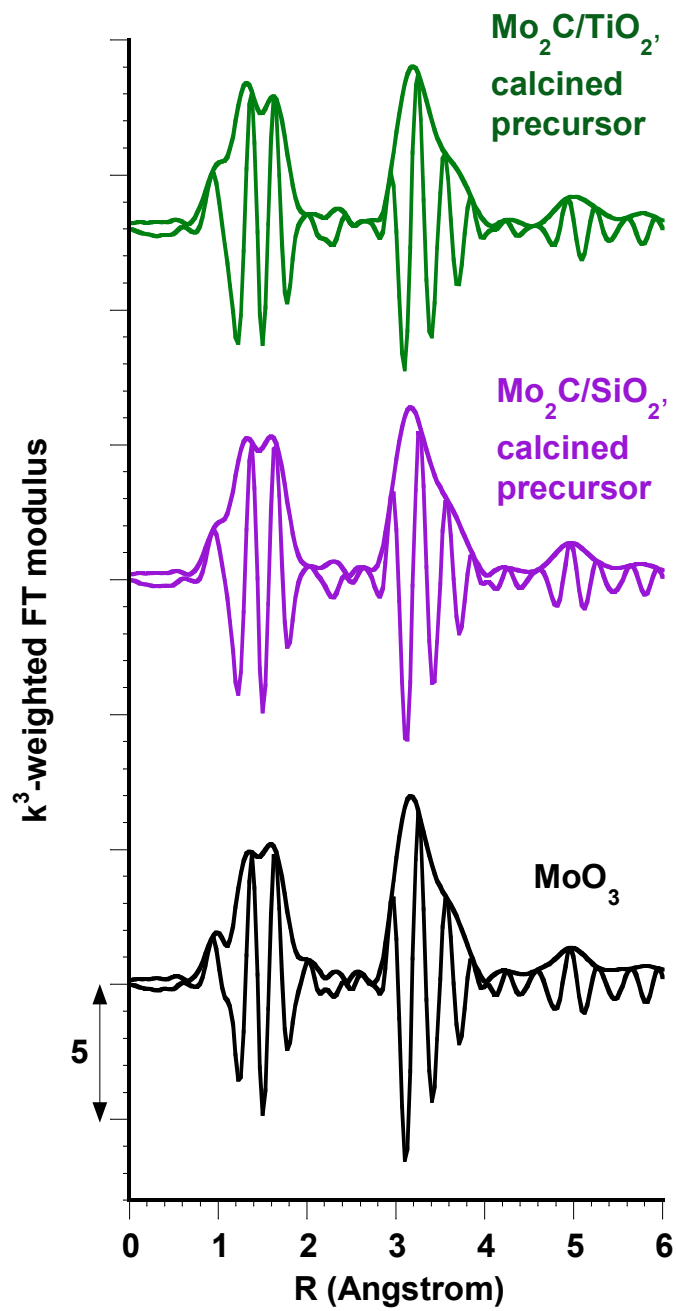
Reference: own author (2023)

Figure 6.6. EXAFS signals recorded at the Mo K-edge for the calcined precursors of Mo<sub>2</sub>C/SiO<sub>2</sub> and Mo<sub>2</sub>C/TiO<sub>2</sub>. Comparison with reference MoO<sub>3</sub>.



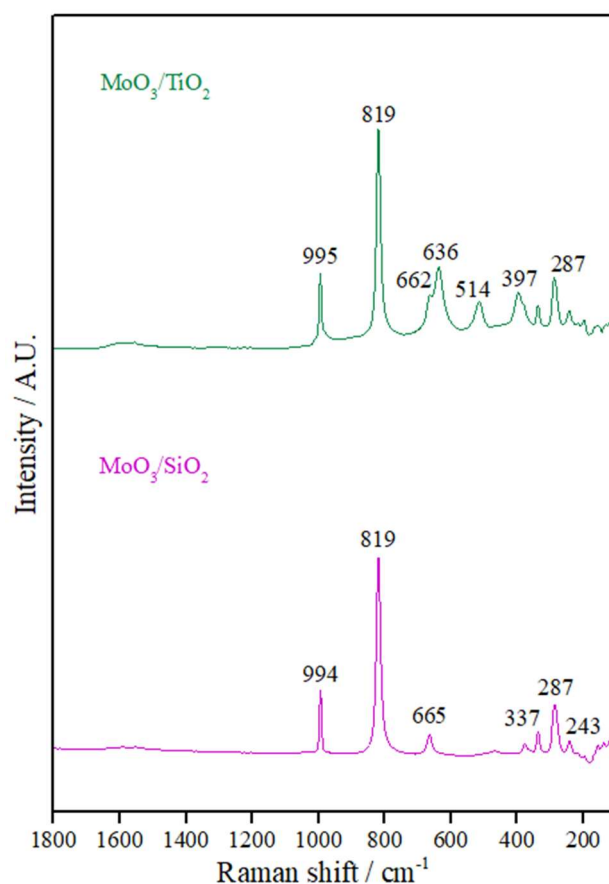
Reference: own author (2023)

Figure 6.7. Fourier transforms of the EXAFS signals recorded at the Mo K-edge for the calcined precursors of Mo<sub>2</sub>C/SiO<sub>2</sub> and Mo<sub>2</sub>C/TiO<sub>2</sub> ( $k = 3.5 - 15 \text{ \AA}^{-1}$ ). Comparison with reference MoO<sub>3</sub>.



Reference: own author (2023)

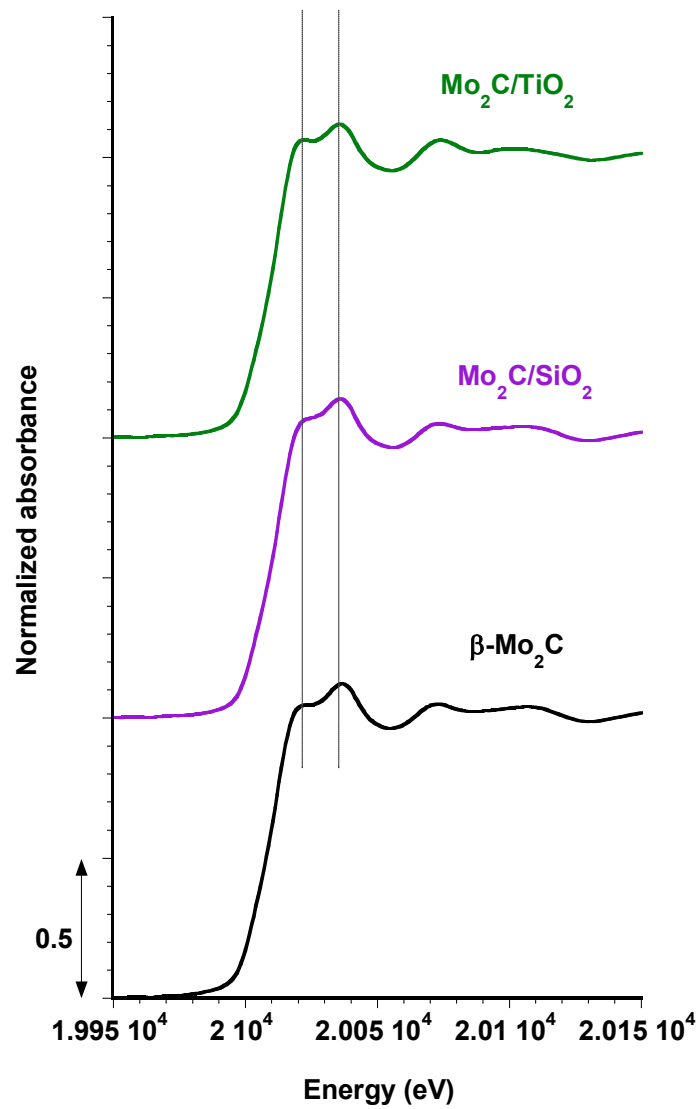
Figure 6.8. Raman spectra of the calcined precursors of  $\text{Mo}_2/\text{SiO}_2$  and  $\text{Mo}_2\text{C}/\text{TiO}_2$  (recorded at room temperature).



Reference: own author (2023)

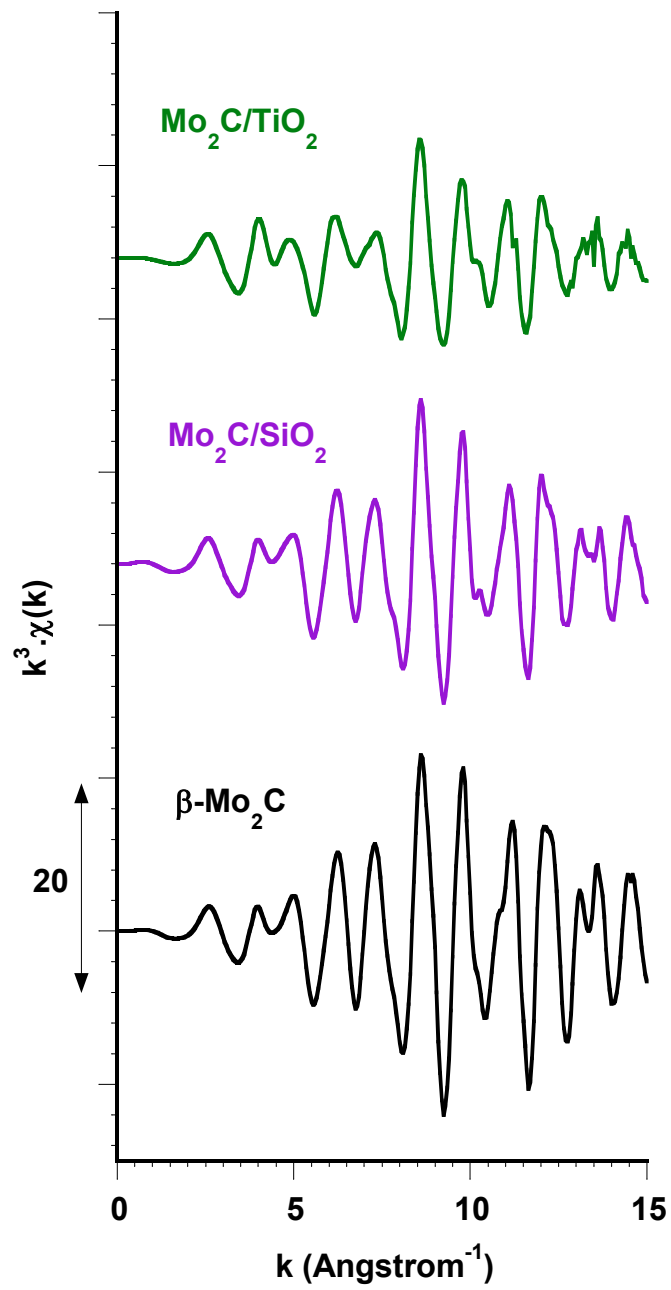
After carburization, the XANES spectra, EXAFS oscillations and Fourier transforms of  $\text{Mo}_2\text{C}/\text{SiO}_2$  and  $\text{Mo}_2\text{C}/\text{TiO}_2$  catalysts are rather similar and resemble that of reference bulk  $\beta\text{-Mo}_2\text{C}$  (an unsupported standard whose structure was identified by XRD after passivation, and that was reactivated under  $\text{H}_2$  at 400 °C before recording the XAS spectrum) (Figures 6.9 - 6.11). However, the shape of the XANES spectrum (Figure 6.9) after the edge is slightly different. The two features between 20020 and 20040 eV are better defined for  $\text{Mo}_2\text{C}$  supported on  $\text{TiO}_2$ . In fact, EXAFS oscillations (Figure 6.10) are much less intense for the  $\text{Mo}_2\text{C}/\text{TiO}_2$  catalyst above  $k = 5 \text{ \AA}^{-1}$  (where the oscillations are dominated by the contribution of the heavier atoms), which is reflected by a peak of Mo neighbors significantly less intense than for  $\text{Mo}_2\text{C}/\text{SiO}_2$  on the Fourier transform (Figure 6.11).

Figure 6.9. XANES spectra recorded at the Mo K-edge for carburized  $\text{Mo}_2\text{C}/\text{SiO}_2$  and  $\text{Mo}_2\text{C}/\text{TiO}_2$  (spectra recorded at room temperature). Comparison with reference  $\beta\text{-Mo}_2\text{C}$ .



Reference: own author (2023)

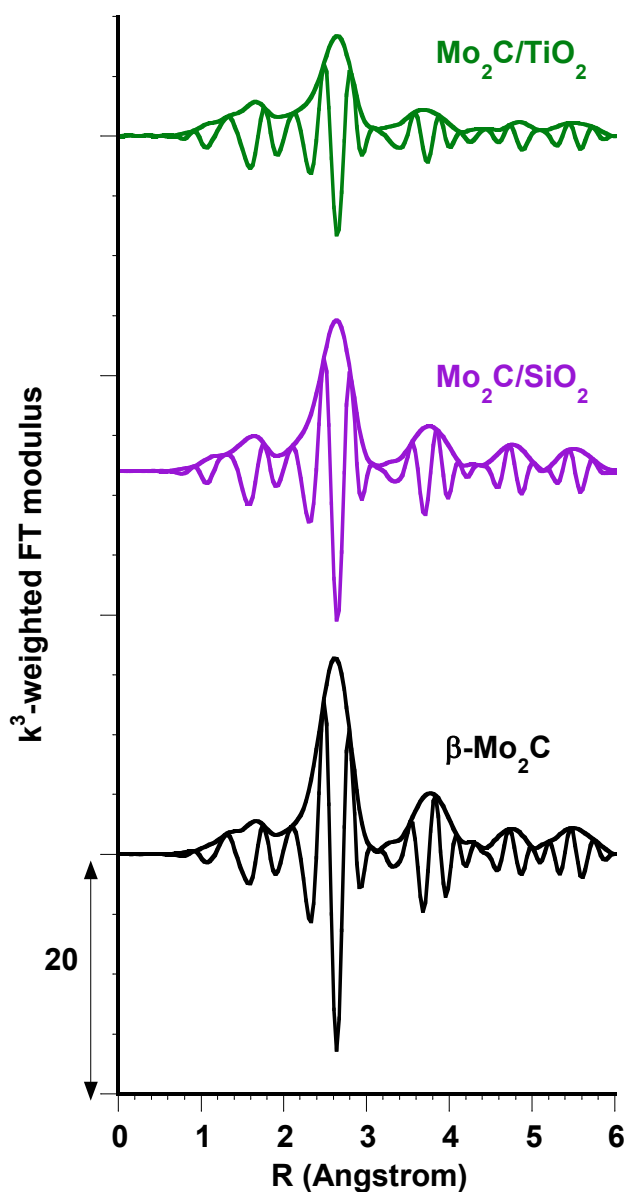
Figure 6.10. EXAFS signals recorded at the Mo K-edge for carburized  $\text{Mo}_2\text{C}/\text{SiO}_2$  and  $\text{Mo}_2\text{C}/\text{TiO}_2$  (spectra recorded at room temperature). Comparison with reference  $\beta\text{-Mo}_2\text{C}$ .



Reference: own author (2023)



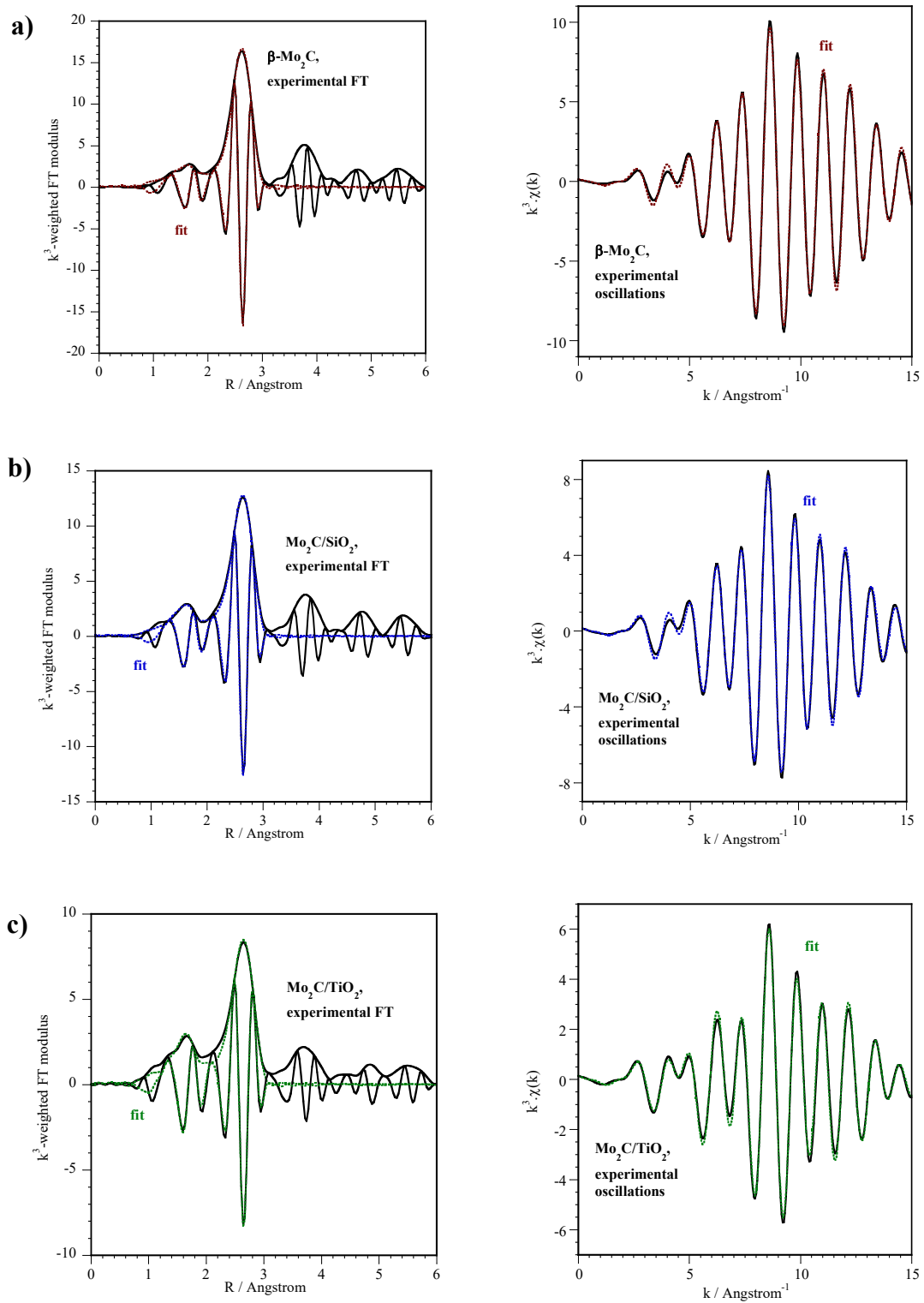
Figure 6.11. Fourier transforms of the EXAFS signals recorded at the Mo K-edge for carburized  $\text{Mo}_2\text{C}/\text{SiO}_2$  and  $\text{Mo}_2\text{C}/\text{TiO}_2$  (spectra recorded at room temperature,  $k = 3.5 - 15 \text{ \AA}^{-1}$ ). Comparison with reference  $\beta\text{-Mo}_2\text{C}$ .



Reference: own author (2023)

The results of the fits for the first two shells of neighbors (C and Mo atoms) are presented in and Table 6.2. They are consistent with the formation of Mo carbides. The number of Mo neighbors found by EXAFS fitting is 5 in  $\text{Mo}_2\text{C}/\text{TiO}_2$ , against 7 on the  $\beta\text{-Mo}_2\text{C}$  standard and  $\text{Mo}_2\text{C}/\text{SiO}_2$ : possibly smaller particles of Mo carbide exist on  $\text{TiO}_2$  after carburization.

Figure 6.12. XAS data at the Mo K-edge of a)  $\beta$ -Mo<sub>2</sub>C (reactivated in H<sub>2</sub> at 400 °C) and after carburization of b) Mo<sub>2</sub>C/SiO<sub>2</sub> and c) Mo<sub>2</sub>C/TiO<sub>2</sub> (spectra recorded at room temperature). Fit of the first and second shells of neighbors: Fourier transform (left) and EXAFS oscillations (right).  $k = 3.5 - 15 \text{ \AA}^{-1}$ .



Reference: own author (2023)

Table 6.2. Fitted parameters at the Mo K-edge ( $E_0 = 20013$  eV,  $S02 = 0.98$ ) determined from the EXAFS analysis of spectra recorded at room temperature on carburized catalysts.  $k = 3.5 - 15 \text{ \AA}^{-1}$ . Fit of the first peak(s) from the Fourier transform between 1 and 3  $\text{\AA}$ .

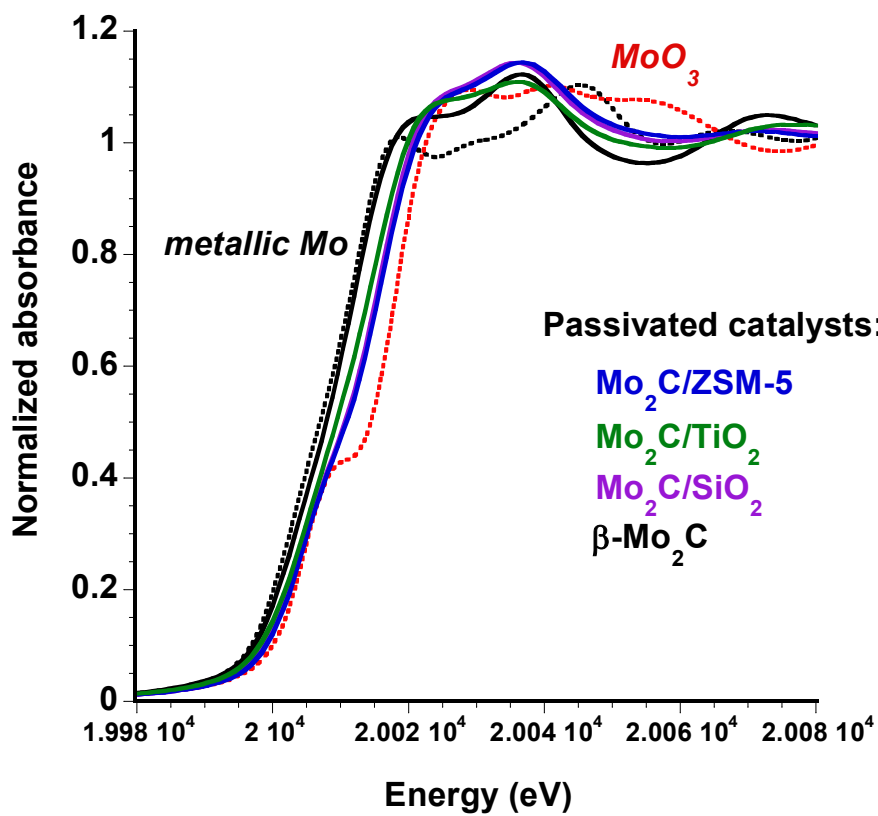
Catalyst	Backscatter	N	$\sigma^2 (\text{\AA}^2) \times 10^3$	R ( $\text{\AA}$ )
$\beta\text{-Mo}_2\text{C}^a$	C	$2.7 \pm 0.9$	$4.1 \pm 0.3$	$2.08 \pm 0.02$
	Mo	$7.3 \pm 0.8$	$5.7 \pm 0.5$	$2.966 \pm 0.005$
$\Delta E_0 = -5.5$ eV, r-factor = 0.01575, $\chi^2 = 592$ , $N_{\text{ind}} = 13$ , $N_{\text{var}} = 7$				
$\text{Mo}_2\text{C}/\text{SiO}_2$	C	$3.5 \pm 0.9$	$6 \pm 2$	$2.10 \pm 0.01$
	Mo	$7.3 \pm 0.8$	$7.3 \pm 0.6$	$2.978 \pm 0.005$
$\Delta E_0 = -3.8$ eV, r-factor = 0.01462, $\chi^2 = 441$ , $N_{\text{ind}} = 13$ , $N_{\text{var}} = 7$				
$\text{Mo}_2\text{C}/\text{TiO}_2$	C	$3.1 \pm 0.6$	$5 \pm 2$	$2.11 \pm 0.01$
	Mo	$5.1 \pm 0.7$	$7.5 \pm 0.8$	$2.984 \pm 0.005$
$\Delta E_0 = -2.9$ eV, r-factor = 0.01036, $\chi^2 = 121$ , $N_{\text{ind}} = 13$ , $N_{\text{var}} = 7$				

<sup>a</sup> (after reactivation in  $\text{H}_2$  at 400 °C)

Reference: own author (2023)

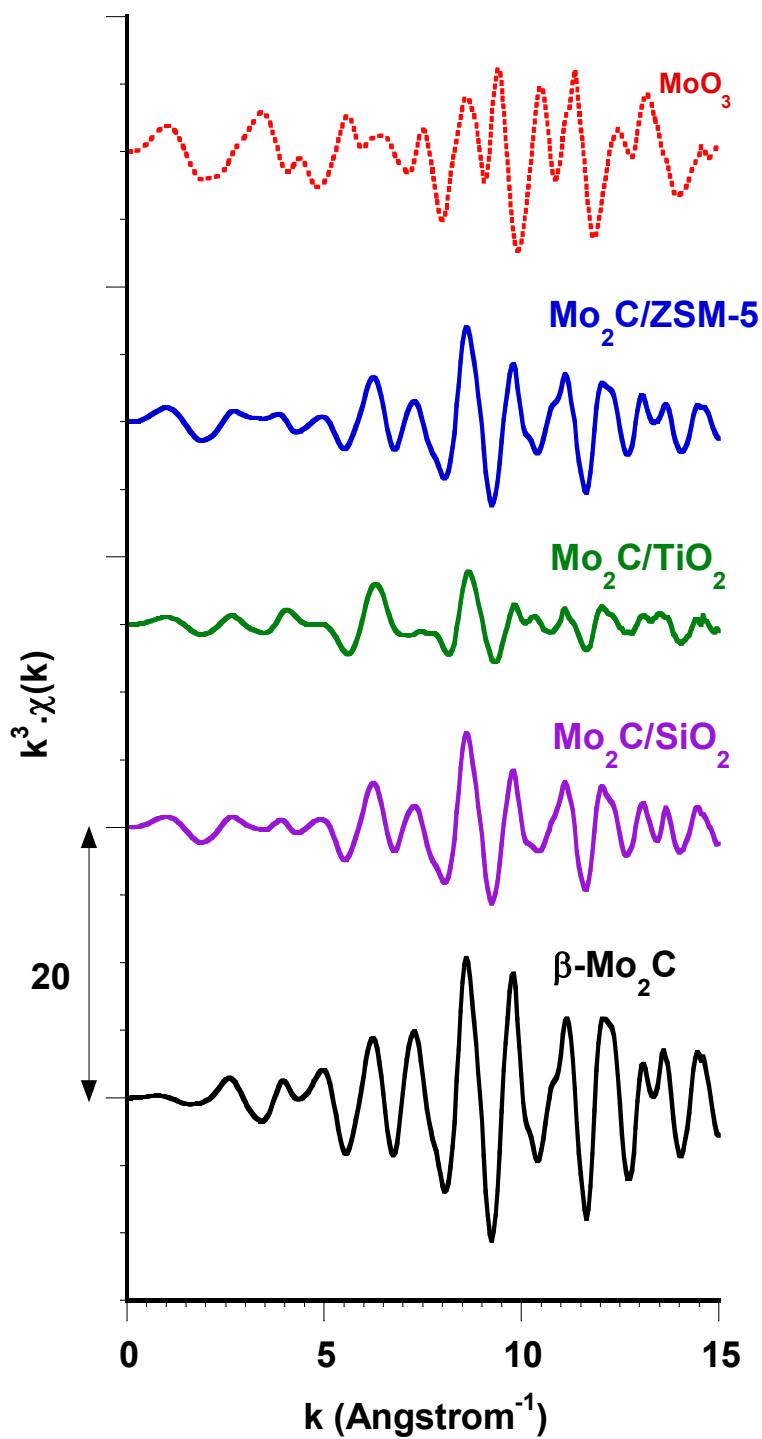
After carburization, the catalysts were passivated under diluted  $\text{O}_2$ . The passivated Mo carbides supported on  $\text{SiO}_2$ ,  $\text{TiO}_2$  and ZSM-5 were evaluated by XAS analysis at the Mo K-edge and the data are reported in Figures 6.13 - 6.15. The XANES spectra (Figure 6.13) reveal that all three catalysts were oxidized to similar degrees. The EXAFS oscillations (Figure 6.14) of Mo carbide are still recognizable for  $\text{Mo}_2\text{C}/\text{SiO}_2$  and  $\text{Mo}_2\text{C}/\text{ZSM-5}$ , while for the  $\text{Mo}_2\text{C}/\text{TiO}_2$  catalyst they appear as quite different. This is also reflected in the poorly intense peaks on the Fourier transform (Figure 6.15). It can suggest that on  $\text{TiO}_2$ , the initially more dispersed carbide became more disorganized upon passivation that the carbides on the other supports.

Figure 6.13. XANES spectra recorded at the Mo K-edge for passivated  $\beta$ - $\text{Mo}_2\text{C}$ ,  $\text{Mo}_2\text{C}/\text{SiO}_2$ ,  $\text{Mo}_2\text{C}/\text{TiO}_2$  and  $\text{Mo}_2\text{C}/\text{ZSM-5}$  (spectra recorded at room temperature). Comparison with references  $\text{MoO}_3$  and metallic Mo (dotted lines).



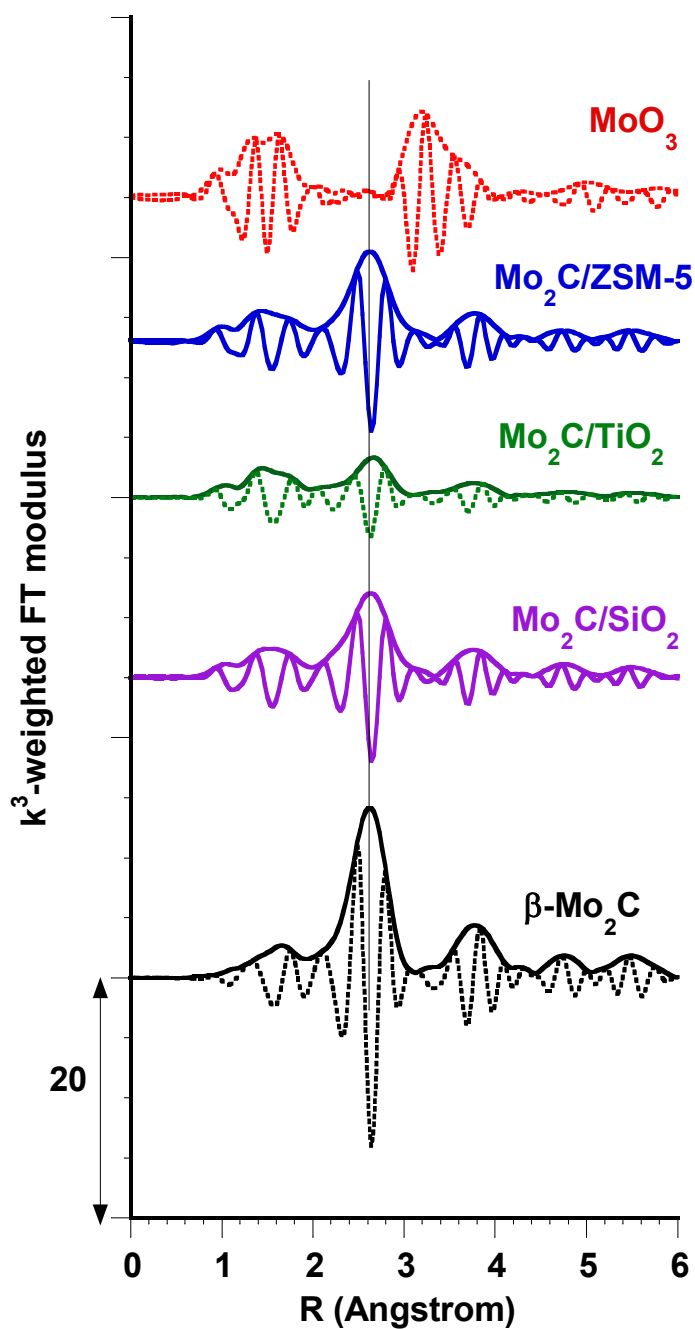
Reference: own author (2023)

Figure 6.14. EXAFS signals recorded at the Mo K-edge for passivated  $\beta$ -Mo<sub>2</sub>C, Mo<sub>2</sub>C/SiO<sub>2</sub>, Mo<sub>2</sub>C/TiO<sub>2</sub> and Mo<sub>2</sub>C/ZSM-5 (spectra recorded at room temperature). Comparison with reference MoO<sub>3</sub>.



Reference: own author (2023)

Figure 6.15. Fourier transforms of the EXAFS signals recorded at the Mo K-edge for passivated  $\beta$ -Mo<sub>2</sub>C, Mo<sub>2</sub>C/SiO<sub>2</sub>, Mo<sub>2</sub>C/TiO<sub>2</sub> and Mo<sub>2</sub>C/ZSM-5 (spectra recorded at room temperature). Comparison with reference MoO<sub>3</sub>,  $k = 3.5 - 15 \text{ \AA}^{-1}$ .

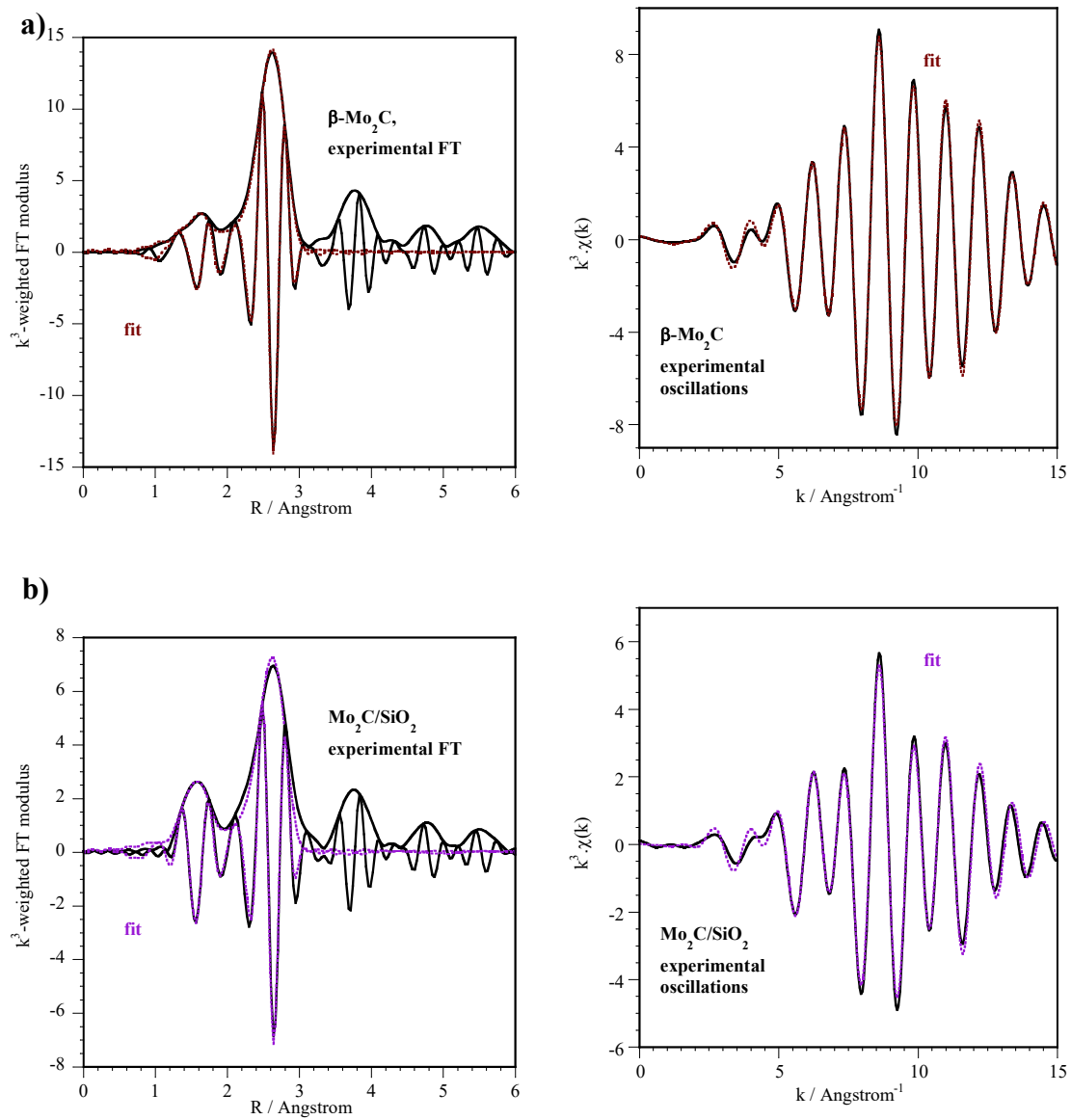


Reference: own author (2023)

The fits for the three supported passivated catalysts are still based on Mo carbide but they are all improved when a small O contribution is added to the first shell of

neighbors (Table 6.3 and Figures 6.16 and 6.17). The large error bar on  $N(C)$  do not allow for a precise discussion on the degree of carburization. Much more significant is the strong decrease of  $N(Mo)$ . Compared with the just-carburized state, this decrease is marginal for bulk  $\beta$ - $Mo_2C$ , but  $N(Mo)$  falls to 4 for  $SiO_2$  and ZSM-5 (initially 7 after carburization on  $SiO_2$ ), and to 2 on  $TiO_2$  (initially 5). The passivation of the catalysts not only oxidized the carbide, but also disorganized the particles into smaller entities, or left crystallized Mo carbide as a minor fraction. Moreover, for  $TiO_2$ , the quality of the fit is improved when it is added a Mo contribution at 2.52 Å (corresponding to the small peak at 2.1 Å on the Fourier transform), which can be interpreted as a Mo-Mo distance in  $MoO_2$ . It thus clearly appears that passivation strongly alters the nature of the carbide phases on the supported systems, with a more pronounced effect when the Mo carbide was already poorly organized after carburization.

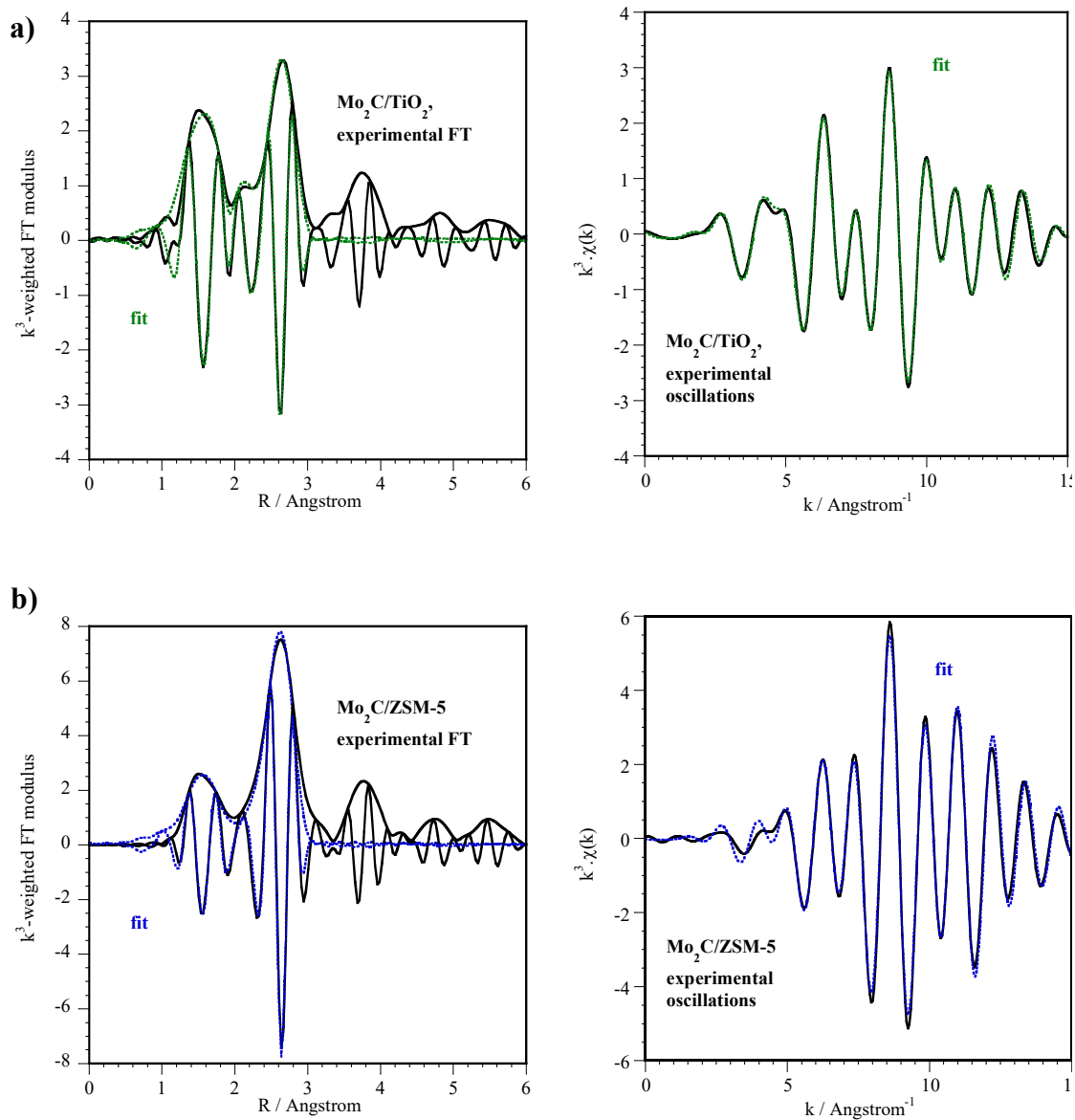
Figure 6.16. Analysis of the data recorded at the Mo K-edge for the passivated catalysts (spectra recorded at room temperature), using linear combinations of MCR-ALS components (see Table 6.3). XANES spectrum (left) and EXAFS oscillations (right), a)  $\beta$ -Mo<sub>2</sub>C and b) Mo<sub>2</sub>C/SiO<sub>2</sub>.



Reference: own author (2023)



Figure 6.17. Analysis of the data recorded at the Mo K-edge for the passivated catalysts (spectra recorded at room temperature), using linear combinations of MCR-ALS components (see Table 6.3). XANES spectrum (left) and EXAFS oscillations (right), a)  $\text{Mo}_2\text{C}/\text{TiO}_2$  and b)  $\text{Mo}_2\text{C}/\text{ZSM-5}$ .



Reference: own author (2023)

Table 6.3. Fitted parameters at the Mo K-edge ( $E_0 = 20013$  eV,  $S02 = 0.98$ ) determined from the EXAFS analysis of spectra recorded at room temperature on catalysts after passivation.  $k = 3.5 - 15 \text{ \AA}^{-1}$ . Fit of the first peak(s) from the Fourier transform between 1 and 3  $\text{\AA}$ .

Catalyst	Backscatter	N	$\sigma^2 (\text{\AA}^2) \times 10^3$	R ( $\text{\AA}$ )
$\beta\text{-Mo}_2\text{C}$	C	$2.9 \pm 0.9$	$5 \pm 3$	$2.09 \pm 0.02$
	Mo	$6.8 \pm 0.8$	$6.4 \pm 0.6$	$2.971 \pm 0.005$
	$\Delta E_0 = -4.9$ eV, r-factor = 0.01493, $\chi^2 = 646$ , $N_{\text{ind}} = 13$ , $N_{\text{var}} = 7$			
$\text{Mo}_2\text{C}/\text{SiO}_2$	O	$0.9 \pm 0.9$	$7 \pm 5$	$1.71 \pm 0.04$
	C	$4 \pm 3$	$7 \pm 5$	$2.08 \pm 0.02$
	Mo	$4 \pm 1$	$7 \pm 2$	$2.97 \pm 0.01$
	$\Delta E_0 = -5.2$ eV, r-factor = 0.03112, $\chi^2 = 1745$ , $N_{\text{ind}} = 13$ , $N_{\text{var}} = 9$			
$\text{Mo}_2\text{C}/\text{TiO}_2$	O	$0.8 \pm 0.4$	$8 \pm 2$	$1.69 \pm 0.03$
	C	$3.7 \pm 0.7$	$8 \pm 2$	$2.13 \pm 0.02$
	Mo	$0.4 \pm 0.2$	$8 \pm 2$	$2.52 \pm 0.03$
	Mo	$2.1 \pm 0.5$	$8 \pm 2$	$2.97 \pm 0.01$
$\Delta E_0 = -0.4$ eV, r-factor = 0.01268, $\chi^2 = 708$ , $N_{\text{ind}} = 13$ , $N_{\text{var}} = 10$				
$\text{Mo}_2\text{C}/\text{ZSM-5}$	O	$0.9 \pm 0.9$	$6 \pm 4$	$1.71 \pm 0.03$
	C	$3 \pm 2$	$6 \pm 4$	$2.10 \pm 0.02$
	Mo	$3.9 \pm 0.9$	$7 \pm 1$	$2.969 \pm 0.009$
$\Delta E_0 = -5.3$ eV, r-factor = 0.02999, $\chi^2 = 1515$ , $N_{\text{ind}} = 13$ , $N_{\text{var}} = 9$				

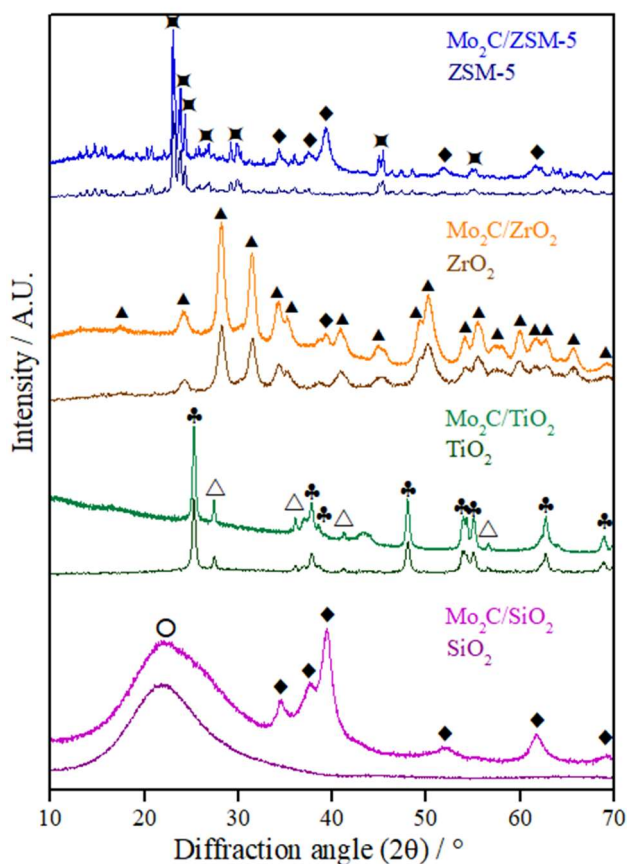
Reference: own author (2023)

Figure 6.18 displays the diffractograms of the supports and passivated Mo carbide catalysts. All supports appeared to be unchanged after the carburization and passivation stages since their crystalline structure was preserved and no new phase resulting from a reaction between the support and Mo oxide or carbide was identified (Vo and Adesina, 2011).

For the diffractograms of the passivated samples (Figure 6.18), the diffraction lines corresponding to the hexagonal  $\beta\text{-Mo}_2\text{C}$  phase (JCPDS 35-0787) at  $2\theta = 34.4$ ,  $37.8$ ,  $39.4$ ,  $61.5$ , and  $74.6^\circ$  could be easily identified for the carbides supported on  $\text{SiO}_2$  and ZSM-5. The mean crystallite diameter ( $D_c$ ) of  $\beta\text{-Mo}_2\text{C}$  for the  $\text{Mo}_2\text{C}/\text{SiO}_2$  and  $\text{Mo}_2\text{C}/\text{ZSM-5}$  catalysts was estimated by the Scherrer equation to be 5 nm (Table 6.1).

Figure 6.18. Diffractograms of supports and passivated Mo carbides supported on different materials.

◆  $\beta$ - $\text{Mo}_2\text{C}$ , ✕ ZSM-5, ▲ m- $\text{ZrO}_2$ , ♣ a- $\text{TiO}_2$ , △ r- $\text{TiO}_2$ , ○  $\text{SiO}_2$

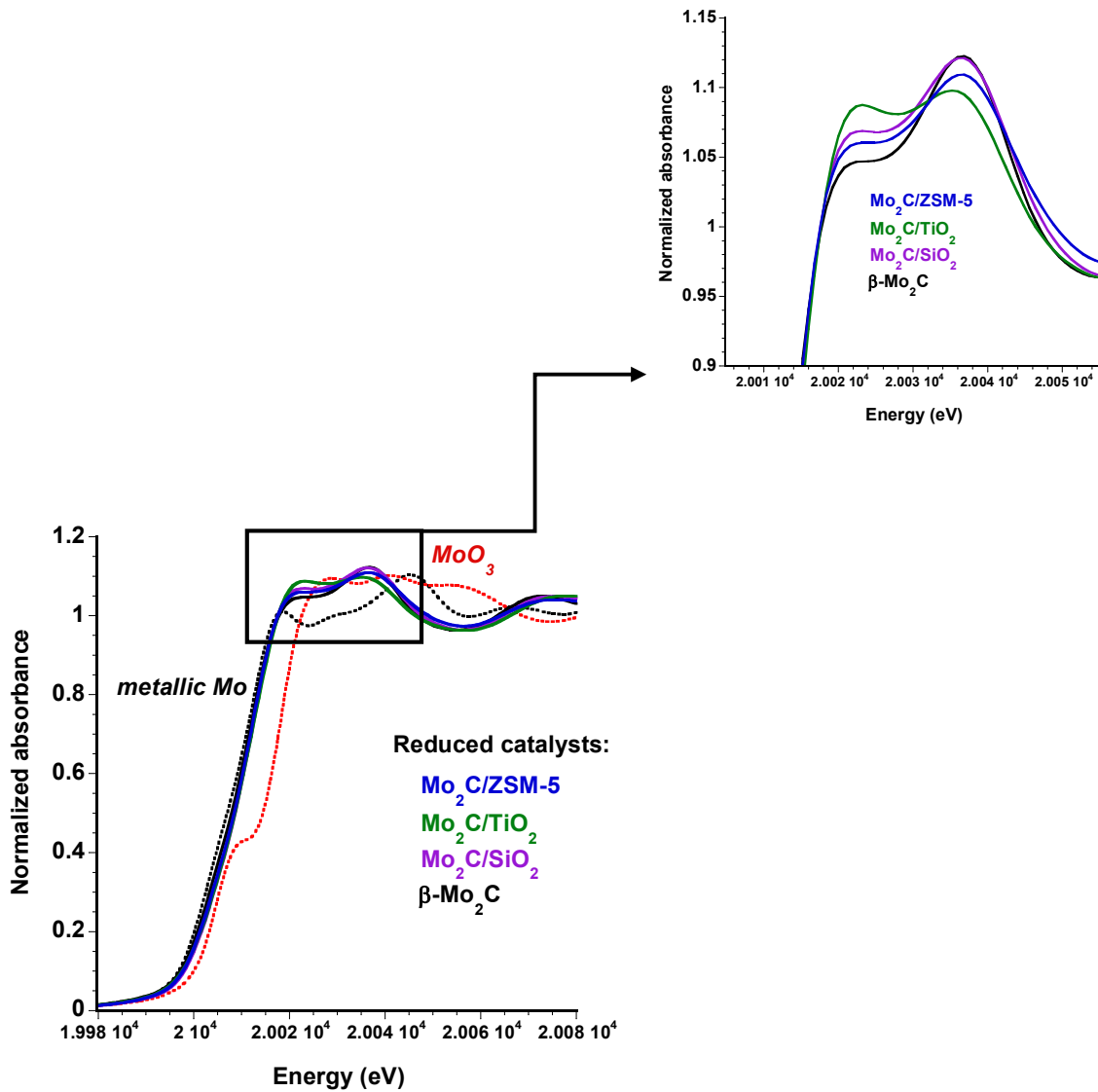


Reference: own author (2023)

After reactivation of the passivated catalysts in  $\text{H}_2$  (Figure 6.19), the carbide spectrum reappears, but the spectrum of  $\text{Mo}_2\text{C}/\text{TiO}_2$  is still quite different as can be seen in the relative intensity of the two features after the edge in the zoomed figure.

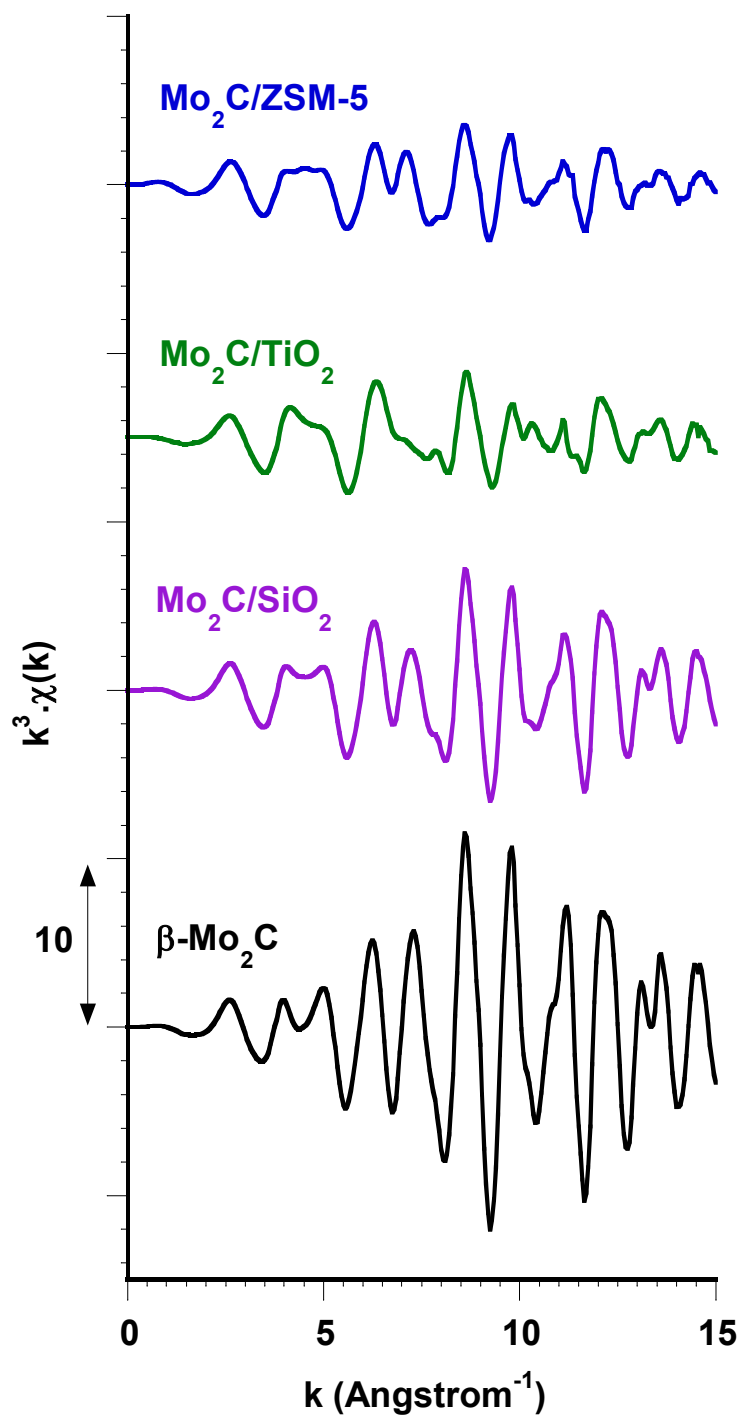
The EXAFS oscillations (Figure 6.20) extracted for the three reactivated catalysts are different: the oscillations measured for  $\text{Mo}_2\text{C}/\text{SiO}_2$  look like those from the  $\beta$ - $\text{Mo}_2\text{C}$  standard; the shape is the same for  $\text{Mo}_2\text{C}/\text{ZSM-5}$  but the oscillations are quite damped; the shape is clearly different for  $\text{Mo}_2\text{C}/\text{TiO}_2$ , which is not restored to its carbide state. These differences mostly come from the Mo shell, as seen when one compares the intensity of the Mo peak in the Fourier transforms (Figure 6.21): it decreases in the order  $\text{SiO}_2$ , ZSM-5 and  $\text{TiO}_2$ .

Figure 6.19. XANES spectra recorded at the Mo K-edge for reactivated  $\beta$ - $\text{Mo}_2\text{C}$ ,  $\text{Mo}_2\text{C}/\text{SiO}_2$ ,  $\text{Mo}_2\text{C}/\text{TiO}_2$  and  $\text{Mo}_2\text{C}/\text{ZSM-5}$  (spectra recorded at room temperature). Comparison with references  $\text{MoO}_3$  and metallic Mo (dotted lines).



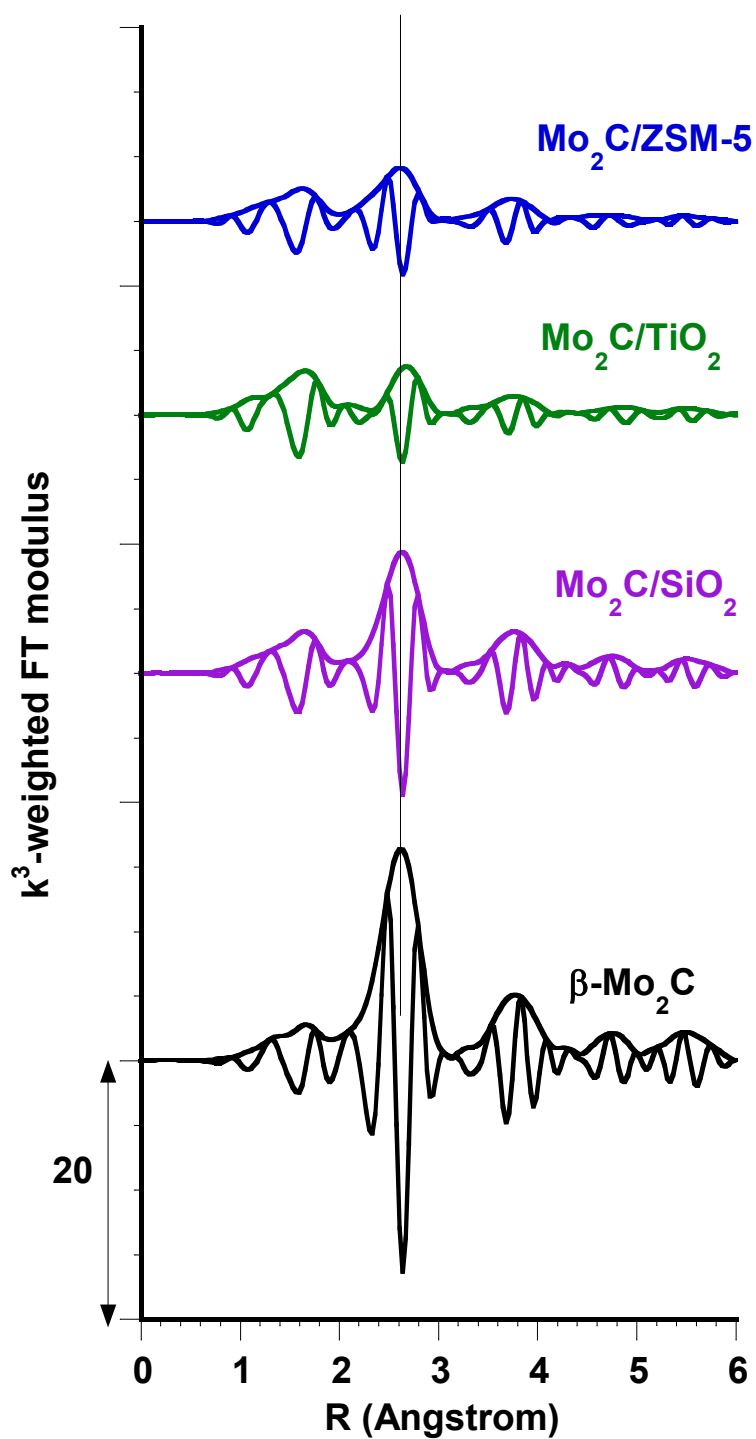
Reference: own author (2023)

Figure 6.20. EXAFS signals recorded at the Mo K-edge for reactivated  $\beta$ -Mo<sub>2</sub>C, Mo<sub>2</sub>C/SiO<sub>2</sub>, Mo<sub>2</sub>C/TiO<sub>2</sub> and Mo<sub>2</sub>C/ZSM-5 (spectra recorded at room temperature).



Reference: own author (2023)

Figure 6.21. Fourier transforms of the EXAFS signals recorded at the Mo K-edge for reactivated  $\beta$ -Mo<sub>2</sub>C, Mo<sub>2</sub>C/SiO<sub>2</sub>, Mo<sub>2</sub>C/TiO<sub>2</sub> and Mo<sub>2</sub>C/ZSM-5 (spectra recorded at room temperature).  $k = 3.5 - 15 \text{ \AA}^{-1}$ .

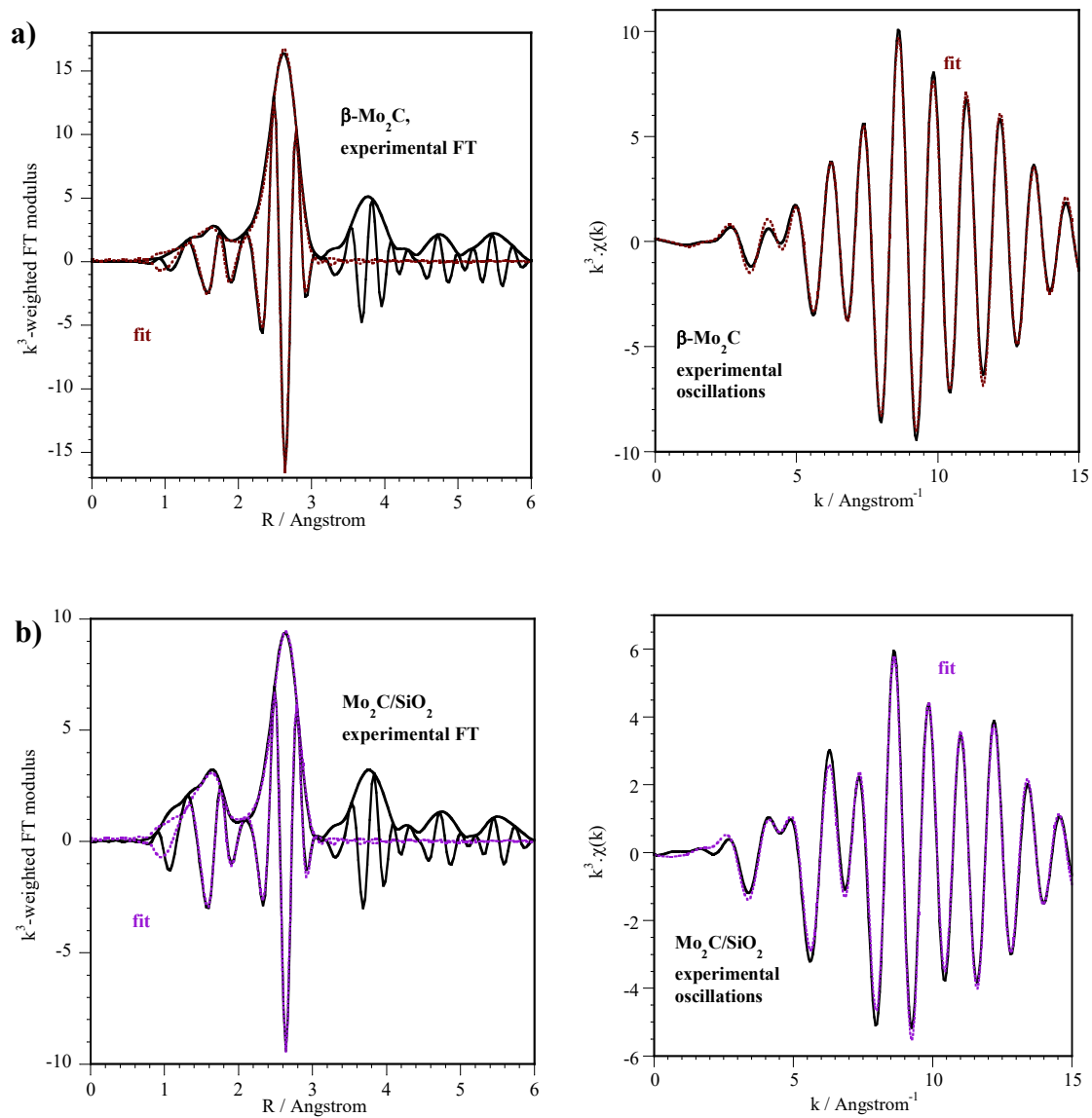


Reference: own author (2023)

The oxidic fraction disappears from the fit, but the number of Mo neighbors remains more or less the same as on the passivated systems (Table 6.4 and Figures 6.22 and 6.23). If passivation contributed to break particles apart compared to the fresh carburized state, the reduction would then lead to a status quo in terms of particle size, and the reactivated state of Mo<sub>2</sub>C/ZSM-5 and especially Mo<sub>2</sub>C/TiO<sub>2</sub> is different from the initial carbide. Moreover, the fits are improved upon addition of a minor contribution of Mo at 2.49 Å for Mo<sub>2</sub>C/TiO<sub>2</sub> (assigned to traces of MoO<sub>2</sub> above) or at 2.69 Å for Mo<sub>2</sub>C/ZSM-5 (possibly attributed to traces of metallic Mo).

The disruption of the carbide particles caused by passivation and maintained upon reactivation could be accompanied by the persistence of minor oxidic and decarburized Mo phases that either remain unreduced, or that are reduced to metallic Mo upon reactivation.

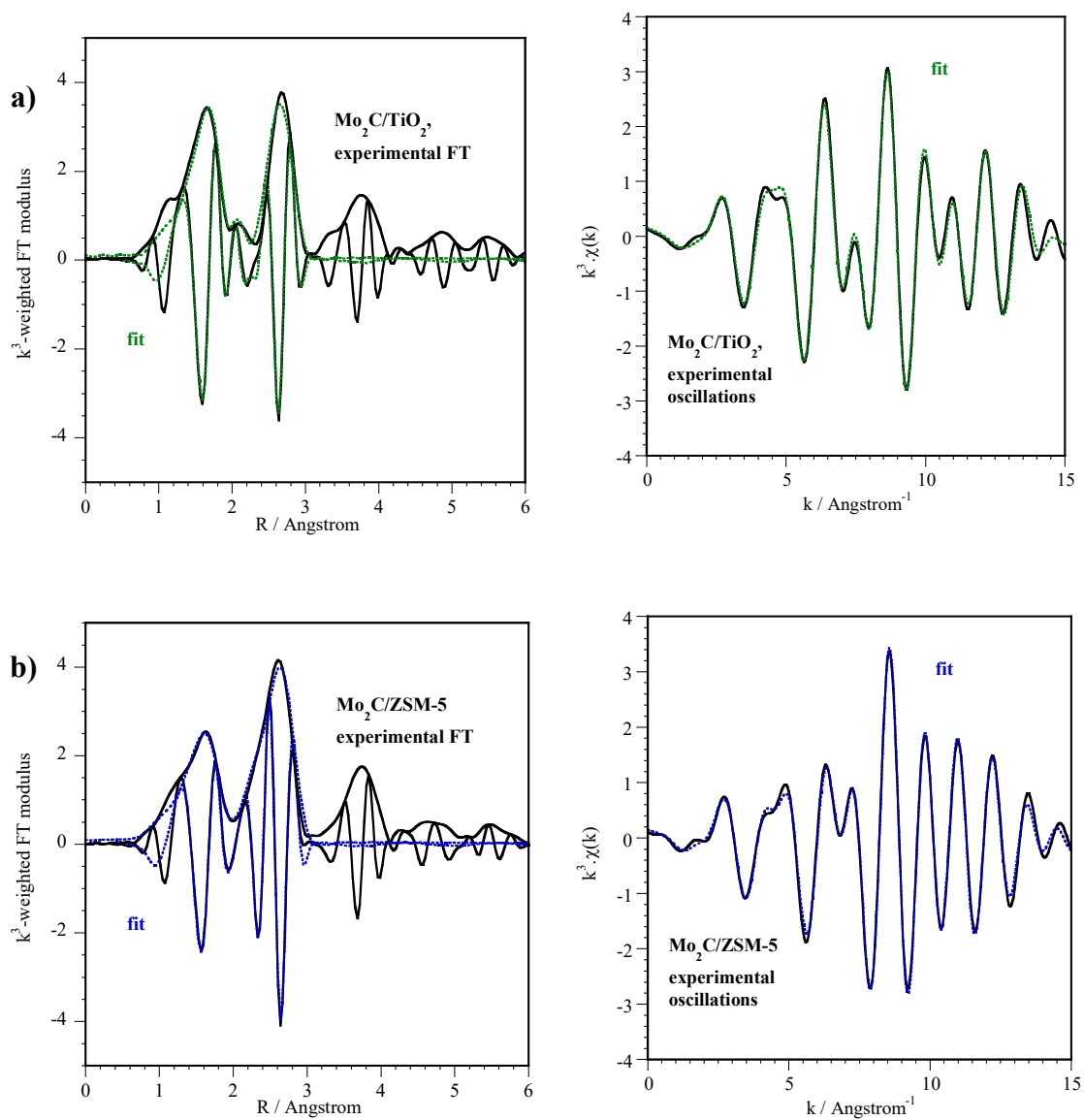
Figure 6.22. XAS data at the Mo K-edge of the catalysts after reactivation (spectrum recorded at room temperature). Fit of the first and second shells of neighbors: Fourier transform ( $k = 3.5 - 15 \text{ \AA}^{-1}$ , left) and EXAFS oscillations (right), a)  $\beta\text{-Mo}_2\text{C}$  and b)  $\text{Mo}_2\text{C}/\text{SiO}_2$ .



Reference: own author (2023)



Figure 6.23. XAS data at the Mo K-edge of the catalysts after reactivation (spectrum recorded at room temperature). Fit of the first and second shells of neighbors: Fourier transform ( $k = 3.5 - 15 \text{ \AA}^{-1}$ , left) and EXAFS oscillations (right), a)  $\text{Mo}_2\text{C}/\text{TiO}_2$  and b)  $\text{Mo}_2\text{C}/\text{ZSM-5}$ .



Reference: own author (2023)

Table 6.4. Fitted parameters at the Mo K-edge ( $E_0 = 20013$  eV,  $S02 = 0.98$ ) determined from the EXAFS analysis of spectra recorded at room temperature on catalysts after passivation and reactivation in  $H_2$ .  $k = 3.5 - 15 \text{ \AA}^{-1}$ . Fit of the first peak(s) from the Fourier transform between 1 and 3  $\text{\AA}$ .

Catalyst	Backscatter	N	$\sigma^2 (\text{\AA}^2) \times 10^3$	R ( $\text{\AA}$ )
$\beta$ -Mo <sub>2</sub> C	C	$2.7 \pm 0.9$	$4.1 \pm 0.3$	$2.08 \pm 0.02$
	Mo	$7.3 \pm 0.8$	$5.7 \pm 0.5$	$2.966 \pm 0.005$
$\Delta E_0 = -5.5$ eV, r-factor = 0.01575, $\chi^2 = 592$ , $N_{\text{ind}} = 13$ , $N_{\text{var}} = 7$				
Mo <sub>2</sub> C/SiO <sub>2</sub>	C	$4.1 \pm 0.6$	$6 \pm 1$	$2.105 \pm 0.006$
	Mo	$4.1 \pm 0.4$	$6.1 \pm 0.4$	$2.976 \pm 0.003$
$\Delta E_0 = -2.7$ eV, r-factor = 0.00717, $\chi^2 = 202$ , $N_{\text{ind}} = 13$ , $N_{\text{var}} = 7$				
Mo <sub>2</sub> C/TiO <sub>2</sub>	C	$4.0 \pm 0.7$	$5 \pm 2$	$2.13 \pm 0.01$
	Mo	$0.3 \pm 0.2$	$8 \pm 2$	$2.49 \pm 0.04$
	Mo	$2.3 \pm 0.7$	$8 \pm 2$	$2.977 \pm 0.009$
$\Delta E_0 = -0.1$ eV, r-factor = 0.01630, $\chi^2 = 514$ , $N_{\text{ind}} = 13$ , $N_{\text{var}} = 9$				
Mo <sub>2</sub> C/ZSM-5	C	$3.9 \pm 0.7$	$8 \pm 2$	$2.10 \pm 0.01$
	Mo	$0.7 \pm 0.5$	$9 \pm 2$	$2.69 \pm 0.02$
	Mo	$3.0 \pm 0.9$	$9 \pm 2$	$2.980 \pm 0.009$
$\Delta E_0 = -2.9$ eV, r-factor = 0.01134, $\chi^2 = 271$ , $N_{\text{ind}} = 13$ , $N_{\text{var}} = 9$				

Reference: own author (2023)

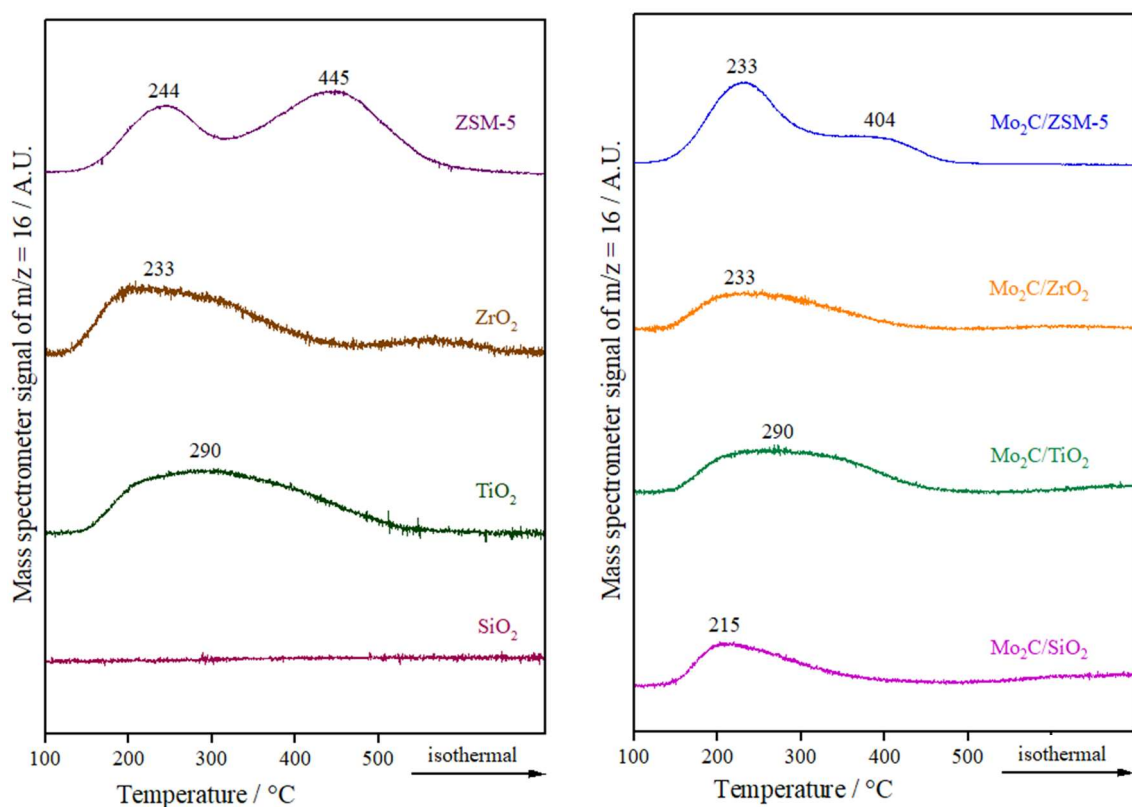
The  $NH_3$  desorption profiles of supports and catalysts are displayed in Figure 6.24. ZSM-5 profile presents two main peaks, one located at low temperature ( $< 300$  °C) and one at high temperature (around 500 °C). In general, the low-temperature peak is associated with ammonia adsorbed on weak acidic sites and the high-temperature peak is ascribed to the strong adsorption of ammonia on acidic sites (Yang *et al.*, 2017). Acidic sites of weak strength are ascribed to silanol groups or extra framework aluminium species, while acidic sites of strong strength are attributed to bridging hydroxyl groups (Si-OH-Al) (Yu *et al.*, 2019).

For  $ZrO_2$ , two  $NH_3$  desorption peaks below 300 °C related to weak and moderate acidic sites are usually observed (Ma *et al.*, 2005). In the obtained profile, these peaks seem to have overlapped forming a broad curve. A similar profile to  $ZrO_2$  was observed for  $TiO_2$ , but the maximum temperature for the latter (290 °C) was higher

compared to the former (233 °C) in agreement with the literature (Manríquez *et al.*, 2004). In contrast, SiO<sub>2</sub> showed almost no acidity.

NH<sub>3</sub> desorption profiles of catalysts shows a change related to the strength of acidic sites for Mo<sub>2</sub>C/ZSM-5 catalyst. When Mo<sub>2</sub>C is supported on ZSM-5 more weak acidic sites appear compared with the bare support, which shows mainly strong acidic sites. The Mo<sub>2</sub>C/TiO<sub>2</sub> and Mo<sub>2</sub>C/ZrO<sub>2</sub> catalysts showed a similar NH<sub>3</sub> desorption profile as their supports. For Mo<sub>2</sub>C supported on SiO<sub>2</sub> a broad peak in a low-temperature region can be seen, which indicates the presence of weak acidic sites on this catalyst.

Figure 6.24. NH<sub>3</sub> desorption profiles of supports and reactivated Mo carbides.



Reference: own author (2023)

In comparison with the bare supports, the amount of NH<sub>3</sub> desorbed from the materials (Table 6.5) show that the total acidity is reduced after impregnation and

synthesis of Mo<sub>2</sub>C with exception of Mo<sub>2</sub>C/SiO<sub>2</sub> catalyst, which showed a slight increase, indicating that pure Mo<sub>2</sub>C already has acidity (Bej *et al.*, 2003). This loss of acidity for most materials is ascribed to the coverage or neutralisation of the acid sites of the support by the active phase.

Although TiO<sub>2</sub> has more acidic sites than ZrO<sub>2</sub>, which is in agreement with the literature (Manríquez *et al.*, 2004), similar values were obtained when Mo<sub>2</sub>C was supported on these materials. The Mo<sub>2</sub>C/ZSM-5 catalyst showed the highest number of total acidic sites.

Table 6.5. Acidic properties of supports and supported Mo carbides.

<b>Material</b>	<b>Ammonia desorbed (<math>\mu\text{mol g}_{\text{cat}}^{-1}</math>)</b>	<b>Ammonia desorbed (<math>\mu\text{mol m}^{-2}</math>)</b>
SiO <sub>2</sub>	13	0.07
TiO <sub>2</sub>	162	3.95
ZrO <sub>2</sub>	125	1.28
ZSM-5	2061	4.00
Mo <sub>2</sub> C/SiO <sub>2</sub>	41	0.29
Mo <sub>2</sub> C/TiO <sub>2</sub>	82	1.86
Mo <sub>2</sub> C/ZrO <sub>2</sub>	86	1.23
Mo <sub>2</sub> C/ZSM-5	632	1.99

Reference: own author (2023)

## 6.1.2 Catalytic results

In the first step of the catalytic evaluation, a screening of the catalysts for the HDO of furfural was performed using CPME as solvent at 200 °C, 30 bar of H<sub>2</sub> for 4 hours. The results are reported in Table 6.6. A similar FF conversion was obtained for the test carried out without catalyst (15%) and with SiO<sub>2</sub> (13%), indicating that silica support has no activity due to the lack of acidity in this material. For the supports presenting acidic properties, a slightly higher FF conversion was observed (27% for TiO<sub>2</sub>, 22% for ZrO<sub>2</sub>, and 28% for ZSM-5). The activity of all catalysts was higher than

their respective supports and obeyed the following order: Mo<sub>2</sub>C/ZrO<sub>2</sub> (71%) > Mo<sub>2</sub>C/ZSM-5 (51%)  $\cong$  Mo<sub>2</sub>C/SiO<sub>2</sub> (47%) > Mo<sub>2</sub>C/TiO<sub>2</sub> (36%). The highest catalytic activity was hence observed for the Mo<sub>2</sub>C supported on ZrO<sub>2</sub>, while the other catalysts showed lower and similar activities.

Table 6.6. FF conversion and product yields for the HDO of FF over supported Mo carbides catalysts

(Reaction conditions: 200 °C, 30 bar H<sub>2</sub>, 4 hours, R = 21, CPME, SPR).

Material	X <sub>FF</sub> (%)	Yield (%)					CB (%)
		FA	2MF	FMMF	EBF	Other <sup>a</sup>	
Blank	15	0	1	0	0	0	87
SiO <sub>2</sub>	13	0	0	0	0	0	88
TiO <sub>2</sub>	27	3	0	0	0	1	79
ZrO <sub>2</sub>	22	4	0	0	0	1	84
ZSM-5	28	0	0	0	0	4	77
Mo <sub>2</sub> C/SiO <sub>2</sub>	47	0	2	0	7	0	63
Mo <sub>2</sub> C/TiO <sub>2</sub>	36	0	1	0	3	0	69
Mo <sub>2</sub> C/ZrO <sub>2</sub>	71	5	6	1	7	0	50
Mo <sub>2</sub> C/ZSM-5	51	2	2	1	6	0	61

<sup>a</sup> methyl 2-furoate, 5-methylfurfural,  $\beta$ -methoxy-(S)-2-furanethanol.

Reference: own author (2023)

Low 2MF yields (< 6%) were obtained over all materials when using an aprotic solvent such as CPME. For this reason, the next screening was performed using 2-butanol as solvent under the same reaction conditions as before (200 °C, 30 bar of H<sub>2</sub>, 4 hours). The results are reported in Table 6.7.

Table 6.7. FF conversion and product yields for the HDO of FF over supported Mo carbides catalysts

(Reaction conditions: 200 °C, 30 bar of H<sub>2</sub>, 4 hours, R = 21, 2-butanol, SPR).

Material	X <sub>FF</sub> (%)	Yield (%)					CB (%)
		FA	2MF	FMMF	EBF	Other <sup>a</sup>	
Blank	22	5	1	0	0	0	85
SiO <sub>2</sub>	24	6	1	0	0	0	84
TiO <sub>2</sub>	67	12	1	0	0	4	51
ZrO <sub>2</sub>	100	79	1	0	0	2	83
ZSM-5	87	2	8	1	0	19	47
Mo <sub>2</sub> C/SiO <sub>2</sub>	100	0	26	8	8	2	46
Mo <sub>2</sub> C/TiO <sub>2</sub>	100	0	18	3	13	3	39
Mo <sub>2</sub> C/ZrO <sub>2</sub>	100	1	22	5	6	6	42
Mo <sub>2</sub> C/ZSM-5	80	7	7	2	7	3	47

<sup>a</sup> 2-(sec-butoxymethyl)furan, 1,4-pentanediol, levulinic acid,  $\gamma$ -valerolactone, cyclopentenone, 5-hydroxy-2-pentanone, sec-butyl 4-oxopentanoate.

Reference: own author (2023)

Again, the same results were obtained for the blank test (without catalyst) and test carried out with SiO<sub>2</sub>, confirming that this support has no activity in this reaction, regardless the type of the solvent used. Similar to the tests performed in CPME, the supports presenting acidic properties (TiO<sub>2</sub>, ZrO<sub>2</sub> and ZSM-5) showed higher FF conversions. The activity of the supports does not seem to be directly related to the total number of acidic sites, since TiO<sub>2</sub> and ZSM-5, which present the highest densities of acidic sites (around 4  $\mu\text{mol m}^{-2}$ ) estimated by TPD-NH<sub>3</sub> and N<sub>2</sub> physisorption (Table 6.5), do not exhibit the highest activity. The same observation can be done for the nature of the acidic sites, since although TiO<sub>2</sub> and monoclinic ZrO<sub>2</sub> exhibit mainly Lewis acidic sites (Ma *et al.*, 2005; Manríquez *et al.*, 2004), ZrO<sub>2</sub> was much more active than TiO<sub>2</sub>. These differences might be related to the ability of each support to carry out the CTH reaction, in which 2-butanol is dehydrogenated to 2-butanone and hydrogen, which is then transferred to furfural by MPV forming furfuryl alcohol (Xu *et al.*, 2020).

In contrast to the results obtained in CPME, a complete FF conversion was observed for most of the supported Mo carbides over a protic solvent as 2BuOH, which provided additional hydrogen. Only Mo<sub>2</sub>C/ZSM-5 catalyst exhibited a slightly smaller activity in converting FF (80%). The main compounds produced over supported Mo

carbides in the presence of 2-butanol were 2-methylfuran (2MF), furfuryl alcohol (FA), 2-(furan-2-methyl)-5-methylfuran (FMMF) and 2,2-(1,2-ethenediyl)bis-furan (EBF).

FA is the primary product obtained by the reduction of FF, while 2MF is produced by the deoxygenation of FA (Chen *et al.*, 2018; Mariscal *et al.*, 2016). EBF and FMMF are C<sub>10</sub> compounds produced by condensation reactions favoured in acidic sites. The first one is formed from two molecules of FF, followed by hydrogenation and dehydration reactions (Deng *et al.*, 2018), while FMMF can be obtained by FA dimerization, hydroxyalkylation/alkylation of 2MF or more likely by the reaction of FA with 2MF (Panagiotopoulou and Vlachos, 2014).

As most of the catalysts show full conversion of furfural, the comparison of the product yields will not be made at this stage to avoid drawing incorrect conclusions. Therefore, in order to carry out a more in-depth comparative study, the catalysts were tested individually in a larger volume reactor to achieve lower conversions and the results are reported in Table 6.8.

Table 6.8. FF conversion and product yields for the HDO of FF over supported Mo carbides catalysts

(Reaction conditions: 200 °C, 30 bar of H<sub>2</sub>, 4 hours, 2-butanol, Parr reactor).

Entry	Material	R	X <sub>FF</sub> (%)	Yield (%)					CB (%)
				FA	2MF	FMMF	EBF	Other <sup>a</sup>	
1	SiO <sub>2</sub>	32	2	1	0	0	0	2	100
2	TiO <sub>2</sub>	32	20	12	0	0	0	1	94
4	ZrO <sub>2</sub>	32	93	90	0	0	0	0	97
5	ZSM-5	32	0	0	0	0	0	0	-
6	Mo <sub>2</sub> C/SiO <sub>2</sub>	32	77	5	16	6	18	2	69
7	Mo <sub>2</sub> C/TiO <sub>2</sub>	32	55	8	16	2	9	2	81
8	Mo <sub>2</sub> C/ZrO <sub>2</sub>	32	46	11	6	1	1	3	79
9	Mo <sub>2</sub> C/ZSM-5	26	54	4	8	2	10	6	76
10	Mo <sub>2</sub> C/SiO <sub>2</sub>	19	100	0	34	7	11	4	57
11	Mo <sub>2</sub> C/SiO <sub>2</sub>	48	62	7	12	4	14	0	76
12	Mo <sub>2</sub> C/SiO <sub>2</sub>	127	30	7	2	1	8	2	91
13	Mo <sub>2</sub> C/TiO <sub>2</sub>	16	81	7	34	3	10	1	75
14	Mo <sub>2</sub> C/TiO <sub>2</sub>	21	68	7	22	3	7	3	74
15	Mo <sub>2</sub> C/TiO <sub>2</sub>	64	34	9	5	1	2	5	89

<sup>a</sup> 2-(sec-butoxymethyl)furan (SBMF), 2-(dibutoxymethyl)furan (FDA), sec-butyl 4-oxopentanoate (SBOP).

Reference: own author (2023)

The activity of the supports and catalysts was compared at the same furfural and active phase molar ratio ( $R = 32$ ), with exception of the Mo<sub>2</sub>C/ZSM-5 catalyst, which showed a lower activity in the screening tests and was therefore tested with  $R = 26$ . Lower conversions of FF were observed for all supports when increasing the  $R$  value to 32 from that used in the screening tests ( $R = 21$ ). Nevertheless, ZrO<sub>2</sub> showed almost full conversion of FF producing FA with high yield (90%). The excellent performance of this material in the MPV reduction involving furfural and a secondary alcohol has been observed previously and it was attributed to a variety of catalytic active sites found in ZrO<sub>2</sub>. The presence of weak basic sites assists the formation of alkoxide species with acidic sites by the deprotonation of alcohol molecules (Manríquez *et al.*, 2004; Xu *et al.*, 2020). The solvent used in this work, 2-butanol, is adsorbed as an alkoxide on ZrO<sub>2</sub>, which strongly favors the hydrogen transfer step (Nagaiah *et al.*, 2018; Scotti *et al.*, 2018). On the other hand, the lower FF conversion and consequently a lower yield to



FA over TiO<sub>2</sub> might be related to a lower number of basic sites. In any case, these results reveal that the reduction of FF to FA is catalyzed not only by acidic, but also basic sites.

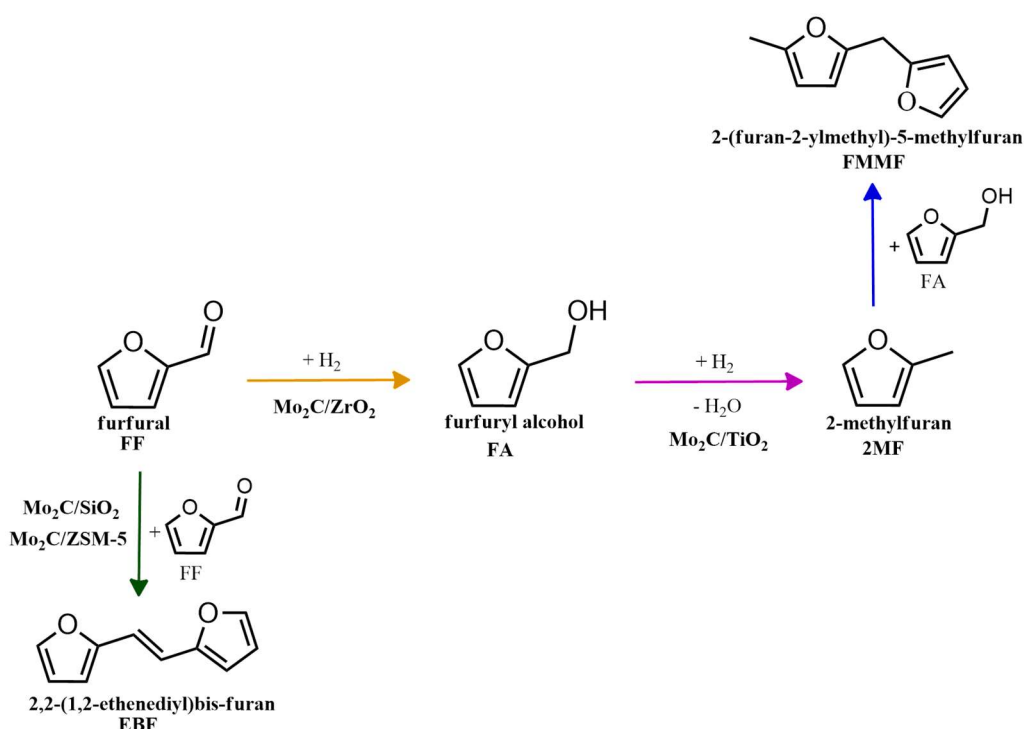
Most of the catalysts were more active in converting FF compared to their respective supports (entries 1-9). In the case of the Mo<sub>2</sub>C/SiO<sub>2</sub> catalyst, the significant gain in activity is attributed to the Mo carbide phase since the support SiO<sub>2</sub> exhibits no activity (entries 1 and 6). On the contrary, a different trend was observed for the Mo<sub>2</sub>C/ZrO<sub>2</sub> catalyst, which was much less active than its corresponding support (entries 4 and 8). This effect has already been observed in the hydrogen transfer reduction of FF when using bare ZrO<sub>2</sub> and Cu/ZrO<sub>2</sub> catalyst and it was attributed to the reduction of the specific surface area of the catalyst and consequent loss of basic active sites (Scotti *et al.*, 2018).

The comparison of the supported Mo carbides activity (entries 6 - 9) shows that a higher FF conversion is obtained when Mo<sub>2</sub>C is supported on SiO<sub>2</sub> (77%), while lower conversions were observed over TiO<sub>2</sub> (55%), ZrO<sub>2</sub> (46%) and ZSM-5 (54%, even when using a higher amount of catalyst, R = 26). These results seem to be related to the final state of the carbides after passivation and reactivation procedures. As observed by XAS, the particles of Mo<sub>2</sub>C were disordered after passivation for the catalysts supported on TiO<sub>2</sub> and ZSM-5, and the carburization degree was not the same for these materials after reactivation. On the other hand, the Mo<sub>2</sub>C/SiO<sub>2</sub> catalyst was less de-carburized and, for this reason, presents a higher activity. These results show that the type of support used influences the final state of the carbide after reactivation.

In order to evaluate the product distribution, all catalysts were compared in conditions close to iso-conversion (entries 7, 8, 9, and 11) by modification of the furfural and active phase molar ratio. The highest yield to 2MF was observed over the Mo carbide supported on TiO<sub>2</sub> (16%) followed by SiO<sub>2</sub> (12%). Meanwhile, the Mo<sub>2</sub>C/ZrO<sub>2</sub> and Mo<sub>2</sub>C/ZSM-5 catalysts were less effective in obtaining 2MF. A higher FA yield was observed over Mo<sub>2</sub>C/ZrO<sub>2</sub>, which agrees to the high selectivity of the bare ZrO<sub>2</sub> support to promote the conversion of furfural to furfuryl alcohol. This also limits the FF condensation, which was reflected by the reduction in the EBF and FMMF yields. In contrast, a higher production of these products was observed for the other

catalysts. Condensation reactions are reported to occur in acidic sites (Corma *et al.*, 2012; G. Li *et al.*, 2014; S. Li *et al.*, 2014; Y.-J. Luo *et al.*, 2019), which are present in all materials, as demonstrated by TPD-NH<sub>3</sub>. The main route followed by each catalyst is shown in Scheme 6.1.

Scheme 6.1. Main routes for the FF conversion over Mo carbides supported on SiO<sub>2</sub>, TiO<sub>2</sub>, ZrO<sub>2</sub>, and ZSM-5.



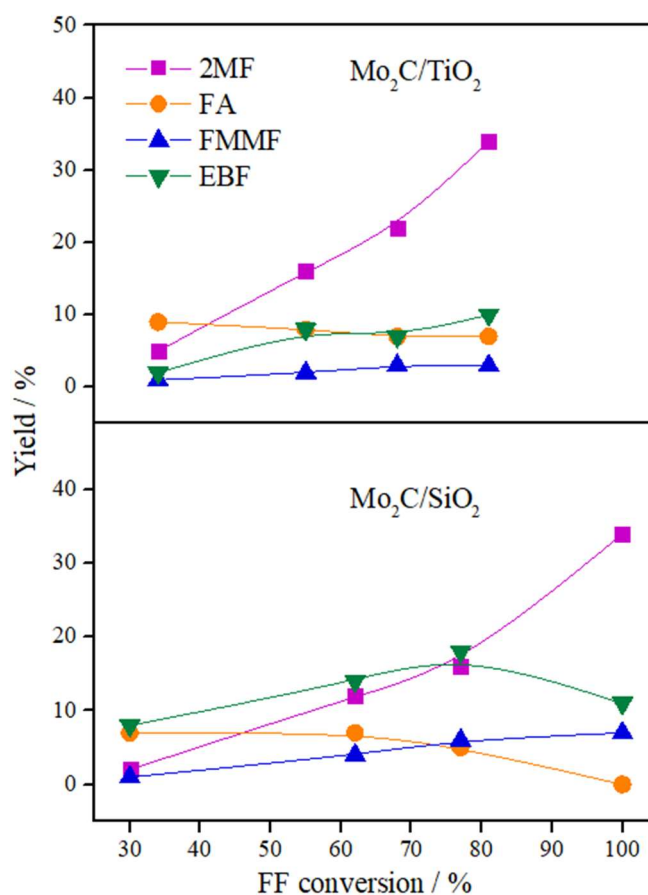
Reference: own author (2023)

The variation in the yield of products as a function of the FF conversion was evaluated for the Mo<sub>2</sub>C/SiO<sub>2</sub> and Mo<sub>2</sub>C/TiO<sub>2</sub> catalysts (Figure 6.25). The increase in the conversion of FF was accompanied by the increase in the yield to 2MF and decrease in the FA yield, confirming that furfuryl alcohol is a reaction intermediate. Both catalysts showed similar trends regarding the evolution of the products. Over the Mo<sub>2</sub>C/TiO<sub>2</sub> catalyst, lower yields of EBF were observed in comparison with Mo<sub>2</sub>C/SiO<sub>2</sub>. This is ascribed to the higher initial reaction rate of the former catalyst, which converts FF faster avoiding the formation of EBF. The FMMF yield remained below 7% for both catalysts.

In summary,  $\text{Mo}_2\text{C}/\text{TiO}_2$  is a suitable catalyst to produce 2MF, while a mixture containing both 2MF and  $\text{C}_{10}$  compounds are yielded over the  $\text{Mo}_2\text{C}/\text{SiO}_2$  catalyst.

Figure 6.25. Product yields versus FF conversion for  $\text{Mo}_2\text{C}/\text{SiO}_2$  and  $\text{Mo}_2\text{C}/\text{TiO}_2$  catalysts

(Reaction conditions: 200 °C, 30 bar of  $\text{H}_2$ , 4 hours, 2-butanol, Parr reactor).



Reference: own author (2023)

## 6.2 Conclusions

The effect of the support used for dispersing Mo carbides ( $\text{SiO}_2$ ,  $\text{TiO}_2$ ,  $\text{ZrO}_2$ , and ZSM-5) was evaluated for the HDO of furfural in liquid phase at 200 °C, 30 bar of  $\text{H}_2$  for 4 hours using CPME and 2-butanol as solvent. The carburization, passivation, and reactivation of the supported Mo carbides were evaluated by XAS analysis. The Mo

carbide supported on  $\text{TiO}_2$  was the most affected by these treatments. Smaller  $\text{Mo}_2\text{C}$  particles formed during carburization were disorganized after passivation and a minor fraction of crystallized Mo carbide remained in the  $\text{Mo}_2\text{C}/\text{TiO}_2$  catalyst. After reactivation, the  $\text{Mo}_2\text{C}/\text{SiO}_2$  catalyst was the less de-carburized among all, while traces of  $\text{MoO}_2$  and metallic Mo were observed for the  $\text{Mo}_2\text{C}/\text{TiO}_2$  and  $\text{Mo}_2\text{C}/\text{ZSM-5}$  catalysts, respectively.

Higher activities for the supported Mo carbides were found when using a protic solvent such 2BuOH in comparison with an aprotic solvent as CPME due to higher availability of hydrogen.  $\text{SiO}_2$  exhibited lack in activity to convert FF, while higher conversions were observed over the supports presenting acidic properties ( $\text{TiO}_2$ ,  $\text{ZrO}_2$ , and ZSM-5). This activity, however, was not directly related to the total number or nature of the acidic sites, but to the presence of both Lewis acidic sites and basic sites that promotes the conversion of FF to FA by the MPV reaction, in which  $\text{ZrO}_2$  exhibited the highest conversion of FF and yield to FA. Nevertheless, the presence of acidic and basic sites in the supports was not relevant after impregnation and synthesis of the Mo carbides in the supports. In this case, the supports influenced the final state of the Mo carbides after carburization, passivation, and reactivation. The highest activity was observed for the less de-carburized catalyst,  $\text{Mo}_2\text{C}/\text{SiO}_2$ , even though  $\text{SiO}_2$  was not active in the reaction, therefore the activity is mainly attributed to the Mo carbide.

Although the  $\text{Mo}_2\text{C}/\text{SiO}_2$  catalyst is more active than the  $\text{Mo}_2\text{C}/\text{TiO}_2$  catalyst, in similar conversions, the latter produced 2MF in higher yields. In any case, a mixture containing 2MF and  $\text{C}_{10}$  compounds can be achieved using  $\text{Mo}_2\text{C}/\text{SiO}_2$  as catalyst.

## 6.3 References

- Abou Hamdan, M., Loridant, S., Jahjah, M., Pinel, C., Perret, N., 2019. TiO<sub>2</sub>-supported molybdenum carbide: An active catalyst for the aqueous phase hydrogenation of succinic acid. *Appl. Catal. Gen.* 571, 71–81. <https://doi.org/10.1016/j.apcata.2018.11.009>
- Bej, S.K., Bennett, C.A., Thompson, L.T., 2003. Acid and base characteristics of molybdenum carbide catalysts. *Appl. Catal. Gen.* 250, 197–208. [https://doi.org/10.1016/S0926-860X\(02\)00664-6](https://doi.org/10.1016/S0926-860X(02)00664-6)
- Boullousa-Eiras, S., Lødeng, R., Bergem, H., Stöcker, M., Hannevold, L., Blekkan, E.A., 2014. Catalytic hydrodeoxygenation (HDO) of phenol over supported molybdenum carbide, nitride, phosphide and oxide catalysts. *Catal. Today* 223, 44–53. <https://doi.org/10.1016/j.cattod.2013.09.044>
- Chang, X., Liu, A.-F., Cai, B., Luo, J.-Y., Pan, H., Huang, Y.-B., 2016. Catalytic Transfer Hydrogenation of Furfural to 2-Methylfuran and 2-Methyltetrahydrofuran over Bimetallic Copper-Palladium Catalysts. *ChemSusChem* 9, 3330–3337. <https://doi.org/10.1002/cssc.201601122>
- Chen, S., Wojcieszak, R., Dumeignil, F., Marceau, E., Royer, S., 2018. How Catalysts and Experimental Conditions Determine the Selective Hydroconversion of Furfural and 5-Hydroxymethylfurfural. *Chem. Rev.* 118, 11023–11117. <https://doi.org/10.1021/acs.chemrev.8b00134>
- Corma, A., de la Torre, O., Renz, M., 2012. Production of high quality diesel from cellulose and hemicellulose by the Sylvan process: catalysts and process variables. *Energy Environ. Sci.* 5, 6328. <https://doi.org/10.1039/c2ee02778j>
- de Gonzalo, G., Alcuntara, A.R., de María, P.D., 2019. Cyclopentyl Methyl Ether (CPME): A Versatile Eco-Friendly Solvent for Applications in Biotechnology and Biorefineries 15.

- Deng, Y., Gao, R., Lin, L., Liu, T., Wen, X.-D., Wang, S., Ma, D., 2018. Solvent Tunes the Selectivity of Hydrogenation Reaction over  $\alpha$ -MoC Catalyst. *J. Am. Chem. Soc.* 140, 14481–14489. <https://doi.org/10.1021/jacs.8b09310>
- Juan, J. L. X., Maldonado, C. S., Sánchez, R. A. L., Díaz, O. J. E., Ronquillo, M. R. R., Sandoval-Rangel, L., Aguilar, N. P., Delgado, N. A. R, Martínez-Vargas, D. X, 2022, TiO<sub>2</sub> doped with europium (Eu) - Synthesis, characterization and catalytic performance on pesticide degradation under solar irradiation. *Catal. Today* 394-396, 304–313.
- Li, G., Li, N., Wang, Xinkui, Sheng, X., Li, S., Wang, A., Cong, Y., Wang, Xiaodong, Zhang, T., 2014. Synthesis of Diesel or Jet Fuel Range Cycloalkanes with 2-Methylfuran and Cyclopentanone from Lignocellulose. *Energy Fuels* 28, 5112–5118. <https://doi.org/10.1021/ef500676z>
- Li, S., Li, N., Li, G., Wang, A., Cong, Y., Wang, X., Zhang, T., 2014. Synthesis of diesel range alkanes with 2-methylfuran and mesityl oxide from lignocellulose. *Catalysis Today* 234, 91–99. <https://doi.org/10.1016/j.cattod.2014.01.028>
- Liu, P., Sun, L., Jia, X., Zhang, C., Zhang, W., Song, Y., Wang, H., Li, C., 2020. Efficient one-pot conversion of furfural into 2-methyltetrahydrofuran using non-precious metal catalysts. *Mol. Catal.* 490, 110951. <https://doi.org/10.1016/j.mcat.2020.110951>
- Luo, Y., Li, Z., Li, X., Liu, X., Fan, J., Clark, J.H., Hu, C., 2019. The production of furfural directly from hemicellulose in lignocellulosic biomass: A review. *Catalysis Today* 319, 14–24. <https://doi.org/10.1016/j.cattod.2018.06.042>
- Ma, Z.-Y., Yang, C., Wei, W., Li, W.-H., Sun, Y.-H., 2005. Surface properties and CO adsorption on zirconia polymorphs. *J. Mol. Catal. Chem.* 227, 119–124. <https://doi.org/10.1016/j.molcata.2004.10.017>
- Manriquez, M.E., López, T., Gómez, R., Navarrete, J., 2004. Preparation of TiO<sub>2</sub>–ZrO<sub>2</sub> mixed oxides with controlled acid–basic properties. *J. Mol. Catal. Chem.* 220, 229–237. <https://doi.org/10.1016/j.molcata.2004.06.003>
- Mariscal, R., Maireles-Torres, P., Ojeda, M., Sádaba, I., López Granados, M., 2016. Furfural: a renewable and versatile platform molecule for the synthesis of chemicals and fuels. *Energy Environ. Sci.* 9, 1144–1189. <https://doi.org/10.1039/C5EE02666K>

- Mo, T., Xu, J., Yang, Y., Li, Y., 2016. Effect of carburization protocols on molybdenum carbide synthesis and study on its performance in CO hydrogenation. *Catal. Today* 261, 101–115. <https://doi.org/10.1016/j.cattod.2015.07.014>
- Molina, M.J.C., 2012. Cyclopentyl methyl ether: A green co-solvent for the selective dehydration of lignocellulosic pentoses to furfural. *Bioresour. Technol.* 7.
- Nagaiah, P., Pramod, C.V., Rao, M.V., Raju, B.D., Rao, K.S.R., 2018. Liquid phase hydrogenation of furfural using 2-propanol over  $\text{ZrO}_2$ . *J. Chem. Sci.* 130, 66. <https://doi.org/10.1007/s12039-018-1469-5>
- Panagiotopoulou, P., Vlachos, D.G., 2014. Liquid phase catalytic transfer hydrogenation of furfural over a Ru/C catalyst. *Appl. Catal. Gen.* 480, 17–24. <https://doi.org/10.1016/j.apcata.2014.04.018>
- Scotti, N., Zaccheria, F., Bisio, C., Vittoni, C., Ravasio, N., 2018. Switching Selectivity in the Hydrogen Transfer Reduction of Furfural. *ChemistrySelect* 3, 8344–8348. <https://doi.org/10.1002/slct.201801974>
- Seemala, B., Cai, C.M., Kumar, R., Wyman, C.E., Christopher, P., 2018. Effects of Cu–Ni Bimetallic Catalyst Composition and Support on Activity, Selectivity, and Stability for Furfural Conversion to 2-Methylfuran. *ACS Sustain. Chem. Eng.* 6, 2152–2161. <https://doi.org/10.1021/acssuschemeng.7b03572>
- Srivastava, S., Jadeja, G.C., Parikh, J., 2016. A versatile bi-metallic copper–cobalt catalyst for liquid phase hydrogenation of furfural to 2-methylfuran. *RSC Adv.* 6, 1649–1658. <https://doi.org/10.1039/C5RA15048E>
- Thommes, M., Kaneko, K., Neimark, A.V., Olivier, J.P., Rodriguez-Reinoso, F., Rouquerol, J., Sing, K.S.W., 2015. Physisorption of gases, with special reference to the evaluation of surface area and pore size distribution (IUPAC Technical Report). *Pure and Applied Chemistry* 87, 1051–1069. <https://doi.org/10.1515/pac-2014-1117>
- Toledo, F., Ghampson, I.T., Sepúlveda, C., García, R., Fierro, J.L.G., Videla, A., Serpell, R., Escalona, N., 2019. Effect of Re content and support in the liquid phase conversion of furfural to furfuryl alcohol and 2-methyl furan over ReOx catalysts. *Fuel* 242, 532–544. <https://doi.org/10.1016/j.fuel.2019.01.090>

- Vo, D.-V.N., Adesina, A.A., 2011. Kinetics of the carbothermal synthesis of Mo carbide catalyst supported on various semiconductor oxides. *Fuel Process. Technol.* 92, 1249–1260. <https://doi.org/10.1016/j.fuproc.2011.02.012>
- Wang, B., Sun, Q., Liu, S., Li, Y., 2013. Synergetic catalysis of CuO and graphene additives on TiO<sub>2</sub> for photocatalytic water splitting. *Int. J. Hydrog. Energy* 38, 7232–7240.
- Wang, B., Wang, C., Yu, W., Li, Z., Xu, Y., Ma, X., 2020. Effects of preparation method and Mo<sub>2</sub>C loading on the Mo<sub>2</sub>C\_ZrO<sub>2</sub> catalyst for sulfur-resistant methanation. *Mol. Catal.* 482, 110668.
- Wang, H., 2013. Support effects on hydrotreating of soybean oil over NiMo carbide catalyst 7.
- Xu, C., Paone, E., Rodríguez-Padrón, D., Luque, R., Mauriello, F., 2020. Recent catalytic routes for the preparation and the upgrading of biomass derived furfural and 5-hydroxymethylfurfural. *Chem. Soc. Rev.* 49, 4273–4306. <https://doi.org/10.1039/D0CS00041H>
- Yang, L., Liu, Zhiyuan, Liu, Zhi, Peng, W., Liu, Y., Liu, C., 2017. Correlation between H-ZSM-5 crystal size and catalytic performance in the methanol-to-aromatics reaction. *Chin. J. Catal.* 38, 683–690. [https://doi.org/10.1016/S1872-2067\(17\)62791-8](https://doi.org/10.1016/S1872-2067(17)62791-8)
- Yu, X., Liu, B., Zhang, Y., 2019. Effect of Si/Al ratio of high-silica HZSM-5 catalysts on the prins condensation of isobutylene and formaldehyde to isoprene. *Heliyon* 5, e01640. <https://doi.org/10.1016/j.heliyon.2019.e01640>



## 7. CONCLUSIONS AND SUGGESTIONS

The carburization, passivation, and reactivation of Mo carbides catalysts were evaluated by XAS analysis. From the results presented in this work one can conclude that:

- Four successive groups of Mo species were involved in the carburization process: (i)  $\text{MoO}_3$  for  $\text{Mo}_2\text{C}/\text{SiO}_2$ , and a mixture of  $\text{MoO}_3$  and Ni/Cu-Mo(VI) molybdates for Ni- $\text{Mo}_x\text{C}_y/\text{SiO}_2$  and Cu- $\text{Mo}_x\text{C}_y/\text{SiO}_2$ , representing the Mo(VI) oxides present on the calcined precursors; (ii)  $\text{Mo}_4\text{O}_{11}$  ( $\text{Mo}_2\text{C}/\text{SiO}_2$ ) and  $\text{MoO}_2$  (Ni- $\text{Mo}_x\text{C}_y/\text{SiO}_2$  and Cu- $\text{Mo}_x\text{C}_y/\text{SiO}_2$ ) for Mo suboxides (oxidation state between IV and VI) formed by reduction of the Mo(VI) oxides; (iii)  $\text{MoO}_{2-x}\text{C}_x$  formed by reduction of the Mo suboxides and characterized by a limited degree of carburization (low production of CO); (iv)  $\text{Mo}_2\text{C}$  formed by the full carburization of  $\text{MoO}_{2-x}\text{C}_x$  (important production of CO).
- The metallic Cu particles assisted the initial reduction of the Mo species in the Cu-promoted Mo carbide by providing more hydrogen, once they were reduced at lower temperatures in comparison with Mo species in the monometallic carbide;
- Ni molybdates found in the calcined precursor of the Ni- $\text{Mo}_x\text{C}_y/\text{SiO}_2$  catalyst were reduced at higher temperatures than the Mo oxide species and did not contribute to the first step of reduction;
- The presence of Cu and Ni as promoters did not assist in the formation of the Mo carbide at higher temperatures, since it occurred at the same range of temperature as observed for the monometallic  $\text{Mo}_2\text{C}/\text{SiO}_2$  catalyst;
- No bimetallic NiMo or CuMo carbide phases were formed and Ni and Cu were found only as nanoparticles in contact with the carbide phase;
- The passivation treatment strongly affects the nature of the carbide phase. Higher degrees of oxidation were observed for the supported catalysts

( $\beta$ - $\text{Mo}_2\text{C}/\text{SiO}_2$ ,  $\text{Ni-Mo}_x\text{C}_y/\text{SiO}_2$ ,  $\text{Cu-Mo}_x\text{C}_y/\text{SiO}_2$ ) in comparison with the unsupported one ( $\beta$ - $\text{Mo}_2\text{C}$ ). This effect was more pronounced for the bimetallic Mo carbides, in special for the one promoted with Cu, which showed more disordered species that were more easily oxidized;

- The reactivation at 400 °C under pure  $\text{H}_2$  did not restore the original carbides. For the unsupported  $\beta$ - $\text{Mo}_2\text{C}$  and monometallic  $\beta$ - $\text{Mo}_2\text{C}/\text{SiO}_2$ , between 80 - 90% of the carbide phase was restored, while for the bimetallic carbides this value did not exceed 65%;
- The reactivation of passivated  $\text{Ni-Mo}_x\text{C}_y/\text{SiO}_2$  produced, besides the Mo carbide, reduced Mo species in strong interaction with Ni;
- The Mo carbide supported in  $\text{TiO}_2$  was the most affected by carburization, passivation, and reactivation in comparison with the ones supported in  $\text{SiO}_2$ ,  $\text{ZrO}_2$ , and ZSM-5. Smaller  $\text{Mo}_2\text{C}$  particles were formed during carburization and the passivation treatment contributed to disorganize these particles, remaining a minor fraction of crystallized Mo carbide in the  $\text{Mo}_2\text{C}/\text{TiO}_2$  catalyst;
- After reactivation, the  $\text{Mo}_2\text{C}/\text{SiO}_2$  catalyst was the less de-carburized among all supported Mo carbides, while traces of  $\text{MoO}_2$  and metallic Mo were observed for the  $\text{Mo}_2\text{C}/\text{TiO}_2$  and  $\text{Mo}_2\text{C}/\text{ZSM-5}$  catalysts, respectively.

The effect of supporting the Mo carbide phase (unsupported and  $\text{SiO}_2$ -supported  $\beta$ - $\text{Mo}_2\text{C}$ ), of the Mo carbide phase type ( $\beta$ - $\text{Mo}_2\text{C}$  and  $\alpha$ - $\text{MoC}$ ), of the addition of Ni and Cu promoters ( $\text{Ni-Mo}_x\text{C}_y/\text{SiO}_2$  and  $\text{Cu-Mo}_x\text{C}_y/\text{SiO}_2$ ), and the effect of the support for Mo carbides ( $\text{Mo}_2\text{C}/\text{SiO}_2$ ,  $\text{Mo}_2\text{C}/\text{TiO}_2$ ,  $\text{Mo}_2\text{C}/\text{ZrO}_2$ , and  $\text{Mo}_2\text{C}/\text{ZSM-5}$ ) were evaluated for the HDO of furfural in liquid phase at 200 °C, 30 bar of  $\text{H}_2$  for 4 hours using 2-butanol as solvent. In addition, the use of CPME as solvent was also tested for the Mo carbides supported on different materials. The results obtained allow us to conclude that:

- The dispersion of the active phase ( $\beta$ - $\text{Mo}_2\text{C}$ ) is improved by supporting it in  $\text{SiO}_2$ , which promoted the activity of the catalyst. The increase in the dispersion,

however, led to higher oxidation of the carbide phase after passivation, which reduced the 2MF yield in comparison with the unsupported catalyst ( $\beta$ -Mo<sub>2</sub>C). It was observed that the Mo carbide phase favored the formation of 2MF, while the presence of oxycarbide species promoted condensation reactions and the formation of C<sub>10</sub> compounds, which can be used as diesel precursors;

- The  $\beta$ -Mo<sub>2</sub>C crystalline phase is more active than  $\alpha$ -MoC in supported Mo carbides for the HDO of furfural. However, in similar conversions, the same product distribution is observed regardless of the Mo carbide phase;
- The use of Ni as promoter for the  $\beta$ -Mo<sub>2</sub>C/SiO<sub>2</sub> increased the activity of the catalyst but did not improve the yield to 2MF. In contrast, a lower activity than that of the monometallic one was observed for the carbide promoted with Cu, which was attributed to the deep oxidation of the Cu-Mo<sub>x</sub>Cy/SiO<sub>2</sub> catalyst;
- Mo carbides proved to be very active in converting FF, but their deoxygenating ability is widely affected by the degree of oxidation of the catalyst;
- The use of a protic solvent such 2-butanol favors the activity of the supported Mo carbides in comparison with an aprotic solvent such as CPME due to its higher availability to provide hydrogen;
- SiO<sub>2</sub> exhibited a lack of activity to convert FF, while higher conversions were observed over the supports presenting acidic properties (TiO<sub>2</sub>, ZrO<sub>2</sub>, and ZSM-5). This was attributed to the presence of both Lewis acidic sites and basic sites that promotes the conversion of FF to FA by the MPV reaction. In this case, an excellent performance was obtained over ZrO<sub>2</sub>, which exhibited a conversion of FF and yield to FA higher than 90%. The supports influence the first step of the reaction, i. e., the hydrogenation of FF to FA;
- The acidic and basic properties of the supports were not relevant after impregnating and synthesizing the Mo carbides in the supports. In this case, the supports influenced the final state of the Mo carbides after carburization, passivation, and reactivation. The highest activity to convert FF was observed for the less de-carburized catalyst, Mo<sub>2</sub>C/SiO<sub>2</sub>, even though SiO<sub>2</sub> was not active in the reaction, therefore the activity is mainly attributed to the Mo carbide;

- Higher 2MF yields were observed for the Mo carbide supported on TiO<sub>2</sub>;
- Mo<sub>2</sub>C/TiO<sub>2</sub> is a suitable catalyst to produce 2MF, while a mixture containing 2MF and C<sub>10</sub> compounds that can be used as diesel precursors can be achieved using Mo<sub>2</sub>C/SiO<sub>2</sub> as catalyst.

Based on the results presented in this work, we suggest for future work:

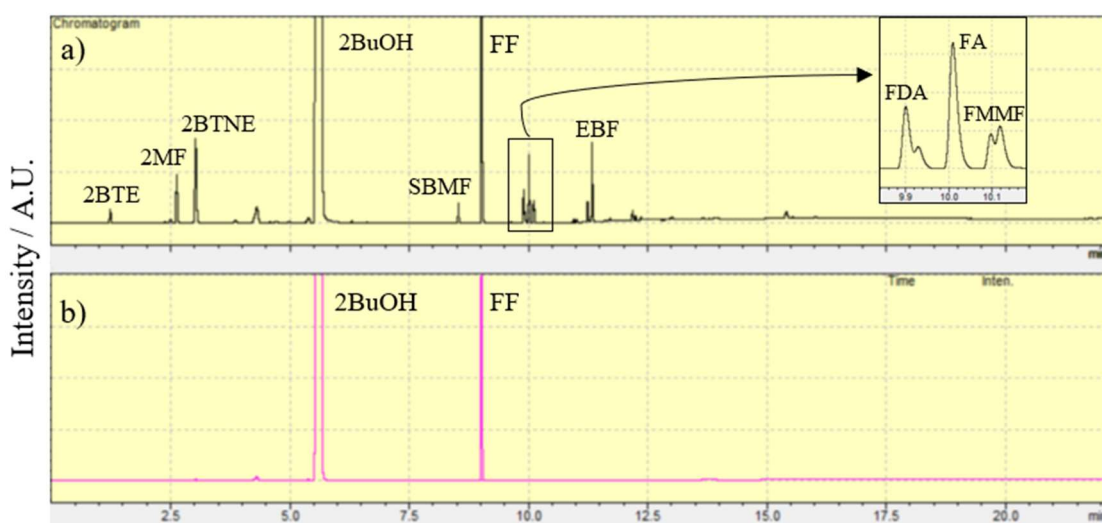
- To investigate the reactivation conditions of the Mo carbides, since this is extremely important for reactions in liquid phase;
- To evaluate the hydrodeoxygenation reaction of furfural using Mo carbides synthesized *in situ* and compare their catalytic performance with that of passivated and reactivated Mo carbide catalysts;
- To study the hydrodeoxygenation reaction of furfural in an inert atmosphere to deeply evaluate the hydrogen donating ability of the 2-butanol solvent and the ability of the supports to promote the hydrogen transfer reaction;
- To compare the different crystalline phase of Mo carbides in the hydrodeoxygenation of furfural using unsupported Mo carbides;
- To investigate the reaction mechanism by carrying out reactions with the intermediates to understand the formation of EBF and FMMF over Mo carbides;
- To perform the hydrodeoxygenation of the mixture containing the C<sub>10</sub> compounds obtained using Mo carbides under more severe conditions.

## ANNEX A - Typical chromatograms and mass spectra

The reactants and products of the furfural hydrodeoxygenation reaction were identified and quantified by the chromatographic method described in Chapter 3. The fragmentation standards were obtained from the NIST Mass Spectrometry Data Center database.

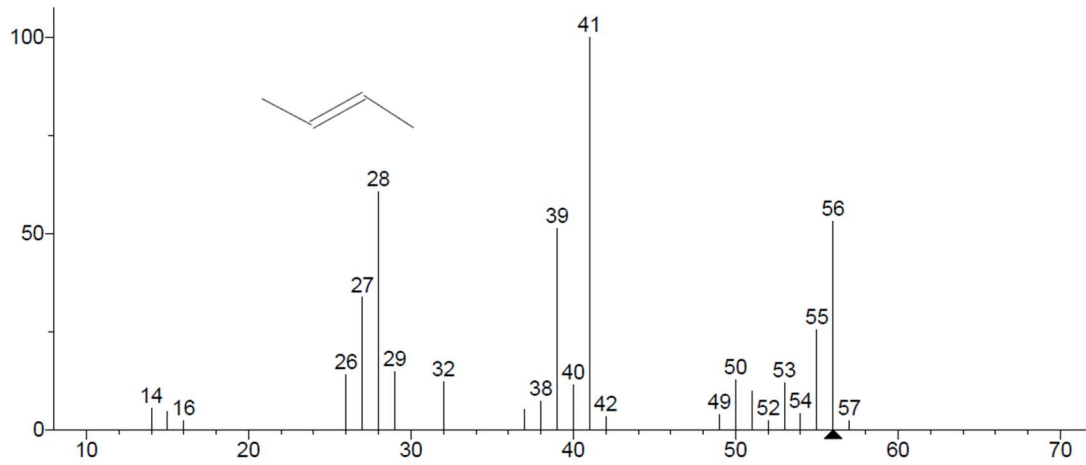
Typical chromatograms of the reaction mixture consisting of 0.25 or 0.5 M of furfural in CPME or 2BuOH and the reaction products of furfural hydrodeoxygenation using Mo carbides are presented in Figure A.1. The mass spectrum of each product is shown in Figures A.2 - A.10.

Figure A.1. Typical chromatograms of the a) reaction products for the HDO of furfural using Mo carbides-based catalysts and b) reaction mixture (0.25 or 0.5 M of FF in 2BuOH).



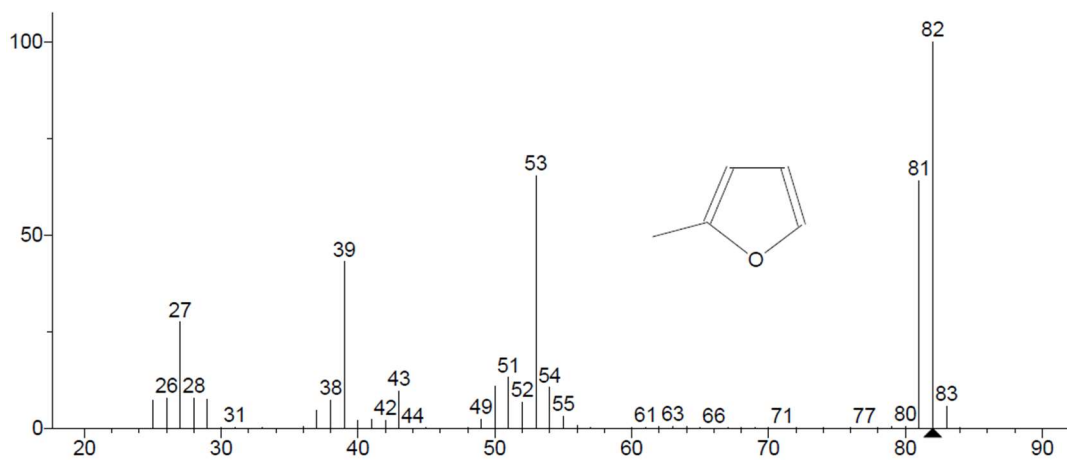
Reference: own author (2023)

Figure A.2. Mass spectrum of 2-butene (2BTE).



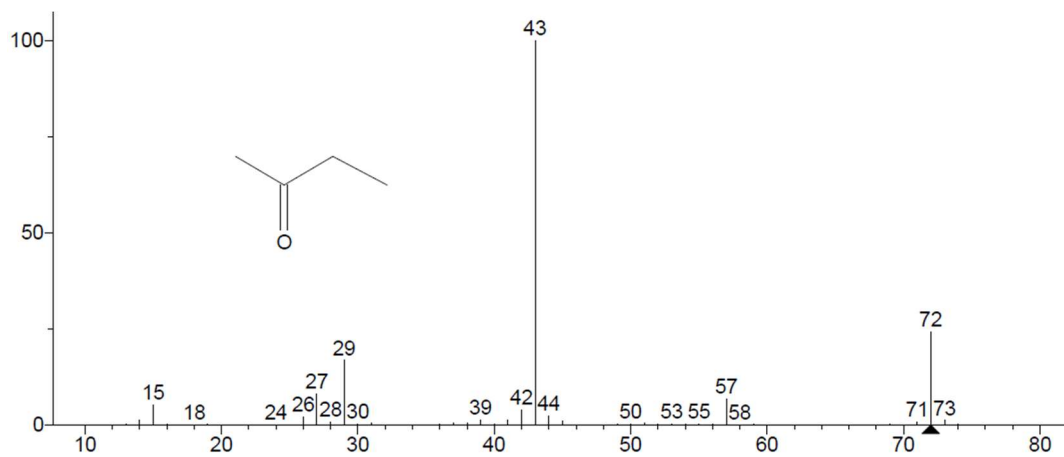
Reference: own author (2023)

Figure A.3. Mass spectrum of 2-methylfuran (2MF).



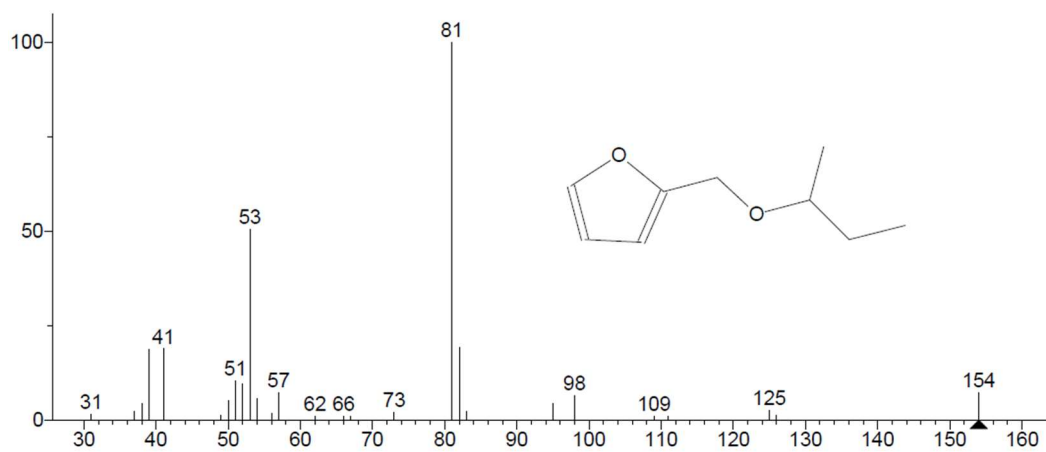
Reference: own author (2023)

Figure A.4. Mass spectrum of 2-butanone (2BTNE).



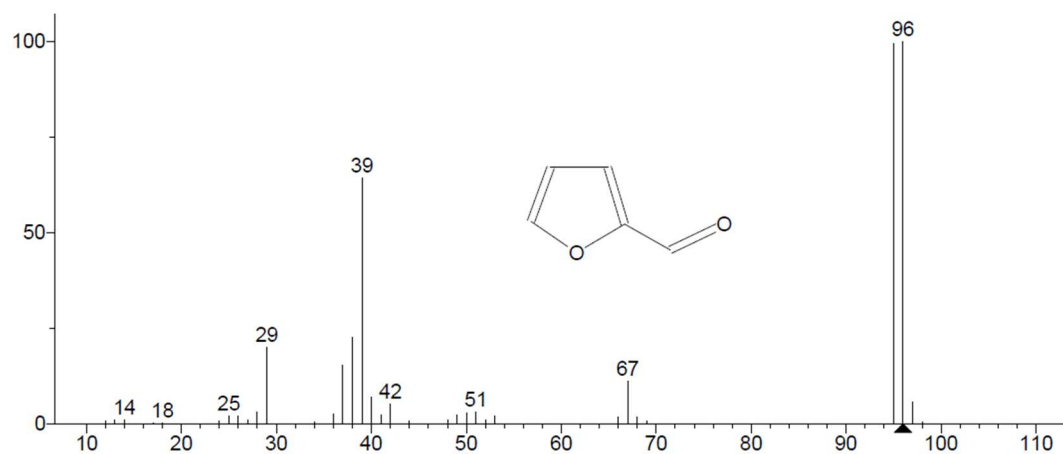
Reference: own author (2023)

Figure A.5. Mass spectrum of 2-(sec-butoxymethyl)furan (SBMF).



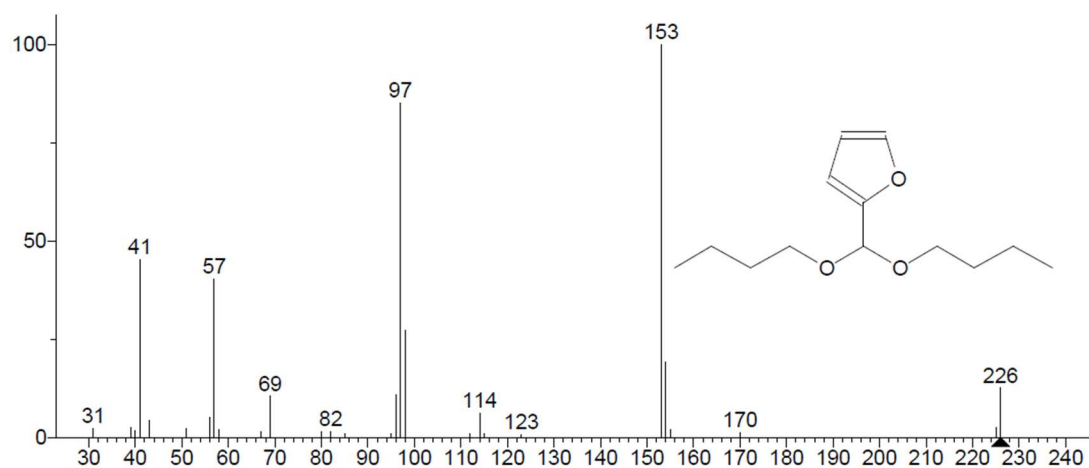
Reference: own author (2023)

Figure A.6. Mass spectrum of furfural (FF).



Reference: own author (2023)

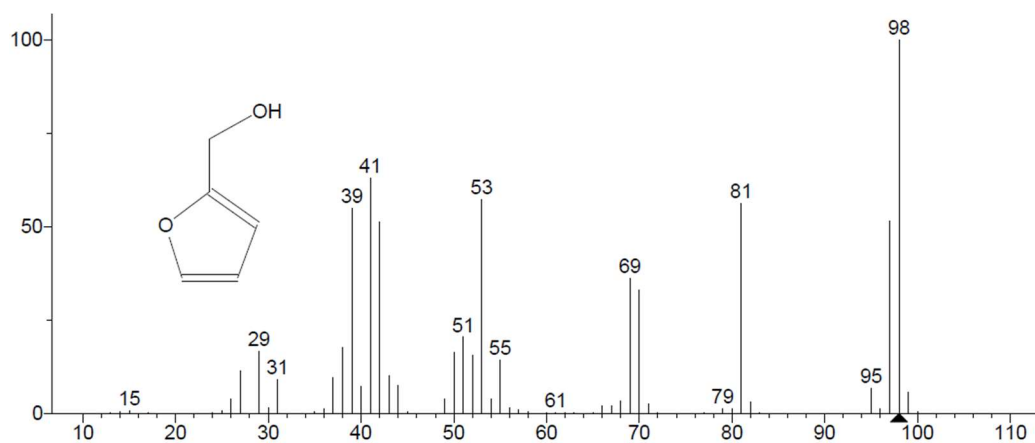
Figure A.7. Mass spectrum of 2-(dibutoxymethyl)furan (FDA).



Reference: own author (2023)

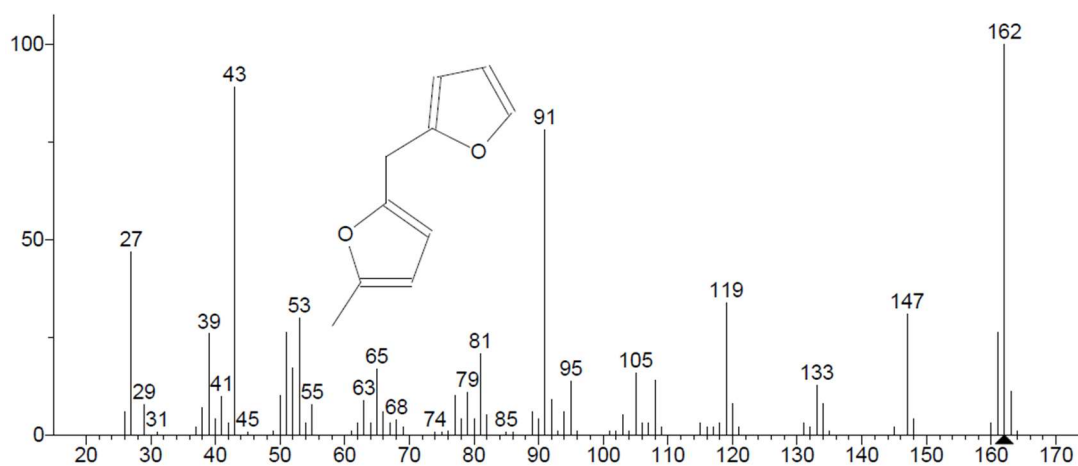


Figure A.8. Mass spectrum of furfuryl alcohol (FA).



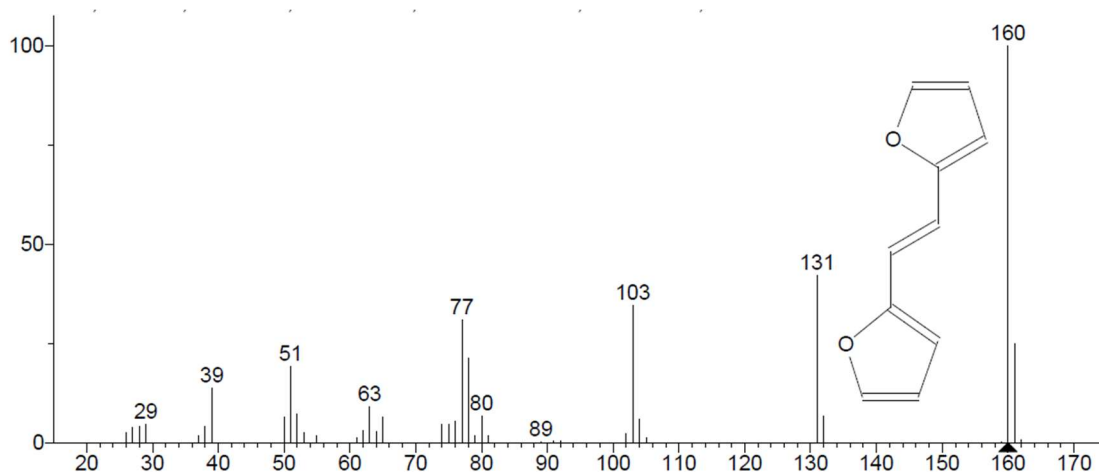
Reference: own author (2023)

Figure A.9. Mass spectrum of 2-(furan-2-methyl)-5-methylfuran (FMMF).



Reference: own author.

Figure A.10. Mass spectrum of 2,2-(1,2-ethenediyl)bis-furan (EBF).

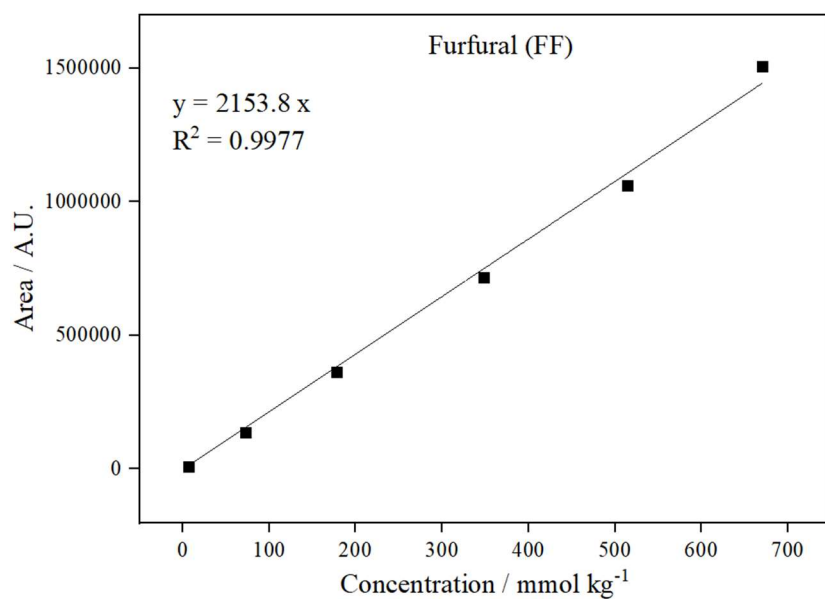


Reference: own author (2023)

Furfural (FF), Furfuryl alcohol (FA), 2-methylfuran (2MF), tetrahydrofurfuryl alcohol (THFA), 2-methyltetrahydrofuran (2MTHF), tetrahydrofuran (THF), Furan (F), cyclopentane (CPA), cyclopentene (CPE), cyclopentanone (CPO), cyclopentanol (CPOH), 1,4-pentanodiol (1,4PDO), 1,5-pentanodiol (1,5PDO), levulinic acid (LA),  $\gamma$ -valerolactona (GVL), 2-butanone (2BTNE) were used for GC calibration.

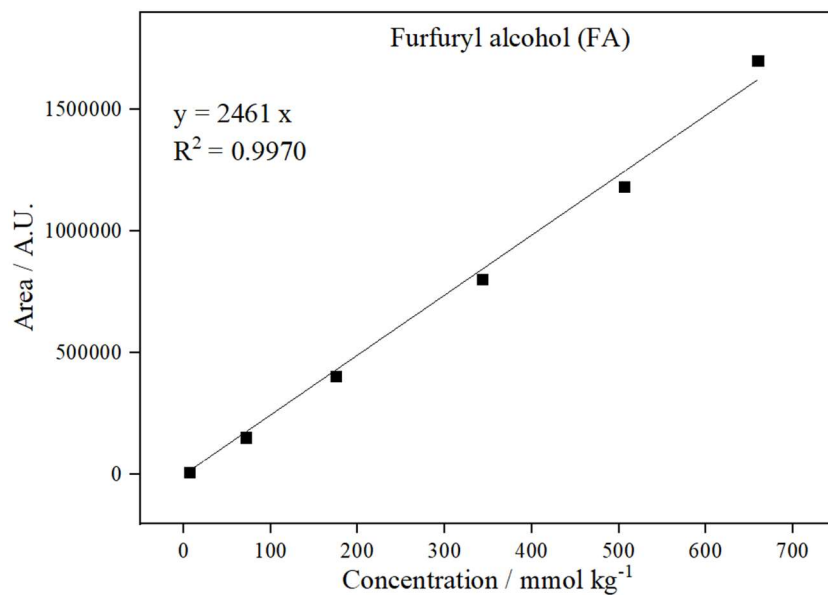
Two stock solutions (solution 1 - S<sub>1</sub> and solution 2 - S<sub>2</sub>) containing the reagents were prepared in both CPME and 2BuOH at specific concentrations: S<sub>1</sub> (CPA: 0.8 M, F: 0.8 M, 2MTHF: 0.65 M, CPOH: 0.65 M, THFA: 0.55 M, GVL: 0.55 M, 1,4PDO: 0.55 M, LA: 0.5 M) and S<sub>2</sub> (CPE: 0.8 M, THF: 0.8 M, 2MF: 0.7 M, CPO: 0.7 M, FF: 0.6 M, FA: 0.6 M, 1,5PDO: 0.5 M, 2BTNE: 0.8 M). Then these solutions were diluted in the corresponding solvent at 75, 50, 25, 10 and 1%. All the calibration curves (Figures A.11 - A.26) have a linear correlation > 99%.

Figure A.11. Calibration curve for furfural (FF) in 2-butanol.



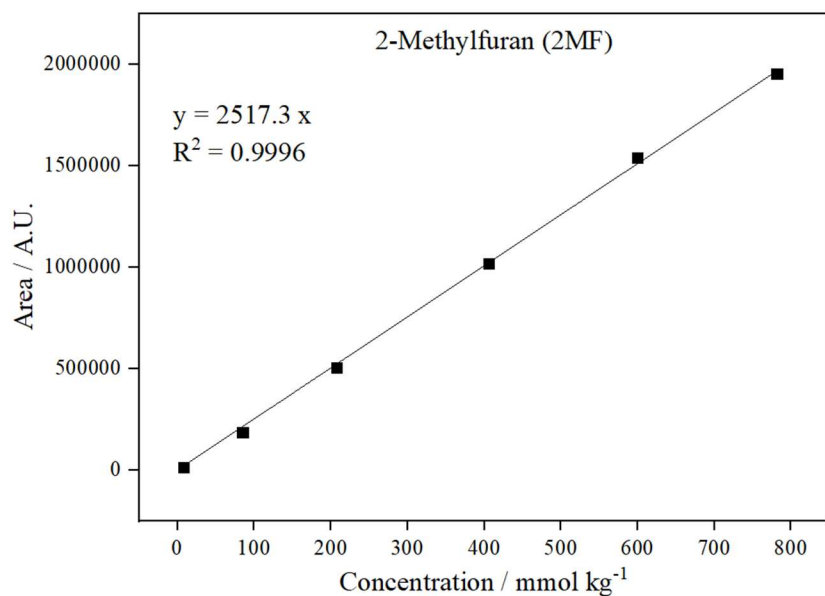
Reference: own author (2023)

Figure A.12. Calibration curve for furfuryl alcohol (FA) in 2-butanol.



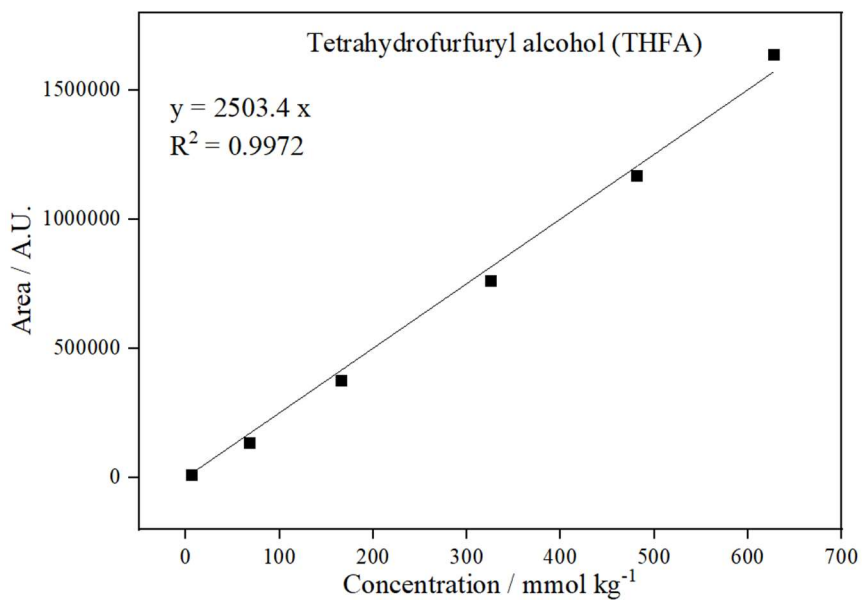
Reference: own author (2023)

Figure A.13. Calibration curve for 2-methylfuran (2MF) in 2-butanol.



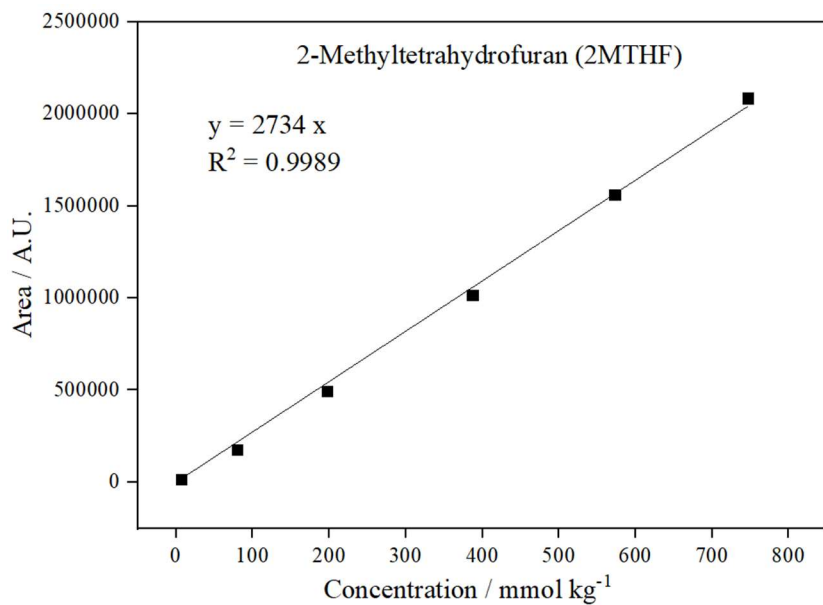
Reference: own author (2023)

Figure A.14. Calibration curve for tetrahydrofurfuryl alcohol (THFA) in 2-butanol.



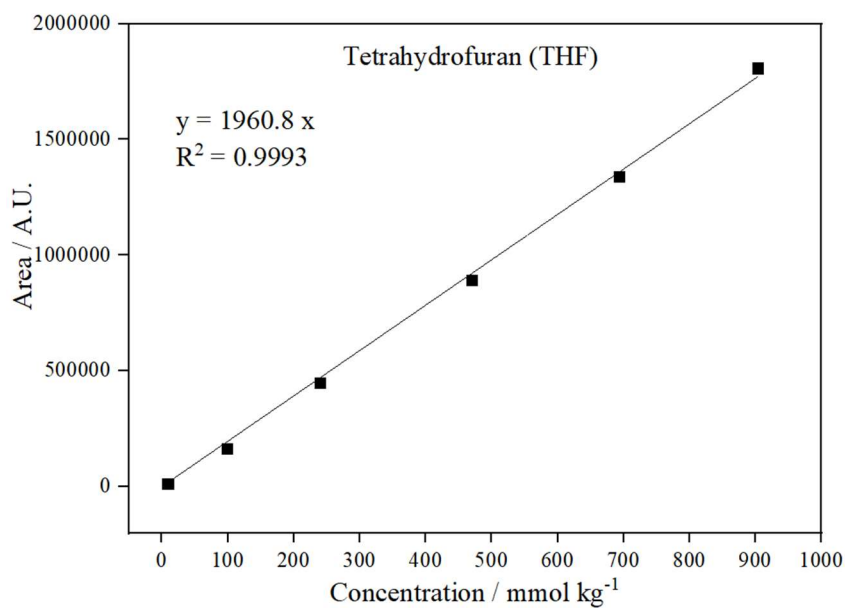
Reference: own author (2023)

Figure A.15. Calibration curve for 2-methyltetrahydrofuran (2MTHF) in 2-butanol.



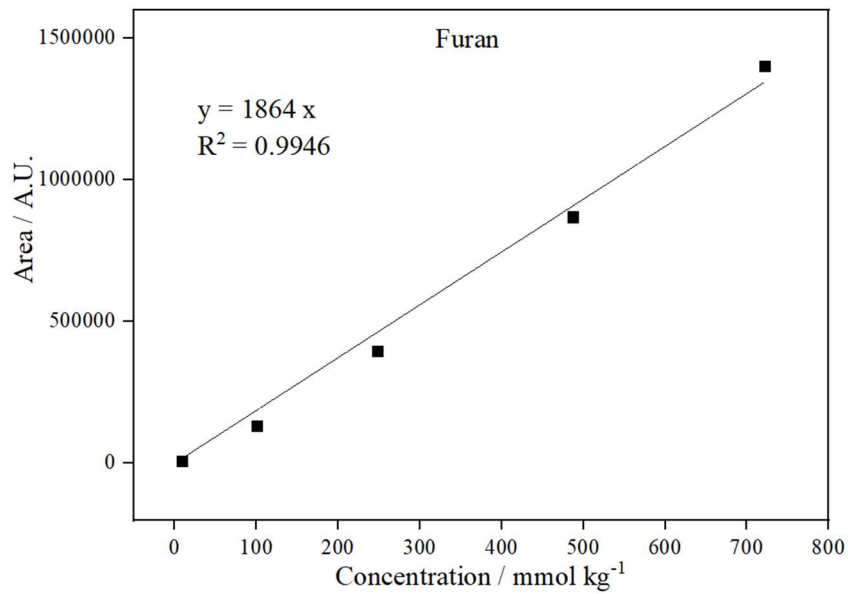
Reference: own author (2023)

Figure A.16. Calibration curve for tetrahydrofuran (THF) in 2-butanol.



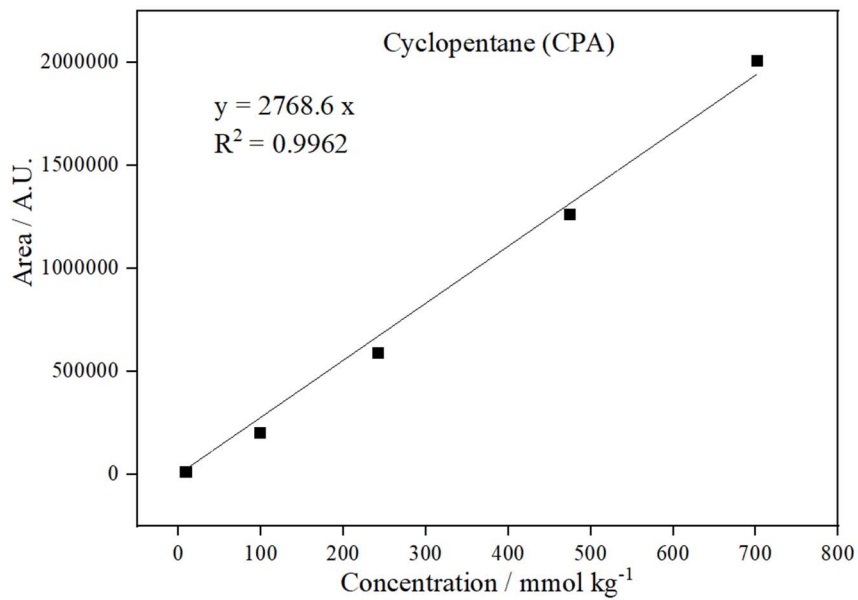
Reference: own author (2023)

Figure A.17. Calibration curve for furan (F) in 2-butanol.



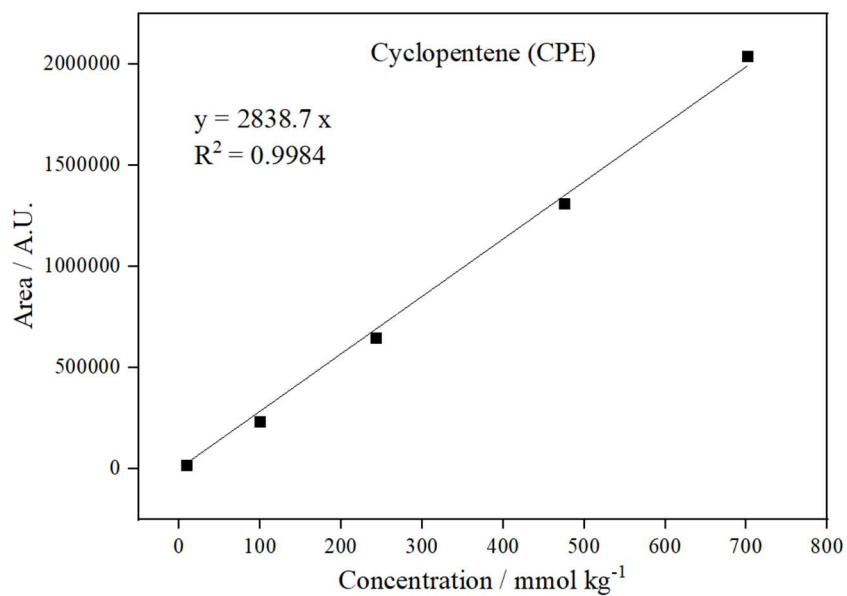
Reference: own author (2023)

Figure A.18. Calibration curve for cyclopentane (CPA) in 2-butanol.



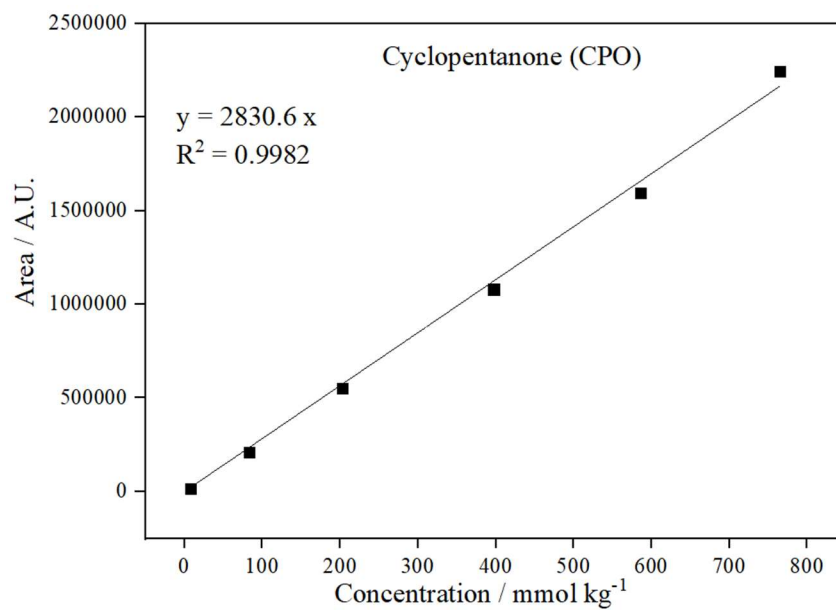
Reference: own author (2023)

Figure A.19. Calibration curve for cyclopentene (CPE) in 2-butanol.



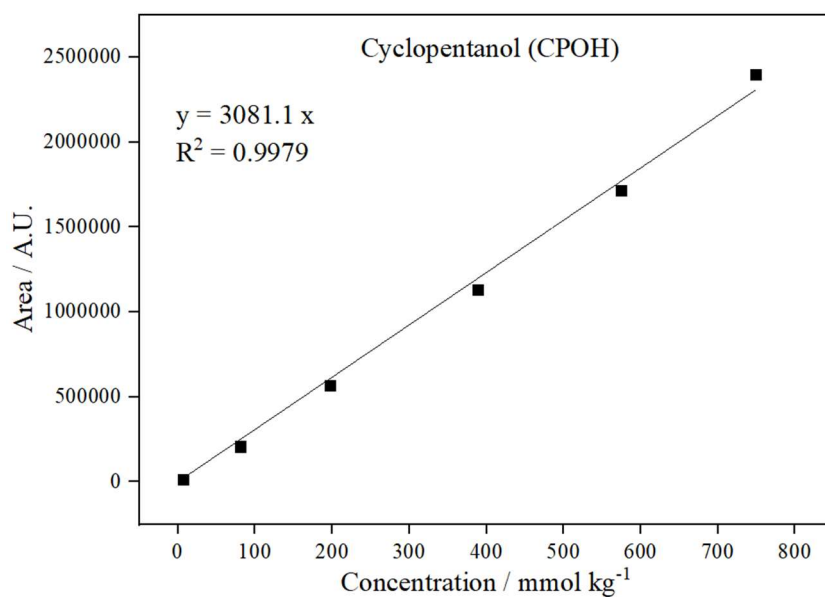
Reference: own author (2023)

Figure A.20. Calibration curve for cyclopentanone (CPO) in 2-butanol.



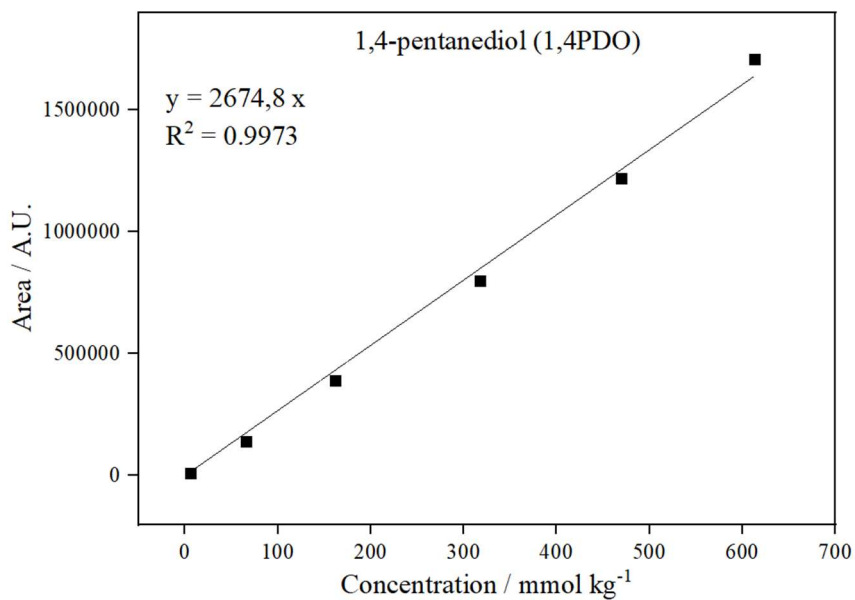
Reference: own author (2023)

Figure A.21. Calibration curve for cyclopentanol (CPOH) in 2-butanol.



Reference: own author (2023)

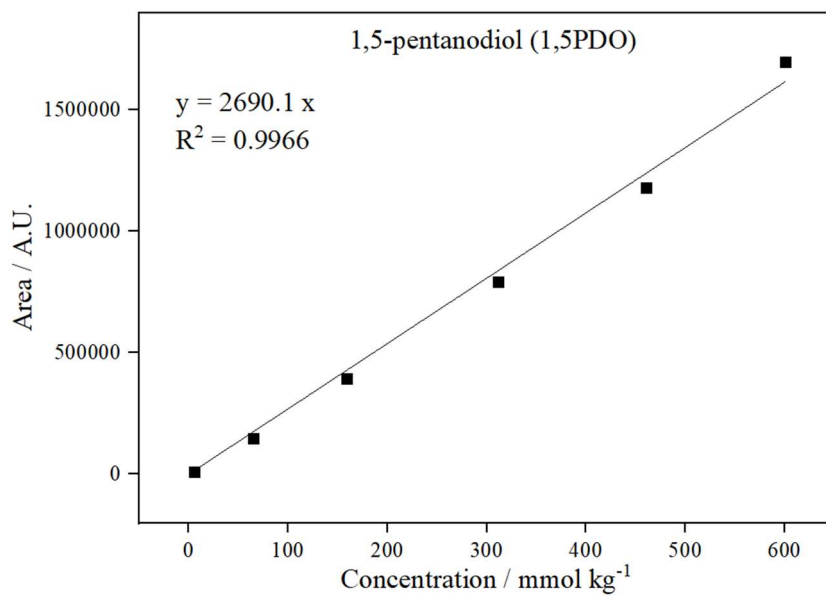
Figure A.22. Calibration curve for 1,4-pentanediol (1,4PDO) in 2-butanol.



Reference: own author (2023)

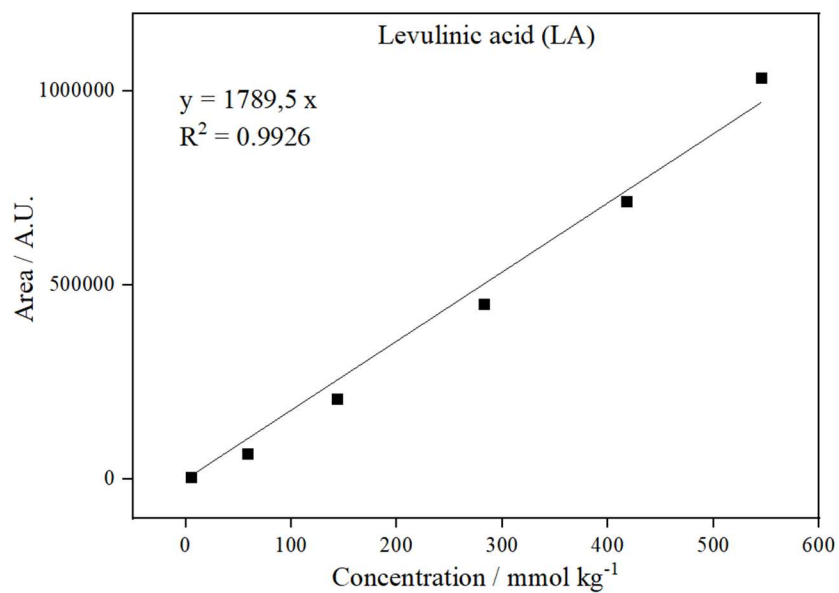


Figure A.23. Calibration curve for 1,5-pentanediol (1,5PDO) in 2-butanol.



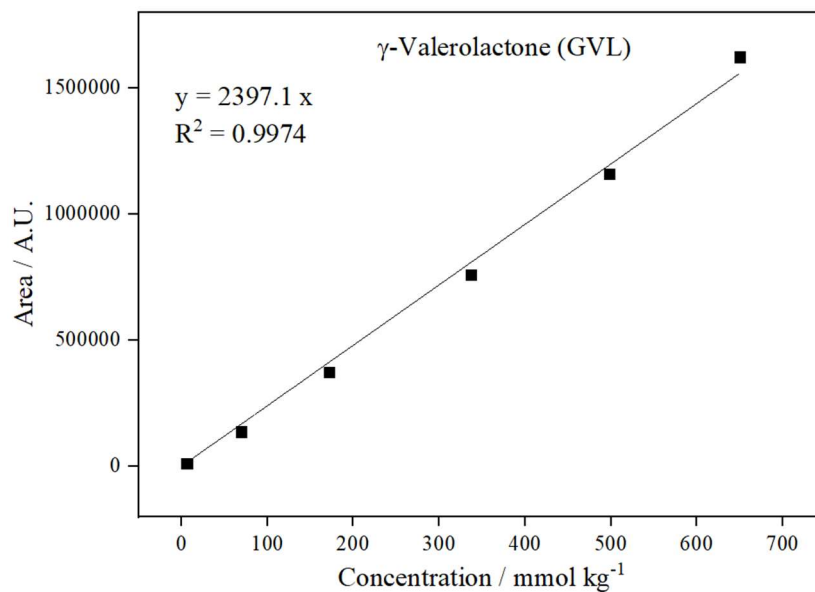
Reference: own author (2023)

Figure A.24. Calibration curve for levulinic acid (LA) in 2-butanol.



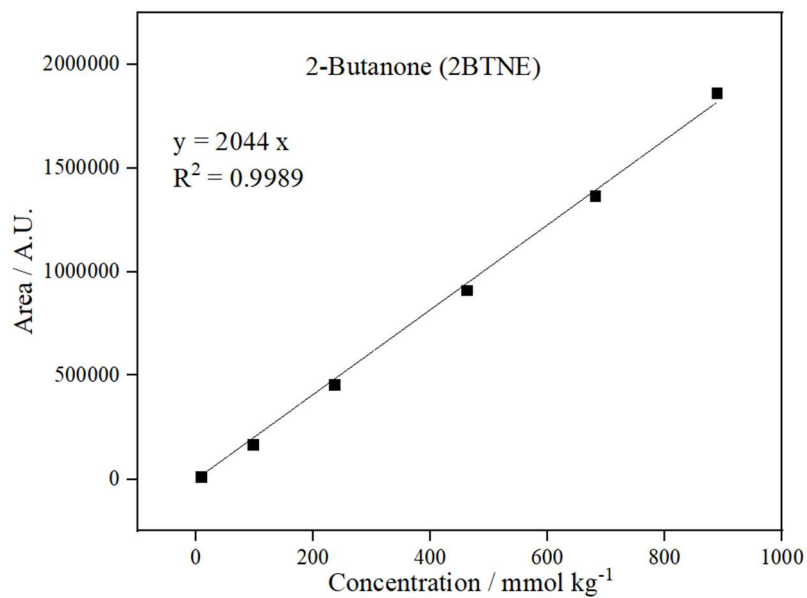
Reference: own author (2023)

Figure A.25. Calibration curve for  $\gamma$ -valerolactone (GVL) in 2-butanol.



Reference: own catalyst (2023)

Figure A.26. Calibration curve for 2-butanone (2BTNE) in 2-butanol.



Reference: own author (2023)

For the other compounds, not commercially available, identified by mass spectrometry such as 2-(sec-butoxymethyl)furan (SBMF), 2-(dibutoxymethyl)furan

(FDA), 2,5-bis(furan-2-ylmethyl)furan (BFMF), 1,2-di-2-furyl-1,2-ethanediol (DFE), 2-(furan-2-methyl)-5-methylfuran (FMMF), 2,2-(1,2-ethenediyl)bis-furan (EBF), 5-hydroxy-2-pentanone (HPTE) and sec-butyl 4-oxopentanoate (SBOP), the quantification was performed using the effective carbon number (ECN) concept. This methodology considers the use of a flame ionization detector (FID) for quantification. The FID response is proportional to the number of carbons in a saturated aliphatic molecule, so when the complexity of the molecular structure increases there will be a decrease in the FID response. These deviations will occur in a predictable way depending on the functional groups in the molecule according to Faiola *et al.*, (2012).

This methodology was validated in this work by comparing the calibration made for the commercial reagents and the response factors (RF) obtained by ECN calculations (Tables A.1 - A.4). The substrate FF was always used as reference. For this, the Equations A.1 - A.5 was used.

$$T_{ECN}M = CN + ON \quad \text{Equation 7.1}$$

$$RF_{theor.} = \frac{T_{ECN}M}{T_{ECN}FF} \quad \text{Equation 7.2}$$

$$\alpha_{theor.} = RF_{theor.}M \times \alpha_{exper.}FF \quad \text{Equation 7.3}$$

$$RF_{exp.}M = \frac{\alpha_{exp.}M}{\alpha_{exp.}FF} \quad \text{Equation 7.4}$$

$$error (\%) = \frac{RF_{theor.} - RF_{exp.}M}{RF_{theor.}M} \quad \text{Equation 7.5}$$

where

$T_{ECN}M$  is the total effective carbon number of a molecule,

$T_{\text{ECNFF}}$  is the total effective carbon number of furfural,

CN is the carbon number contribution,

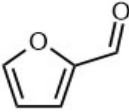
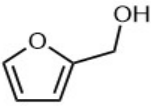
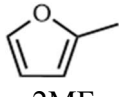
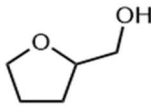
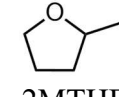
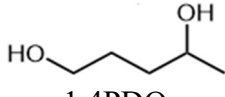

ON is the oxygen number contribution,

$RF_{\text{theor.}}$  is the theoretical FID response factor,

$A_{\text{exp.}}\text{FF}$  is the experimental FID response factor of FF,

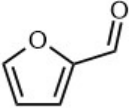


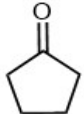
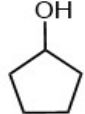

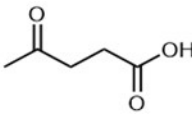
$\alpha_{\text{theor.}}$  is the theoretical FID response factor of a molecule.

Table A.1. Comparison of the experimental and theoretical response factors of the commercially available compounds determined by calibration and ECN calculation, respectively.

Contribution		Value	Compound						
			 FF	 FA	 2MF	 THFA	 2MTHF	 1,4PDO	 GVL
carbon number (CN)	aliphatic	1	0	1	1	5	5	5	4
	aromatic	1	4	4	4	0	0	0	0
	carbonyl	0	0	0	0	0	0	0	0
	carboxyl	0	0	0	0	0	0	0	0
	olefinic	0.95	0	0	0	0	0	0	0
oxygen number (ON)	ether	-1	-1	-1	-1	-1	-1	0	-1
	primary alcohol	-0.6	0	-0.6	0	-0.6	0	-0.6	0
	secondary alcohol	-0.75	0	0	0	0	0	-0.75	0
	tertiary alcohol or ester	-0.25	0	0	0	0	0	0	0
Total ( $T_{ECN}$ )			3	3.4	4	3.4	4	3.65	3
$RF_{theor.}$			1	1.13	1.33	1.13	1.33	1.22	1
$\alpha_{theor.}$			2235	2533	2979	2533	2979	2719	2235
$\alpha_{exper.}$			2235	2492	2812	2472	3012	2556	2334
$RF_{exper.}$			1	1.12	1.26	1.11	1.35	1.14	1.04
error (%)			-	1	12	2	2	7	4

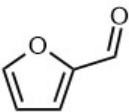
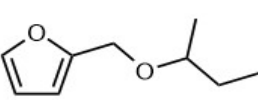
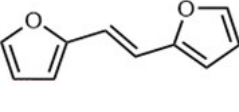
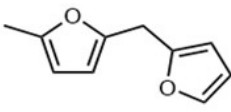
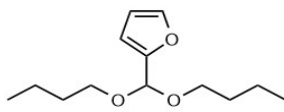
Reference: own author (2023)

Table A.2. Comparison of the experimental and theoretical response factors of the commercially available compounds determined by calibration and ECN calculation, respectively.

Contribution		Values	Compound						
			 FF	 F	 THF	 CPO	 CPOH	 1,5PDO	 LA
carbon number (CN)	aliphatic	1	0	0	4	4	5	5	3
	aromatic	1	4	4	0	0	0	0	0
	carbonyl	0	0	0	0	0	0	0	0
	carboxyl	0	0	0	0	0	0	0	0
	olefinic	0.95	0	0	0	0	0	0	0
oxygen number (ON)	ether	-1	-1	-1	-1	0	0	0	0
	primary alcohol	-0.6	0	0	0	0	0	-1.2	0
	secondary alcohol	-0.75	0	0	0	0	-0.75	0	0
	tertiary alcohol or ester	-0.25	0	0	0	0	0	0	0
	Total ( $T_{ECN}$ )		3	3	3	4	4.25	3.80	3
	$RF_{theor.}$		1	1	1	1.33	1.42	1.27	1
	$\alpha_{theor.}$		2235	2235	2235	2979	3166	2830	2235
	$\alpha_{exper.}$		2235	1911	2128	2965	3048	2765	2005
	$RF_{exper.}$		1	0.86	0.95	1.33	1.36	1.24	0.9
	error (%)		-	14	5	0	4	2	10

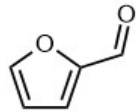
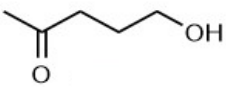
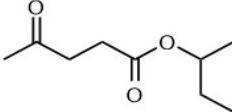
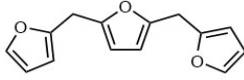
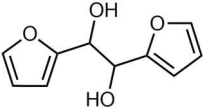
Reference: own author (2023)

Table A.3. Determination of the theoretical response factors of the non-commercially available compounds determined by ECN calculation considering FF as reference.

Contribution		Compound					
		Value	 FF	 SBMF	 EBF	 FMMF	 FDA
carbon number (CN)	aliphatic	1	0	5	0	2	9
	aromatic	1	4	4	8	8	4
	carbonyl	0	0	0	0	0	0
	carboxyl	0	0	0	0	0	0
	olefinic	0.95	0	0	1.9	0	0
oxygen number (ON)	ether	-1	-1	-2	-2	-2	-3
	primary alcohol	-0.6	0	0	0	0	0
	secondary alcohol	-0.75	0	0	0	0	0
	tertiary alcohol or ester	-0.25	0	0	0	0	0
Total ( $T_{ECN}$ )			3	7	7.9	8	10
$RF_{theor}$			1	2.33	2.63	2.67	3.33
$\alpha_{theor}$			2235	5214	5884	5959	7449

Reference: own author (2023)

Table A.4. Determination of the theoretical response factors of the non-commercially available compounds determined by ECN calculation considering FF as reference.

Contribution		Compound					
		Value	 FF	 HPTE	 SBOP	 BFMF	 DFE
carbon number (CN)	aliphatic	1	0	4	7	2	2
	aromatic	1	4	0	0	12	8
	carbonyl	0	0	0	0	0	0
	carboxyl	0	0	0	0	0	0
	olefinic	0.95	0	0	0	0	0
oxygen number (ON)	ether	-1	-1	0	0	-3	-2
	primary alcohol	-0.6	0	-0.6	0	0	0
	secondary alcohol	-0.75	0	0	0	0	-1.5
	tertiary alcohol or ester	-0.25	0	0	-0.25	0	0
Total ( $T_{ECN}$ )			3	3.4	7	11	6.5
$RF_{theor}$			1	1.13	2.33	3.67	2.17
$\alpha_{theor.}$			2235	2533	5214	8194	4842

Reference: own author (2023)



## **A.1. References**

Faiola, C.L., Erickson, M.H., Fricaud, V.L., Jobson, B.T., VanReken, T.M., 2012. Quantification of biogenic volatile organic compounds with a flame ionization detector using the effective carbon number concept. *Atmospheric Meas. Tech.* 5, 1911–1923. <https://doi.org/10.5194/amt-5-1911-2012>